

ABSTRACT

KESHAVARZI, BEHROOZ. Prediction of Thermal Cracking in Asphalt Pavements Using Simplified Viscoelastic Continuum Damage (S-VECD) Theory. (Under the direction of Dr. Y. Richard Kim).

Thermal cracking, which is usually manifested as a series of parallel, surface-initiated cracks, is one of the major types of distress in asphalt concrete pavements built in cold regions where air temperature shows a significant drop. Propagation of thermal cracks in asphalt layers will eventually allow water to come into the pavement system and causes deterioration of pavement structure which in turn reduces its serviceability. In addition, asphalt pavement sections constructed in warmer regions experience significant daily temperature variation and tolerate thermal cracks.

The Asphalt concrete is a viscoelastic material which its response depends on loading rate and temperature. ANY failure criterion should be able to consider loading rate and temperature into consideration. Simplified viscoelastic continuum damage (S-VECD) is a continuum damage approach that is able to model macrocrack evolution with parameters that are measurable at the macroscale level.

In this study, to characterize the material behavior in monotonic loading, uniaxial direct tension monotonic test is performed on asphalt mixtures that have different percent of reclaimed asphalt pavement (RAP) content. It is shown that the measured evolution of stress during the test up to strength value can be predicted using S-VECD model that is characterized by the Asphalt Mixture Performance Tester (AMPT) dynamic modulus and cyclic fatigue tests.

The coefficient of thermal contraction (CTC) transfers temperature drop to the thermal strain. This research performs a comprehensive review on the suggested procedure for measuring

and predicting the CTC parameters and suggests a composite model for predicting the CTC of mixtures. The accuracy of the proposed procedure was tested and verified through the measurements conducted and reported in previous research efforts as well as the measurements performed at North Carolina State University (NCSU).

The mixture stiffness transfers induced thermal strain to the thermal stress. The estimation of mixture modulus at low temperature region has an important effect on the calculated thermal stress. In addition, the time-temperature shift factor is used to calculate the reduced rate and the reduced frequency. This research investigates different suggested forms of dynamic modulus mastercurve and time-temperature shift factor functions and picks the final form that is able to estimate the mixture modulus for a wide range of frequency.

The failure criterion intends to predict the failure for asphalt mixture. This study measures the dissipated pseudo strain energy (DPSE) developed during the uniaxial direct tension monotonic test and expresses it as a function of reduced strain rate. In addition, S-VECD-based framework is developed and verified to predict the DPSE value based on the given reduced strain rate. It is shown that the DPSE criterion is able to predict the fracture stress and fracture temperature in thermal stress restrained specimen test (TSRST). The accuracy of DPSE criterion is further verified through predicting the fracture temperature of mixtures that have a different range of RAP content, binder content, binder PG grade, and aging levels. It is shown that DPSE criterion is able to rank the mixture based on the expected performance.

A structural framework, FlexTC, was developed to predict the performance of asphalt concrete pavement sections subjected to air temperature variation. FlexTC is able to calculate the response of pavement sections subjected to air temperature variation and predicts thermal stress and associated thermal damage. FlexTC is able to update material properties based on

temperature, reduced rate, and aging level. FlexTC defines experienced damage through the damage factor (DF) parameter and ranks the sections based the DF value.

© Copyright 2019 by Behrooz Keshavarzi
All Rights Reserved

Prediction of Thermal Cracking in Asphalt Pavements Using Simplified Viscoelastic Continuum
Damage Theory

by
Behrooz Keshavarzi

A thesis submitted to the Graduate Faculty of
North Carolina State University
in partial fulfillment of the
requirements for the degree of
Doctor of Philosophy

Civil Engineering

Raleigh, North Carolina

2019

APPROVED BY:

Dr. Y. Richard Kim
Committee Chair

Dr. Murthy N. Guddati

Dr. Cassie Castorena

Dr. Ranji Ranjithan

DEDICATION

To the magnificence of God and to my parents and my brother, who always sacrifice their comfort for me and made this work possible with their endless love and support.

BIOGRAPHY

Behrooz was born as a first child of two children to Mehdi and Zohreh Keshavarzi in Tehran, Iran on September 15, 1986. He attended Atomic Energy High School for talented students and graduated in 2004. He entered Amirkabir university of Technology (AUT) in 2004 and earned a bachelor's degree in Civil Engineering in 2008. Behrooz studied Structural Engineering as a master student at Sharif University of Technology (SUT) in 2009 under the direction of Professor Ali Bakhshi. Behrooz focused on the effect of near field seismic excitation on the performance of reinforced cement concrete frames. In January 2013, Behrooz enrolled in North Carolina State University to pursue his Doctor of Philosophy in Transportation Materials under the guidance of Professor Youngsoo Richard Kim. Behrooz's PhD research has been supported by Federal Highway Administration. Behrooz earned his PhD degree in 2019.

ACKNOWLEDGMENTS

I would like to thank Professor. Y. Richard Kim and M. N. Guddati, for their support and sincere friendship. I would never be able to accomplish this work without their continuous support of my research.

Secondly, I would like to thank all of the committee members Dr. Cassie Castorena and Dr. Ranji Ranjithan for their invaluable recommendations. Special thanks for Dr. Mehran Eslaminia who helped me to grasp the LVECD software when I first came in.

Also, I really feel grateful to work with my friends and colleagues including Amirhosein Norouzi, Mohammad Sabouri, Shayan Safavizadeh, Afshin Karshenas, Luis Alberto Herrmann do Nascimento, Michael D. Elwardany, Farinaz Safaie, Mary Rawls, Arash Dehghan Banadaki, Meron Getachew, Amir Ghanbari, Sonja Pape, Kangjin “Caleb” Lee, Yizhuang David Wang, Jaehoon Jeong, Jaemin Heo, Douglas Mocelin, Felipe Pivetta, Noorhuda F. Saleh, Nithin Sudarsanan, Allen Zhe Zeng, Lei Xue, Jing Ding, Elizabeth Brawls, Ern-Yeong Song, Mukesh Ravichandran, Narges Matini, Boris Goenaga, and Saqib Golzar.

I would like to express my sincere appreciation to my friends including Ashtad Javanmardi, Alireza Abbasian, Soha Baziar, Shirin Joybanpour, Shayan Hosseini, Shivpal Yadav, Milad Hallaji, Ali Tohidi, Navid Zolghadri, Khashayar Asadi, Mojtaba Noghabaie, Abdullah Alsharef, Abilash Kusam, Ali Marjani, Mehdi Habibpour, Javid H. Hosseini, Niloofar Ghanbari, Sara Yaghobi, Amirhosein Mazrouie, Amin Rafiei, Morteza Jafarabadi, Amir Koolivand, Arash Bozorgi, Hamid Kazem, and Hamid Hooshmandi. My former colleagues, Diane Gilmore and Allen Piper also deserve much appreciation.

TABLE OF CONTENTS

LIST OF TABLES	viii
LIST OF FIGURES	ix
CHAPTER 1. INTRODUCTION	1
1.1. Introduction.....	1
1.2. Objectives	4
1.3. Dissertation Organization	5
CHAPTER 2. A VISCOELASTIC-BASED MODEL FOR PREDICTING THE STRENGTH OF ASPHALT COCNRETE IN DIRECT TENSION	7
2.1. Introduction.....	7
2.2. Objectives	11
2.3. Theoretical Background.....	11
2.3.1. VECD Theory	11
2.4. Materials and Test Method	15
2.4.1. Materials	15
2.4.2. Testing.....	16
2.5. Results.....	17
2.5.1. Monotonic Simulations.....	17
2.6. Conclusion	23
CHAPTER 3. EXTRAPOLATION OF DYNAMIC MODULUS DATA FOR ASPHALT CONCRETE AT LOW TEMPERATURES	24
3.1. Abstract	24
3.2. Introduction.....	25
3.2.1. Analytical Models.....	27
3.2.1.1. Models for Dynamic Modulus Mastercurve	28
3.2.1.2. Models for time-temperature shift factor.....	31
3.3. Materials and Specimen Fabrication.....	33
3.4. Test Method	36
3.5. Results and Discussion	36
3.6. Conclusions.....	57
CHAPTER 4. A COMPOSITE MODEL FOR PREDICTING THE COEFFICIENT OF THERMAL CONTRACTION FOR ASPHALT CONCRETE MIXTURES	59
4.1. Abstract:.....	59

4.2. Introduction.....	60
4.2.1. Measuring the Coefficient of Thermal Contraction of Asphalt Mixtures.....	61
4.2.2. Predicting the Coefficient of Thermal Contraction of Asphalt Mixtures	65
4.3. Materials and Testing.....	70
4.4. Methodology	79
4.5. Discussion of Results	93
4.6. Conclusions.....	97
CHAPTER 5. A DISSIPATED PSEUDO STRAIN ENERGY-BASED FAILURE CRITERION FOR THERMAL CRACKING AND ITS VERIFICATION USING THERMAL STRESS RESTRAINED SPECIMEN TESTS	99
5.1. Abstract:.....	99
5.2. Introduction:.....	100
5.2.1. Review of Literatures on the TSRST	102
5.3. Test Methods:.....	105
5.3.1. Dynamic Modulus Testing.....	106
5.3.2. Direct Tension Cyclic Fatigue Testing	107
5.3.3. Direct Tension Monotonic Testing	107
5.3.4. TSRST.....	107
5.4. Materials	108
5.5. Development of Dissipated Pseudo Strain Energy Failure Criterion	114
5.6. Application of DPSE Failure Criterion to Prediction of TSRST Results	122
5.7. Verification of Proposed Methodology for Prediction of TSRST Results	129
5.8. Conclusions.....	137
CHAPTER 6. FLEXTC: A THERMAL CRACKING ANALYSIS FRAMEWORK FOR ASPHALT PAVEMENTS.....	139
6.1. Abstract:.....	139
6.2. Introduction:.....	139
6.3. Existing Thermal Cracking Prediction Models.....	141
6.4. FlexTC	145
6.4.1. Input Material Properties	146
6.5. Methodology:.....	149
6.5.1. Thermal Loading:.....	149
6.5.2. Structural Analysis.....	150

6.5.3. Study Pavement Sections	155
6.6. Materials and Test Methods.....	156
6.6.1. Test Methods.....	160
6.6.1.1. Dynamic Modulus Testing.....	160
6.6.1.2. AMPT Cyclic Fatigue Testing.....	160
6.6.1.3. Correlating Measured Data to Field Conditions	160
6.7. Results:.....	162
6.7.1. Measured Mixture Properties:.....	162
6.8. Structural Simulation Results	170
6.9. Predicted Fracture Temperature in TSRST:	176
6.10. Predicted Maximum Experienced DF.....	177
6.11. Discussion of Results.....	179
6.12. Conclusion	181
APPENDICES	190
Appendix A. Applying non-uniform fourier finite method in analyzing asphalt concrete pavements	191
Appendix B. Investigation into fatigue damage growth direction in asphalt concrete pavement sections based on simplified viscoelastic continuum damage (s-vecd) theory.....	212

LIST OF TABLES

Table 2.1. Study mixtures properties	15
Table 3.1. Mixture information for first group	34
Table 3.2. Mixture information for second group	35
Table 4.1. Binder information for first dataset	72
Table 4.2. Mixture information for first dataset	72
Table 4.3. Mixture information for second dataset.....	73
Table 4.4. Results of LVDT calibration.....	75
Table 4.5. Fitting results for mixtures tested	77
Table 4.6. Summary of mixtures used to backcalculate binder shear modulus from mixtures dynamic modulus	85
Table 5.1. Test methods and test purposes for four material groups	109
Table 5.2. Mixture properties for material group 1: North Carolina mixture and Vermont mixtures.....	110
Table 5.3. Mixture properties for material group 2: New Hampshire and New York mixtures..	112
Table 5.4. Mixture properties for material group 3: New Hampshire mixtures with changing mixture designs	113
Table 5.5. Details for material group 4: Texas, Washington, South Dakota, and North Carolina mixtures.....	114
Table 5.6. Thermal coefficients for material groups 1 and 2.....	124
Table 5.7. Thermal coefficients for materials groups 3 and 4	125
Table 5.8. Thermal coefficients for material group 4	126
Table 6.1. Details regarding pavement sections used in this research.....	156
Table 6.2. Properties of study mixtures	157
Table 6.3. Selected mixture paiRS in Mnroad sections	158
Table 6.4. Aging durations for eleven mixtures	159
Table 6.5. Climatic aging index values as functions of time and depth for Mnroad sections	161
Table 6.6. Climatic aging index values as functions of time and depth for North Carolina sections.....	161
Table 6.7. Comparisons of expected data, field survey data, predicted fracture temperatures ,and FlexTC rankings for Mnroad pavement sections.....	181
Table A.1. Selected frequency values (hz)	200
Table A.2. Coordinates of the selected points in the NCAT sections.....	208
Table A.3. Coordinates of the selected points in the MIT sections	208

LIST OF FIGURES

Figure 2-1. Test data and prediction results for RS9.5b mix.....	18
Figure 2-2. Test data and prediction results for Vta00 mixture.....	18
Figure 2-3. Test data and prediction results for Vta20 mixture.....	19
Figure 2-4. Test data and prediction results for Vta30 mixture.....	19
Figure 2-5. Test data and prediction results for Vta40 mixture.....	20
Figure 2-6. Test data and prediction results for Vte00 mixture.....	20
Figure 2-7. Test data and prediction results for Vte20 mixture.....	21
Figure 2-8. Test data and prediction results for Vte30 mixture.....	21
Figure 2-9. Test data and prediction results for Vte40 mixture.....	22
Figure 2-10. Predicted ν RSus measured strength values for all the study mixtures.....	22
Figure 3-1. Example for using the uNConstrained shift method: (a) measured dynamic modulus data for MIT RAP 50SB and (b) finding the shift factor for $t = 0^\circ\text{C}$	37
Figure 3-2. Dynamic modulus mastercurves obtained from uNConstrained shift method in semi-log space: (a) NC RS9.5b, (b) NC RS9.5b WMA, (c) NY surface, (d) MIT RAP 50SB, (e) MIT Control, (f) MIT Advera, and (g) MIT Sasobit.....	39
Figure 3-3. Dynamic modulus mastercurves obtained from unconstrained shift method in log-log space: (a) NC RS9.5b, (b) NC RS 9.5B WMA, (c) NY surface, (d) MIT RAP 50SB, (e) MIT Control, (f) MIT Advera, and (g) MIT Sasobit.....	40
Figure 3-4. Dynamic modulus mastercurves obtained from different fitting and shift methods in semi-log space: (a) NC RS9.5B, (b) NC RS 9.5b WMA, (c) NY surface, (d) MIT RAP 50SB, (e) MIT Control, (f) MIT Advera, and (g) MIT Sasobit	41
Figure 3-5. Dynamic modulus mastercurves obtained from the different fitting and shifting methods in log-log space: (a) NC RS9.5b, (b) NC RS 9.5B WMA, (c) NY Surface, (d) MIT RAP 50SB, (e) MIT Control, (f) MIT Advera, and (g) MIT Sasobit.	43
Figure 3-6. Time-temperature shift factors obtained from the different shift methods: (a) NC RS9.5b, (b) NC RS 9.5b WMA, (c) NY surface, (d) MIT RAP 50sb, (e) MIT control, (f) MIT advera, and (g) MIT sasobit.	45
Figure 3-7. Dynamic modulus mastercurves obtained from the liMiTEd data set using different fitting and shift methods: (a) NC RS9.5b, (b) NC RS 9.5b WMA, (c) NY surface, (d) MIT RAP 50sb, (e) MIT control, (f) MIT advera, and (g) MIT sasobit.....	47
Figure 3-8. Dynamic modulus mastercurves calculated from the liMiTEd data set using different fitting and shift methods: (a) NC RS9.5b, (b) NC RS 9.5b WMA, (c) NY surface, (d) MIT RAP 50SB, (e) MIT control, (f) MIT advera, and (g) MIT sasobit.....	48
Figure 3-9. Dynamic modulus mastercurves obtained from the liMiTEd data set using different fitting and shift methods: (a) NC RS9.5b, (b) NC RS 9.5b WMA, (c) NY surface, (d) MIT RAP 50sb, (e) MIT control, (f) MIT advera, and (g) MIT sasobit.....	49
Figure 3-10. Phase angle mastercurve functions determined from the liMiTEd dataset using the 2S2P1D function: (b) NC RS 9.5b WMA, (c) NY surface, (d) MIT RAP 50SB, (e) MIT Control, (f) MIT Advera, and (g) MIT Sasobit.	52

Figure 3-11. Dynamic modulus mastercurve, (b) time-temperature shift factor, and (c) phase angle mastercurve. (1) ALF- control, (2) ALF-SBS, (3) ALF-Terpolymer, and (4) ALF- Crumb rubber. Empty circles represent data that were fitted and shifted based on the 2S2P1D model and second-order polynomial function. Filled circles represent the measured data.	54
Figure 3-12. Dynamic modulus mastercurve, (b) time-temperature shift factor, and (c) phase angle mastercurve. (1) aad (STA), (2) aad (LTA1), (3) aad (LTA2), and (4) and (LTA3). Empty circles represent data that were fitted and shifted based on the 2S2P1D model and second-order polynomial function. Filled circles represent the measured data.....	55
Figure 3-13. Dynamic modulus mastercurve, (b) time-temperature shift factor, and (c) phase angle mastercurve. (1) NCs9.5b (STA), (2) NC S9.5b (LTA1), (3) NC S9.5b (LTA2), and (4) NC S9.5b (LTA3). Empty circles represent data that were fitted and shifted based on the 2S2P1D model and second-order polynomial function. Filled circles represent the measured data.	56
Figure 3-14. Predicted veRSus measured dynamic modulus data for all the mixtures listed in table 3.2	57
Figure 4-1. Coefficient of thermal contraction (ctc) plots for bindERS and mixtures in the first dataset: (a) binder, and (b) mixture data.....	73
Figure 4-2. LVDTs attached to samples: (a) zerodur® sample and (b) asphalt coNcrete sample.....	75
Figure 4-3. LVDT strain readings while lvdts attached to zerodur® sample and subjected to constantt temperature drop.	75
Figure 4-4. Test results: (a) lvdt readings, (b) temperature variation, and (c) fitting results.....	76
Figure 4-5. Classification of binder thermo-volumetric properties based on low performance grade: (a) glassy temperature (Tg), (b) liquid coefficient of thermal contraction (ctcl), and (c) glassy coefficient of thermal contraction (CTCg).	77
Figure 4-6. Temperature gradients within the sample at different inSTANCes of time for different rates of air temperature change: (a) -60°c/hour and (b) -10°c/hour.	78
Figure 4-7. Averaged temperature evolution as a function of time.	79
Figure 4-8. Schematic view of composite elements in asphalt mixtures: (a) series model and (b) parallel model.....	80
Figure 4-9. Schematic view of (a) Hirsch model (christenson et al. 2003) and (b) counto model (Young et al. 1981).....	81
Figure 4-10. Schematic view of building block of parallel model and internal force that occurs at the interface.	82
Figure 4-11. Comparison between backcalculated and measured binder shear modulus ($ G^* $) data for eight mixtures obtained from the Hirsch and modified Hirsch models: (a) shear modulus values of the binder in the vta mixtures backcalculated from Hirsch model, (b) shear modulus values of the binder in the vta mixtures backcalculated from modified Hirsch model, (c) shear modulus values of the binder in the vte mixtures backcalculated from Hirsch model, and (d) shear modulus values of the binder in the vte mixtures backcalculated from modified Hirsch model.....	86

Figure 4-12. Comparisons of predicted shear modulus, $ G^* $, and phase angle data for Vermont mixtures with measured data:(a) $ G^* $ comparison in log-log scale, (b) $ G^* $ comparison in arithmetic scale, and (c) phase angle comparison.	90
Figure 4-13. Comparisons between predicted ctcs from parallel and series models with the actual measured values: (a) cell 20, (b) cell 22, (c) cell 33, (d) cell 34, (e) cell 19, and (f) cell 35.	92
Figure 4-14. Comparison between predicted ctcs obtained from equation (4.12) and measured data obtained from marasteanu et al. (2007).	93
Figure 4-15. Comparison between predicted ctcs of mixtures obtained from level III analysis and measured data obtained from: (a) marasteanu et al. (2007) and (b) NCSU	94
Figure 4-16. Air temperatures for the surface of pavement sections located in different geographical locations: (a) North Carolina, (b) North Varolina, (c) New York, and (d) New York.	95
Figure 4-17. Comparison between stress predicted from level I analysis and the corresponding values obtained from level II analysis for the first dataset.	96
Figure 4-18. Comparison between stress predicted from level I analysis and the corresponding values obtained from level III analysis for the first dataset.	96
Figure 4-19. Comparison between stress predicted from level I analysis and the corresponding values obtained from level III analysis for the second dataset.	97
Figure 5-1. Stress vs. Strain curves for RS9.5b mixture subjected to different temperatures and loading rates.	111
Figure 5-2. Induced stress in uniaxial direct tension monotonic test: (a) stress versus pseudo strain and (b) evolution of dissipated pseudo strain energy as a function of reduced time equation (5.5) expresses the relationship for defining pseudo strain energy in linear.	116
Figure 5-3. Prediction of induced stress and measured strength based on S-VECD theory: (a) measured versus predicted induced stress in the uniaxial direct tension monotonic test for Vte20 mixture, (b) predicted versus measured strength for material group 1.	117
Figure 5-4. Example of bilinear strain history for rve sample: (a) strain history, (b) induced stress within the sample, (c) decrease in pseudo stiffness calculated from the S-VECD model, and (d) increase in damage parameter calculated from the S-VECD model.	119
Figure 5-5. Dissipated pseudo strain energy mastercurves for vermont mixtures: (a) VTa00, (b) VTa20, (c) VTa30, (d) VTa40, (e) VTe00, and (f) VTe20.	120
Figure 5-6. Measured verSus predicted dissipated pseudo strain energy for mixtures in material group 1.	121
Figure 5-7. Dissipated pseudo strain energy criteria for Vta00 mixture at different initial damage levels: (a) in arithmetic scale and (b) in log-log scale.	122
Figure 5-8. Steps for failure detection in a tsRSt using the DPSE failure criterion.	127
Figure 5-9. Prediction of TSRST results using S-VECD theory: (a) induced stress as a function of temperature, (b) pseudo stiffness variation as a function of temperature, (c) evolution of reduced strain rate as a function of temperature, and (d) evolution of DPSE as a function of reduced strain rate.	128
Figure 5-10. Prediction of TSRST fracture stress and fracture temperature using S-VECD theory: (a) interpolation of DPSE for any C value, (b) prediction of fracture	

temperature from the reduced strain rate, and (c) prediction of fracture stress from fracture temperature.....	129
Figure 5-11. Predicted temperatures in a circular asphalt sample: (a) temperature distribution inside the sample and (b) inside temperature as a function of air temperature.....	130
Figure 5-12. Measured and predicted stress values as a function of temperature for the vermont mixtures: (a) Vta00, (b) Vta20, (c) Vta30, and (d) Vta40.	131
Figure 5-13. Measured and predicted stress values as a function of temperature for the vermont mixtures: (a) Vte00, (b) Vte20, (c) Vte30, and (d) Vte40.	132
Figure 5-14. Measured and predicted stress values as a function of temperature for the New Hampshire mixtures in material group 2: (a) NHe00, (b) NHe20, (c) NHe30, (d) NHe40, (e) NYb30, (f) NYb40, (g) NYd20, (h) NYd30, and (i) NYd40.	133
Figure 5-15. Measured and predicted stress values as a function of temperature for the New York mixtures in material group 2: (a) NYb30, (b) NYb40, (c) NYd20, (d) NYd30, and (e) NYd40.....	134
Figure 5-16. Comparisons between averaged measured and predicted values for material groups 1 and 2: (a) fracture temperature and (b) fracture stress.	135
Figure 5-17. Predicted fracture temperatures for material group 3: (a) NHe5820-opt and NHe5840-opt, (b) NHe6400-opt, NHe6420-opt, and NHe6440-opt, (c) NHe6440-opt, NHe6440opt, and NHe6440+opt, and (d) NHe5820-opt, NHe6420-opt, NHe5840-opt, and NHe6440-opt.	136
Figure 5-18. Predicted fracture temperatures for material group 4: (a) Texas mixture, (b) South Dakota, (c) Washington mixture, and (d) North Carolina mixture.	137
Figure 6-1. Magnitude of fourier transform of surface temperatures for a mnroad pavement section.....	150
Figure 6-2. Schematic view of sublayerRS assumed in FlexTC.....	150
Figure 6-3. Example for defining the damage factor based on the DPSE failure criterion.	154
Figure 6-4. Algorithm implemented in FlexTC for calculating pseudo strain, thermal stress, pseudo stiffness, and dissipated pseudo strain energy, and detecting failure.....	155
Figure 6-5. Layouts of study sections: (a) mnroad sections and (b) North Carolina sections.....	156
Figure 6-6. Measured material properties at short term aging (STA): (a) dynamic modulus mastercurves, (b) phase angle mastercurves, (c) time-temperature shift factors, and (d) damage characteristics for mnroad sections.	163
Figure 6-7. Measured material properties at long-term aging (LTA): (a) dynamic modulus mastercurves, (b) phase angle mastercurves, (c) time-temperature, and (d) damage characteristics for mnroad sections.	164
Figure 6-8. Measured material properties at short term aging (STA): (a) dynamic modulus mastercurves, (b) phase angle mastercurves, (c) time-temperature shift factors, and (d) damage characteristics for North Carolina sections.....	165
Figure 6-9. Measured material properties at long term aging (LTA): (a) dynamic modulus mastercurves, (b) phase angle mastercurves, (c) time-temperature shift factors, and (d) damage characteristics for North Carolina sections.....	166
Figure 6-10. Material properties at different aging levels for RS 9.5b 50: (a) dynamic modulus mastercurves, (b) phase angle mastercurves, (c) time-temperature shift factors, and (d) damage characteristic curves.	167

Figure 6-11. Predicted DPSE of mnroad and North Carolina mixtures: (a) DPSE at STA for mnroad mixtures, (b) DPSE at LTA for mnroad mixtures, (c) DPSE at STA for North Carolina mixtures, and (d) DPSE at LTA for North Carolina mixtures.....	168
Figure 6-12. Comparisons between measured and predicted material properties under STA (open circles) and LTA (filled circles) for cell 16: (a) measured dynamic modulus mastercurves, (b) measured phase angle mastercurves, (c) measured time-temperature shift factors, (d) measured damage characteristic curves, and (e) predicted DPSE values.....	169
Figure 6-13. Maximum induced daily thermal stress as a function of pavement depth and day for a synthetic section located in North Carolina (RS 9.5b 0%RAP).....	171
Figure 6-14. Evolution of thermal damage-related parameters as function of time and pavement depth for a pavement section constructed in North Carolina (RS 9.5b 0%RAP): (a) pseudo stiffness (c) evolution vs. Time (day) for different nodes and (b) DPSE evolution vs. Time (day) for different nodes in terms of pavement depth.	172
Figure 6-15. Thermal stress and temperature variations for the day at which maximum stress occurs at the pavement surface.....	173
Figure 6-16. Temperature and reduced strain rate evolution as a function of time for surface of the section and for day of maximum thermal stress and ± 24 hours of that day: (a) temperature distribution and (b) reduced strain rate.	175
Figure 6-17. Predicted fracture temperature for mixtures studied in this study: (a) Mnroad section's materials and (b) North Carolina mixtures.....	177
Figure 6-18. Maximum experienced damage as a function of depth for eight cells constructed in phase III of mnroad test facility.	178
Figure 6-19. Maximum experienced damage as a function of depth for three synthetic sections constructed in North Carolina.	178
Figure 6-20. Number of transverse cracks based on field survey data for Mnroad sections.	179
Figure A-1. The algorithm for calculating pavement response by using fourier transform in time and space.....	198
Figure A-2. Selected frequencies picked by using geometrical progression approach: (a) storage modulus for NCAT-OGFC, (b) loss modulus for NCAT-OGFC, (c) storage modulus for MIT-control, and (d) loss modulus for MIT-control.....	199
Figure A-3. The results of interpolation method for predicting the storage and loss modulus of mixtures: (a) storage modulus for NCAT-OGFC, (b) loss modulus for NCAT-OGFC, (c) storage modulus for MIT-Control, and (d) loss modulus for MIT-Control	200
Figure A-4. Typical tire loading magnitude and corresponding fourier transform spectra: (a) tire loading in the time domain and (b) fourier spectra magnitude, position of selected frequencies, and interpolation based on selected frequencies.....	201
Figure A-5. Overview of the proposed methodology for the non-uniform method	202
Figure A-6. Three types of loading applied on rve sample: (a) sine wave loading, (b) block loading, and (c) random loading.....	203
Figure A-7. Different types of loading applied on asphalt mixture: (a) sine wave, (b) block wave, and (c) loading corresponds to the multiaxial truck.....	204
Figure A-8. Reference versus approximate response for NCAT-OGFC mixture, material-level verification: (a) sinusoidal loading at 10°C , (b) block loading at -10°C , (c) multiple	

axle loading at -10°C, (d) sinusoidal loading at 20°C, (e) block loading at 20°C (f) multiple axle loading at 20°C, (g) sinusoidal loading at 54°C, (h) block loading at 54°C, and (i) multiple axle loading at 54°C (note: dashed line represents the results from fourier transform approach whereas circles represent the results from non-uniform fourier transform approach)	205
Figure A-9. Reference versus approximate response for MIT-control mixture, material-level verification :(a) sinusoidal loading at -10°C, (b) block loading at -10°C, (c) multiple axle loading at -10°C, (d) sinusoidal loading at 20°C, (e) block loading at 20°C (f) multiple axle loading at 20°C, (g) sinusoidal loading at 54°C, (h) block loading at 54°C, and (i) multiple axle loading at 54°C (note: dashed line represents the results from fourier transform approach whereas circles represent the results from non-uniform fourier transform approach)	206
Figure A-10. Temperature distribution through the pavement section depth: (a) NCat section and (b) MIT section	207
Figure A-11. The schematic view of the selected points location within the pavement sections: (a) NCAT and (b) MIT	208
Figure A-12. Reference response and predation results obtained from the proposed methodology for NCAT-OGFC section.....	209
Figure A-13. Reference response and predation results obtained from the proposed methodology for MIT-control section	210

CHAPTER 1. INTRODUCTION

1.1. Introduction

Thermal cracking is one of the interesting topics in asphalt concrete modeling work. Thermal cracking due to severe thermal shots or significant variation in the daily air temperature is one of the main types of distress for asphalt concrete pavement sections constructed in cold regions (Marasteanu et al. 2007). In addition, pavement sections constructed in warmer regions, where the difference between the maximum and minimum daily temperature is high enough, are also prone to thermal cracks (Alavi 2014). Thermal cracking is manifested as a series of parallel surface-initiated transverse cracks which are perpendicular to the traffic direction. Propagation of thermal cracks in the pavement sections will eventually allow water to come into the pavement system and cause deterioration of pavement structure which in turn reduces pavement serviceability. The severity and magnitude of thermal cracks depend on air temperature, material properties, and pavement age.

Thermal cracking is a top-down procedure in which top sublayers are imposed to significant higher thermal variation in comparison with bottom ones (Kim 2008). The temperature variation in time and gradient in the depth of asphalt concrete sections imposes longitudinal thermal stress in the pavement sections. The material fails once the induced thermal damage passes a certain threshold (Rahbar-Rastegar et al. 2018). One way to investigate the material behavior subjected to longitudinal thermal stress is to perform uniaxial direct tension monotonic test in the laboratory (Chehab 2003, Keshavarzi and Kim 2016).

The uniaxial direct tension test can be performed to obtain the mixture strength as a function of reduced strain rate. While the strength criterion can be considered to be a criterion for failure detection, the field loading is quite different from monotonic tests. The daily thermal

variation imposes a significant amount of thermal stress in early mornings when the temperature is low. The imposed reduced rate and the corresponding thermal stress decrease as the air temperature gets warmer. While this type of loading induces thermal damage in the material level, the associated failure cannot be fully captured through using strength mastercurve criterion (Keshavarzi and Kim 2019a). The candidate failure criterion should be able to consider the evolution of thermal damage as well as the viscoelastic properties of asphalt mixtures (Keshavarzi and Kim 2019a).

The simplified viscoelastic continuum damage (S-VECD) is able to keep track of material integrity and follows microscale damage evolution through measurements performed at the macroscale level (Sabouri and Kim 2014). In addition, the S-VECD theory is able to incorporate rate and temperature dependency of asphalt concrete mixtures without imposing lots of experiment. These benefits motivate the author of this study to examine the applicability of S-VECD theory to predict the low-temperature performance of asphalt mixtures (Mensching et al. 2016, Zhu et al. 2017). Thermal stress restrained specimen test (TSRST) is able to simulate the behavior of asphalt concrete in the field (Jung and Vinson 1994). It is known that the fracture temperature measured in the TSRST has a good correlation with the low-temperature performance of asphalt mixtures in the field (Tabatabaee et al. 2012, Morian 2014). The candidate failure criterion should be verified by predicting the measured fracture temperature in the TSRST. This verification will enable pavement engineers and pavement agencies to have a tool to rank mixtures performance (Velasquez et al. 2013, Majidifard et al. 2019a).

The CTC parameter transfers temperature variation to thermal strain. The CTC parameter can be either measured or tested (Jones et al. 1968, Lytton 1980, Mehta et al. 1990, Islam and Tarefder 2014, Kim et al. 2010, Marasteanu et al. 2012, Bahia et al. 2012, Akentuna 2017).

While the suggested methodologies based on measurement techniques offer an accurate estimation of mixture's CTC, the predicted methodologies are easier to conduct and less accurate. The CTC depends on mixture properties and should be measured in the interesting range of temperature (Keshavarzi et al. 2019b).

The mixture's stiffness transfers the imposed thermal strain to the thermal stress. The measurement of mixture modulus at a very low temperature or high reduced frequency is a time-consuming task that requires a testing machine that can go to the low-temperature range (Majidifard et al. 2019b, Nemati and Dave 2018). Most of the pavement agencies benefit from AMPT for their measurements which is not capable to go to the temperature range interested in low-temperature cracking modeling. The suggested methodology should be able to estimate the mixture modulus and time-temperature shift factor by using the data measured at the range of temperature conduct able by AMPT machine (Keshavarzi et al. 2019c).

The final goal of the thermal cracking project is to predict the performance of asphalt concrete pavement sections subjected to air temperature variation. To this end, all the suggested methodologies for estimating the mixture's CTC for a wide range of temperature, predicting mixture moduli and time-temperature shift factor for high reduced frequency domain, and failure criterion should be incorporated in a structural framework. The structural framework should be able to analyze the pavement section and calculate the thermal stress. The thermal stress should be used to update the thermal damage. The prediction of failure should be done based on the thermal stress and thermal damage level (Keshavarzi et al. 2019d).

The crack depth or the damage caused by temperature variation should be transferred to crack spacing. The crack spacing is the parameter that is being calculated from observable field data.

Calculating the response of pavement sections subjected to either traffic or thermal loadings in the time domain requires lots of computational resources. The Fourier finite element was introduced to alleviate the computational cost by performing the response calculation in the frequency domain (Eslaminia et al. 2012, Eslaminia and Guddati 2015). The Fourier finite element still suffers from considerable computational cost once number of required frequency increases. In addition, performing response calculation in the two-dimensional space increases the degree of freedoms in the finite element discretization and makes the application of Fourier finite element impractical. This research presents a new computational algorithm, which is given the name of non-uniform Fourier finite element, to alleviate the computational cost associated with large number of frequencies required in Fourier finite element (Keshavarzi et al. 2019e). It is shown that non-uniform Fourier finite element is able to analyze pavement section response subjected to traffic loading in a significantly lower time.

The fatigue damage growth direction has a substantial impact on the magnitude of cracked area predicted for asphalt concrete pavement sections. This research presents the result of a study that performed to understand the effect of damage growth direction on pavement performance analysis (Keshavarzi and Kim 2019f). It is found out that the maximum principal direction is able to give more meaningful results.

1.2. Objectives

Characterizing the S-VECD based on dynamic modulus and cyclic fatigue tests and demonstrating its ability to predict the induced stress in the uniaxial direct tension test.

Developing a failure criterion for predicting asphalt concrete mixture failure in the constant reduced rate and constant reduced strain rate tests.

Investigating into different forms of dynamic modulus mastercurve and time-temperature shift factor functions and picking the ones that are able to characterize mixture's moduli and estimates the reduced strain rate and reduced frequency based on the AASHTO T 378/ R 84 testing protocol.

Developing a new model for predicting asphalt mixture's CTC as a function of temperature.

Predicting the fracture stress and fracture temperature of asphalt concrete mixtures in TSRST.

Developing a structural analysis framework that is able to analyze pavement section's response to the imposed temperature variation and calculate thermal stress, thermal damage, and detects failure.

Developing the non-uniform Fourier finite element methodology for reducing the computational cost associated with analyzing pavement section response to traffic and thermal loadings.

Developing a new methodology to detect fatigue damage propagation direction in asphalt concrete pavement sections.

1.3. Dissertation Organization

This dissertation consists of 6 chapters. Chapter 1 presents the introduction and objectives of the study; this is while Chapter 2 focuses on demonstrating the S-VECD, which characterized by the dynamic modulus and cyclic fatigue tests, ability to predict the induced stress in the uniaxial direct tension test to the strength value. Chapter 3 presents the study that was performed on the different dynamic modulus and time-temperature shift factor functions to

estimate the mixture moduli and reduced frequency at low temperature region. Chapter 3 suggests the final form of stiffness moduli and time-temperature shift factor that can be characterized based on AASHTO T 378/ R 84 and estimates the linear viscoelastic at low temperature region. Chapter 4 benefits from Chapter 3 results and investigates about the CTC of asphalt mixtures. Chapter 4 consists of testing results that were done at NCSU as well as the one reported in reports. It suggests a composite formula that can be used to estimate mixture's CTC as a function of temperature. To this end, based on desired levels of accuracy, three levels for measuring or estimating the CTC of asphaltic mixtures have been reported. Chapter 5 presents the study that was done to develop a failure criterion that can be used to predict the failure of asphalt concrete mixture subjected to uniaxial monotonic loadings. Chapter 5 proves that the suggested failure criterion, which is developed based on uniaxial direct tension loading based on constant reduced strain rate, can be utilized to predict the failure in TSRST test. It is shown that the proposed failure criterion is able to rank the mixtures that have different RAP content, PG binder content and grade, and aging levels. Chapter 6 presents the software's engine that was developed for predicting the performance of asphalt concrete sections subjected to air temperature variation. The software, which has been given the name of FlexTC, is verified for predicting the performance of eight sections constructed in North Carolina and three synthetic sections in North Carolina. This dissertation has two appendixes. Appendix I presents a computational algorithm for the reducing the computational cost of Fourier finite element method. The suggested methodology, which has the name of non-uniform finite element method, is verified through using the FlexPAVETM software. Appendix II presents the result of a study that was done to the top-down cracking of asphalt concrete sections. It is shown that the damage propagation based on maximum principal stress criterion can lead to more intuitive results.

CHAPTER 2. A VISCOELASTIC-BASED MODEL FOR PREDICTING THE STRENGTH OF ASPHALT COCNRETE IN DIRECT TENSION

The modeling of asphalt concrete behavior under monotonic loading plays an important role in investigating the low temperature behavior of pavement material. Further, any proposed method should be able to consider the rate and temperature dependency of asphalt concrete. This paper presents a new method for simulating the behavior of asphalt concrete in uniaxial tension. Direct tension monotonic testing that incorporates a constant crosshead displacement rate and various temperatures was used in the experimental investigation to simulate thermal cracking of asphalt concrete. Viscoelastic continuum damage theory was applied to simulate the asphalt behavior in direct tension. This theory is able to model distributed damage within the material under both constant and dropping temperatures. A damage characteristic curve, which has been proven to represent the intrinsic property of the material, was used to simulate the damage evolution during testing. The proposed method features a single ordinary differential equation that is solved to provide the damage evolution. The results show that the predicted stress matches the measured data well for tests conducted at North Carolina State University and by other agencies. Implementing the proposed method in a finite element code provides a strong mechanistic model to predict asphalt fracture under thermal loading.

2.1. Introduction

Thermal cracking is indicative of a Rapid drop in air temperature and thus is one of the main pavement failure modes in the northern parts of the United States and Canada (Marasteanu et al. 2004). As the pavement temperature drops, thermal stress builds and cracking occurs once a certain threshold has been passed. Low temperature cracking typically is manifested as a set of

parallel surface-initiated transverse cracks of various lengths and widths (Marasteanu et al. 2007).

Models that are currently available to address thermal cracking tend to be based on one of four different perspectives. The first approach utilizes empirical-based formulations that were developed by fitting observed thermal cracking in the field with material and pavement structure parameters (Fromm and Phang 1972, Hass et al. 1987). These empirical models are helpful in identifying critical factors that affect thermal cracking; however, they do not identify the fundamental basis that underlies the cracking process (Alavi 2014). The second perspective incorporates methods that are based on parameters (i.e., strength, fracture toughness) obtained at certain rates and temperatures (Hills and Brien 1966, Finn and Saraf 2004, Hiltunen and Roque 1994, Timm et al. 2003, Yin et al. 2007). Although these methods may be considered to be superior over the empirical-based methods, they have the disadvantage of being inconsistent with the natural behavior of asphalt concrete that is loading rate-dependent. A third approach includes methods that are based on building a strength mastercurve for a wide range of loading rates (Chehab 2003). These methods have some advantages over the previous ones, but, on the experimental side, obtaining a mastercurve that covers a wide range of reduced loading rates is difficult and time-consuming. Lastly, methods are available that are based on a so-called ‘cohesive zone’ that considers the progressive zone ahead of the crack tip (Song et al. 2006, Dave et al. 2013). The cohesive zone approach considers the low temperature fracture properties of asphalt concrete. It has the advantage of taking into account both the softening behavior of asphalt and the progressive zone ahead of the crack tip. However, there has been some discussion about the effects of mesh discretization on crack trajectory as well as numerical divergence when dealing with mixed mode simulations (Han et al. 2002, Roy and Dodd’s 2001).

All of the thermal cracking models differ based on the material model that is used for the inherent fracture model. Based on this observation, a more reliable fracture model is needed to enhance the reliability of thermal cracking prediction.

Modeling the performance of asphalt concrete using continuum damage theories is an approach that has gained international attention in recent years. The benefit of these types of methods is that they ignore complicated physical interactions at the microscale level and model behavior based on parameters that can be obtained at the macroscale level (Underwood et al. 2010). Schapery's work potential theory (Schapery 1987), which was built upon thermodynamic principles, is one of these continuum damage theories whereby damage is quantified as an internal State variable (S). Nonlocal elastic-based continuum damage has been proposed to quantify damage (Bazant and Pijaudier 1989, Bodin et al. 2004). Continuum damage theories assume that the viscoelastic and viscoplastic responses of the material depend on the internal State variable of the material.

Kim and Little (1990) were the first researchers to apply Schapery's nonlinear viscoelastic theory to materials with distributed damage in order to describe the behavior of sand asphalt under controlled strain cyclic loading. They later applied their viscoelastic continuum damage (VECD) theory to describe asphalt concrete behavior under both controlled stress and controlled strain loading (Kim and Little 1998). Also, research conducted by Daniel and Kim as part of a WesTrack project shows that the damage characteristics of asphalt concrete are independent of the mode of loading and can be determined using a simple test, such as the constant crosshead rate monotonic test (Daniel and Kim 2002). Findings from (Lee and Kim 1998) and (Zhang et al. 2013) have extended the range of VECD theory's applications. For example, Chehab extended VECD theory further by proving that time-temperature superposition

(t-TS) undertaken in the linear State is valid for a highly damaged State of asphalt concrete (Chehab 2003). Underwood conducted work at the Federal Highway Administration Accelerated Load Facility (FHWA-ALF) in MacLean, Virginia and applied these principles to both modified and unmodified asphalt concrete mixtures. The Underwood study proved that modeling principles can successfully predict mixture behavior (Underwood et al. 2010).

Zhang (Zhang et al. 2013) found a characteristic relationship between the rate of released pseudo strain energy and the pavement's fatigue life that is independent of strain amplitude and temperature. That is, the fatigue life of an asphalt mixture can be assessed using this relationship. The application of this characteristic relationship has been verified for reclaimed asphalt pavement (RAP) and non-RAP mixtures, modified and unmodified mixtures, and warm mix asphalt mixtures (Sabouri et al. 2015, Norouzi et al. 2015, Norouzi et al. 2016, Cao et al. 2016).

Although conducting constant rate tests to characterize asphalt concrete is theoretically appropriate for the work potential formulation, such tests have limitations with regard to test machine load capacity requirements. This issue is particularly critical because the capacity of the Asphalt Material Performance Tester (AMPT) is nearly the same as the threshold value needed for constant rate testing. For practicality's sake then, these continuum models must be formulated in such a way that cyclic fatigue tests can be performed easily for characterization. This concern has motivated the authors to develop their model based on material characterization that can be obtained using the AMPT.

VECD theory was applied in this study to examine the stress within samples that developed at a constant displacement rate with a constant temperature and the temperature-induced stress that developed during thermal stress restrained specimen tests (TSRSTs). The proposed method has been verified for different mixture types under constant loading rates and

for TSRSTs. The results indicate that VECD theory can predict the drop in stress for a constant strain loading rate. In this way, the corresponding maximum point in the predicted stress curve is considered the strength value.

Because the TSRST can simulate a thermal cracking scenario in the field more closely than other test methods due to the continuous temperature drop during testing, verification of this test method would greatly enhance the viability of the proposed method. The proposed method can be implemented as a failure module in a finite element code to provide a strong mechanistic model to predict thermal cracking. This implementation effort is currently the subject of ongoing research at North Carolina State University.

2.2. Objectives

This paper takes advantage of VECD theory to simulate asphalt concrete under monotonic loading. The proposed method benefits from experimental data obtained from cyclic tests to simulate monotonic tests. This simulation is useful for thermal cracking predictions. The results show that the predictions are accurate for both monotonic and thermal strain-restrained specimen testing.

2.3. Theoretical Background

2.3.1. VECD Theory

VECD theory is based on three main factors: 1) the viscoelastic behavior of the material is modeled by utilizing the correspondence principle, which is based on pseudo strain (ϵ_R); (2) the work potential theory models the effects of micro cracks on the macroscale-level behavior of the material, and (3) the t-TS principle for any level of damage helps to unite the effects of time/rate and temperature.

The basic equations necessary for viscoelastic continuum damage theory are:

The strain energy density function (Equation(2.1)):

$$W^R = f(\varepsilon^R, S) \quad (2.1)$$

The stress-pseudo strain relationship (Equation(2.2)):

$$\sigma = \frac{\partial W^R}{\partial \varepsilon^R} \quad (2.2)$$

The damage evolution law (Equation(2.3)):

$$\frac{dS}{dt} = \left(-\frac{\partial W^R}{\partial S} \right) \quad (2.3)$$

Where W^R is the pseudo strain energy, ε^R is the pseudo strain, S is the internal State variable representing damage, α is the damage evolution rate, σ is stress, and t is time. All the formulations presented in this paper pertain only to the region of the material behavior that relates to localization, i.e., before the damage coalesces and localizes into a single dominant macrocrack. At this point, VECD theory is valid to the point at which the continuum nature of the material is violated, i.e., strain localization.

Pseudo strain is a consequence of the aforementioned elastic-viscoelastic correspondence principle. Pseudo strain may be calculated rigorously using Equation(2.4), where ε is the measured strain, $E(\xi)$ is the linear viscoelastic relaxation modulus, E_R is the reference modulus (typically taken as 1) used for dimensional compatibility, ξ is reduced time, and τ is a dummy time parameter used for integration.

$$\varepsilon^R(\xi) = \frac{1}{E_R} \times \int_0^\xi E(\xi - \tau) \frac{d\varepsilon}{d\tau} d\tau \quad (2.4)$$

Pseudo strain energy is defined as the area under the stress versus pseudo strain curve (Equation(2.5)).

$$W^R = \frac{1}{2} \times \sigma \times \varepsilon^R \quad (2.5)$$

In VECD theory, stress (σ) at any point before localization can be obtained from the linear stress (pseudo strain) and pseudo stiffness (C), i.e., Equation(2.6). According to Daniel (Daniel and Kim 2002), pseudo stiffness evolution is related to the internal damage (S) value and can be expressed by Equation (2.7).

$$\sigma = C \times \varepsilon^R \quad (2.6)$$

$$C = 1 - c_{11} S^{c_{12}} \quad (2.7)$$

Where C_{11} and C_{12} are the material parameters, and C varies from 1 (undamaged State) to 0 (totally damaged State). It should be noted that, depending on the applied load, the C value at failure changes and is always greater than 0. Substituting Equations (2.5) through (2.7) into Equation (2.3) gives the damage evolution differential equation with respect to time (Equation (2.8))

$$\frac{dS}{dt} = \left(\frac{1}{2} a \times b \times S^{b-1} \times e^{-aS^b} \right)^\alpha \times \left(\frac{1}{E_R} \int_0^\xi E(\xi - \tau) \frac{d\varepsilon}{d\tau} d\tau \right)^\alpha \quad (2.8)$$

Where ξ is reduced time and should be calculated from Equation (2.9).

$$\xi = \int_0^t \frac{dt}{a_T} \xrightarrow{\text{Cons tan t Temperature}} \xi = \frac{t}{a_T} \quad (2.9)$$

Reduced time (ξ) may be calculated rigorously using Equation (2.9) where t is real time and T is a time-temperature parameter obtained from Equation (2.10).

$$a_T = 10^{a_1 T^2 + a_2 T + a_3} \quad (2.10)$$

Where a_1 , a_2 , and a_3 are time-temperature coefficients that are obtained from testing.

Solving Equation (2.8) in terms of time gives the damage evolution (S) in terms of time. Plugging S into Equation (2.7) gives C (pseudo stiffness) as a function of time. Inserting the C values on the right side of Equation (2.6) gives the nonlinear developed stress. This nonlinearity is a direct result of the damage accumulation within a specimen over time. It should be noted that the strain in Equation (2.8) comes from attaching the LVDTs to the specimen. In pavement simulation software, the strain can be obtained from the finite element solution.

Next we must prove that VECD theory can predict the drop in stress, which is important because the point of the stress drop is defined as the point of failure of the material. Here, a mathematical description of this phenomenon is explained. In the Results section, this stress drop is proved using experimental evidence.

Differentiating Equation (2.6) with respect to time can give the rate of stress development in terms of time. If it is proven that this rate can be zero, then mathematically it is proven that maximum stress (i.e., strength) can be predicted from this equation (2.11).

$$\frac{d\sigma}{dt} = \frac{dc}{dt} \times \varepsilon^R + c \times \frac{d\varepsilon^R}{dt} \quad (2.11)$$

In Equation (2.11) the first term on the right-hand side is the product of two terms: the pseudo stiffness rate and the pseudo strain. In monotonic testing, damage always increases; thus, it is expected that the pseudo stiffness rate will always be negative. Pseudo strain can be seen as linear stress and is always positive in monotonic testing. In this way, the first term of the right-hand side is always negative. As mentioned before, C is always greater than zero, and the rate of

the change in the linear stress can be regarded as an increase in the linear stress, which is obviously greater than zero. In this way, the second term on the right-hand side of the equation is always positive. Therefore, these two terms can define a curve that Starts from a positive value and, by passing from the point that corresponds to the strength value, enters into a negative region.

2.4. Materials and Test Method

2.4.1. Materials

In this study, experiments were performed using nine mixtures to investigate a possible failure criterion. The first mixture is the Superpave surface 9.5 mm (S9.5B) mix that is commonly used in North Carolina, and the eight other mixtures are 9.5 mm Superpave mixes from Vermont that are part of the New England RAP project. The Vermont mixes are designated as VTeXX and VTaXX, with XX representing the percentage of RAP. Table 2.1 presents a summary of the properties of these nine mixtures.

Table 2.1. Study mixtures properties

Mix Type	Binder	AC (%)	NMAS (mm)	RAP (%)	Target Air Void (%)
S9.5B	PG 64-28	5.2	9.5	0	5.5
VTe00	PG 64-28	6.5	9.5	0	6.0
VTe20	PG 64-28	6.7	9.5	20	6.0
VTe30	PG 64-28	6.6	9.5	30	6.0
VTe40	PG 64-28	6.6	9.5	40	6.0
VTa00	PG 52-34	6.7	9.5	0	6.0
VTa20	PG 52-34	6.8	9.5	20	6.0
VTa30	PG 52-34	6.6	9.5	30	6.0
VTa40	PG 52-34	6.6	9.5	40	6.0

2.4.2. Testing

Three main tests were carried out in this study: (1) dynamic modulus tests were performed to determine the linear viscoelastic characteristics using the AMPT; (2) controlled crosshead (CX) cyclic direct tension tests were conducted to describe the viscoelastic damage characteristics using the AMPT following AASHTO TP 107; and (3) CX monotonic direct tension tests were conducted using a MTS 810 machine. The dynamic modulus testing was carried out in compression under load control mode following the protocol given in AASHTO TP 79. The dynamic modulus tests were performed for all the study mixtures at 4°C, 20°C, 40°C, and 54°C and at frequencies of 25, 10, 5, 1 and 0.5 Hz. The load levels were specified by trial and error so that the strain amplitudes were between 50 and 75 microstrain to prevent damage to the specimens. The dynamic modulus ($|E^*|$) values were fitted for the coefficient of the sigmoidal function and time temperature shift factor by optimizing the dynamic modulus mastercurve. After determining the shift factors, the dynamic modulus value was converted to the relaxation modulus, $E(t)$, value of the Prony series form to obtain a constitutive relationship between the strain and stress in the time domain. Finally, a power term, alpha (α), used in VECD theory, was calculated from the maximum log-log slope, m , of the relaxation modulus and time using the relationship $\alpha = 1 + 1/m$. Underwood and Kim (2012) showed that the dynamic modulus values obtained from compression-only tests and tension compression tests are equal to each other.

All the specimens were compacted using a Superpave gyratory compactor to a diameter of 150 mm and a height of 178 mm. To obtain specimens of uniform air void distribution, these samples were cored and cut to a height of 150 mm and diameter of 100 mm for testing. Prior to testing, the air void content was measured for each specimen using the CoreLok method. All the

test specimens used in this study had air void ratios within the range of 5.5 ± 0.5 percent for the S9.5 B mixture and 6.0 ± 0.5 percent for the VTeXXLC and VTaXXLC mixtures. All direct tension test specimens were glued to metal plates at both ends before they were prepared for testing in the machine. Vertical deformation was measured in the middle of each specimen using four linear variable differential transducers (LVDTs) at intervals of 90 degrees with a gauge length of 70 mm for both the AMPT and MTS 810. Devcon® steel putty was used to glue the steel end plates and targets for the LVDTs that were used for testing in MTS machine.

2.5. Results

2.5.1. Monotonic Simulations

It should be noted that, because VECD theory formulation depends on continuum damage theory, VECD is valid up to the point of localization. Clearly, the localization point cannot go below the point of maximum stress (strength). Thus, in this way, it can be said that VECD theory is able to predict strength. The simulation results for all the mixtures at constant crosshead displacement rates are shown in Figure 2-1 to Figure 2-9.

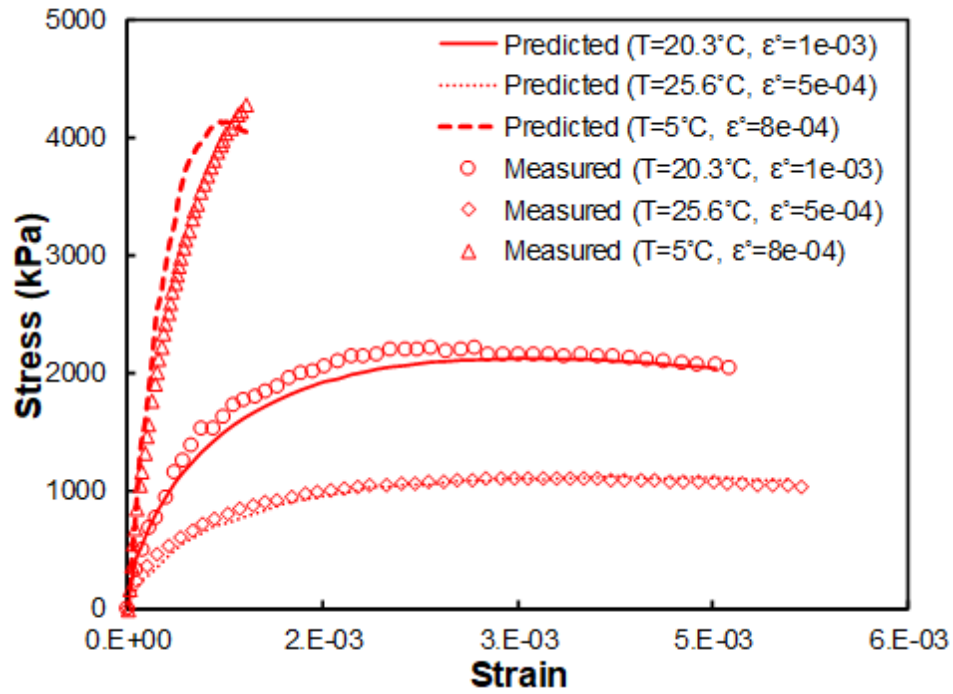


Figure 2-1. Test data and prediction results for RS9.5B mix.

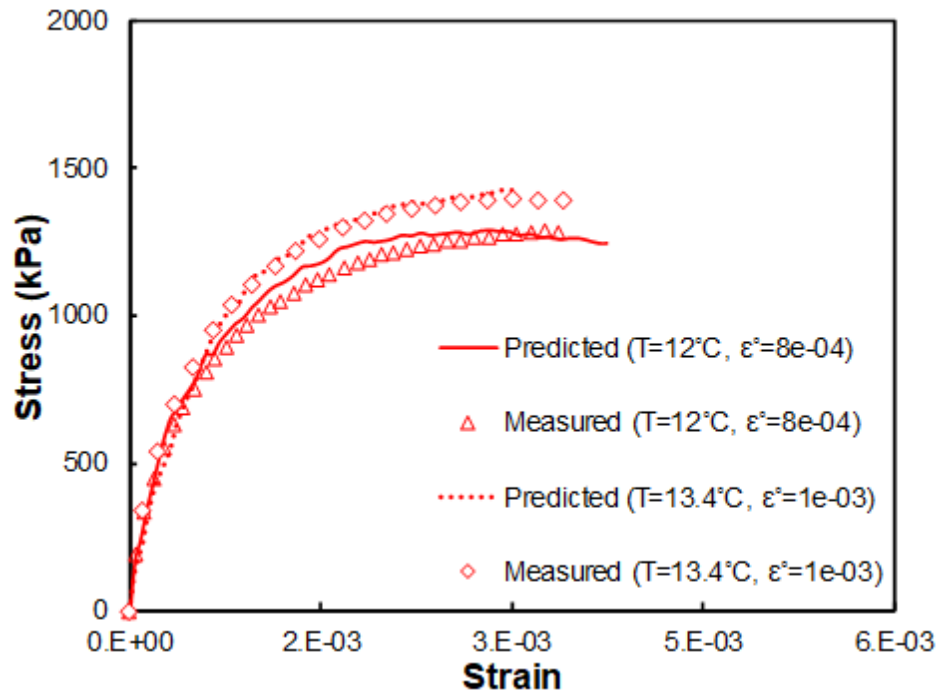


Figure 2-2. Test data and prediction results for VTa00 mixture.

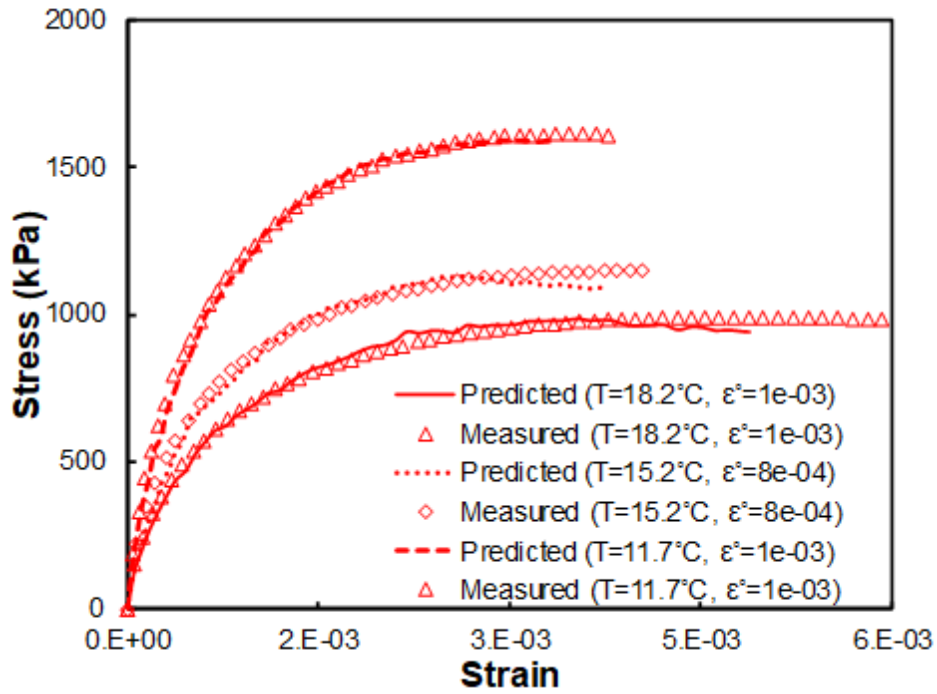


Figure 2-3. Test data and prediction results for VTa20 mixture.

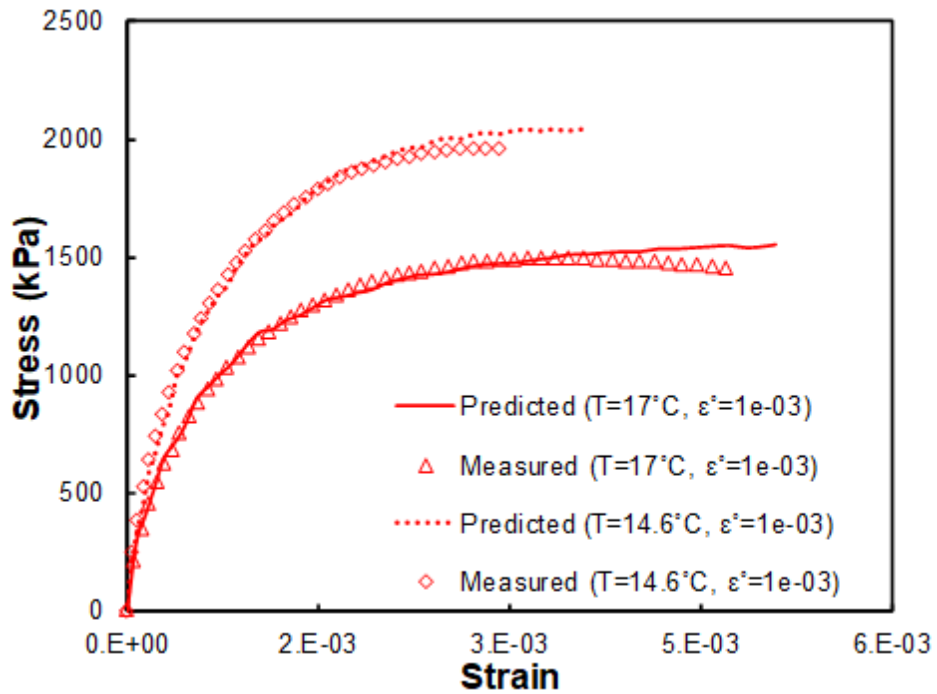


Figure 2-4. Test data and prediction results for VTa30 mixture.

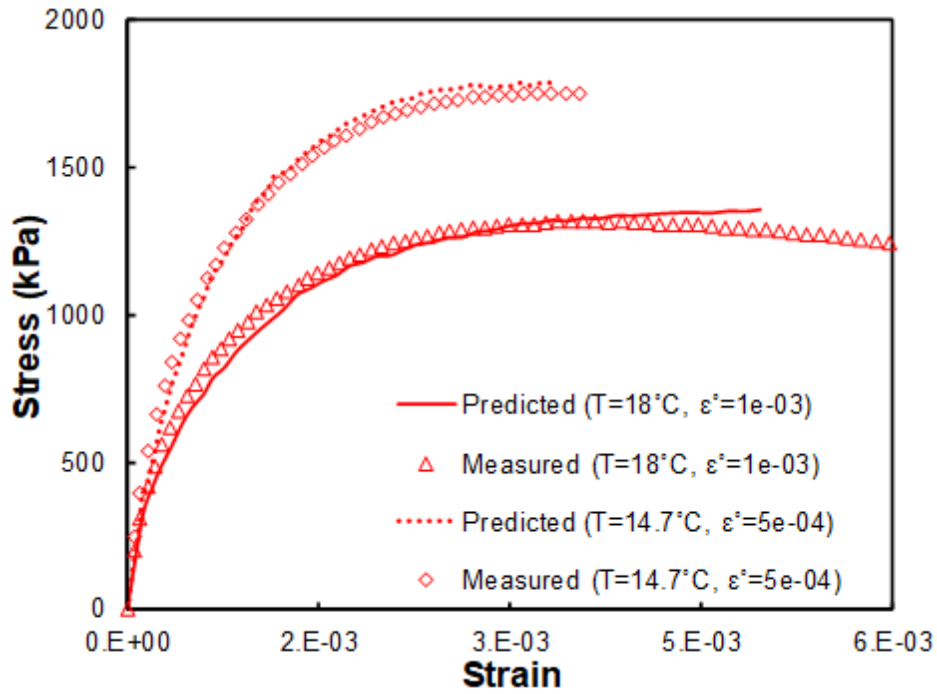


Figure 2-5. Test data and prediction results for VTa40 mixture.

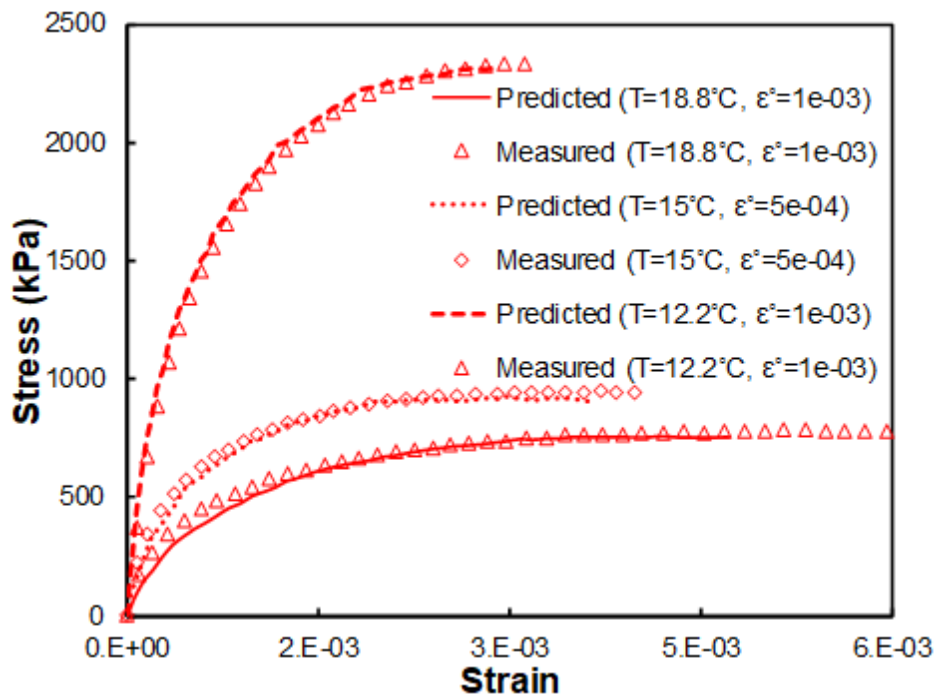


Figure 2-6. Test data and prediction results for VTe00 mixture.

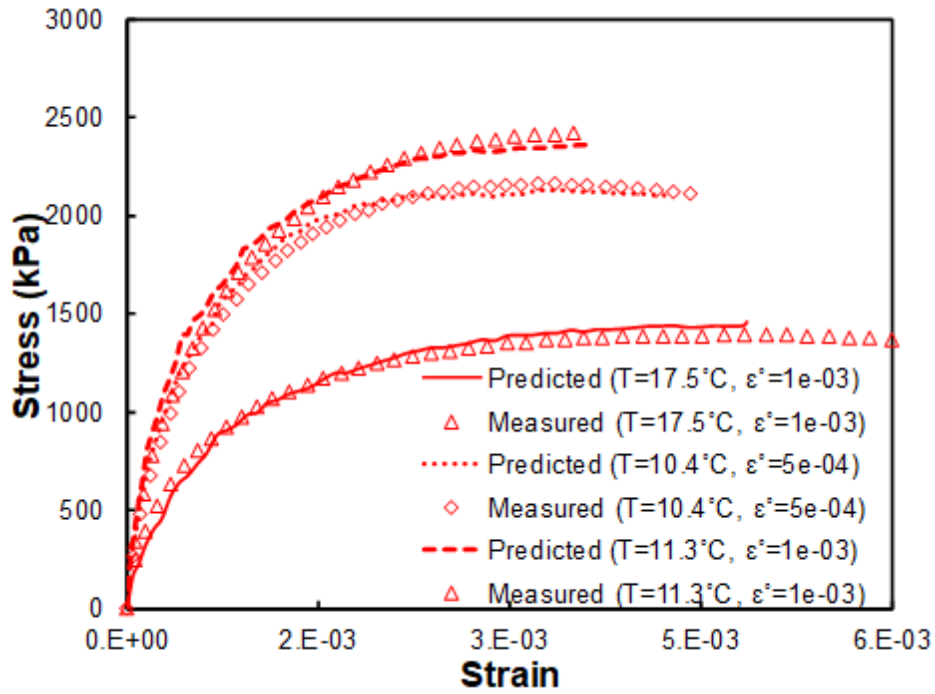


Figure 2-7. Test data and prediction results for VTe20 mixture.

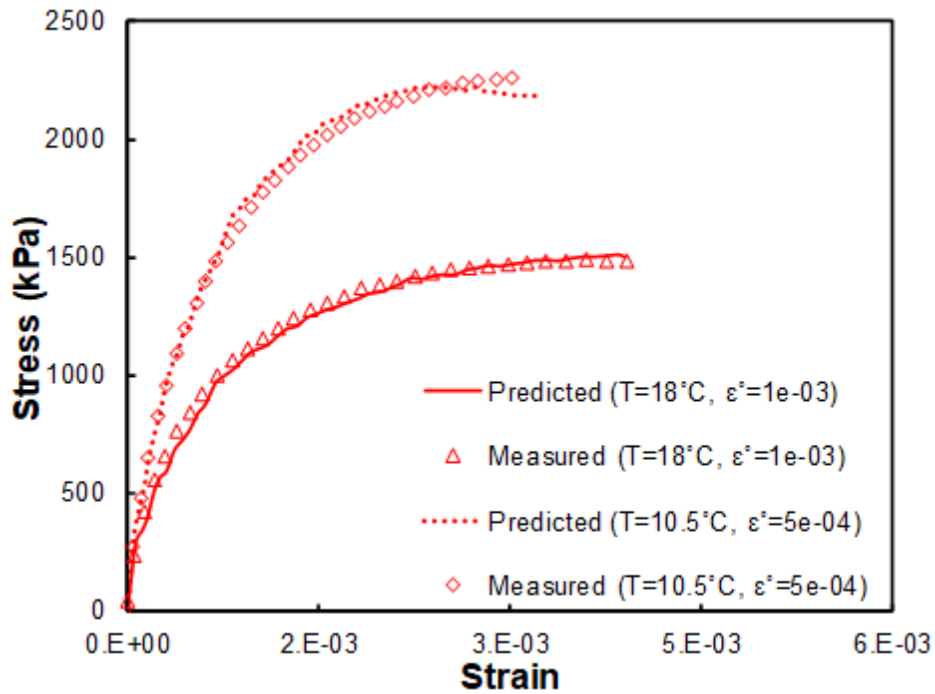


Figure 2-8. Test data and prediction results for VTe30 mixture.

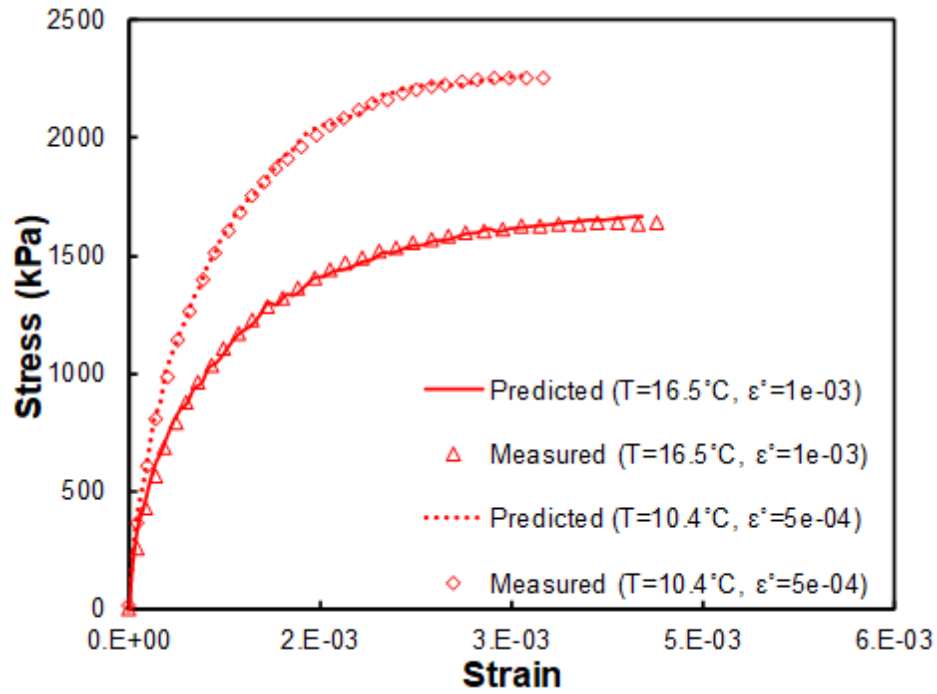


Figure 2-9. Test data and prediction results for VTe40 mixture.

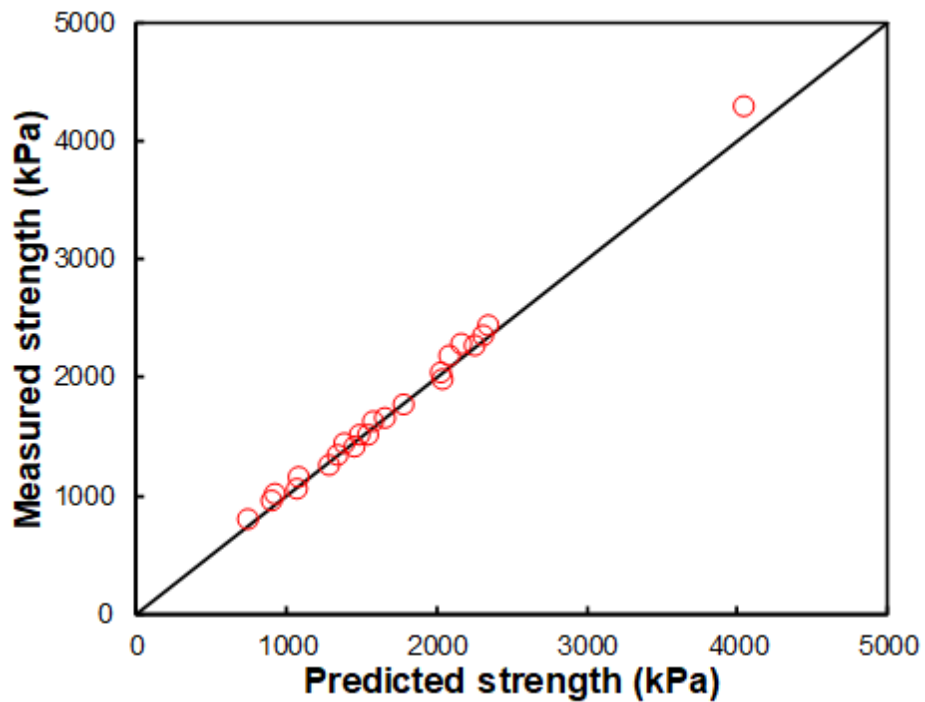


Figure 2-10. Predicted versus measured strength values for all the study mixtures.

Figure 2-1 through Figure 2-9 show that the proposed method provides good stress predictions. These figures show that increasing the reduced rate leads to higher strength and lower failure strain values. Figure 2-10 proves that the proposed method can capture the strength values of different types of mixtures very well.

2.6. Conclusion

Thermal cracking is one of the predominant failure modes of pavements in the northern parts of the United States and Canada. The currently available test methods propose different ways to define the failure of asphalt concrete. This study assessed failure stress based on the well-known VECD theory whereby a governing differential equation for the damage evolution over time was obtained. Due to the widespread availability of AMPTs, the damage characteristics of the study mixtures could be obtained using this machine. All the monotonic tests were conducted using an MTS 810 system. According to the monotonic simulation results, the predictions match the measured data very well up to the point of maximum stress.

CHAPTER 3. EXTRAPOLATION OF DYNAMIC MODULUS DATA FOR ASPHALT CONCRETE AT LOW TEMPERATURES

3.1. Abstract

AASHTO T 378/R 84 specifications have become the industry Standard for measuring the dynamic modulus of asphalt concrete using the Asphalt Mixture Performance Tester (AMPT). The lowest test temperature specified by R 84 is 4°C; however, predicting the cracking behavior of asphalt pavement at low temperatures requires knowing the dynamic modulus at temperatures much lower than 4°C. To address this problem, this study investigated the ability of various dynamic modulus mastercurve functions and time-temperature shift factor functions to predict the dynamic modulus, phase angle, and time-temperature shift factor at temperatures lower than 4°C using data obtained from dynamic modulus tests conducted at 4°C, 20°C, and 40°C in accordance with AASHTO T 378/R 84 specifications. This research is the first to study the accuracy of suggested methodologies for predicting the asphalt mixture modulus at very high frequency or low temperature when limited experimental data set is available. Two sets of experimental data were used in this study. The first set included dynamic modulus, phase angle, and time-temperature shift factor data from 40°C to -30°C for seven mixtures, which covers different binder grades, nominal maximum aggregate sizes, and binder modification types. The second set of data was obtained using the AASHTO T 342 procedure, with the range of test temperatures covering between -10°C and 54°C. Twelve mixtures with a wide range of mixture characteristics were used for this second dataset. Analysis of both datasets revealed that, although all the available methods could be used to fit the measured data, only the 2S2P1D model combined with a second-order polynomial shift factor function was able to predict the measured data at temperatures below the lowest temperature used in the tests (i.e., 4°C for the

first dataset and -10°C for the second dataset). All the other methods significantly under predicted mixture modulus at temperatures lower than the lowest temperature used in the tests. It is proved that the coefficients for the 2S2P1D formula can reasonably capture the aging evolution of the selected mixtures.

3.2. Introduction

Thermal cracking is one of the most prevalent types of distress found in asphalt pavements built in the northern parts of the United States and Canada (Marasteanu et al. 2012). Of all the parameters that may affect induced thermal stress in a pavement section, the stiffness of the material plays the most important role. Because thermal loading is mechanically similar to strain-controlled loading, the induced stress within a pavement section is proportional to the stiffness of the material. Due to the fact that thermal cracking is a top-down process that occurs at cold temperatures, the stiffness of the material at a very low temperature is important to consider for an analysis and prediction framework (Alavi 2014).

Dynamic modulus has become the primary material property of asphalt concrete in mechanistic-empirical pavement analysis methods. Measuring the dynamic modulus of asphalt concrete at low temperatures and at different frequencies is a cumbersome task that requires special test machines. The Asphalt Mixture Performance Tester (AMPT) is specifically designed to measure asphalt mixture engineering properties, including the dynamic modulus. Use of the AMPT has considerably simplified the testing efforts to develop dynamic modulus mastercurves that are needed for pavement structural analysis. Testing with the AMPT has received national support because the AMPT's simplicity has motivated multiple vendors to produce AMPTs, develop test protocols, and coordinate training and support.

The dynamic modulus of asphalt concrete depends on both temperature and rate of loading. Thus, the modulus of asphalt concrete cannot be expressed as a single value and should be defined for a wide range of temperatures and loading frequencies. The dynamic modulus mastercurve is constructed based on the assumption that asphalt concrete is a thermorheologically simple material. Thermorheological simplicity can be proven valid if a smooth mastercurve can be constructed by shifting the dynamic modulus versus loading frequency curve at different temperatures horizontally along the frequency axis toward the dynamic modulus versus frequency curve at a preselected reference temperature. The resulting mastercurve is a function of reduced frequency, which incorporates temperature and frequency in a single parameter. The amount of horizontal shift for a specific temperature is the time-temperature shift factor for that temperature.

With growing interest in the ability to predict the response and performance of asphalt pavements under a wide range of loading conditions that include high temperatures (where permanent deformation is a concern) (Ghanbari et al., 2019, Wang et al., 2019) to very low temperatures (where thermal cracking is a concern) (Dave et al. 2013, Farrar et al. 2013, Keshavarzi and Kim 2016), the ability to predict dynamic modulus values accurately is inherently critical. Moreover, any algorithm that is used to analyze pavement responses and predict pavement performance requires the dynamic modulus mastercurve a priori. The mastercurve allows the analysis engine to calculate the correct modulus value that corresponds to any reduced frequency. The test framework thus must incorporate construction of the dynamic modulus mastercurve, which in turn requires that the test equipment must be able to test material at a broad range of temperatures.

The current version of the AMPT does not have the capacity to test materials at temperatures below -5°C , and the lowest temperature specified in AASHTO R 84 is 4°C . Therefore, the dynamic modulus mastercurve obtained from the AASHTO T 378/R 84 procedure must be extrapolated to obtain the desired moduli values at higher reduced frequencies, i.e., low temperatures. Such extrapolation should be investigated carefully for any possible flaws. In addition to the dynamic modulus mastercurve, the time-temperature shift factor and phase angle mastercurve also should be examined to see how well they can predict the corresponding measured values. ANY error in the extrapolation step may lead to significant error in the prediction of low-temperature performance of asphalt concrete. This paper presents research efforts to identify the combination(s) of the dynamic modulus mastercurve function and time-temperature shift factor function that will allow suitable representation of the dynamic modulus values and phase angles at low temperatures using data based on the AASHTO T 378/R 84 specifications.

3.2.1. Analytical Models

Since the early 1990s, many researchers have studied the viscoelastic behavior of asphalt mixtures, Starting with the Strategic Highway Research Program (SHRP) (Kennedy and Cominsky 1990). The linear viscoelastic properties of asphalt concrete are usually expressed in terms of dynamic modulus ($|E^*|$) and phase angle (δ) mastercurves along with the shift factor function to bring the loading condition to the reduced space at which the material properties can be measured and constructed. The equations shown together in Equation (3.1) indicates the relationships between the magnitude of the dynamic modulus at any reduced frequency (fR) as well as the storage (E') and loss (E'') modulus values.

$$\begin{aligned}
E^* &= E' + iE'' \\
E' &= |E^*| \cos \delta \\
E'' &= |E^*| \sin \delta
\end{aligned}
\tag{3.1}$$

where E^* is the complex modulus. Several functions have been proposed to fit the measured dynamic modulus data at different temperatures and frequencies to build a mastercurve; some of these functions are reviewed in the next section.

3.2.1.1. Models for Dynamic Modulus Mastercurve

A sigmoidal function shown in Equation (3.2) was suggested by Witczak and Fonseca (1996) to analytically represent the dynamic modulus mastercurve and later used in the Pavement ME Design software. The sigmoidal function parameters define the ordinates of the two asymptotes and central/inflection point of the sigmoidal functional form (Witczak and Fonseca 1996).

$$\log(|E^*|) = \delta + \frac{\alpha}{1 + e^{\beta + \gamma \log(f_r)}}
\tag{3.2}$$

Where $|E^*|$ is absolute value of mixture's modulus, and δ , α , λ , β , γ are model parameters. One concern about the sigmoidal function is that it assumes that the dynamic modulus mastercurve is symmetric, which is experimentally proven incorrect when the shapes of the mastercurve at high and low reduced frequencies are compared. Rowe et al. (2000) introduced a generalized logistic function to better describe the shape of the mastercurve for an asphalt mixture, expressed here as Equation (3.3). In contrast to the sigmoidal function, the modified sigmoidal function does not impose any symmetry on the mastercurve.

$$\log(|E^*|) = \delta + \frac{\alpha}{\left(1 + \lambda e^{\beta + \gamma \log(f_r)}\right)^{\frac{1}{\lambda}}} \quad (3.3)$$

Where δ , α , λ , β , γ are model parameters. The Huet model consists of two parabolic elements that are located in a series with a spring (Huet 1963). The creep compliance function for the parabolic elements can be expressed by a power form function, as shown in Equation (3.4).

$$J(t) = a \times t^h \quad (3.4)$$

where a and h are the model parameters. The Huet model was proposed for binders and mixtures. The analytical expression of the Huet model for creep compliance is written as Equation (3.5) (Marasteanu et al. 2012).

$$D(t) = \frac{1}{E_\infty} \left(1 + \delta \frac{\left(\frac{t}{\tau}\right)^k}{\Gamma(k+1)} + \frac{\left(\frac{t}{\tau}\right)^h}{\Gamma(h+1)} \right) \quad (3.5)$$

where $D(t)$ is the creep compliance, E_∞ is the glassy modulus, h and k are exponents such that $0 < k < h < 1$, δ is a dimensionless constant, Γ is the gamma function, and τ is reduced time. Equations (3.6) and (3.7) express the analytical form of the complex modulus for the Huet model.

$$E^*(i\omega\tau) = \frac{E_\infty}{1 + \delta(i\omega\tau)^{-k} + (i\omega\tau)^{-h}} \quad (3.6)$$

$$\tau = \tau_0 \times a_T \quad (3.7)$$

Where E^* is the dynamic modulus of mixture. The Huet model is unable to characterize mixture behavior at a low reduced frequency. This shortcoming comes from the fact that the limiting value of the mixture modulus that is related to the aggregate skeleton is not considered in the model. The Huet-Sayegh model includes a spring that is assumed to be in parallel with that of the Huet model and takes the form expressed as Equation (3.8) for the complex modulus of the mixture (Huet 1999).

$$E^*(i\omega\tau) = E_0 + \frac{E_\infty}{1 + \delta(i\omega\tau)^{-k} + (i\omega\tau)^{-h}} \quad (3.8)$$

where E_0 is the limit of the complex modulus. Six constants are required to fit the dynamic modulus data. Note that several researchers have confirmed the accuracy and efficiency of the Huet-Sayegh model (Ferry 1948, Shenoy 2002, Cannone-Falchetto et al. 2011a, Cannone-Falchetto et al. 2011b, Evans et al. 2011, Marasteanu et al. 2012). Orald and Di Benedetto (2003) suggested the 2S2P1D function for fitting dynamic modulus mastercurve. The advantages of the 2S2P1D function over the Huet-Sayegh model is improved binder fitting. The 2S2P1D function consists of a generalization of the Huet and Sayegh analogical models (Huet 1963, 1999; Sayegh 1965). Orald and Di Benedetto (2003) fitted the suggested function to four mixes and showed that the introduced model fits the measurements well. The measurements were taken from +15°C to -30°C and from 10^{-3} to 30 Hz. All the measured data were used to fit the suggested function. The results show that the 2S2P1D model can fit measured data accurately. Equation (3.9) expresses the 2S2P1D function.

$$E^*(\omega) = E_0 + \frac{E_\infty - E_0}{1 + \delta(i\omega\tau)^{-k} + (i\omega\tau)^{-h} + (i\omega\beta\tau)^{-1}} \quad (3.9)$$

$$\tau = \tau_0 a_T$$

Where E_0 is the fluid modulus of the asphalt mixture (lower asymptote), E_∞ is the glassy modulus of the asphalt mixture, ω is loading frequency, i is the square root of -1, and δ , τ_0 , k , h , and β are the model coefficients that are specific to the mixture.

3.2.1.2. Models for time-temperature shift factor

Constructing a dynamic modulus mastercurve requires shifting measured isothermal data. That shift can be orchestrated to produce a smooth mastercurve. Through the mastercurve and shift factor relationship, the measured data can be extrapolated to include a broader range of loading frequency and temperature that may exist in the field. Different forms of time-temperature shift factor functions are available in the literature, including the Arrhenius (Kandiyoti and Herod 2006), Williams-Landel-Ferry (WLF) (Williams et al. 1995), polynomial (Rowe and Sharrock 2011), Kalble (Rowe et al. 2000), and modified Kalble (Rowe and Sharrock 2011). Equation (3.10) presents the functional form for the Arrhenius relationship.

$$\log(a_T) = a \left(\frac{1}{T} - \frac{1}{T_{ref}} \right) \quad (3.10)$$

Where a is the model parameter, and T_{ref} is the reference temperature. Equations (3.11) and (3.12) express the WLF relationship and second-order polynomial function, respectively.

$$\log(a_T) = -\frac{C_1(T - T_g)}{C_2 + (T - T_g)} \quad (3.11)$$

Where C1, and C2 are model parameters and T is temperature.

$$\log(a_T) = a_1 T^2 + a_2 T + a_3 \quad (3.12)$$

Where a1, a2 and a3 are model parameters. The second-order polynomial function is the same form used by Witczak and Fonseca (1996). Equations (3.13) and (3.14) present the functional forms of the Kalble and modified Kalble relationships, respectively.

$$\log(a_T) = -\frac{C_1(T - T_d)}{C_2 + |T - T_d|} \quad (3.13)$$

$$\log(a_T) = -C_1 \left(\frac{T - T_d}{C_2 + |T - T_d|} - \frac{T_r - T_d}{C_2 + |T_r - T_d|} \right) \quad (3.14)$$

Where T_d is the temperature corresponds to the inflection point. In addition, shift factors have been calculated using binder viscosity parameters (AASHTO R62). Equation (3.15) describes the A+ VTS time-temperature shift factor function, which is used in the Mechanistic-Empirical Pavement Design Guide (MEPDG) software (AASHTO R62.)

$$\begin{aligned} \log(a_T) &= c(\log \eta - \log \eta_{T_r}) \\ \log(\eta) &= 10^{A+VTS \log(T)} \end{aligned} \quad (3.15)$$

Where c is a fitting coefficient, η is the viscosity of the binder, η_{TR} is the viscosity of the binder at the reference temperature, A and VTS are the parameter's of the viscosity-temperature relationship, and T is temperature.

Rowe et al. (2000) used the Kalble function to analyze mixture complex modulus data obtained from the MEPDG database. Rowe et al. concluded that the Kalble function is able to

describe the functional form of the shift factor in a more accurate way than the Arrhenius, WLF, or polynomial fittings. Note that the Kalble function was recently modified to a functional form called the modified Kalble. The modification offers the benefit of separating the reference temperature and inflection temperature.

3.3. Materials and Specimen Fabrication

The experimental data developed in this research were divided into two datasets for two respective groups of materials according to the range of temperatures used in the dynamic modulus tests. The temperatures used for the first group are 40°C, 20°C, 4°C, 0°C, -10°C, -20°C, and -30°C. The temperatures used for the second group are 54°C, 40°C, 20°C, 4°C, and -10°C.

Seven different mixtures from different climatic regions were included in the first group. The considered mixtures have different reclaimed asphalt pavement (RAP) contents, nominal maximum aggregate size (NMAS), and warm mix asphalt (WMA) technologies. Table 3.1 presents the different mixture characteristics for the seven mixtures that were used in the first group. The mixtures used in the first task were surface course mixtures obtained from the New York Infrastructure and Transportation (MIT) project, New York Department of Transportation (NYDOT), and North Carolina DOT.

The MIT project is located on Provincial Highway 8 in New York, Canada. The total project length is about 17 miles that is divided into two parts. The first part includes eight mixtures from four sections that were used to evaluate the effects of three WMA technologies: Advera, Sasobit, and Evotherm. Due to a shortage of the mixtures, only some of the mixtures from the first part of the MIT project were selected for the current study.

Table 3.1. Mixture Information for First Group

Mixture Number	Mixture Name	NMAS (mm)	Additive	RAP Content (%)	Binder Grade	Air Void (%)
1	NC RS9.5B ^a	9.5	NA ^h	30	PG 64-22	4.0
2	NC RS9.5B WMA ^b	9.5	Evotherm	35	PG 58-28	4.0
3	NY Surface ^c	9.5	NA	0	PG 58-28	3.2
4	MIT RAP 50SB ^d	16	NA	50	PG 52-34	5.7
5	MIT-Control ^e	16	NA	0	PG 58-28	3.9
6	MIT-Advera ^f	16	Advera	0	PG 64-22	3.0
7	MIT-Sasobit ^g	16	Sasobit	0	PG 58-28	3.2

Note:

^a North Carolina surface mixture with RAP

^b North Carolina surface mixture with RAP and Evotherm

^c Surface mixture used in New York

^d New York Infrastructure and Transportation 50% RAP mix, SB is soft binder

^e New York Infrastructure and Transportation mixture with no warm mix additive

^f New York Infrastructure and Transportation mixture with Advera warm mix additive

^g New York Infrastructure and Transportation mixture with Sasobit warm mix additive

^h Not applicable

For the second task, a broad range of mixtures properties, such as binder performance grade (PG), RAP content, NMAS, and aging level, were considered. Table 3.2 presents the mixture properties for this task. The purpose of the second task is to verify the conclusions drawn from the first task.

Table 3.2. Mixture Information for Second Group

Mixture Number	Mixture Name	NMAS (mm)	Additive	RAP Content (%)	Binder Grade	Air Void (%)
1	ALF ^a -Control	12.5	NA ^h	0	PG 70-22	4
2	ALF-SBS	12.5	SBS	0	PG 70-28	4
3	ALF-Terpolymer	12.5	Terpolymer	0	PG 70-28	4
4	ALF-Crumb Rubber	12.5	Crumb Rubber	0	PG 70-28	4
5	AAD ^b (STA ^c)	9.5	NA	0	PG 58-22	4
6	AAD (LTA1 ^d)					
7	AAD (LTA2 ^e)					
8	AAD (LTA3 ^f)					
9	NC S9.5B ^g (STA)	9.5	NA	0	PG 64-22	4
10	NC S9.5B (LTA1)					
11	NC S9.5B (LTA2)					
12	NC S9.5B (LTA3)					

Note:

^a Federal Highway Administration's Accelerated Loading Facility

^b Mixture with SHRP AAD binder and limestone aggregate

^c Short term aging for four hours at 135°C

^d Long term aging level 1 according to AASHTO R 30 (2 days at 85°C)

^e Long term aging level 2 according to AASHTO R 30 (4 days at 85°C)

^f Long term aging level 3 according to AASHTO R 30 (8 days at 85°C)

^g North Carolina surface mixture

^h Not applicable

All the specimens were compacted using the Superpave gyratory compactor to a diameter of 150 mm and a height of 178 mm. To obtain specimens of uniform air void distribution, these samples were cored and cut to a height of 150 mm and 100 mm diameter for testing.

3.4. Test Method

Dynamic modulus tests were performed on both groups of materials using a Material Testing System (MTS) machine. The test procedure for the first group of materials followed the AASHTO T 378/R 84 protocol in general, except that the test temperatures were 40°C, 20°C, 4°C, 0°C, -10°C, -20°C, and -30°C. The test procedure for the second group of materials followed the AASHTO T 342 protocol with the test temperatures of 54°C, 40°C, 20°C, 4°C, and -10°C. Sinusoidal cyclic loading was applied in stress-controlled mode using the loading frequencies of 25, 10, 5, 1, 0.5, and 0.1 Hz. For each step of the loading, the strain magnitude was kept between 60 $\mu\epsilon$ and 70 $\mu\epsilon$.

Axial deformations were measured in the middle of each specimen using four linear variable differential transducers (LVDTs) at intervals of 90° with a gauge length of 70 mm. Devcon® steel putty was used to glue the targets for the LVDTs onto the specimens. LabVIEW software was used for data collection and processing. The averaged readings from the four LVDTs were used to determine the dynamic modulus and phase angle values.

3.5. Results and Discussion

Two basic approaches can be considered to construct mastercurves: unconstrained shifting and constrained shifting. In the unconstrained shift method, the data are manually shifted from successive pairs of isotherms to form a resultant smooth curve. The shift factor functions are derived independently each time a mastercurve is constructed. In the constrained shift method, an underlying model is used to force the mastercurve and/or shift factors to fit a predefined functional form using an optimization technique.

As explained, unconstrained shifting offers the benefit that no presumptions are made when building the dynamic modulus mastercurve, therefore, allowing the evaluation of the

accuracy of different mastercurve functions and time-temperature shift factor functions when extrapolation is necessary. Another advantage of unconstrained shifting is that the dynamic modulus mastercurve and shift values can be calculated independently of each other; thus, the mastercurve generated from this method is used as the reference mastercurve, and other methods are compared against the results from the unconstrained shifting method.

The dynamic modulus test provided the dynamic modulus value for each set of temperature and frequency. Then, the measured data could be shifted to construct the mastercurve. For the unconstrained shift method, two isothermal curves were selected and shifted to overlap each other. The first isothermal curve is the one whose temperature is around 4°C. The best overlap is defined based on the minimum summation of the absolute difference between the base curve and the curve whose frequencies should be shifted. The shift factor that gives the minimum value for the difference is adopted for the shift factor. The shift is made for the $\log(|E^*|)$ versus $\log(f)$ curve. Figure 3-1 shows the steps involved in constructing the mastercurve using the unconstrained shift method.

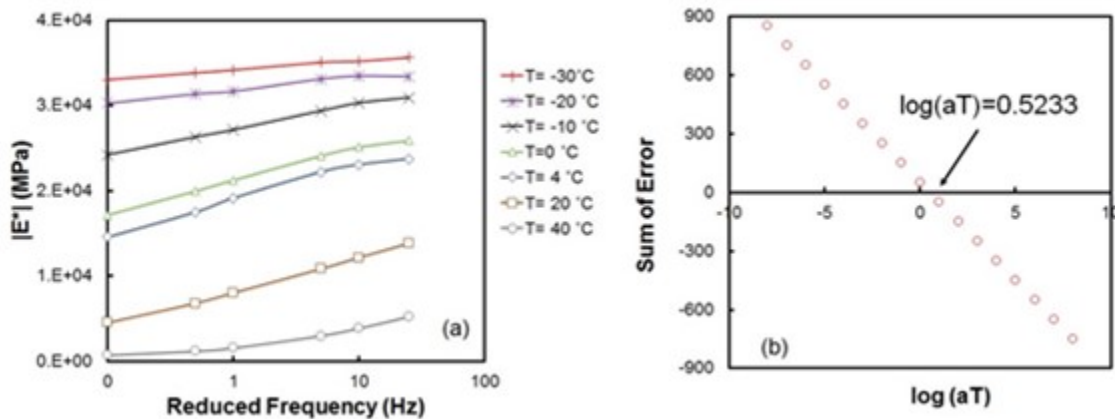


Figure 3-1. Example for using the unconstrained shift method: (a) measured dynamic modulus data for MIT RAP 50SB and (b) finding the shift factor for $T = 0^\circ\text{C}$.

Figure 3-2 shows the dynamic modulus mastercurves obtained using the unconstrained shift method in semi-log space for the seven mixtures. The figure shows that the unconstrained

shift method provides good overlap between the measured isothermal data. It also clearly indicates that the modulus value at very low temperatures and high reduced frequencies continues to increase, which suggests that the viscosity effect still exists at those low temperatures. As a result, all the material properties of the asphalt concrete at very low temperatures should be expressed in the reduced domain.

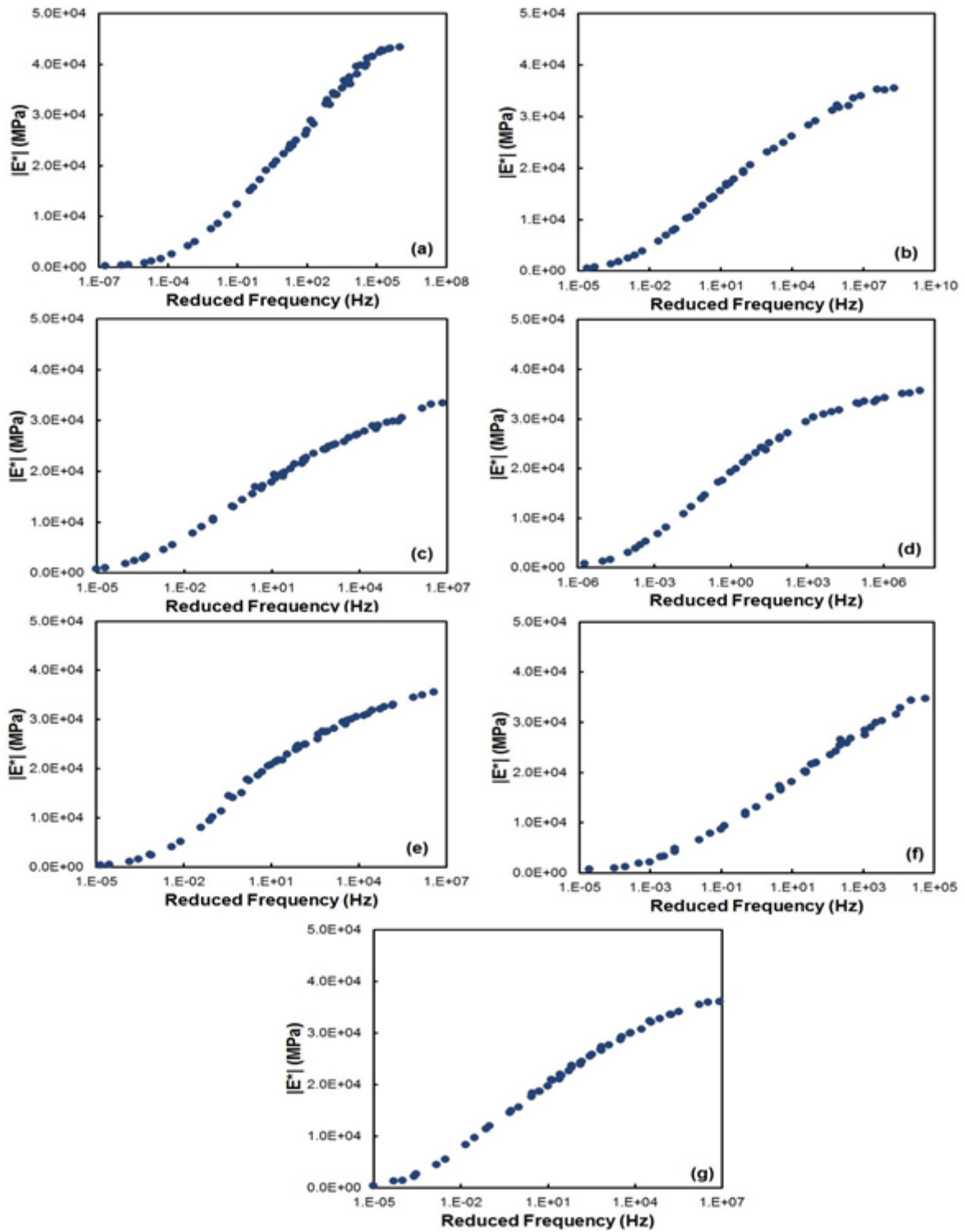


Figure 3-2. Dynamic modulus mastercurves obtained from unconstrained shift method in semi-log space: (a) NC RS9.5B, (b) NC RS 9.5B WMA, (c) NY Surface, (d) MIT RAP 50SB, (e) MIT Control, (f) MIT Advera, and (g) MIT Sasobit.

Figure 3-3 plots the data in Figure 3-2 in log-log scale and thus puts more emphasis on the accuracy of the unconstrained shift method at low reduced frequencies.

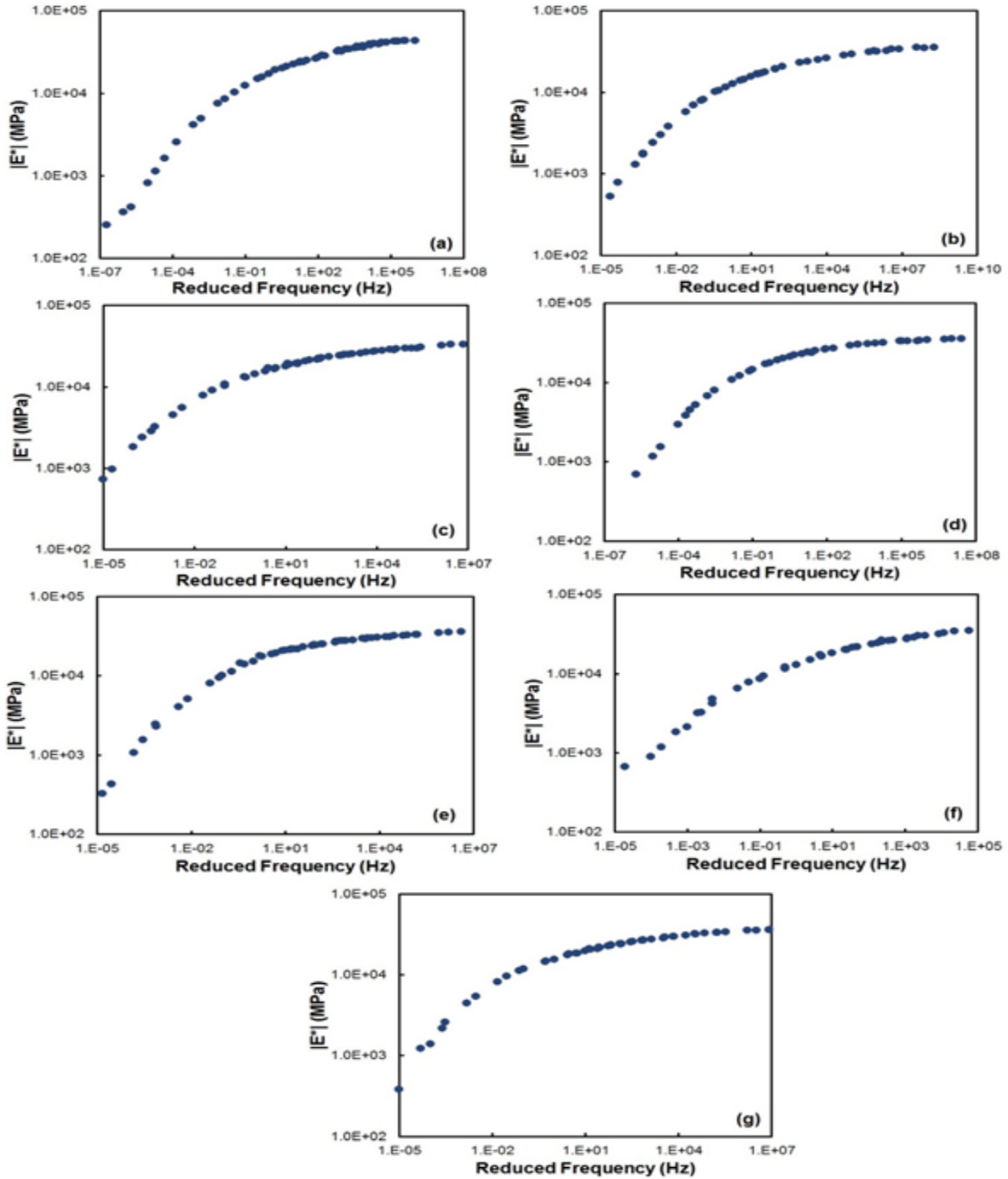


Figure 3-3. Dynamic modulus mastercurves obtained from unconstrained shift method in log-log space: (a) NC RS9.5B, (b) NC RS 9.5B WMA, (c) NY Surface, (d) MIT RAP 50SB, (e) MIT Control, (f) MIT Advera, and (g) MIT Sasobit.

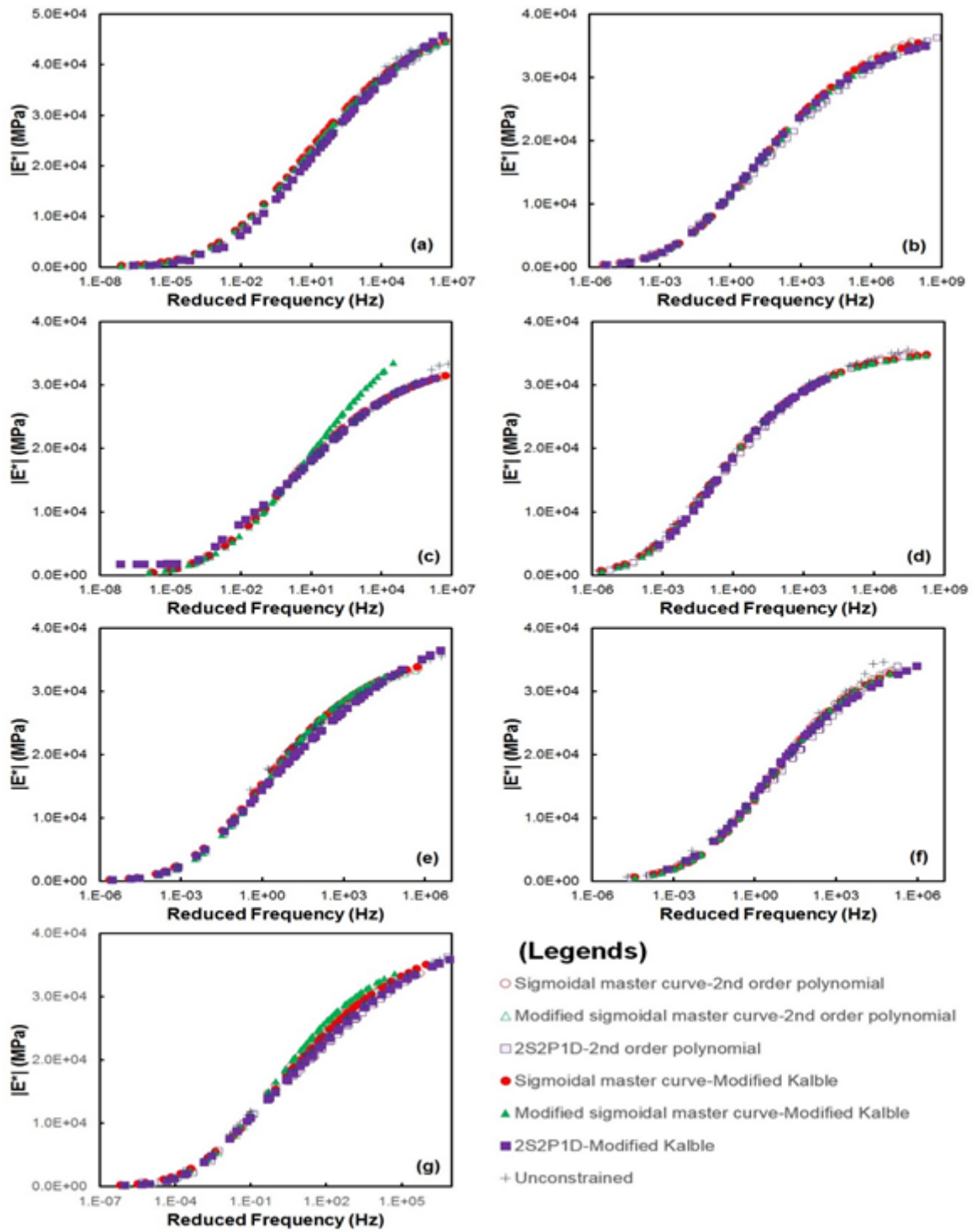


Figure 3-4. Dynamic modulus mastercurves obtained from different fitting and shift methods in semi-log space: (a) NC RS9.5B, (b) NC RS 9.5B WMA, (c) NY Surface, (d) MIT RAP 50SB, (e) MIT Control, (f) MIT Advera, and (g) MIT Sasobit.

Figure 3-5 presents the shifted results of the dynamic modulus data in log-log space. As shown, all the methods can provide a good fit with the measured data.

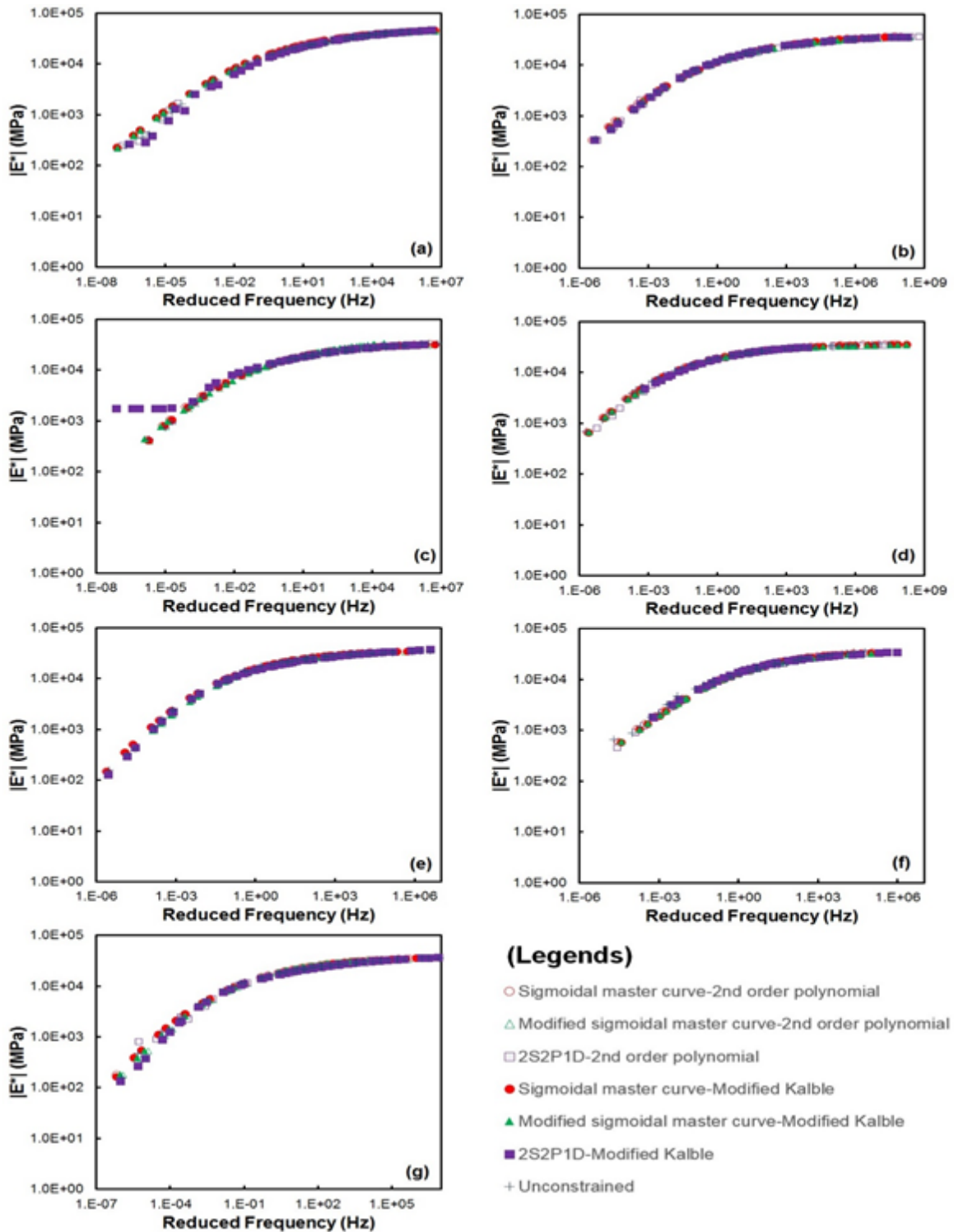


Figure 3-5. Dynamic modulus mastercurves obtained from the different fitting and shifting methods in log-log space: (a) NC RS9.5B, (b) NC RS 9.5B WMA, (c) NY Surface, (d) MIT RAP 50SB, (e) MIT Control, (f) MIT Advera, and (g) MIT Sasobit.

Figure 3-6 presents comparisons of the shift factors obtained from the different methods. All of the methods, except 2S2P1D combined with modified Kalble, can provide values that are close to the unconstrained data points.

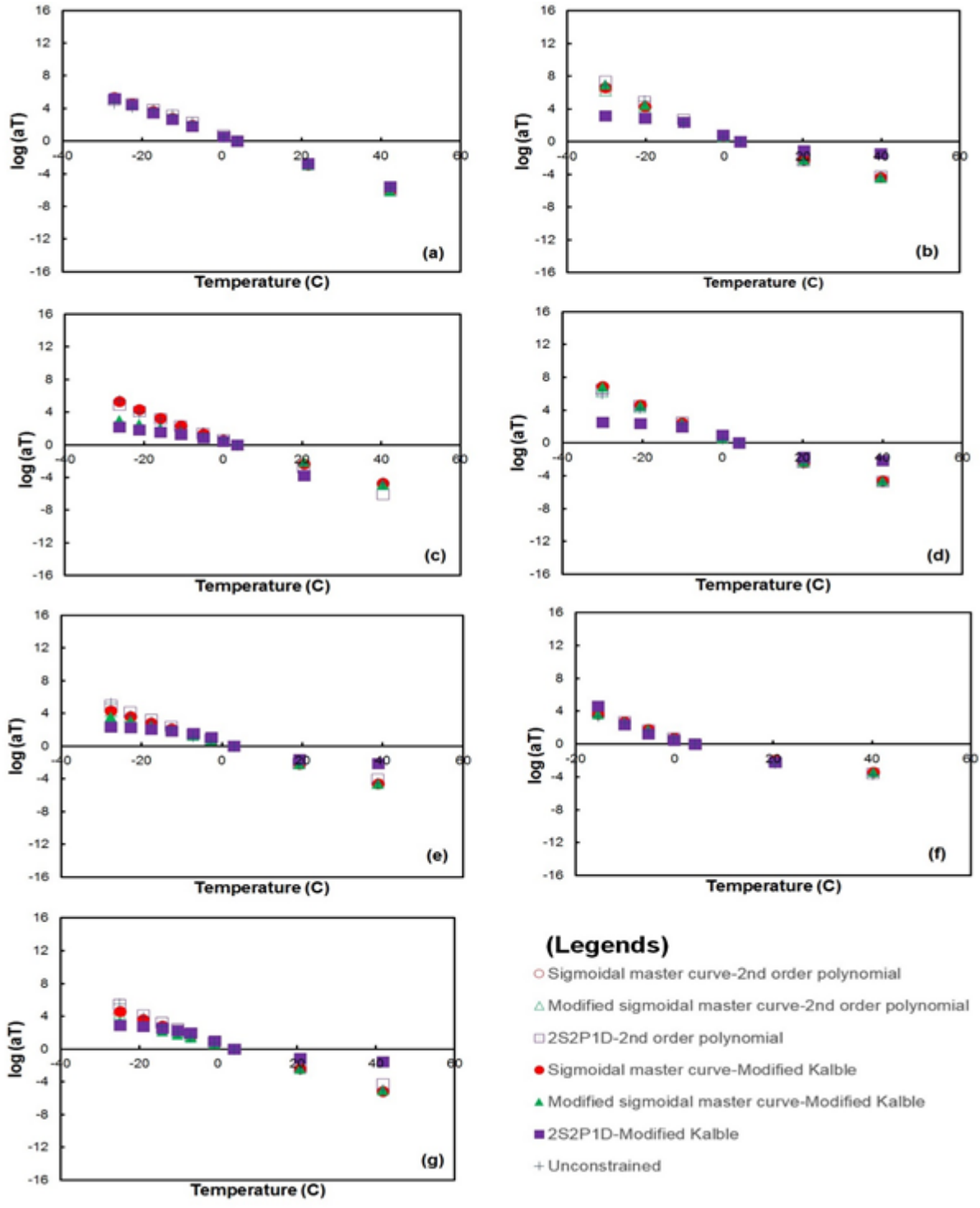


Figure 3-6. Time-temperature shift factors obtained from the different shift methods: (a) NC RS9.5B, (b) NC RS 9.5B WMA, (c) NY Surface, (d) MIT RAP 50SB, (e) MIT Control, (f) MIT Advera, and (g) MIT Sasobit.

As mentioned before, both the AMPT and AASHTO T 378/R 84 test procedure were used to measure the dynamic modulus values and phase angles between 4°C and 40°C. Hereafter, that set of data is referred to in this report as limited data. The limited data were used to develop a mastercurve using different mastercurve functions and shift factor functions. Figure 3-7 presents the comparison of the dynamic moduli values predicted from the fitted functions and the measured dynamic moduli values from the first dataset. Figure 3-7 shows that, with the exception of the 2S2P1D method combined with the second-order polynomial and the 2S2P1D method combined with the modified Kalble function, the other methodologies under predicted the actual measured data at high reduced frequencies. This under prediction could lead to considerable error in pavement response analysis where thermal cracking is concerned. It should be noted that the semi-log space plots aid comparisons of the extrapolated dynamic modulus data at high reduced frequencies using the fitting functions and the measured dynamic modulus data at those reduced frequencies. The mastercurve fitting results calculated from the different methods are presented in Figure 3-8 in log-log space to show the fitting at low reduced frequencies. As shown, use of the limited data set for fitting the data does not lead to any significant error for the dynamic modulus data that correspond to low reduced frequency values.

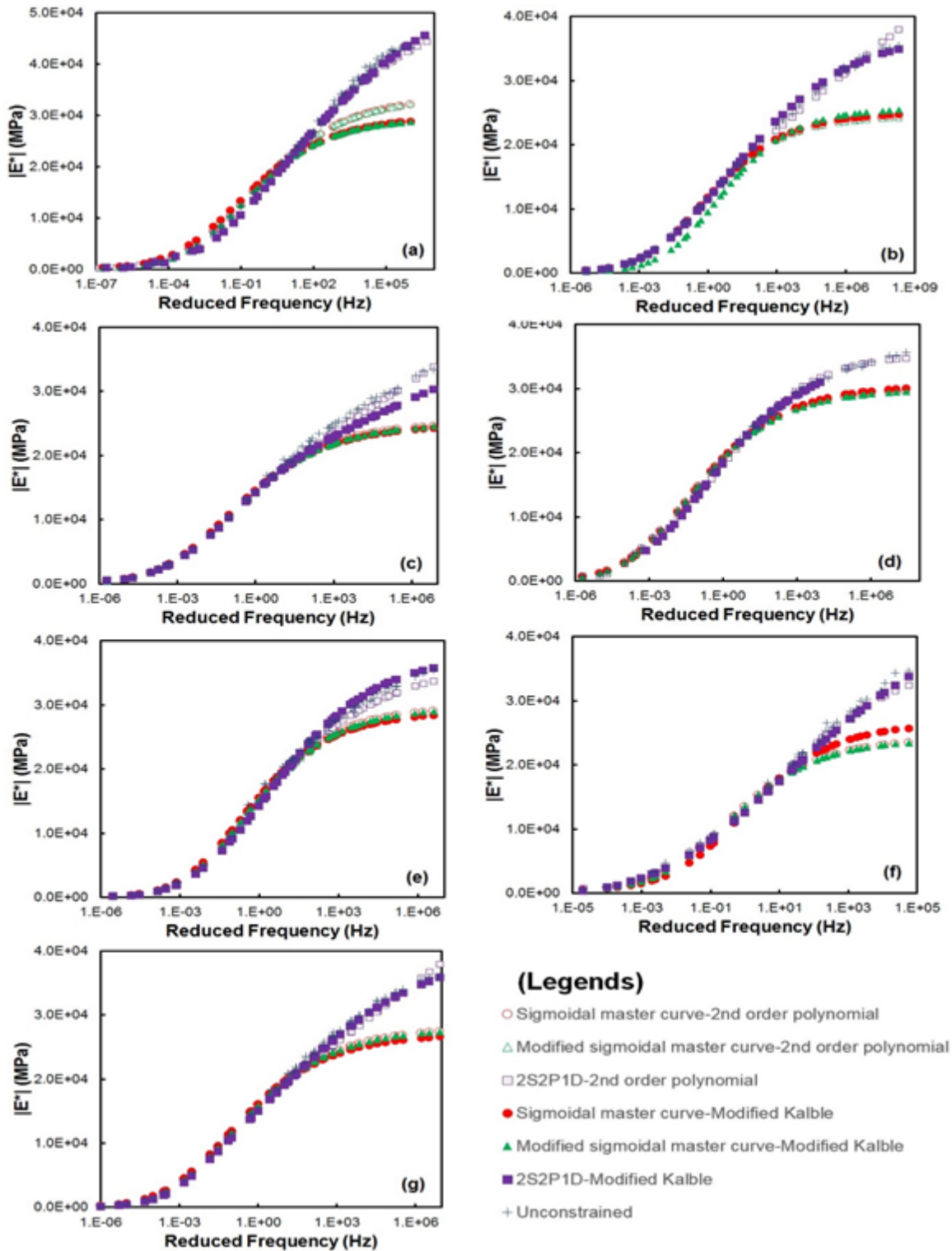


Figure 3-7. Dynamic modulus mastercurves obtained from the limited data set using different fitting and shift methods: (a) NC RS9.5B, (b) NC RS 9.5B WMA, (c) NY Surface, (d) MIT RAP 50SB, (e) MIT Control, (f) MIT Advera, and (g) MIT Sasobit.

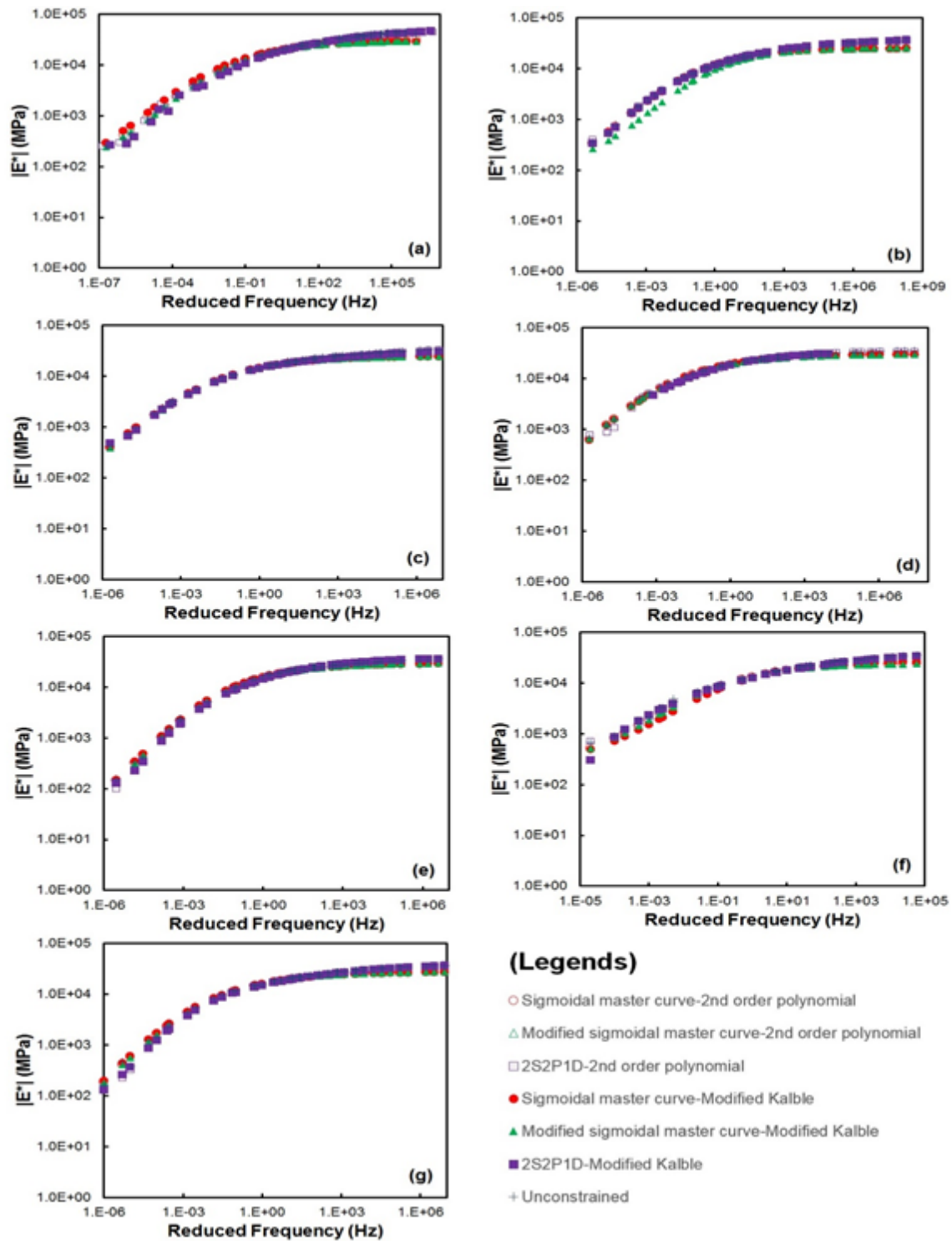


Figure 3-8. Dynamic modulus mastercurves calculated from the limited data set using different fitting and shift methods: (a) NC RS9.5B, (b) NC RS 9.5B WMA, (c) NY Surface, (d) MIT RAP 50SB, (e) MIT Control, (f) MIT Advera, and (g) MIT Sasobit.

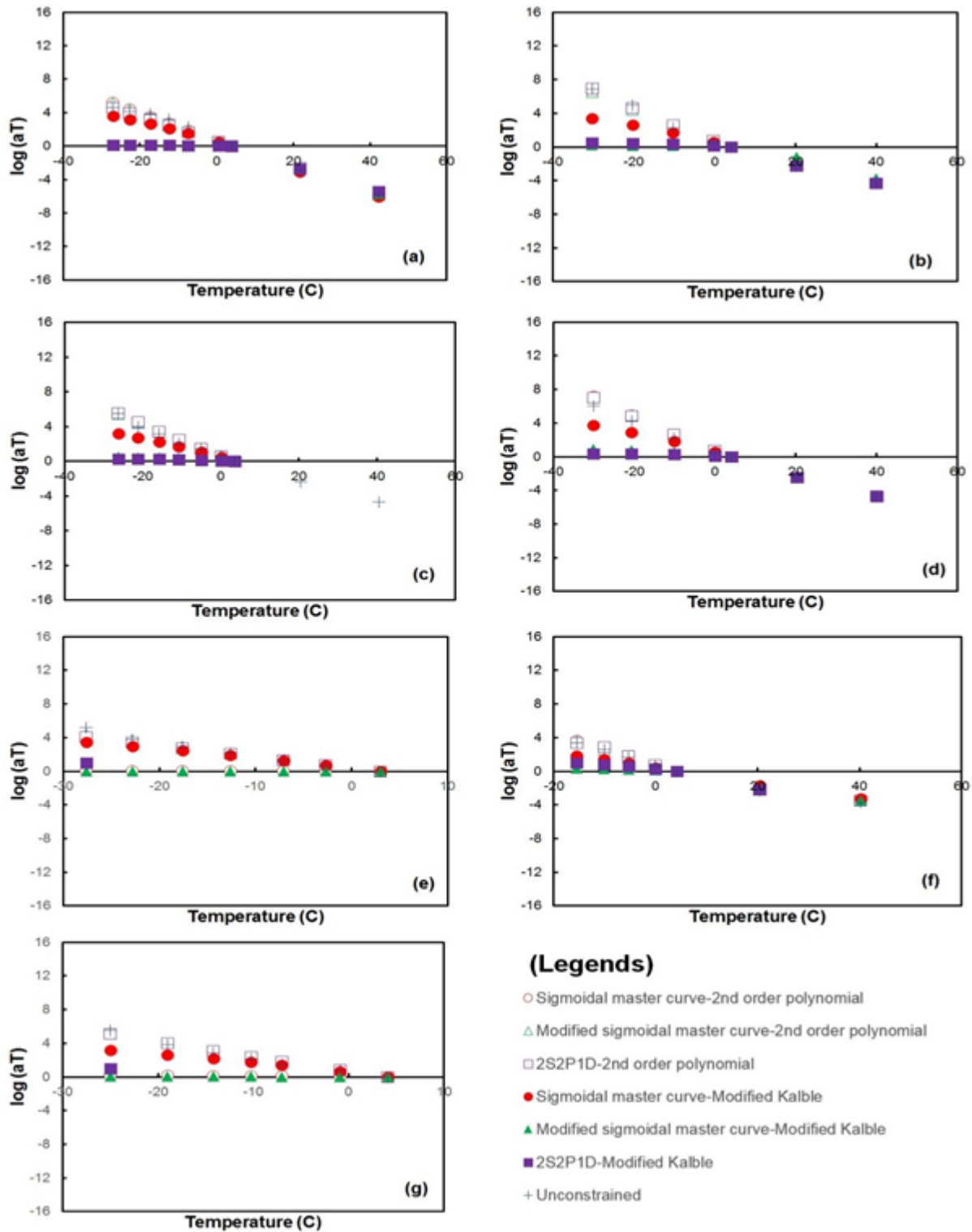


Figure 3-9. Dynamic modulus mastercurves obtained from the liMITed data set using different fitting and shift methods: (a) NC RS9.5B, (b) NC RS 9.5B WMA, (c) NY Surface, (d) MIT RAP 50SB, (e) MIT Control, (f) MIT Advera, and (g) MIT Sasobit.

Figure 3-9 shows that the 2S2P1D expression for the dynamic modulus mastercurve combined with the second-order polynomial function for the time-temperature shift factor is able to obtain the best estimation of the shift factor coefficients. The 2S2P1D function and modified Kalble model greatly underestimated the shift factors at low temperatures. Figure 3-9 shows that different fitting functions give a large difference in logarithm of shift factor for temperatures below 0°C. Equation (2.27) expresses the induced loading rate in the mathematical form. As can be seen in Equation (3.16), the reduced strain rate is proportional to the shift factor in arithmetic scale. That is, one order of magnitude underestimation of shift factor causes one order of magnitude underestimation in reduced loading rate. Therefore, the underestimation of shift factor shown in Figure 3-9 can lead to a significant error in the prediction of low temperature cracking performance of asphalt mixture.

$$\begin{cases} \varepsilon'_r = \frac{d\varepsilon}{d\xi} = a_T \times \frac{d\varepsilon}{dt} \\ \frac{d\varepsilon}{dt} = \frac{d}{dt}(CTC \times (T - T_0)) \end{cases} \rightarrow \varepsilon'_r = a_T \times CTC \times \frac{d}{dt}(T - T_0) \quad (3.16)$$

Where ε'_r is reduced strain rate, ξ is reduced time, a_T is the time-temperature shift factor for any given temperature, ε is strain, t is time, CTC is the coefficient of thermal contraction of asphalt concrete, T is temperature, and T_0 is the reference temperature.

Figure 3-10 shows that the 2S2P1D model with the second-order polynomial function used for the horizontal shift of the data is able to give a good estimate of the measured phase angle values. Figure 3-10 shows also that the fitting method cannot predict the phase angle data that correspond to the low reduced frequency (high temperature) region. This finding can be explained once the nature of the behavior of the mixture is considered. At high temperatures, the contribution of the binder during loading decreases significantly and, as a result, the aggregate-

to-aggregate contact can play a role in the global behavior of the mixture. Obviously, the current method is unable to capture the aggregate-to-aggregate interlock phenomenon. Because one of the objectives of this research effort is to find a methodology that satisfies structural-level modeling, the phase angle data that correspond to high temperatures can be used directly from the measurements. It should be noted that the predicted phase angle for RS 9.5B WMA matches the measured data very well, even for high-temperature regions. One reason for this outcome is that this specific mixture uses 30% RAP and, thus, its constitutive binder is less prone to thermal changes.

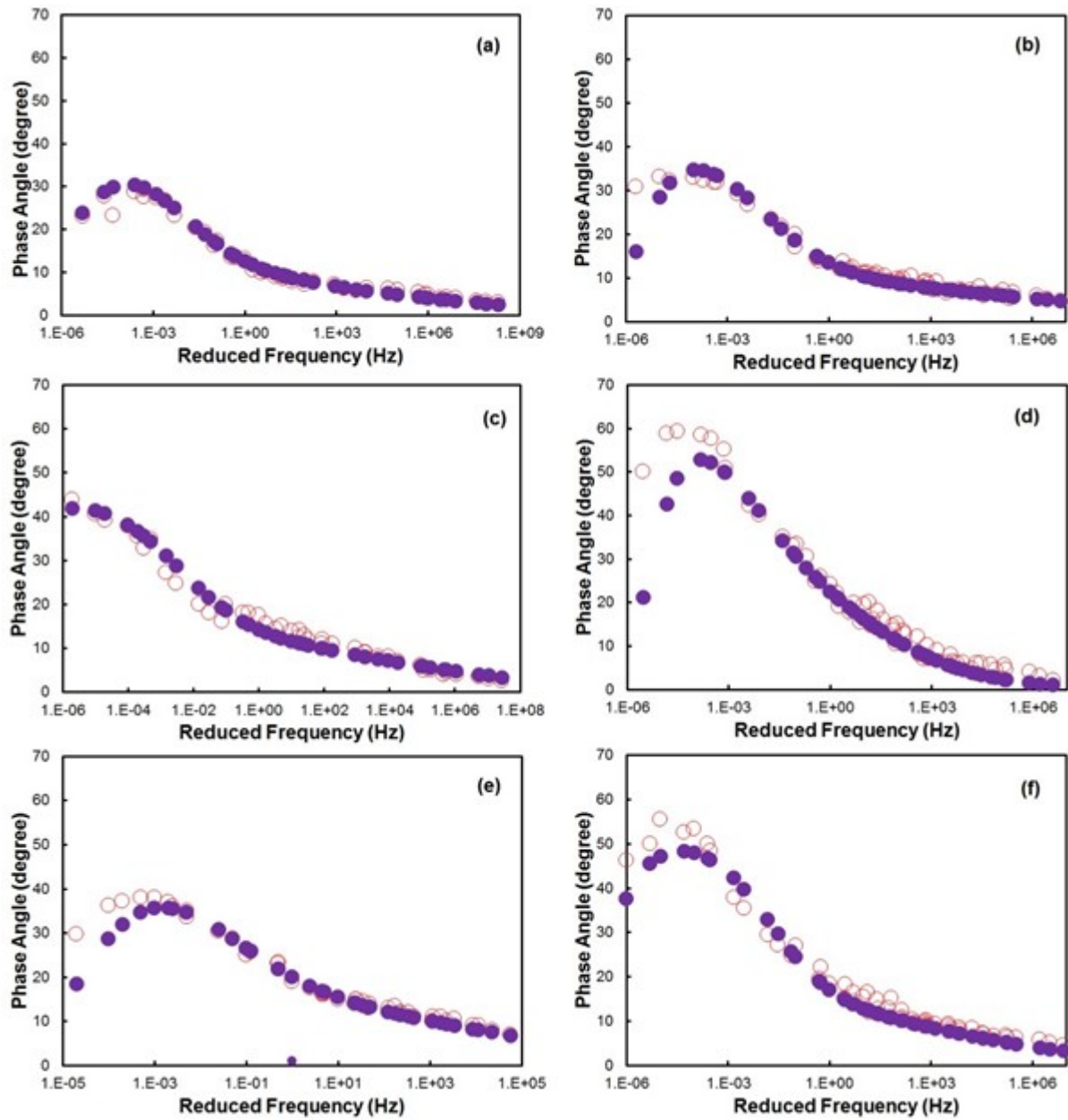


Figure 3-10. Phase angle mastercurve functions determined from the limited dataset using the 2S2P1D function: (b) NC RS 9.5B WMA, (c) NY Surface, (d) MIT RAP 50SB, (e) MIT Control, (f) MIT Advera, and (g) MIT Sasobit.

According to observations of the data that were measured at temperatures between -30°C and 40°C , the appropriate method for fitting the dynamic modulus data is the 2S2P1D function. In this method, the second-order polynomial is used to shift the measured data horizontally. Once

the two forms of the function are used simultaneously, the measured data can be fitted and extrapolated to low temperatures well.

The analysis method that was used for the first task of analysis was applied to the second dataset. The goal of this study is to verify the accuracy of the suggested methodology for more mixture data. The isothermal measured data in the range of 4°C to 40°C were used to fit the data and obtain the required parameters. Once the fitting was complete, then the extrapolation for lower temperatures was done and the results compared with the actual measured data obtained from the unconstrained shift method. Once again, the verification was for the dynamic modulus mastercurve, the time-temperature shift factor, and the phase angle mastercurve. Figure 3-11, Figure 3-12, and Figure 3-13 present the results of the verification.

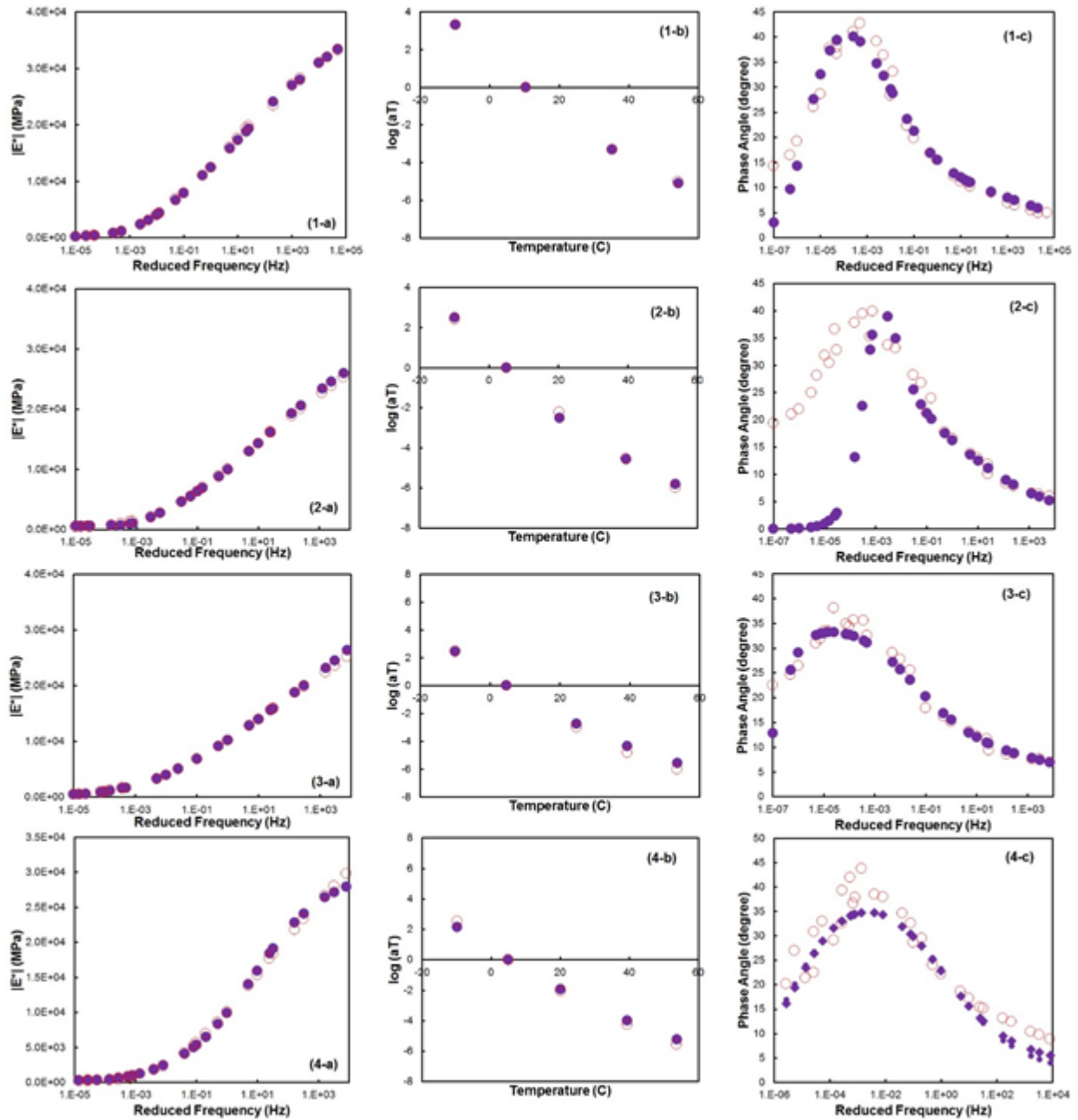


Figure 3-11. Dynamic modulus mastercurve, (b) time-temperature shift factor, and (c) phase angle mastercurve. (1) ALF- Control, (2) ALF-SBS, (3) AFL-Terpolymer, and (4) ALF- Crumb Rubber. Empty circles represent data that were fitted and shifted based on the 2S2PID model and second-order polynomial function. Filled circles represent the measured data.

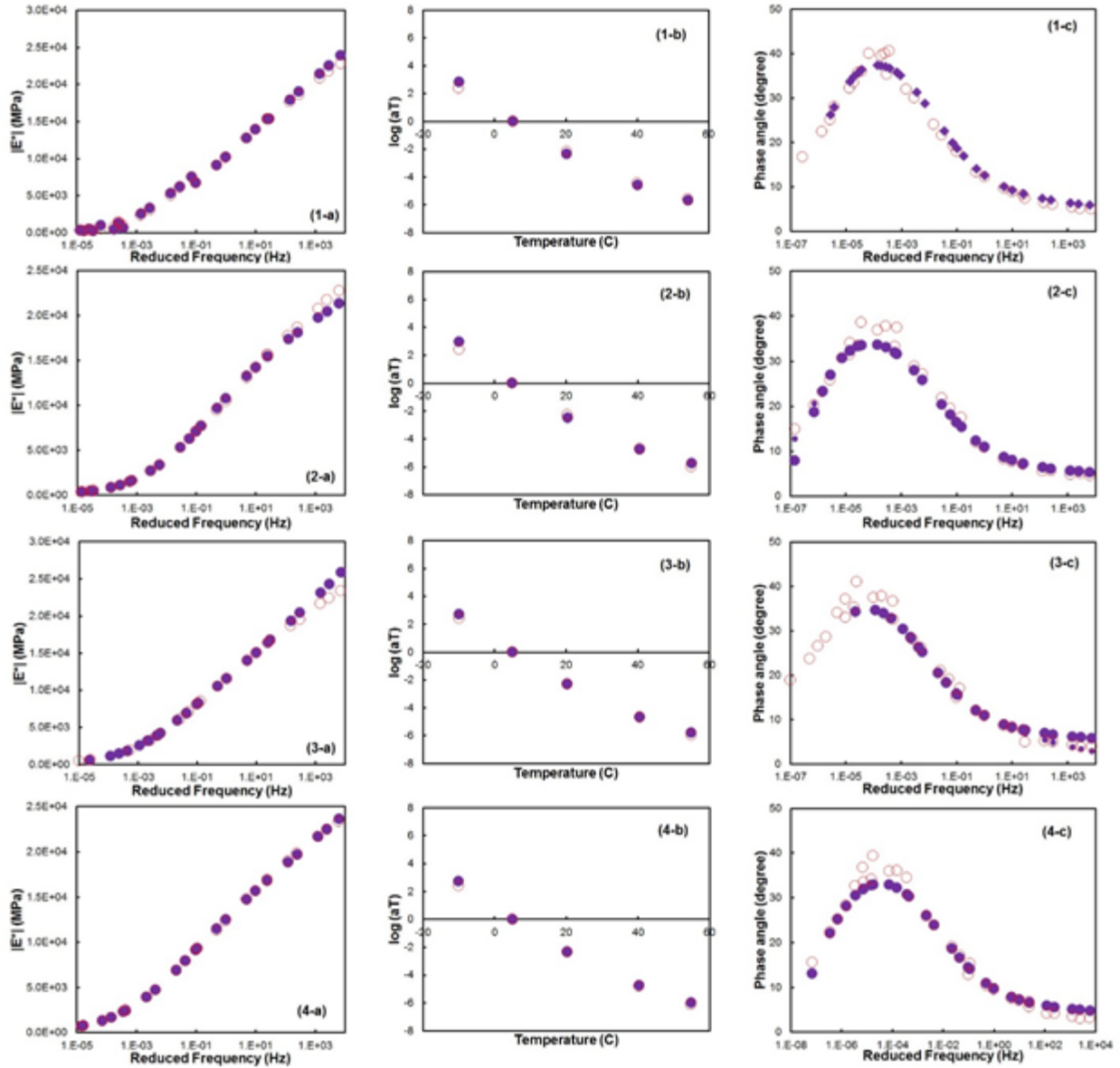


Figure 3-12. Dynamic modulus mastercurve, (b) time-temperature shift factor, and (c) phase angle mastercurve. (1) AAD (STA), (2) AAD (LTA1), (3) AAD (LTA2), and (4) AAD (LTA3). Empty circles represent data that were fitted and shifted based on the 2S2P1D model and second-order polynomial function. Filled circles represent the measured data.

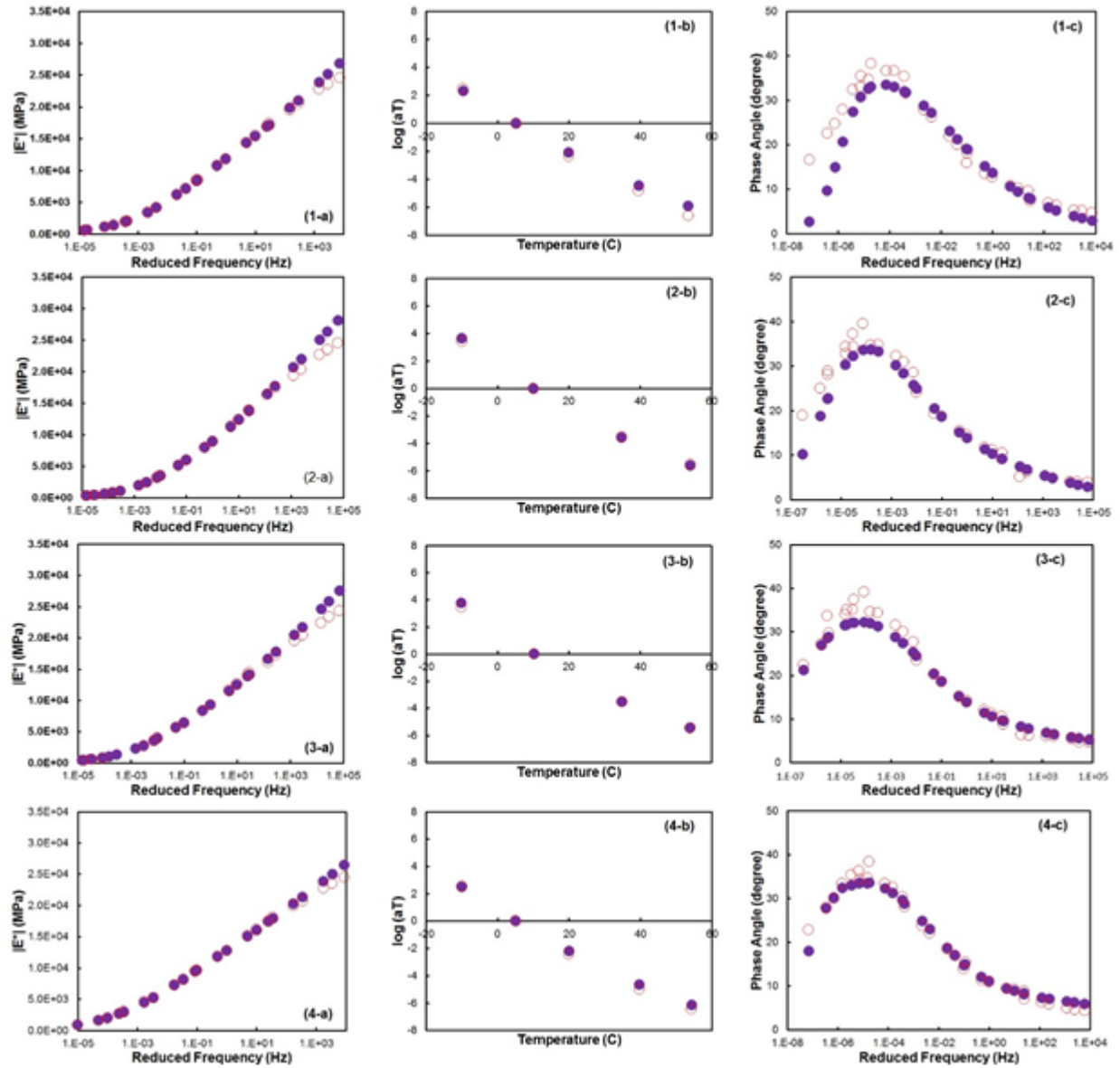


Figure 3-13. Dynamic modulus mastercurve, (b) time-temperature shift factor, and (c) phase angle mastercurve. (1) NC S9.5B (STA), (2) NC S9.5B (LTA1), (3) NC S9.5B (LTA2), and (4) NC S9.5B (LTA3). Empty circles represent data that were fitted and shifted based on the 2S2PID model and second-order polynomial function. Filled circles represent the measured data.

Figure 3-14 compares the predicted data obtained from the fitting procedure to the measured data for the mixtures in the second group.

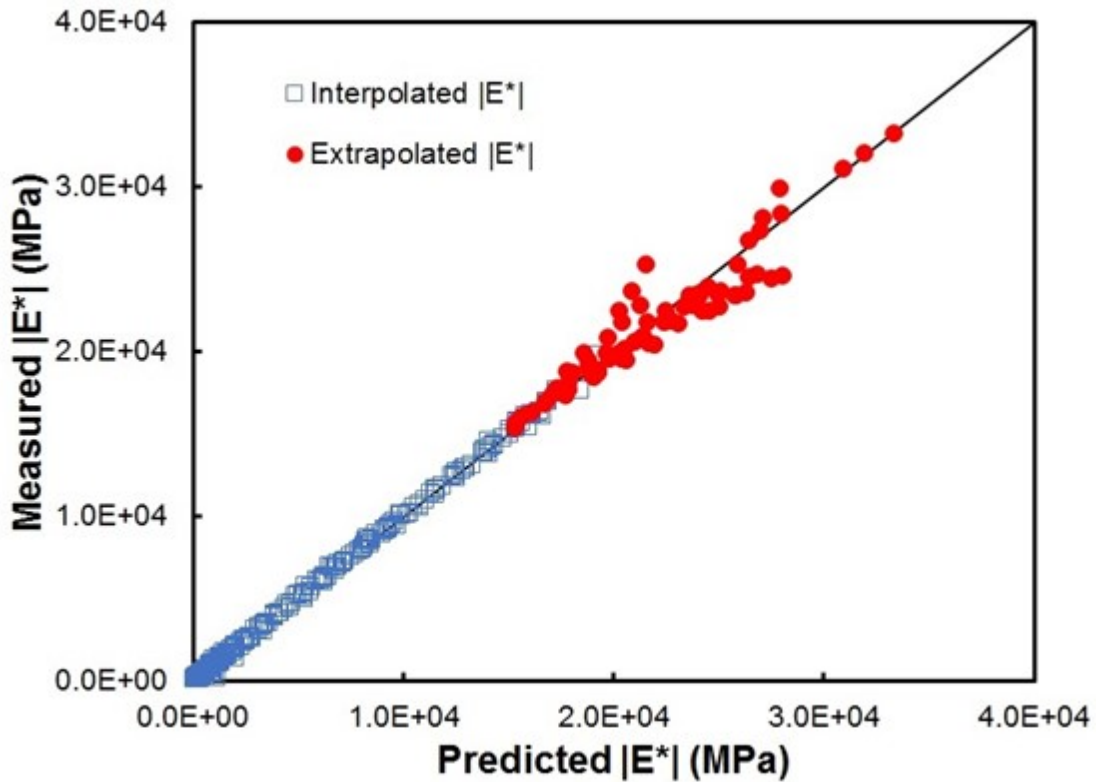


Figure 3-14. Predicted versus measured dynamic modulus data for all the mixtures listed in Table 3.2 .

3.6. Conclusions

This study investigated the ability of various dynamic modulus mastercurve functions and time-temperature shift factor functions to predict the dynamic modulus, phase angle, and time-temperature shift factor at temperatures lower than 4°C using data obtained from dynamic modulus tests conducted at 4°C, 20°C, and 40°C in accordance with AASHTO T 378/R 84 specifications. Sigmoidal, modified sigmoidal, and 2S2P1D functions were selected for the dynamic modulus mastercurve function. With regard to the time-temperature shift factor function, second-order polynomial and modified Kalble functions were selected for the study. Various combinations of mastercurve functions and shift factor functions were tried in order to fit the dynamic modulus test data that were measured from asphalt mixtures with a wide range of binder grades, NMAS, RAP content, binder modification technologies, and aging levels. This

study found that the 2S2P1D function for constructing a mastercurve along with the second-order polynomial shift factor function could adequately extrapolate dynamic modulus and phase angle data measured at 4°C, 20°C, and 40°C to temperatures much lower than 4°C.

CHAPTER 4. A COMPOSITE MODEL FOR PREDICTING THE COEFFICIENT OF THERMAL CONTRACTION FOR ASPHALT CONCRETE MIXTURES

4.1. Abstract:

Thermal cracking is one of the most prevalent types of distress found in asphalt concrete pavement sections. The thermal stress cannot be relieved because the viscosity of pavement mixtures reduces in low-temperature regions. The coefficient of thermal contraction (CTC) is the intrinsic parameter that determines the thermal contraction of asphalt mixtures subjected to temperature drop. Thus, thermal stress and associated thermal damage are greatly affected by the CTC of the mixture. CTC measurements and predictions have proven to be challenging tasks. The direct measurement of a mixture's CTC is the most reliable and at the same time cumbersome method for predicting the thermal contraction of asphaltic mixtures. In this study, for Level I analysis, we measured the CTCs of mixtures that have a wide range of properties and reported the data. In order to remedy the difficulties associated with directly measuring CTC, we herein propose a simple yet accurate composite model. The suggested approach enables pavement engineers to predict CTC values as the temperature drops. The formulation requires the mixture's volumetric properties, elastic modulus, and CTC of the aggregate a priori. With regard to binder, the formulation requires the CTC and relaxation modulus as input parameters. The 2S2P1D formulation was used to obtain the binder relaxation modulus from the given dynamic modulus of the mixture. This procedure constitutes the Level II analysis for which the binder CTC is required beforehand. A database which constitutes a basis for estimating binder CTC was developed from measurements reported in the literature. The predicted binder CTC is then input into the developed composite model to predict the CTCs of mixtures. This procedure constitutes Level III analysis. The CTC values from the measurements and predicted from the

composite model (Levels II and III) are compared. In order to fully understand the effects of Levels II and III errors in estimating mixture CTCs, we also compared the induced thermal stress obtained from the predicted CTCs and the corresponding stress obtained from the measured CTCs.

4.2. Introduction

Thermal cracking is one of the most prevalent types of distress for pavement sections located in the northern part of the United States and Canada (Marasteanu et al. 2007). The Rapid and significant drop in air temperature in these geographical regions induces considerable stress in asphalt concrete pavement layers. Because the viscosity of the pavement mixture reduces as the temperature drops, the thermal stress cannot ‘relax’ and, as a result, creates internal damage in the asphalt mixture that originates from the evolution of micro damage within the asphalt mixture. Once the induced damage passes the mixture’s tolerance threshold, the microcracks coalesce and appear as a macrocrack (Keshavarzi and Kim 2016). The new crack allows water and deleterious materials to penetrate the pavement structure. This mechanism significantly reduces the load-bearing capacity of pavement sections.

Such thermal cracking also imposes significant maintenance costs on highway agencies, which has motivated pavement researchers to find a reliable framework for assessing asphalt mixtures’ resistance to thermal loading and develop an algorithm for predicting pavement performance under the effect of thermal loading (Dave et al. 2013, Alavi 2014, Rehbar-Rastegar et al. 2018, Zhu et al. 2017, Nemati et al. 2019). Among all the parameters that affect the magnitude of thermal stress in asphalt mixtures, the coefficient of thermal contraction (CTC) is the factor that determines the amount of contraction that asphalt mixtures undergo for any given temperature drop. As a result, the CTC is a critical input parameter for predicting the damage

associated with thermal cracking in asphalt pavement sections. The study that was conducted as part of the calibration of the thermal cracking model in the AASHTO Mechanistic Empirical Pavement Design Guide (MEPDG) software emphasizes the importance of the CTC on predicted crack spacing (Kim 2009).

This paper presents the experimental study to measure the CTCs of asphalt mixtures and the analytical study to develop predictive models of CTC from constituent material properties. Three levels of analysis are proposed in this paper for measuring and/or predicting the CTCs of asphalt concrete mixtures. The CTC of an asphalt mixture should be measured directly at Level I. Although Level I may impose extra testing and additional testing equipment, Level II suggests a simple yet efficient formulation (a composite model) for predicting mixture CTCs. This method requires measured binder CTCs a priori. Level III analysis groups binders based on their low performance grade and uses average CTC values for each group. In Level III analysis, the estimated binder CTC is input into the composite model to predict the CTC of the mixture. Then the validity and accuracy of different methods were investigated based on comparisons of the measured and predicted CTC values. To study the effect of error in the mixture CTC predictions, we compared the induced thermal stress in a representative volume element (RVE) sample subjected to thermal variation using the measured CTC or predicted CTC from Level II or III analyses. Before the work in this study is described in details, the following two sections summarize the previous research efforts to measure and predict the CTC of asphalt mixtures.

4.2.1. Measuring the Coefficient of Thermal Contraction of Asphalt Mixtures

Researchers have long known that the CTC is a function of temperature (Nam and Bahia 2004, 2009, Marasteanu et al. 2007, 2012, Kim et al. 2010, Bahia et al. 2012, Alavi 2014, Islam and Tarefder 2014). Several researchers have developed various test methods to measure the

CTC of asphalt mixtures. For example, Stoffels et al. (1996) used the resistance strain gauge method to capture the CTC variation of asphalt mixtures for temperatures ranging from 0°C to -25°C. However, the installation of strain gauges on specimens makes this approach cumbersome, and thus, other researchers have not adopted this methodology. Mehta et al. (1998) used linear variable differential transducers (LVDTs) to measure the CTC of asphalt concrete as part of indirect tensile strength testing. The values obtained from the Mehta et al. (1998) study of three different mixtures and an aluminum sample agreed with the values reported by Stoffels et al. (1996). Zeng and Shields (1999) attached LVDTs to asphalt concrete beam specimens (51 mm x 51 mm x 340 mm) and applied temperatures ranging from -40°C to 40°C to measure the thermal deformation of the asphalt mixtures.

Based on the measured data, Zeng and Shields (1999) concluded that thermal deformation cannot be approximated by a linear function, which means that the CTC is a nonlinear function of temperature. Bahia and Anderson (Bahia and Anderson 1993) developed a hyperbolic relationship to express the volume changes of binder when it is subjected to temperature variation, expressed here as Equation (4.1). Several researchers (Marasteanu et al. 2007, 2012, Kim et al. 2010) have used this relationship to fit measured data. Therefore, because of its widespread usage and accuracy, we decided to adopt this relationship to fit the measured data in this research.

$$v = c_v + CTC_g \times (T - T_g) + R \times (CTC_L - CTC_g) \times \ln \left(1 + \exp \left(\frac{T - T_g}{R} \right) \right) \quad (4.1)$$

where v is the specific volume change, c_v is a constant, R is the regression constant that is related to the rate of volume change at or near the glassy transition temperature, T is the test

temperature ($^{\circ}\text{C}$), and CTCL and CTCg are the coefficients of thermal contraction above and below the glassy temperature, respectively.

Later, Bahia and a research group at the University of Wisconsin, Madison developed a test set-up for measuring the CTCs of asphalt mixtures that consists of a control chamber where an asphalt sample is placed on a frictionless Teflon base (Marasteanu et al. 2007). The asphalt sample is attached to two LVDTs at its ends. A beam (65 mm x 65 mm x 380 mm) is placed in a temperature-controlled chamber to measure the mixture CTC. The test starts at 40°C and finishes at -80°C with a rate of $1^{\circ}\text{C}/\text{min}$. Marasteanu et al. 2007 placed a dummy sample in the chamber to record the surface and inside temperatures during testing. The samples they used were compacted with a kneading compactor and sawn to the required size. (It is known that a kneading compactor is unable to bring the sample air void content close to the air void content of asphalt mixtures in the field where the air void content drops significantly because of passing traffic a few years after construction.) Later, Bahia et al. 2012 used samples sawn and glued from Superpave gyratory-compacted asphalt mixture samples. This test set-up is called the ‘asphalt thermal cracking analyzer’ (ATCA). The ATCA is laborious because it requires the gluing of sawn samples to form the test specimen. The ATCA can measure two sets of properties in each run: (1) the fracture temperature of an asphalt sample that is restrained at both ends and experiences damage as the temperature decreases and (2) the CTC of another sample that is free to deform as the temperature drops. The high temperature drop rate imposes a considerable temperature gradient within the sample. The ATCA does not provide a tool to measure the temperature inside the samples; therefore, the air temperature is used to calculate the CTC of the mixture.

Alavi (2014) developed the uniaxial thermal stress and strain test after making modifications to the thermal stress restrained strain test (TSRST) and measured the CTC of the mixture during this test. Alavi included two samples that were side-cored from the Superpave gyratory-compacted sample and glued them together to make a long enough specimen that would fit inside the temperature chamber. In this test, the sample is placed on top of a frictionless pad and attached to two LVDTs at its ends. The sample is placed horizontally and used in addition to a vertical restrained sample. Once the test starts at 25°C and the air temperature inside the chamber drops at the rate of -10°C/h, the longitudinal deformation of the horizontal unrestrained specimen is recorded. These measurements can be used to find the CTCs of asphalt mixtures (Farrar et al. 2013).

Islam and Tarefder (2014) measured the CTCs and coefficient of thermal expansion (CTE) of asphalt mixtures in the laboratory. They used the temperature range of -20°C to 55°C and used field-cored as well as laboratory Superpave gyratory-compacted samples to study the variations in the CTCs and CTEs as a function of temperature. They also investigated the effects of anisotropy, air void content, aggregate gradation, and aggregate source. These researchers attached two LVDTs to cylindrical samples (100 mm in diameter and 150 mm in height) and measured the CTCs and CTEs of the asphalt mixtures. They used lithium aluminosilicate glass-ceramic, also known as ZERODUR®, to calibrate the LVDTs. ZERODUR® has very low CTC and CTE values and thus can be used to calibrate LVDTs. Islam and Tarefder (2014) concluded that the CTC and CTE are nonlinear functions of temperature. This observation also confirms the findings of other researchers. Through Statistical hypothesis tests, Islam and Tarefder (2014) also concluded that the CTC and CTE are independent of anisotropic effects. This finding can help in the development of a predictive model by just modeling the asphalt behavior in one direction.

Through Statistical hypothesis tests, Islam and Tarefder (2014) also concluded that air void content and aggregate gradation do not affect the CTC, but that aggregate geology does affect the CTC and CTE.

Bahia and Anderson (1993) developed a dilatometry system to measure the thermo-volumetric properties of asphalt binder. This system consists of two capillary tubes filled with ethyl alcohol that are located above the binder sample. The volumetric variation of the binder that is due to an imposed temperature change changes the amount of alcohol in the tubes. The test starts at 40°C and finishes at -76°C. Binder samples are subjected to a cooling rate of 1°C/minute. For each run of the test, two measurements can be taken. Details about this test are available elsewhere (Bahia and Anderson (1993)). It seems reasonable to correlate the temperature-dependent behavior of an asphalt mixture to its constituent binder. In this way, binder thermo-volumetric properties play a critical role in the dependency of asphalt mixture thermal deformation on the governing temperature.

Akentuna (2017) proposed the Ohio CTE device that consists of two LVDTs with flat tips fixed at the top sides of an aluminum frame. The LVDTs are fixed in such a way that they are mutually perpendicular and coincide with the diameter of the test specimen. Each test sample can be obtained from a Superpave gyratory-compacted sample.

4.2.2. Predicting the Coefficient of Thermal Contraction of Asphalt Mixtures

Jones et al. (1968) developed a volumetric equation to predict CTCs and CTEs. The relationship that they developed, expressed here as Equation (4.2), considers the volumetric thermal variations of the aggregate and binder separately and adds them to obtain the linear CTC and CTE of asphalt mixtures. Jones et al. (1968) assumed that the contributions from the binder and aggregate are proportional to their corresponding volumetric portion.

$$B_{mix} = \frac{V_{AC} \times CTC_{binder} + V_{agg} \times CTC_{agg}}{3 \times V_{total}} \quad (4.2)$$

Where V_{ac} is binder content, CTC_{binder} is the thermal coefficient of contraction for the binder, V_{agg} is the aggregate volume content, and CTC_{agg} is the thermal coefficient of contraction for the aggregate. Lytton et al. (1980) later modified Jones et al.'s relationship to take into account the effect of air voids. Their modified equation is shown here as Equation (4.3).

$$B_{mix} = \frac{(V_{AC} + V_{AIR}) \times CTC_{binder} + V_{agg} \times CTC_{agg}}{3 \times V_{total}} \quad (4.3)$$

where V_{air} is air void content.

Based on a study that was conducted as part of the Strategic Highway Research Program (SHRP), the CTC value of 3.45×10^{-4} ($1/^\circ\text{C}$) was used to represent the CTC of binder (Kennedy et al. 1990). Although using a constant CTC value for binder regardless of the dominant temperature has long been proved to be incorrect, the idea of using a constant value for binder thermo-volumetric properties suggests a method to categorize different binders into separate groups and use a constant set of numbers to represent each group.

Kim et al. (2010) proposed a composite model to predict the CTC of asphalt mixtures. Their model approximates an asphalt mixture as a composite that consists of aggregate, asphalt binder, and air voids. They used the Hirsch model (Christensen 2003) to consider the contributions of binder, aggregate, and air void to determine the thermal deformation of asphalt mixtures. Kim et al. (2010) assumed that the orthotropic nature of asphalt mixtures does affect the thermal deformation responses of asphalt mixtures and, as a result, they considered an idealized packing and a three-dimensional phase diagram of the aggregate and the asphalt binder.

They also considered the volume fraction of the binder phase and of the aggregate phase to be proportional to the cubic power of the relative length of each phase. Equation (4.4) describes this assumption.

$$L_{agg}^3 = 1 - \frac{VMA}{100} \rightarrow L_{agg} = \sqrt[3]{1 - \frac{VMA}{100}}$$

$$L_b^3 = 1 - L_{agg}^3 \rightarrow L_b = \sqrt[3]{1 - \frac{VMA}{100}}$$
(4.4)

where VMA is the void in mineral aggregate. Kim et al. (2010) assumed that the areas of the binder and aggregate phases are proportional to the square power of their corresponding lengths and can be obtained from Equation (4.5). According to the Islam and Tarefder (2014) study, the anisotropic effect can be ignored and, as a result, the Kim et al. (2010) approach could be simplified and the relationship rewritten in one dimension.

$$A_{agg} = L_{agg}^2 = \left(1 - \frac{VMA}{100}\right)^{\frac{2}{3}}$$

$$A_{binder} = L_b^2 = \left(\frac{VMA}{100}\right)^{\frac{2}{3}}$$
(4.5)

Alavi (2014) conducted a comprehensive study to investigate the effects of mixture volumetric properties on the CTCs of mixtures. He extracted important factors regarding the mixtures' thermal deformation. He measured the CTC of mixtures in uniaxial thermal stress and strain tests and proposed regression equations to correlate the liquid coefficient of thermal contraction (CTCL), glassy coefficient of thermal contraction (CTCg), and glass transition temperature (Tg) of mixtures with other volumetric properties. Alavi assumed a universal constant curvature (R) for all the mixtures. He also included the low shear modulus of unaged

binder, asphalt binder content, and aggregate gradation in the regression relationships (Alavi 2014).

Alavi also studied the correlations among the CTCL, CTCg, and Tg as a function of aging. He represented aging using the carbonyl content of the mixture and tried to correlate the variation of the aforementioned parameters to the carbonyl level. Although this approach can simplify the measurement procedure for practical purposes, the low R2 values of the regression relationships make the accuracy of the approach questionable (Alavi 2014).

Teymourpour and Bahia (2014) used the finite element method to develop a semi-empirical model to estimate the CTCs and CTEs of asphalt mixtures. They used dilatometric testing to obtain the glass transition temperature of the mastic and digital images of mixture specimens to represent the internal aggregate structure of the asphalt mixture. The general structure of the model is based on the Hirsch model wherein the asphalt mixture modulus is linked to volumetric properties. The proposed model assumes that the mixture CTE is a weighted average of the upper and lower theoretical bounds of the CTE. The theoretical bounds are calculated based on the volume fractions and the modulus value of each phase. An empirical approach was used to show the contribution of each phase. Equation (4.6) expresses the mathematical definition of this methodology.

$$\begin{aligned}
 CTC_{mixture}^{liquid} &= CTC_{upper}^{liquid} \times F_{liquid} + CTC_{lower}^{liquid} \times (1 - F_{liquid}) \\
 CTC_{mixture}^{glassy} &= CTC_{upper}^{glassy} \times F_{glassy} + CTC_{lower}^{glassy} \times (1 - F_{glassy}) \\
 F_{liquid} &= (0.7 - 0.31 \times \beta) \times E_{liquid}^{100 \times CTC_L} \\
 F_{glassy} &= (0.98 - 0.29 \times \beta) \times E_{aggregate}^{20 \times CTC_{glassy}} \\
 \beta &= \frac{\text{number of contact zones of the mixtures}}{770}
 \end{aligned} \tag{4.6}$$

where τ is the mixture CTC above the glassy temperature, τ_u is the upper limit for the mixture CTC for temperatures above the glassy temperature, α is the contribution factor for temperatures above the glassy temperature, τ_l is the lower limit for the mixture CTC at temperatures below the glassy temperature, τ is the mixture CTC for temperatures below the glassy temperature, τ_u is the upper limit for the mixture CTC for temperatures below the glassy temperature, τ_l is the lower limit for the mixture CTC for temperatures below the glassy temperature, and α is the contribution factor for temperatures below the glassy temperature.

According to Equation (4.6), the developed methodology considers the aggregate-to-aggregate contact points as a parameter that can affect the CTC of mixtures. IPass software was used to obtain this parameter by processing scanned images of the sample surface (Roohi et al. 2012). The requirement of the aggregate-to-aggregate contact points adds to the efforts required to predict the CTC of mixtures. The procedure proposed by Teymourpour and Bahia 2014 assumes that the CTC of mixtures comes from the contribution of parallel and series models. In a study that was undertaken to modify the Hirsch model, Christensen and Bonaquist (2015) found that the effect of a series model in the formulation can be ignored for most mixtures. This finding motivated the authors of this research to examine the contribution of parallel and series models introduced in the Marasteanu et al. 2012 model separately and determine their significance for predicting the CTCs of mixtures. The Methodology section of this paper presents the comparison study and discussion.

In the first step of the research presented in this paper, we gathered data that were measured and reported in the literature (Kennedy et al. 1990, Nam and Bahia 2004, Marasteanu et al. 2012) and then built a dataset. The dataset can be used to examine the validity and accuracy of any proposed models and, as a result, it is referred to as the first dataset.

Based on the work of Kim et al. (2010) and Marasteanu et al. (2012), we decided to investigate the contribution of parallel and series models separately to predict the CTCs of mixtures. The parallel model assumes that the aggregate and binder phases are positioned in parallel to each other whereas the series model assumes that the aggregate and binder phases are acting in a series and independently. The main motivation behind modeling the thermal deformation of mixtures using one-dimensional models is the conclusion drawn by Islam and Tarefder 2016 that the anisotropic effect is negligible. According to the Christensen and Bonaquist (2015) study, the contribution from each model should be examined separately to make sure that the final model is sufficient and efficient.

For this study, we examined the accuracy of the two aforementioned mechanisms in predicting the CTC of mixtures through comparisons of information in the database. The series model requires the relaxation modulus of the binder, $G(t)$, a priori. Because this parameter is not measured in routine mixture characterization procedures, we decided to backcalculate this parameter through other suggested approaches and selected the Hirsch, modified Hirsch, and 2S2P1D models for this purpose. We decided to test the accuracy of the proposed methodology using mixtures that have a wide range of properties. We tested different mixtures and measured their thermo-volumetric properties. These measurements comprised the second dataset.

4.3. Materials and Testing

This section describes the mixture properties, test procedure for Level I analysis, samples of the measurements, and fitting results. We used two datasets to examine the validity and accuracy of the Level II and III analyses. Because the temperature dependency of asphalt mixtures depends on the binder, we decided to divide the testing procedure into three different

analysis levels. The classifications are based on the amount of work required to measure the mixture CTC or its binder. Each level requires different measurement efforts.

Level I: The mixture CTC is measured directly. This level requires test equipment that can apply temperatures up to -60°C with a monotonic and predefined rate of loading.

Level II: The binder CTC is measured to predict the mixture CTC. This level requires the mixture volumetric, aggregate elastic modulus, aggregate thermal properties, and dynamic modulus of the mixtures.

Level III: The binder CTC is taken from the developed database. This level requires all the parameters mentioned for Level II.

The first dataset consists of measured and reported data from Marasteanu et al. (2012). The measured CTCs for both the binders and mixtures are reported for this dataset. Details regarding specimen dimensions and testing procedures are explained elsewhere (Marasteanu et al. 2012). We performed a comprehensive testing campaign to measure the CTCs of mixtures. The mixtures included in those tests cover a broad range of properties. It should be noted that the tests performed were only for mixtures.

Table 4.1 and Table 4.2 present the binder and mixture information used in this research, respectively (first dataset). Figure 4-1 presents details of the mixture properties tested in this study (second dataset).

Table 4.1. Binder Information for First Dataset

Cell Name	T_g (°C)	CTC_g (1/°C)	CTC_l (1/°C)	R
Cell 3	-27.4	2.97E-05	5.48E-04	6.6
Cell 19	-21	3.35E-04	5.56E-04	2.8
Cell 20	-17.4	1.77E-04	7.93E-04	6.9
Cell 22	-20.2	3.30E-04	7.70E-04	2.7
Cell 33	-18.4	3.40E-04	6.90E-04	3.1
Cell 34	-20.7	4.90E-04	9.60E-04	13.1
Cell 35	-17.8	2.60E-04	6.90E-04	4.5

Table 4.2. Mixture Information for First Dataset

Cell Name	VMA (%)	Air Void (%)	T_g (°C)	CTC_g (1/°C)	CTC_l (1/°C)	R
Cell 3	15.2	4	-25.3	9.93E-06	9.93E-06	6.9
Cell 19	16.2	4	-25.3	1.33E-05	3.86E-05	4.7
Cell 20	16.1	4	-20.5	1.40E-05	5.00E-05	4.9
Cell 22	14.8	3.7	-28.7	9.40E-06	4.00E-05	2.6
Cell 33	16.4	4.2	-26.8	6.90E-06	5.10E-05	6
Cell 34	16.2	4.2	-22.2	1.30E-05	5.10E-05	6.2
Cell 35	16.5	4	-25.6	1.40E-05	5.00E-05	3.5

Table 4.3. Mixture Information for Second Dataset

Mixture Number	Mixture Name	VMA	Additive	RAP Content (%)	Binder Grade	Air Void (%)
1	NC RS9.5B WMA	15.8	NA	30	PG 58-28	4
2	MIT*-Advera	15.2	Advera	0	PG 64-22	3.0
3	MIT-Sasobit	15	Sasobit	0	PG 58-28	3.2
4	MIT-Evotherm	14.9	Evotherm	0	PG 58-28	3.8
5	MIT RAP 50SB	15.5	N/A	50	PG 52-34	5.7
6	NY 9.5	15.3	N/A	0	PG 64-22	3.2
7	NY 19	17.1	N/A	0	PG 54-22	5

Note: *MIT Stands for New York Infrastructure and Transportation.

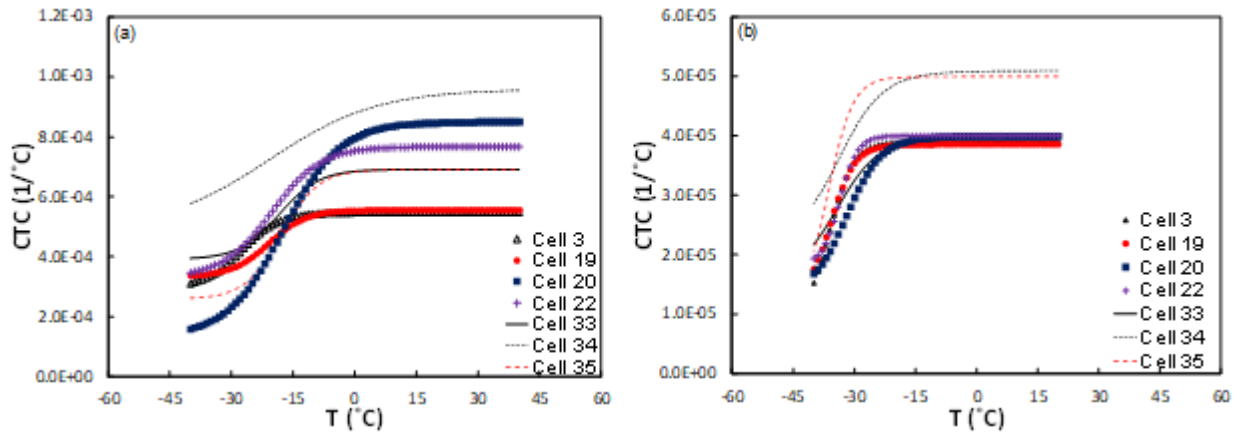


Figure 4-1. Coefficient of thermal contraction (CTC) plots for binders and mixtures in the first dataset: (a) binder, and (b) mixture data.

For the measurements taken in this study, a ZERODUR® sample was used to calibrate the LVDT deformation as the temperature dropped. Figure 4-2 shows the LVDTs attached to the ZERODUR® sample and asphalt concrete sample. After all four LVDTs were attached to the ZERODUR® sample, the sample was placed in the temperature chamber until it reached the equilibrium temperature of 22°C. A Material Testing Machine (MTS), which is capable of changing the temperature in a controlled fashion, was used in this study. The temperature rate was selected to be -30°C/h. The LVDT recordings were measured throughout the test. Figure 4-3

presents the LVDT readings while the LVDTs were attached to the ZERODUR® sample. Table 4.4 presents the calibration results. The LVDTs show positive (expansion) results upon a decrease in temperature. The ZERODUR® sample did not contract due to a decrease in temperature, whereas the LVDT steel rods used in the LVDT did contract. Because the ends of the LVDT were glued to the ZERODUR® sample, the sensor spring expanded to facilitate the contraction of the steel rods. Therefore, upon a decrease in temperature, the LVDTs show an expansion output if the material does not contract.

For the CTC measurement of asphalt mixtures, the 38 mm diameter specimens were used. The sample dimensions and details regarding mixture fabrication, coring, and cutting procedures are reported in Castorena and Kim (2017). The specimen is put on top of a Teflon pad to minimize the friction. A dummy sample is positioned in the chamber in order to record the temperature during the test. At the Start of the test, the specimens and the dummy sample are kept at 22°C for 20 minutes to reach a Stable temperature. After conditioning, the air inside the chamber is decreased with a rate of -30°C/h and lowered to -65°C. During the test, the LVDT measurements are recoded using LabView® software. A thermocouple records the air temperature, the temperature inside the dummy sample, and the surface temperature of the dummy sample during each run (Figure 4-2).

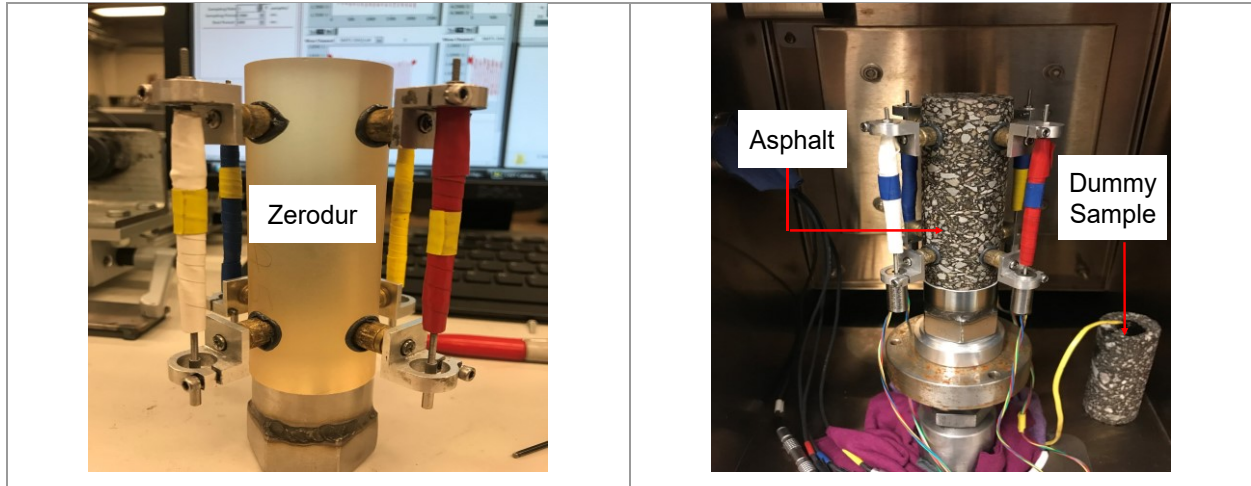


Figure 4-2. LVDTs attached to samples: (a) ZERODUR® sample and (b) asphalt coNcRe sample.

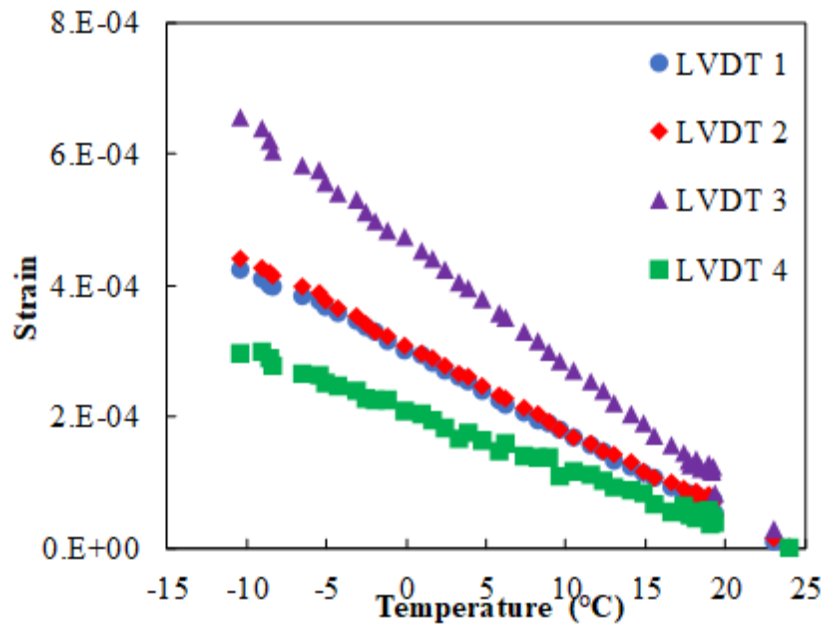


Figure 4-3. LVDT strain readings while LVDTs attached to ZERODUR® sample and subjected to constant temperature drop.

Table 4.4. Results of LVDT Calibration

	Slope (strain/°C)
LVDT 1	-1.26E-05
LVDT 2	-1.28E-05
LVDT 3	-1.85E-05
LVDT 4	-8.87E-06

After correcting the LVDT readings, we fitted the results to Equation (4.1) to find the thermo-volumetric properties of the mixtures. Figure 4-4 presents examples of the LVDT readings, temperature variations, and fitting results. Table 4.5 presents the fitting results. It should be noted that the averages of the inside and surface temperatures were used to fit the recorded data. The temperature used to plot the data shown in Figure 4-4 is the average temperature.

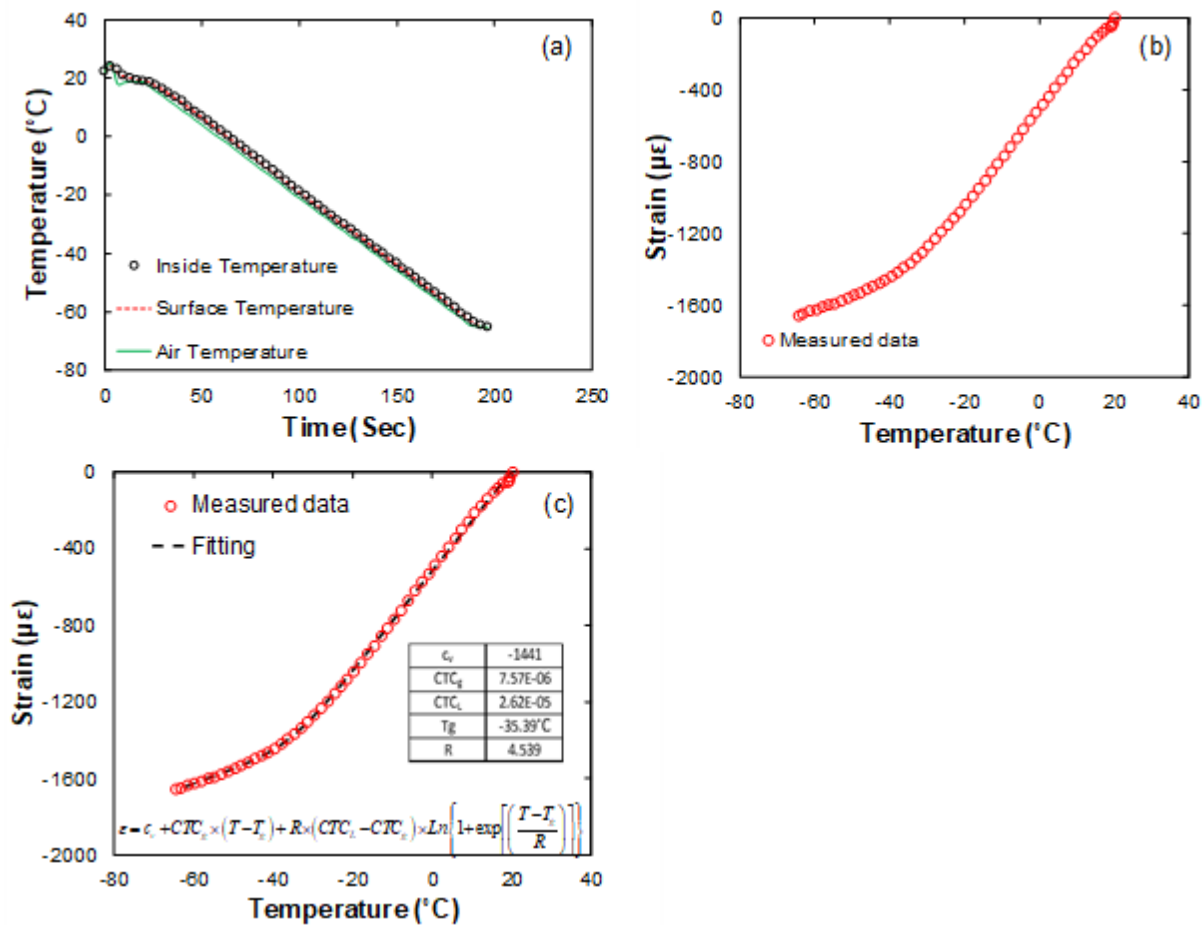


Figure 4-4. Test results: (a) LVDT readings, (b) temperature variation, and (c) fitting results.

Based on the measured data reported in different studies, we constructed a dataset for the thermo-volumetric properties (CTC_g , CTC_L , T_g) of the binders and arranged them based on the low performance grade. Figure 4-5 presents the constructed dataset.

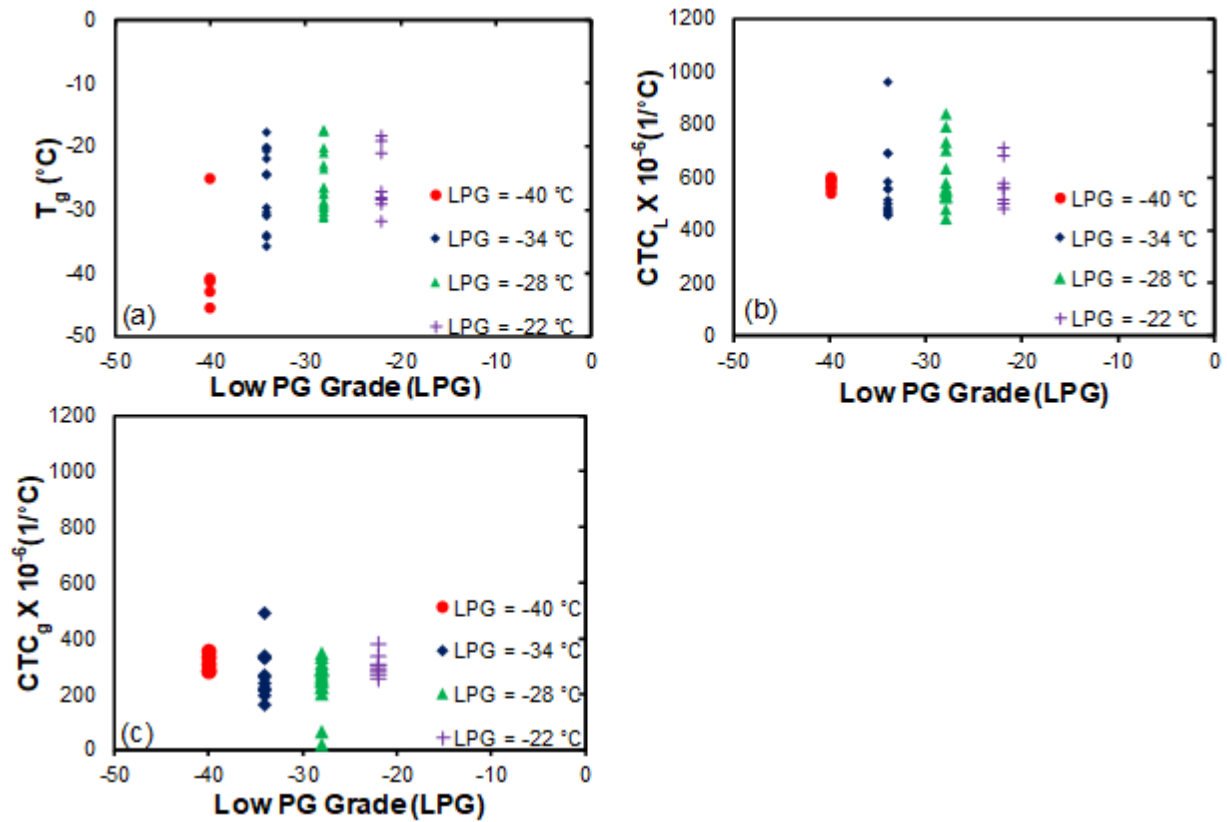


Figure 4-5. Classification of binder thermo-volumetric properties based on low performance grade: (a) glassy temperature (T_g), (b) liquid coefficient of thermal contraction ($CTCL$), and (c) glassy coefficient of thermal contraction (CTC_g).

Table 4.5. Fitting Results for Mixtures Tested

	C_v	CTC_g (1/°C)	CTC_L (1/°C)	T_g (°C)	R
NY 9.5	-1441	7.57E-06	2.63E-05	-35.39	4.538
NY 19	2.229	7.59E-06	2.02E-05	-34.4	2.229
RS 9.5B	2.683	8.03E-06	2.27E-05	-29.03	2.683
MIT 50SB	4.483	6.08E-06	2.08E-05	-34.29	4.483
MIT Advera	1.306	6.17E-06	2.04E-05	-38.22	1.306
MIT Sasobit	1.714	4.53E-06	1.92E-05	-37.25	1.714
MIT Evotherm	1.609	7.73E-06	2.35E-05	-39	1.609

For the first experimental campaign, the temperature of the sample was not reported. To consider the temperature gradient within the sample during the test, we decided to solve the heat

equation, Equation (4.7), and select the temperature in the middle of the sample as the representative temperature.

$$\frac{\partial T}{\partial t} = \kappa \frac{\partial^2 T}{\partial x^2} \quad (4.7)$$

Where T is temperature, t is time, κ is thermal diffusivity, and x is the spatial coordinate. Equation (3.7) is solved by using the finite difference method to find the temperature gradient within the sample as a function of time. The thermal diffusivity is assumed to be equal to $5 \times 10^{-7} \text{ m}^2/\text{°C}$. This value is within the range of reported values for asphalt mixtures. Figure 4-6 shows the temperature gradient within the sample for different air temperature drop rates. Figure 4-7 presents the calculated average temperatures of the sample and air temperature.

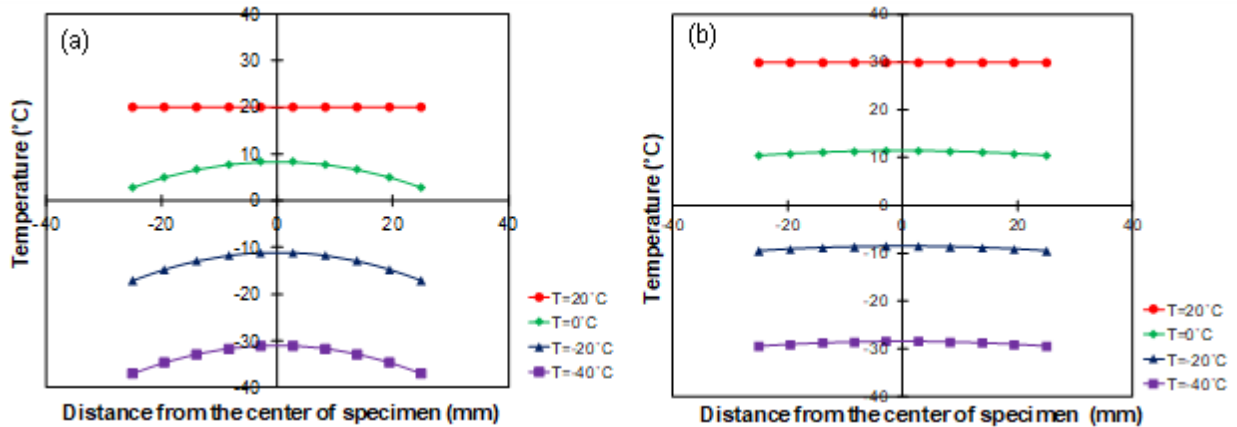


Figure 4-6. Temperature gradients within the sample at different instances of time for different rates of air temperature change: (a) $-60^\circ\text{C}/\text{hour}$ and (b) $-10^\circ\text{C}/\text{hour}$.

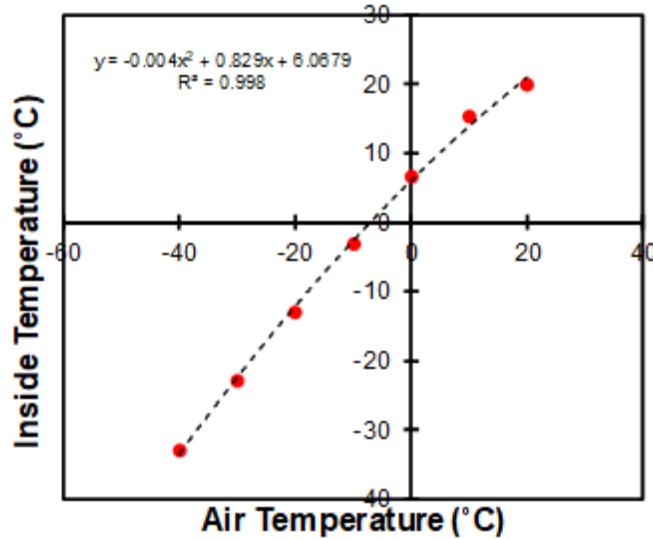


Figure 4-7. Averaged temperature evolution as a function of time.

4.4. Methodology

In this section, the basic formulation of the aforementioned composite model is derived and explained. Different approaches for backcalculating the shear modulus ($|G(\omega)|$) values of mixtures from the given dynamic modulus data are also discussed. Finally, the comparisons between the parallel and series models are made.

An asphalt concrete mixture is a particulate composite material in that it consists of a single continuous phase (asphalt binder) and a single discontinuous particulate phase (aggregate). Simple methods have been developed to illustrate the principle of the behavior of a particulate composite under an external perturbation. Figure 4-8 (a) and (b) show the simplest models in which the composite elements are positioned either in a series or in parallel, respectively, with respect to the external load.

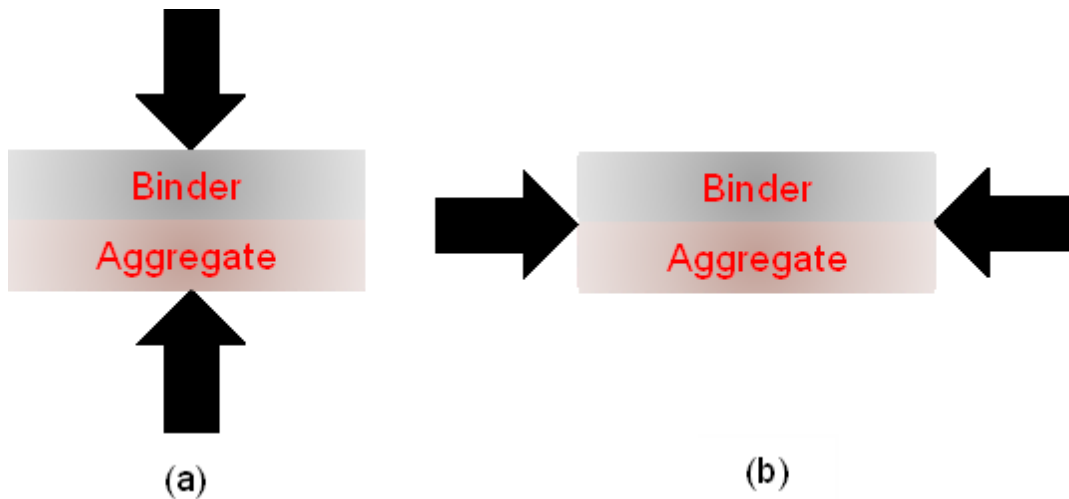


Figure 4-8. Schematic view of composite elements in asphalt mixtures: (a) series model and (b) parallel model.

Different models can be obtained through different assumptions of the relative position of these parallel and series models with respect to each other. Figure 4-9 presents two common models that are used to predict the modulus of a mixture based on its component properties. It may be worth developing simple relationships for both the parallel and series models for combinations of aggregate and binder first and then try to find a combination of them in a way that can best predict the CTC of the mixture.

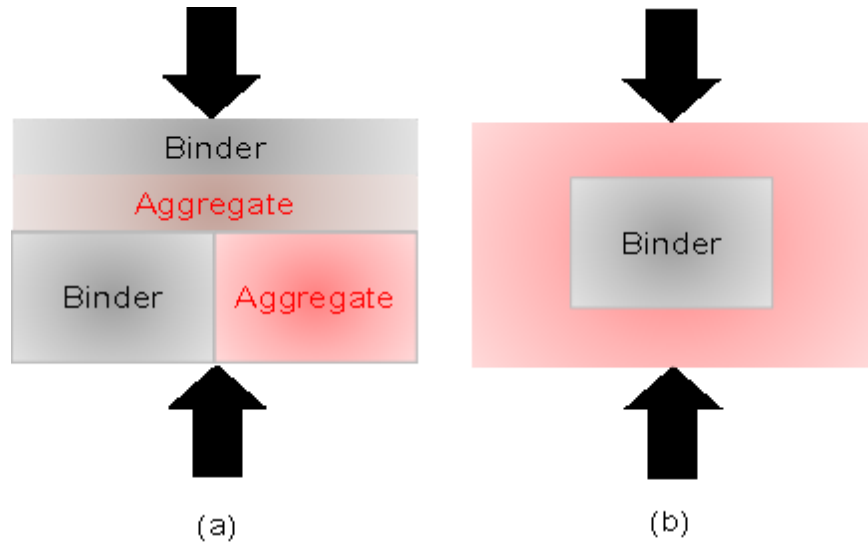


Figure 4-9. Schematic view of (a) Hirsch model (Christenson et al. 2003) and (b) Counto model (Young et al. 1981).

Once the binder and aggregate are positioned in a series with respect to each other, their deformation under external temperature variations can be considered independently. The total deformation can be calculated as Equation (4.8):

$$l_{mixture} CTC_{mixture} \Delta T = l_{binder} CTC_{binder} \Delta T + l_{aggregate} CTC_{aggregate} \Delta T \rightarrow$$

$$CTC_{mixture} = \frac{l_{binder}}{l_{mixture}} \times CTC_{binder} + \frac{l_{aggregate}}{l_{mixture}} \times CTC_{aggregate} \quad (4.8)$$

Where $L_{mixture}$ is the representative length of the mixture, $CTC_{mixture}$ is the coefficient of thermal contraction of the mixture, ΔT is the temperature drop, L_{binder} is the representative length of the binder, CTC_{binder} is the coefficient of thermal contraction of the binder, $L_{aggregate}$ is the representative length of the aggregate, and $CTC_{aggregate}$ is the coefficient of thermal contraction for the aggregate.

It can be assumed that the volume fraction of the aggregate in an asphalt mixture can be expressed as Equation (4.9).

$$\text{Aggregate volume fraction} = 1 - \frac{VMA}{100} \quad (4.9)$$

In this way the relative length of the aggregate and binder in an asphalt mixture can be expressed as $\sqrt[3]{1 - \frac{VMA}{100}}$ and $\sqrt[3]{\frac{VMA}{100}}$, respectively. Substituting these assumptions into Equation (4.8) gives Equation (4.10):

$$CTC_{mixture} = \sqrt[3]{\frac{VMA}{100}} \times CTC_{binder} + \sqrt[3]{1 - \frac{VMA}{100}} \times CTC_{aggregate} \quad (4.10)$$

In the parallel model, due to the relative difference in thermal deformation between the aggregate and binder, an internal force occurs at the interface. Figure 4-10 shows the internal friction that occurs at the interface of the aggregate and binder.

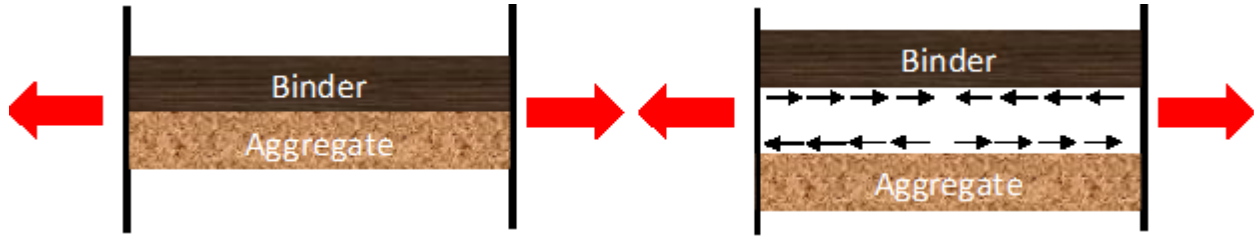


Figure 4-10. Schematic view of building block of parallel model and internal force that occurs at the interface.

Equation (4.11) express the displacement continuity between those two phases.

$$\overbrace{l_{mixture} \times CTC_{mixture} \times \Delta T} = \overbrace{l_{mixture} \times CTC_{aggregate} \times \Delta T + \frac{F \times l_{mixture}}{A_{aggregate} \times E_{aggregate}}} = \overbrace{l_{binder} \times CTC_{binder} \times \Delta T - \frac{F \times l_{mixture}}{A_{binder} \times E_{binder}}} \quad (4.11)$$

Equation (4.11) can be simplified by removing the internal force between the two phases.

Equation (4.12) expresses the final form for those two phases.

$$CTC_{mixture} = \frac{CTC_{aggregate} \times A_{agg} \times E_{agg} + CTC_{binder} \times A_{binder} \times E_{binder}(t)}{A_{agg} \times E_{agg} + A_{binder} \times E_{binder}(t)} \quad (4.12)$$

As can be understood from Equation (4.12), the parallel model does need the binder relaxation modulus, $E(t)$, to be given a priori. The binder relaxation modulus can be calculated from the binder shear modulus by converting the data obtained in the frequency domain to the time domain. Because the binder frequency sweep test is not commonly used in the asphalt characterization procedure, this research investigates different methods for backcalculating binder shear modulus data from given mixture dynamic modulus data.

Equation (4.12) also indicates that the parallel model requires the elastic modulus and CTC of the aggregate. Christensen and Bonaquist (2015) developed Equation (4.13) to calculate the aggregate elastic modulus from the aggregate bulk specific gravity (G_{sb}).

$$E_{aggregate} = 5073 \times G_{sb}^{2.02} \quad (4.13)$$

The mixtures that are used in this research contain granite aggregate; the CTC of such aggregate is assumed to be $9e^{-6}$ ($1/^\circ\text{C}$).

The following models are considered for backcalculating the shear modulus of binder from the given dynamic modulus data: (1) Hirsch model, (2) modified Hirsch model, and (3) 2S2P1D model. Equation (4.14) shows the Hirsch model that requires the VMA, voids filled with asphalt (VFA), and the binder shear modulus, $|G^*|$, to predict the mixture dynamic modulus.

$$\begin{aligned}
|E^*| &= P_c \times \left(29400 \times \left(1 - \frac{VMA}{100} \right) + 3 \times |G^*| \times \frac{VMA \times VFA}{10000} \right) + \\
&(1 - P_c) \times \left(\frac{1 - \frac{VMA}{100}}{29400} + \frac{VMA}{3 \times VFA \times |G^*|_{binder}} \right) \\
P_c &= \frac{\left(0.138 + \frac{VFA \times 3 \times |G^*|_{binder}}{VMA} \right)^{0.58}}{36.2 + \left(\frac{VFA \times 3 \times |G^*|_{binder}}{VMA} \right)^{0.58}}
\end{aligned} \tag{4.14}$$

The modified Hirsch model is shown as Equation (4.15).

$$\begin{aligned}
|E^*|_{mixture} &= P_c \times \left(E_{agg} \times \left(1 - \frac{VMA}{100} \right) + 3 \times |G^*|_{binder} \times \frac{VMA \times VFA}{10000} \right) \\
P_c &= H_1 + (1 - H_1) \frac{\exp \left(H_2 + H_3 \times \ln \left(\frac{VFA}{100} \times |G^*|_{binder} \right) + H_4 \times VMA + H_5 \times \ln(\varepsilon) \right)}{1 + \exp \left(H_2 + H_3 \times \ln \left(\frac{VFA}{100} \times |G^*|_{binder} \right) + H_4 \times VMA + H_5 \times \ln(\varepsilon) \right)}
\end{aligned} \tag{4.15}$$

Eight different mixtures that were studied as part of the New England High Reclaimed Asphalt Pavement Pooled Fund project (Daniel et al. 2014) were used in this study to examine the accuracy of the different methods for predicting binder shear modulus data. The volumetric properties of those mixtures are reported elsewhere (Sabouri et al. 2015). Dynamic modulus measurements were made on the mixtures at NCSU and shear modulus tests of extracted and recovered binders were conducted at the University of Rutgers (Daniel et al. 2014). Table 4.6 presents details about the Vermont mixtures used in this study.

Table 4.6. Summary of mixtures used to backcalculate binder shear modulus from mixtures dynamic modulus

Mix	Virgin PG	NMAS (mm)	RAP Content (%)	VMA	VFA	G _{sb}
VTa00	52-34	9.5	0	20.2	76.3	2.744
VTa20	52-34	9.5	20	18.8	81.9	2.723
VTa30	52-34	9.5	30	17.7	82.9	2.713
VTa40	52-34	9.5	40	18	77.8	2.703
VTe00	64-28	9.5	0	20.3	71.5	2.744
VTe20	64-28	9.5	20	18.7	79.7	2.723
VTe30	64-28	9.5	30	19.1	75.9	2.713
VTe40	64-28	9.5	40	18.2	76.4	2.703

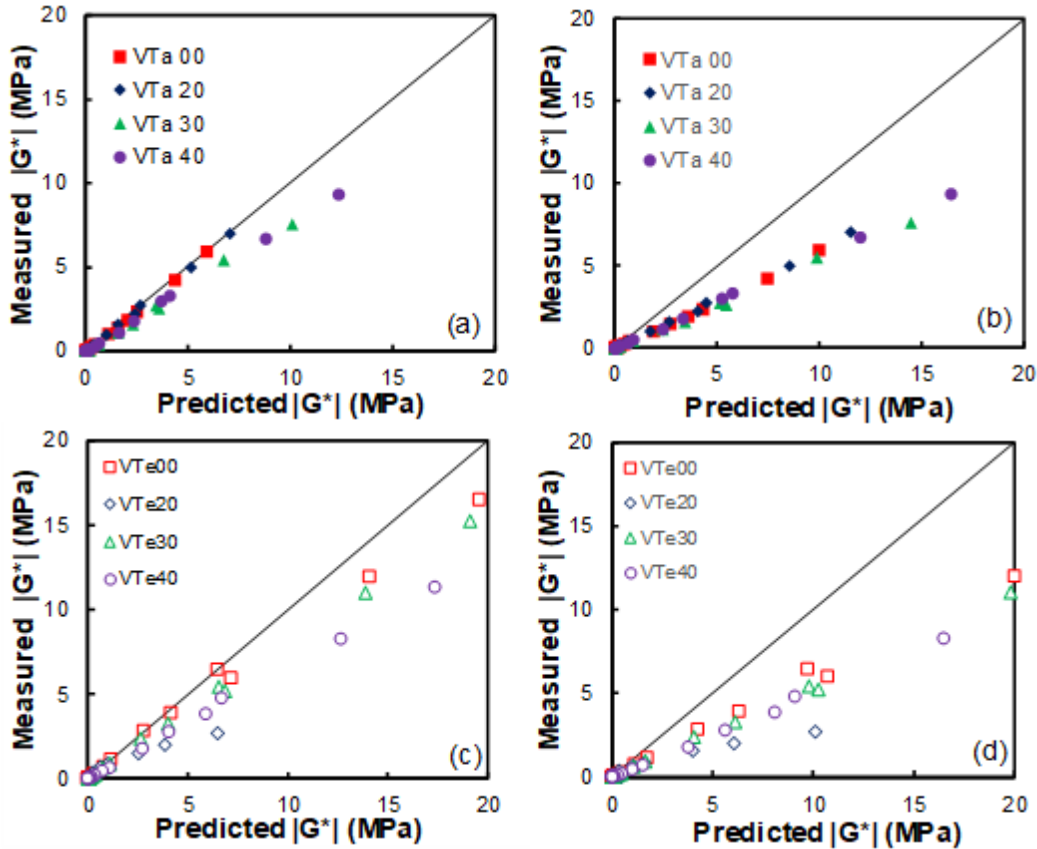


Figure 4-11. Comparison between backcalculated and measured binder shear modulus ($|G^*|$) data for eight mixtures obtained from the Hirsch and modified Hirsch models: (a) shear modulus values of the binder in the VTa mixtures backcalculated from Hirsch model, (b) shear modulus values of the binder in the VTa mixtures backcalculated from modified Hirsch model, (c) shear modulus values of the binder in the VTe mixtures backcalculated from Hirsch model, and (d) shear modulus values of the binder in the VTe mixtures backcalculated from modified Hirsch model.

Figure 4-11 shows that the Hirsch and modified Hirsch methods overpredict the actual measured binder modulus values. This observation agrees with the data reported in SakhaieFar et al. (2009) in which the dynamic modulus values predicted from the aforementioned methods underpredict the corresponding measured values.

Olard and Di Benedetto (2003) proved that there are correlations between the parameters obtained from fitting mixture dynamic modulus data and binder to the 2S2P1D formula.

Equation (4.16) expresses the 2S2P1D formula for mixtures.

$$E^*(\omega) = E_0 + \frac{E_\infty - E_0}{1 + \delta(i\omega\tau)^{-k} + (i\omega\tau)^{-h} + (i\omega\tau)^{-1}} \quad (4.16)$$

$$\tau = \tau_0 a_T$$

where i is the square root of -1, a_T is the time-temperature shift factor for mixtures, E_0 is the lower asymptote of the mixture modulus, E_∞ is the glassy modulus of the mixture, and δ , τ_0 , k , and h are the fitting parameters. Details regarding the physical meaning of the 2S2P1D fitting parameters can be found elsewhere (Marasteanu et al. 2012). Equation (4.17) shows the 2S2P1D formula for binders.

$$E_{binder}^*(\omega) = E_{0_binder} + \frac{E_{\infty_binder} - E_{0_binder}}{1 + \delta(i\omega\tau_{binder})^{-k} + (i\omega\tau_{binder})^{-h} + (i\omega\beta\tau_{binder})^{-1}} \quad (4.17)$$

$$\tau_{binder} = \tau_{0_binder} \times a_T$$

where E_{0_binder} is the lower asymptote value of the binder elastic modulus and E_{∞_binder} is the binder glassy modulus. The measured data show that the E_{0_binder} value is very low and can be ignored in comparison with all the other parameters (Olard and Di Benedetto 2003).

The 2S2P1D formula does not impose any symmetric behavior on the mixture mastercurve and can accurately predict the mixture modulus at temperatures below 4°C by using the data obtained from the AASHTO T 378 testing procedure (Keshavarzi et al. 2019d).

Keshavarzi et al. (2019d) proved that the correct form of the time-temperature shift factor for constructing the mixture mastercurve is the second-order polynomial function that was proposed by Witczak and Fonseca (1996).

Olard and Di Benedetto (2013) and Marasteanu et al. (2012) proved that the δ , k , and h parameters are equal for any mixture and its binder (Equation (4.18)).

$$E_{binder}^*(\omega) = E_{0_binder} + \frac{E_{\infty_binder} - E_{0_binder}}{1 + \delta(i\omega\tau_{binder})^{-k} + (i\omega\tau_{binder})^{-h} + (i\omega\beta\tau_{binder})^{-1}} \quad (4.18)$$

$$\tau_{binder} = \tau_{0_binder} \times a_T$$

Researchers have shown that δ , k , h , and β are equal between any mixture and binder (Olard and Di Benedetto 2003, Marasteanu et al. 2012). Also, Underwood and Kim (2011) has proved that the time-temperature shift factor is the same for mixtures and binders (Underwood and Kim 2011). The only remaining parameter is the τ_0 parameter, characteristic time of a material, that has been shown to differ between mixtures and binders. Olard and Di-Benedetto (2003) tried to find a relationship between the τ_0 of binders and mixtures, as expressed in Equation (4.19).

$$\tau_{0_mixture} = 10^{2.66} \tau_{0_binder} \quad (4.19)$$

Olard and Di Benedetto (2003) Stated that this relationship is empirical and depends on the mix design and aging during mixing. Later, Marasteanu et al. (2012) studied more mixtures and introduced Equation (4.20) for relating τ_0 of binders and mixtures.

$$\tau_{0_mixture} = 10^{3.17} \tau_{0_binder} \quad (4.20)$$

Marasteanu et al. (2012) tested different binder grades and mixtures with different aggregate types that contained those binders. They concluded that the characteristic time of a binder and mixture depends on the mixture design. We investigated the relationship between the characteristic time of binders and mixtures and found the same values as were found by Marasteanu et al. (2012).

Substituting all the fitted parameters from the mixture dynamic modulus fitting in the 2S2P1D formula gives Equation (4.21), which expresses the relationship between the binder

properties that can be obtained from fitting the 2S2P1D relationship to the mixture dynamic modulus data. It should be noted that the binder shear glassy modulus is assumed to have a global value of 2 GPa in this research. This value is similar to the measured data from the Olard and Di Benedetto (2003) study. The Poisson's ratio of the binder is assumed to be 0.5.

$$\frac{E_{binder}^*}{E_{G_binder}} = \frac{1}{1 + \delta_{mixture} \times \left(i\omega\tau_{0,binder}a_T \right)^{-h_{mixture}} + \left(i\omega\tau_{0,binder}a_T \right)^{-k_{mixture}} + \left(i\omega\beta\tau_{0,binder}a_T \right)^{-1}} \quad (4.21)$$

$$E_{G_binder} = 2000 \times 2 \times (1 + 0.5) = 6000 MPa$$

Equation (4.21) was used to backcalculate the elastic modulus, shear modulus, and phase angle of the binder for the Vermont mixtures. Figure 4-12 presents comparisons of the predicted values and measured values.

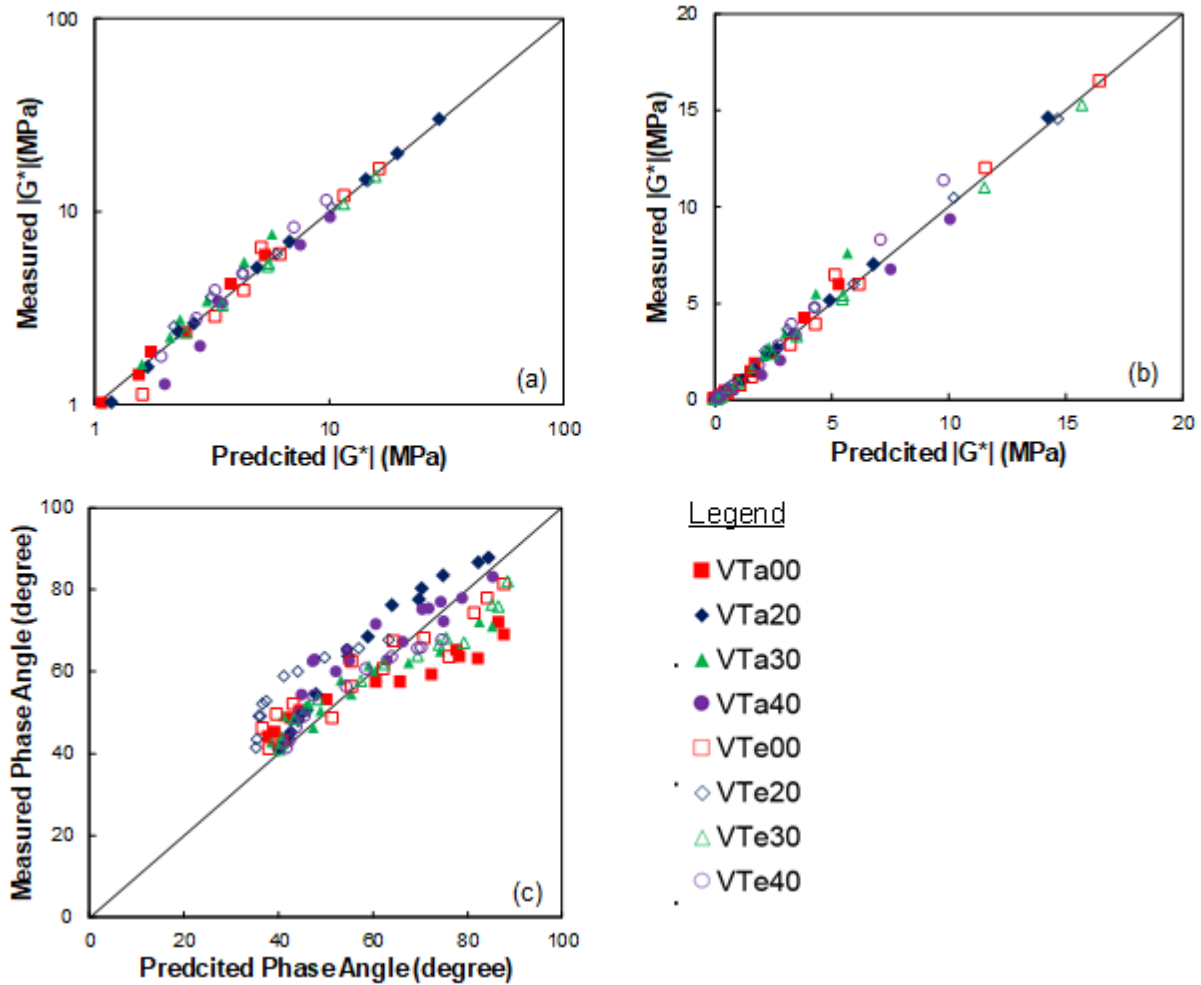


Figure 4-12. Comparisons of predicted shear modulus, $|G^*|$, and phase angle data for Vermont mixtures with measured data: (a) $|G^*|$ comparison in log-log scale, (b) $|G^*|$ comparison in arithmetic scale, and (c) phase angle comparison.

Figure 4-12 proves that the 2S2P1D formula can predict the shear modulus and phase angle of binders. This formula is used to backcalculate the binder shear modulus and phase angle from the given measured dynamic modulus data of a mixture.

As can be observed from Equation (4.12), the relaxation modulus or $E(t)$ of the binder is a required parameter for predicting the CTC of a mixture. The collocation method was used to convert the elastic modulus of binder in the frequency domain to the relaxation modulus of binder in the time domain. Equation (4.22) expresses the Prony series form of the shear modulus in the time domain and the storage modulus in the frequency domain.

$$E(t) = E_{\infty} + \sum_{j=1}^m E_j \exp\left(-\frac{t}{\rho_j}\right)$$

$$E'(\omega) = E_{\infty} + \sum_{j=1}^m \frac{\omega^2 \rho_j^2 E_j}{\omega^2 \rho_j^2 + 1}$$
(4.22)

Finding the binder $E(t)$ from the given dynamic modulus of the mixture allows comparisons of the predicted CTC values from the parallel and series models with the actual measured values. Figure 4-13 presents these comparisons.

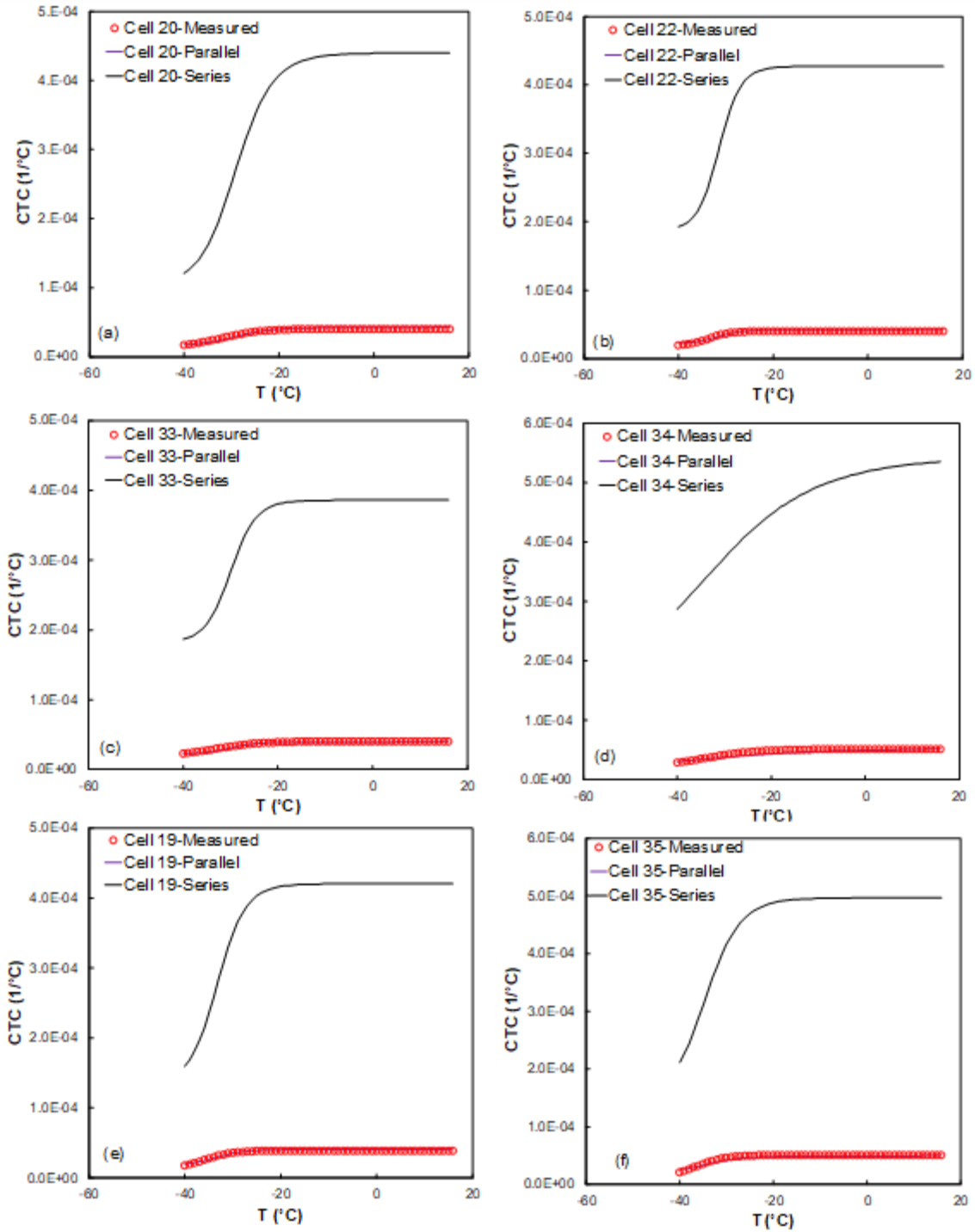


Figure 4-13. Comparisons between predicted CTCs from parallel and series models with the actual measured values: (a) Cell 20, (b) Cell 22, (c) Cell 33, (d) Cell 34, (e) Cell 19, and (f) Cell 35.

4.5. Discussion of Results

Figure 4-14 presents a comparison between the measurements and predictions for Level II analysis. Figure 4-14 compares the predicted and measured values for the CTC parameter for the temperature range of 20°C to -40°C. As shown, the proposed methodology is able to capture the CTC variation with good accuracy. Although Level II analysis requires the measured CTC of the binder a priori, Level III uses the clustering method to obtain the thermo-volumetric properties of the binder. Figure 4-15 presents comparisons between the predictions obtained from Level III analysis and measurements from the two datasets of the mixtures. More scatter can be observed in Figure 4-15 than in Figure 4-14.

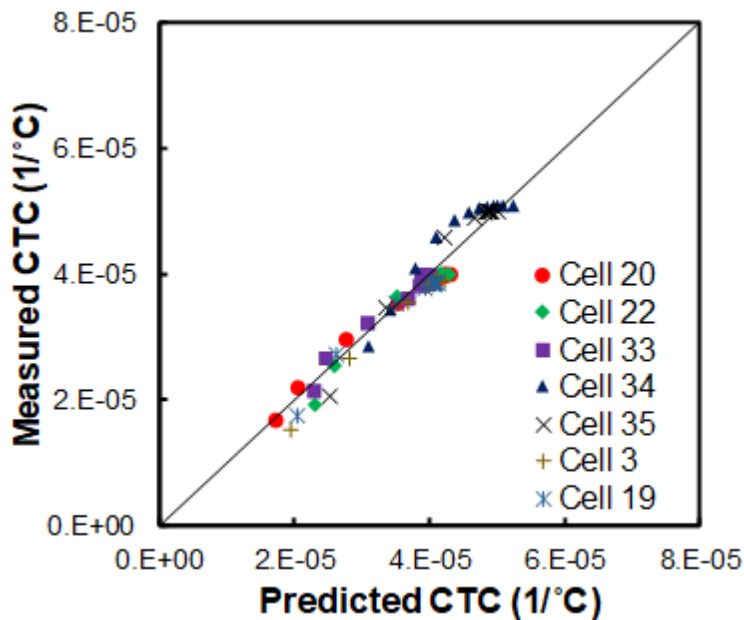


Figure 4-14. Comparison between predicted CTCs obtained from Equation (4.12) and measured data obtained from Marasteanu et al. (2007).

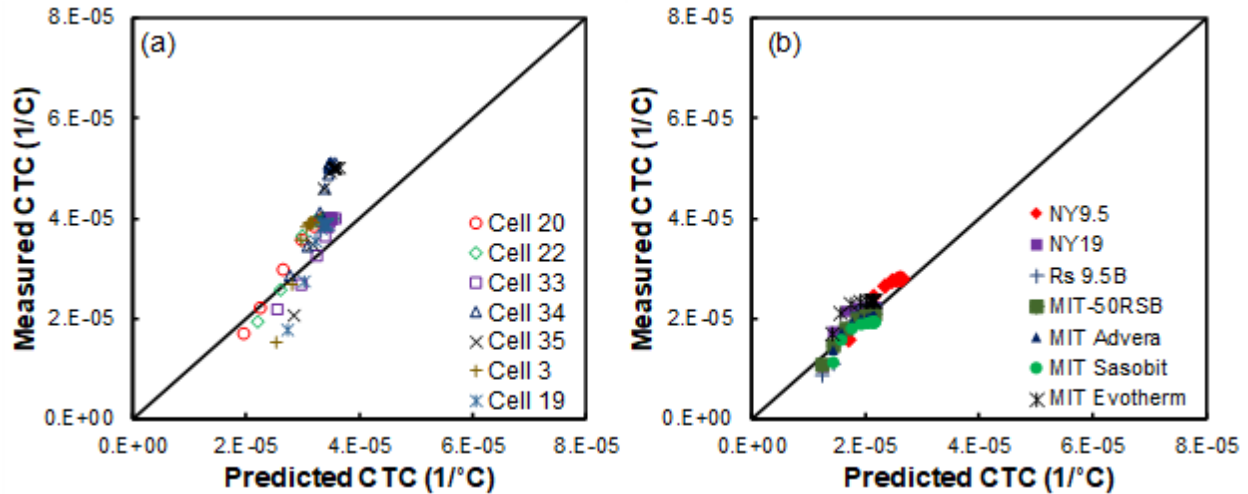


Figure 4-15. Comparison between predicted CTCs of mixtures obtained from Level III analysis and measured data obtained from: (a) Marasteanu et al. (2007) and (b) NCSU.

Figure 4-15 shows some scatter in the high CTC value ranges, which requires further analysis to determine the effect of this error on the accuracy of the induced stress predictions in asphalt pavements. Chapter 6 discusses the details of thermal stress analysis. A typical structure is considered for predicting the thermal distribution. The Enhanced Integrated Climatic Model (EICM) software was used to calculate the temperature distribution in the pavement sections (Barker et al. 2008). Figure 4-16 presents the air temperature distribution for the four geographical regions from which the mixtures were sourced. All of the temperatures were recorded in 2008. The starting date for the temperature analysis of each section coincides with the construction date of that section.

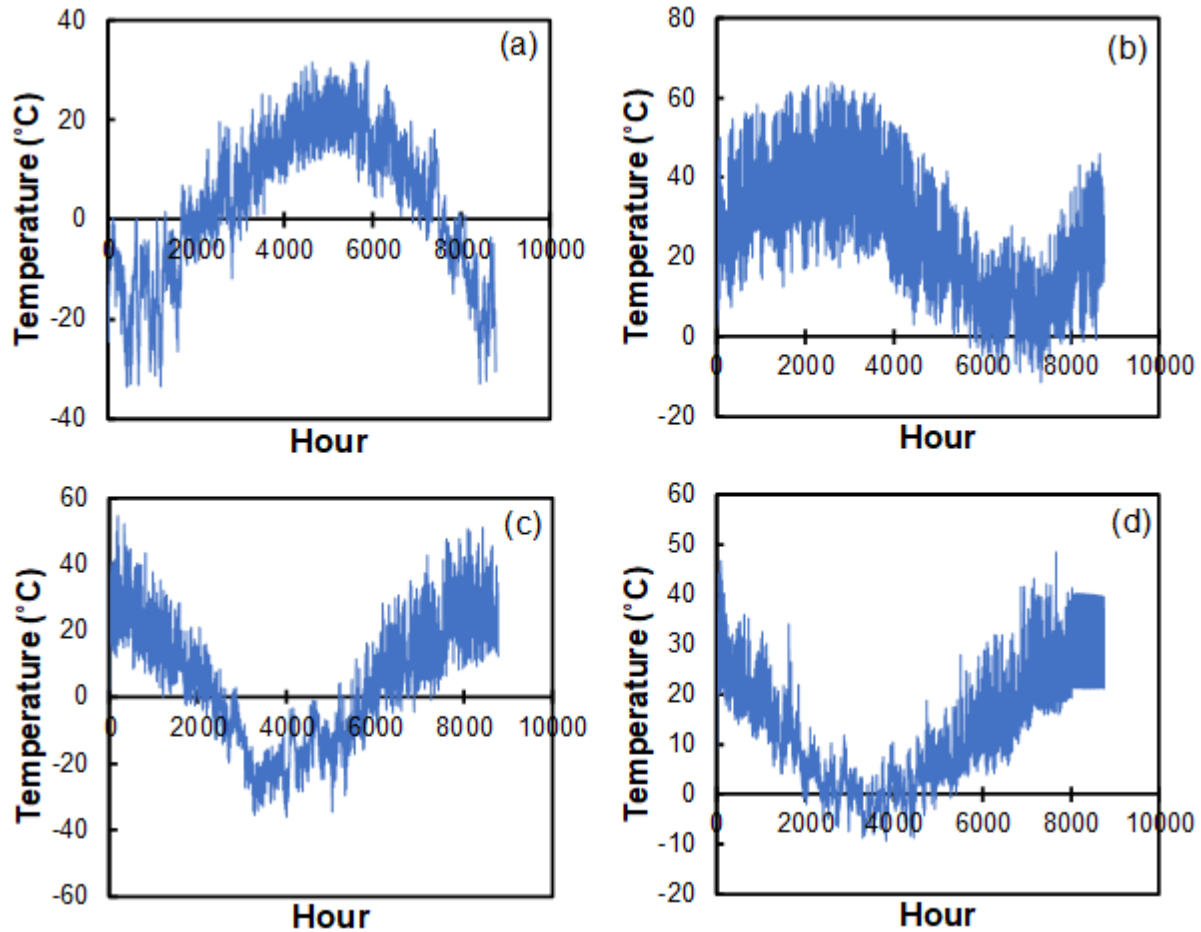


Figure 4-16. Air temperatures for the surface of pavement sections located in different geographical locations: (a) North Carolina, (b) North Carolina, (c) New York, and (d) New York.

Based on the given air temperature data, EICM software was used to calculate the pavement temperatures. The pavement structure that was used in the EICM has 4 inches thick asphalt layer on top of 12 inches thick aggregate base layer.

Figure 4-12 presents a comparison between the stress predicted from the measured CTCs (Level I) and the predicted CTCs obtained from Level II and Level III analyses for the first and second datasets. Figure 4-17 presents a comparison between the stress values obtained based on Level II analysis and the corresponding stress values calculated from Level I analysis. This figure proves the ability of the Level II analysis. Figure 4-18 and Figure 4-19 present comparisons between the stress values obtained based on Level III analysis and the

corresponding stress values calculated from Level I analysis. The comparison proves that Level III analysis is able to match the results of Level I analysis.

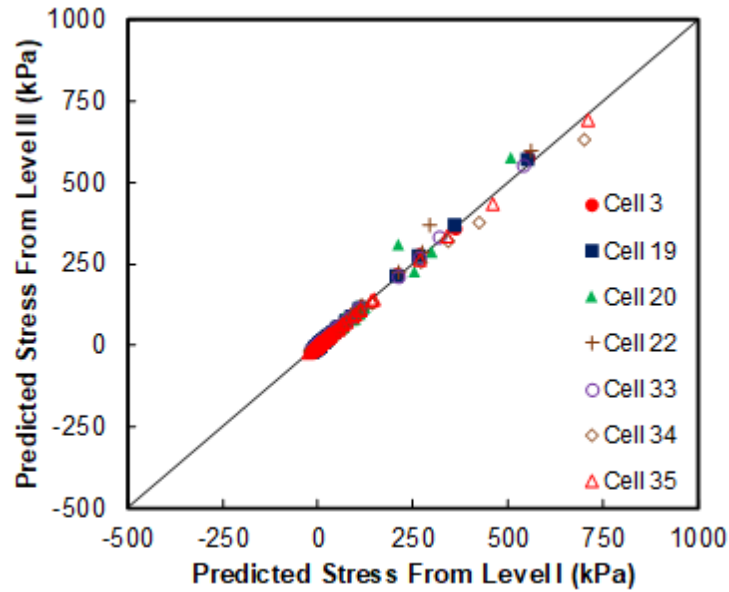


Figure 4-17. Comparison between stress predicted from Level I analysis and the corresponding values obtained from Level II analysis for the first dataset.

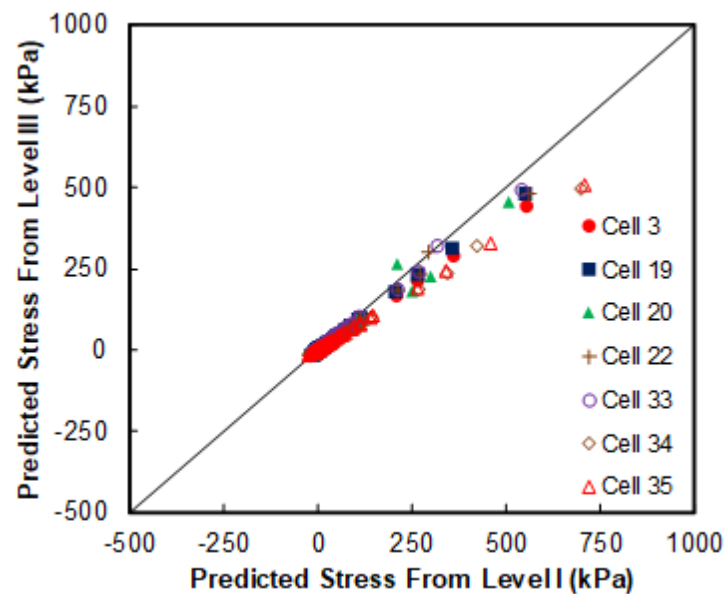


Figure 4-18. Comparison between stress predicted from Level I analysis and the corresponding values obtained from Level III analysis for the first dataset.

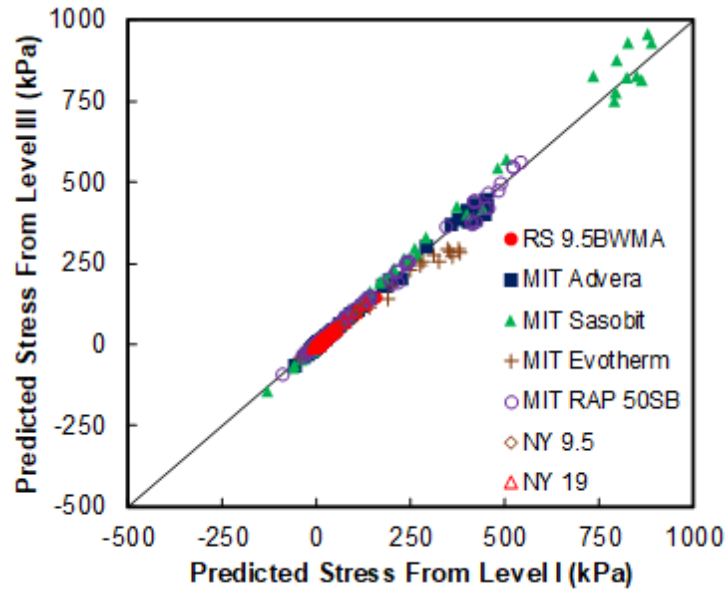


Figure 4-19. Comparison between stress predicted from Level I analysis and the corresponding values obtained from Level III analysis for the second dataset.

4.6. Conclusions

This paper presents the results of an experimental study to measure the CTC of asphalt mixtures as well as analytical study to predict the mixture CTC from given volumetric and mechanical properties. We defined three levels of analysis in this paper. Level I requires to measure the CTC of mixtures. That measurement needs to have a machine that is able to control the temperature at a given rate. In addition, in order to eliminate the LVDT contraction during the test, Level I requires LVDT to be calibrated against thermal deformation before running the mixture testing. We used Zerodur® sample for this task.

Level II suggests a simple yet efficient method (composite model) that is able to predict the mixture CTC for a broad range of temperature. The model requires to have an aggregate modulus of elasticity, aggregate CTC, mixture volumetric properties, and binder relaxation modulus and thermo-volumetric properties. Different methods were investigated for backcalculating binder modulus from the given mixture modulus. It was found that the 2S2P1D

formula is able to give a good estimation of binder modulus and phase angle. We found out that the binder thermo-volumetric properties measured and reported in literature can be grouped based on their low PG grade. This approach makes the Level III analysis.

The experimental plan was used to measure the mixture CTC. The mixtures included in the experimental plan cover a broad range of binder PG grade, additives, and RAP content. The CTC of those mixtures were predicted by using the composite model and classification made for Level III. We found that the Level III can give a reasonable prediction over mixture CTC for a wide range of temperature. Level II was also verified through predicting the data reported in literature.

The data includes both mixture and binder measurements. It was shown that Level II is able to give a good approximation of measurements performed in Level I.

CHAPTER 5. A DISSIPATED PSEUDO STRAIN ENERGY-BASED FAILURE CRITERION FOR THERMAL CRACKING AND ITS VERIFICATION USING THERMAL STRESS RESTRAINED SPECIMEN TESTS

5.1. Abstract:

This paper proposes a failure criterion that correlates the dissipated pseudo strain energy (DPSE) at the time of failure with the reduced strain rate. Uniaxial direct tension monotonic tests, axial compression dynamic modulus tests, and direct tension cyclic fatigue tests were performed using the Asphalt Mixture Performance Tester (AMPT) for a wide range of asphalt mixtures with different reclaimed asphalt pavement (RAP) contents, binder contents, virgin binder performance grades, and aging levels. The results show that the simplified viscoelastic continuum damage (S-VECD) model, which is characterized by the dynamic modulus and cyclic fatigue test results, can predict the stress-strain behavior of a given mixture subjected to monotonic tests at different temperatures and loading rates. This finding allows the prediction of DPSE in monotonic tension tests using the S-VECD model. The thermal stress restrained specimen test (TSRST) was then used to verify the DPSE-based failure criterion and the ability of the S-VECD model to predict thermal fracture behavior. The study results show that the predicted fracture temperatures match the measured ones for the study mixtures with reasonable accuracy. The study also used data from mixtures whose RAP contents, binder contents, virgin binder grades, and aging levels were systematically altered to verify the reasonableness of the proposed procedure to evaluate the differences in thermal fracture performance that are due to changes in these factors. The ability to predict the fracture stress and fracture temperature measured via the TSRST using the S-VECD model and the suggested DPSE failure criterion is of substantial practical and technical importance because it allows the prediction of both fatigue

cracking and thermal cracking using a single set of tests, i.e., AMPT dynamic modulus and cyclic fatigue tests.

5.2. Introduction:

Low-temperature cracking is the predominant failure mode for pavement sections constructed in cold regions where significant air temperature drops induce stress in the pavement layers (Marasteanu et al. 2007). This stress, hereafter referred to as thermal stress, causes damage, referred to as thermal damage. Once the damage passes the mixture's tolerance threshold, macrocracks begin to form in asphalt concrete pavement sections. In addition, significant fluctuations in the daily air temperature also lead to the accumulation of damage within pavement section sublayers and lower the pavement's capacity for resistance to cracking as the pavement ages. This phenomenon usually occurs in warmer regions where stiffer binder is used to resist permanent deformation (Alavi 2014). Both severe thermal shots and daily thermal fluctuation work together to create transverse cracks; when combined, these two mechanisms can be referred to as thermal cracking. Such thermal cracking has been linked traditionally to binder properties at low temperatures. Thus, asphalt binder tests and specifications have been employed to try to make asphalt sections less prone to thermal cracking (Rahbar-Rastegar et al. 2018). However, binder properties alone cannot fully capture the mechanical and thermal properties of asphalt mixtures and the configuration of components in asphalt mixtures, which necessitates mixture characterization for low-temperature regions to help prevent thermal cracking (Kim 2008, Majidifard et al. 2019).

Thermal cracking is considered to be top-down cracking in which the induced thermal contraction has a gradient throughout the depth of the pavement and each sublayer is restrained against movement in the longitudinal direction (Hass et al. 1987, Roque et al. 1993). This

loading condition can be simulated in the laboratory using the thermal stress restrained specimen test (TSRST). The TSRST is one of the few types of tests that can simulate actual thermal loading in the field because it applies loading directly on the specimen. In TSRSTs, the asphalt concrete specimen is subjected to cooling while its ends are restrained from any movement. Due to the imposed restriction, thermal stress occurs in the pavement sublayers. That is, as the temperature decreases in the test chamber, thermal stress builds up and damage occurs at both ends of the fixed asphalt concrete mixture specimen. At a certain temperature, the sample is unable to carry any more loading and fails. The temperature and stress associated with this failure are referred to as the fracture temperature and fracture stress, respectively.

This paper presents a new failure criterion that is based on dissipated pseudo strain energy (DPSE) and can be applied to determine when fracture occurs during TSRSTs. Sabouri and Kim (2014) developed an earlier DPSE-based failure criterion, referred to as GR, for the prediction of the fatigue failure of mixtures when the mixtures are subjected to long cycles of loading. Although this type of failure, considered long cycle failure, can be predicted using the GR criterion, the fracture of asphalt mixtures in TSRSTs is of a different nature and is considered to be monotonic failure. The new failure criterion proposed in this paper is based on the same DPSE concept that underlies the GR failure criterion, but is applicable to the prediction of fracture in the TSRST as well as under more realistic thermal conditions in the field.

The new proposed failure criterion was verified through the experimental evaluation of mixtures that cover a range of reclaimed asphalt pavement (RAP) contents, binder contents, virgin binder performance grades, and aging levels in this study. The fracture stress and fracture temperature measured in TSRSTs are used to verify the applicability of the suggested failure

criterion to realistic field conditions. Before the details of the study are presented, the current literature on the TSRST is summarized in the following section.

5.2.1. Review of Literatures on the TSRST

The TSRST was developed as part of the Strategic Highway Research Program (Jung and Vinson 1994). Jung and Vinson (1994) studied the effects of binder type, aging level, and cooling rate on TSRST results (i.e., the fracture stress and fracture temperature) and found that an increase in the cooling rate leads to an increase in fracture stress. The increment is more substantial for softer binder. They found a similar trend for fracture temperature. These researchers also found that aging increases the fracture temperature while decreasing the fracture stress and that fracture temperature shows less variability than fracture stress. Therefore, fracture temperature is used as the index criterion for low-temperature mixture evaluations.

The uniaxial thermal stress and strain test, developed by Morian (2014), is a modification of the TSRST whereby the loading platen and gluing technique are altered and an additional unrestrained sample is used to determine the thermal strain of the mixture sample. The restrained and unrestrained samples are subjected concurrently to temperature variations (Morian 2014).

Alavi (2014) studied the fracture properties of different mixtures as a function of aging and expressed aging as the level of carbonyl content in the mixture. Alavi (2014) found that aging can significantly increase the fracture temperature and decrease the fracture stress. Alavi (2014) defined ‘crack initiation stress’ as the point at which the material shows the highest modulus value. Crack initiation is believed to indicate the time at which microdamage accumulates in the material. Alavi (2014) developed a relationship to correlate the crack initiation in the material with the carbonyl level.

Jung and Vinson (1994) applied the cooling rate of -10°C/hr , which various researchers have since adopted because it decreases the testing time. The maximum daily cooling rate was found to range from -1.4°C/hr to -2.7°C/hr based on analysis of measured pavement temperature data at several Long-Term Pavement Performance (LTPP) program road sections located in the intermountain regions (i.e., Nevada, Utah, Idaho, Arizona, Colorado, and New Mexico) (Cortez et al. 2011). As a result of this overestimation in selecting the cooling rate, the measured fracture results from TSRSTs cannot be incorporated directly in this study's analysis framework.

Several parameters affect the induced thermal damage and associated thermal cracking in TSRSTs. For example, the stiffness of the material determines the amount of thermal stress in an asphalt sample subjected to cooling. Keshavarzi et al. (2019c) conducted a comprehensive study of different suggested dynamic modulus mastercurves and time-temperature shift factor functions. They found that the so-called 2S2P1D formula for dynamic modulus mastercurves (Olard and Di Benedetto 2003) combined with a second-order formula (Witczak and Fonesca 1996) is able to predict the dynamic modulus and phase angle of asphalt mixtures at temperatures lower than 4°C using data obtained from dynamic modulus tests conducted at 4°C , 20°C , and 40°C in accordance with AASHTO T 378/R 84 specifications. The current study used the findings from Keshavarzi et al. (2019c) to predict the thermal stress developed in TSRSTs.

Thermal loading is similar to that used in displacement-controlled testing where the induced thermal stress depends primarily on the imposed temperature drop. The coefficient of thermal contraction (CTC) is used to determine how much deformation occurs for any given temperature drop. In this way, the CTC of mixtures has a direct effect on the induced thermal stress and predicted pavement performance. Keshavarzi et al. (2019) proposed a composite model to predict the mixture CTC as a function of volumetric properties and measured dynamic

modulus values. The findings from Keshavarzi et al. (2019b) were used in this study to calculate the CTCs of different mixtures.

Modeling the performance of asphalt concrete using continuum damage theory is an approach that has gained international attention in recent years. Continuum damage theory assumes that the viscoelastic and viscoplastic responses of the material depend on the internal State variable of the material. The benefit of these types of methods is that they ignore complicated physical interactions at the microscale level and model behavior based on parameters that can be obtained at the macroscale level (Keshavarzi and Kim 2016). Schapery's work potential theory (Schapery 1987), which was built upon thermodynamic principles, is one such continuum damage theory whereby damage is quantified as an internal State variable (S). Other researchers have proposed nonlocal elastic-based continuum damage to quantify damage (Bazant and Pijaudier 1989, Bodin et al. 2004).

Kim and Little (1990) were the first researchers to apply Schapery's nonlinear viscoelastic theory to materials with distributed damage in order to describe the behavior of sand asphalt under controlled strain cyclic loading. They later applied their viscoelastic continuum damage (VECD) theory to describe asphalt concrete behavior under both controlled stress and controlled strain loading (Lee and Kim 1998). Also, research conducted by Daniel and Kim as part of a WesTrack project showed that the damage characteristics of asphalt concrete are independent of the mode of loading and can be determined using a simple test, i.e., the constant crosshead rate monotonic test (Daniel and Kim 2002). Findings from Lee and Kim (1998) and Daniel and Kim (2002) have extended the range of VECD theory's applications. For example, Chehab extended VECD theory further by proving that time-temperature superposition in the linear State is valid for a highly damaged State of asphalt concrete (Chehab 2002).

Chehab (2002) also used linear viscoelastic theory, VECD theory, and Viscoelastoplastic continuum damage (VEPCD) theory to predict the induced stress in TSRSTs as well as the fracture stress and fracture temperature. He measured the strength of asphalt concrete in uniaxial direct tension monotonic tests at a constant reduced strain rate to construct a strength mastercurve. Chehab (2002) also measured the averaged readings from linear variable differential transducers at the time of failure and plotted the results as a function of reduced strain rate to construct a failure strain mastercurve. Both the strength and the failure strain mastercurves can be expressed as a function of reduced strain rate and can cover a broad range of rates and temperatures. Chehab (2002) intersected the induced stress curve predicted for the TSRST with the measured strength mastercurve and expressed the intersection point as the predicted fracture temperature and fracture stress based on the strength criterion. He also intersected the predicted thermal strain curve obtained from the TSRST with the measured failure strain mastercurve to provide the fracture stress and fracture temperature using the failure strain criterion. Chehab (2002) then used three different cooling rates, -4°C/hr , -8.6°C/hr , and -17.7°C/hr , and found that increasing the cooling rate did not increase the fracture temperature significantly. Chehab (2002) showed that the fracture temperature can be predicted using averaged results obtained using the strength and strain criteria. The predicted responses obtained under the linear viscoelastic condition over predicted the measured stress during testing for all the considered rates. In contrast, the VECD and VEPCD models were able to match the measured and predicted stress values during the tests with accuracy.

5.3. Test Methods:

Results from four test methods were used in this study to develop and verify the proposed failure criterion for thermal cracking. Dynamic modulus and direct tension cyclic fatigue tests

were performed to characterize the S-VECD model and dissipated pseudo strain energy (DPSE) - based failure criterion. Direct tension monotonic tests and TSRSTs were used to verify the S-VECD model's ability to predict the failure of asphalt mixtures under monotonic loading and to verify the ability of the S-VECD model and DPSE-based failure criterion to predict thermal cracking, respectively. These test methods are described in the following sections.

5.3.1. Dynamic Modulus Testing

The dynamic modulus tests were performed using an Asphalt Mixture Performance Tester (AMPT) in load-controlled mode and under axial compression. Two sizes of cylindrical specimens were fabricated for the dynamic modulus tests: 100 mm in diameter and 150 mm in height for all the tests (except the aging study) and 38 mm in diameter and 110 mm in height for the aging study. The procedure in AASHTO PP 99 was followed to fabricate the 38-mm diameter specimens. All the test specimens were cored and cut from Superpave gyratory-compacted samples that were 150 mm in diameter and 180 mm in height. The 100-mm diameter specimens were tested following the protocol given in AASHTO T 378/R 84 whereas the 38-mm diameter specimens were tested according to the protocol found in AASHTO TP 132. Tests were conducted for all mixtures at 4°C, 20°C, and 40°C. The tests were conducted at 25, 10, 5, 1, 0.5, and 0.1 Hz as specified in T 378/R 84 and at 10, 1, and 0.1 Hz as specified in TP 132. The order of testing was from low to high temperatures and from high to low frequencies in order to minimize damage to the specimens. Load levels were determined by a trial and error process so that the resulting strain amplitudes were between 50 and 70 microstrain to prevent damage to the specimens.

5.3.2. Direct Tension Cyclic Fatigue Testing

The direct tension cyclic tests were performed in crosshead-controlled (CX) mode of loading following the protocols specified in AASHTO TP 107 for the 100-mm diameter specimens and in TP 133 for the 38-mm diameter specimens. The heights of the 100-mm diameter and 38-mm diameter specimens were 130 mm and 110 mm, respectively. All the cyclic tests were performed at three to four crosshead displacement amplitudes to cover a range of cycles to failure. The cyclic fatigue tests were conducted at the average temperature of the high and low performance grades determined from LTPPBind Online for the project of interest. The fatigue failure for each of the specimens in the CX cyclic tests was determined using Reese's approach (Reese 1997), which is based on the change in phase angle behavior. The phase angle increases until micro damage coalesces and forms a macro crack. At that point, the phase angle shows a sharp drop, which makes determining the number of cycles to failure accurate and consistent in laboratory tests.

5.3.3. Direct Tension Monotonic Testing

The CX monotonic tests were conducted using an MTS 810. These tests allowed for combinations of crosshead rates and temperatures in order to cover a wide range of reduced strain rates. The sample sizes used for these tests were the same as those used for the direct tension cyclic fatigue tests.

5.3.4. TSRST

The TSRST results used in this study were derived from the project, Evaluation of Plant-Produced RAP Mixtures in the Northeast, Phase I, that was undertaken by researchers at the University of Massachusetts Dartmouth (Daniel et al. 2014). In that project, TSRSTs were

performed in accordance with AASHTO TP 10-93. At least three replicate gyratory-compacted specimens, 185 mm in height by 150 mm in diameter, were fabricated for each mixture. The TSRST specimens were then cored and cut to a final height of 160 mm and 54 mm in diameter. During the TSRSTs, the asphalt specimens were cooled at a constant rate (-10°C/hr).

5.4. Materials

Table 5.1 shows that the materials used in this study can be divided into four groups, depending on the test methods used by various researchers and the purpose of the tests. The first eight mixtures in Material Group 1 are 9.5 mm Superpave mixes from Vermont that were part of the New England RAP project (Daniel et al. 2014). The Vermont mixes were produced in two different asphalt plants and are designated as VT eXX and VT aXX , with XX representing the percentage of RAP. The last mixture in the first group is RS9.5B, a Superpave surface 9.5 mm mix with RAP, that is commonly used in North Carolina. Table 5.2 presents a summary of the properties of these mixtures in terms of binder performance grade (PG), asphalt content (AC (%)), nominal maximum aggregate size (NMAS), RAP content, and air void content. More details regarding specimen fabrication, testing, dynamic modulus and S-VECD characteristics, and ranking of Group 1 mixtures can be found in Sabouri et al. (2015).

Table 5.1. Test Methods and Test Purposes for Four Material Groups

Material Group	Test Methods Used	Purpose	Researchers
1	<ul style="list-style-type: none"> • Dynamic modulus test • Direct tension cyclic fatigue test • Direct tension monotonic test • TSRST 	To develop the failure criterion as well as verify the developed methodology by predicting the measured TSRST fracture results	Daniel et al. (2014) Keshavarzi and Kim (2016)
2	<ul style="list-style-type: none"> • Dynamic modulus test • Direct tension cyclic fatigue test • TSRST 	To evaluate the accuracy of the proposed failure criterion further in predicting the TSRST fracture results	Sabouri (2014)
3	<ul style="list-style-type: none"> • Dynamic modulus test • Direct tension cyclic fatigue test 	To assess the reasonableness of the proposed failure criterion in predicting the effects of the virgin binder PG, RAP content, and asphalt binder content on the TSRST results	Sabouri et al. (2015)
4	<ul style="list-style-type: none"> • Dynamic modulus test • Direct tension cyclic fatigue test 	To assess the reasonableness of the proposed failure criterion in predicting different thermal cracking performance at different aging levels	Kim et al. (2018)

Table 5.2. Mixture Properties for Material Group 1: North Carolina Mixture and Vermont Mixtures

Mix Name	Binder Grade	AC (%)	NMAS (mm)	RAP (%)	Target Air Voids (%)
VTe00	PG 64-28	6.5	9.5	0	6.0
VTe20	PG 64-28	6.7	9.5	20	6.0
VTe30	PG 64-28	6.6	9.5	30	6.0
VTe40	PG 64-28	6.6	9.5	40	6.0
VTa00	PG 52-34	6.7	9.5	0	6.0
VTa20	PG 52-34	6.8	9.5	20	6.0
VTa30	PG 52-34	6.6	9.5	30	6.0
VTa40	PG 52-34	6.6	9.5	40	6.0
RS9.5B	PG 64-28	5.2	9.5	30	5.5

Figure 5-1 presents results of the direct tension monotonic tests of the RS9.5B North Carolina mixture. The ϵ'_r parameter denotes the reduced on-specimen rate that was applied to the specimens. Details regarding these experimental results can be found elsewhere (Keshavarzi and Kim 2016).

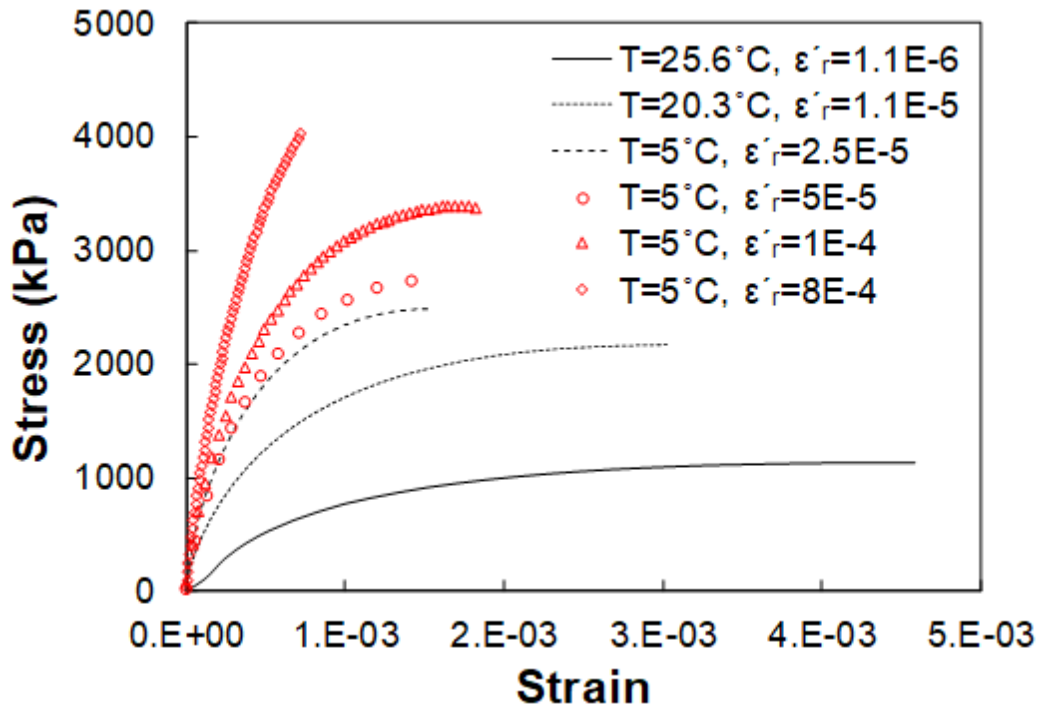


Figure 5-1. Stress vs. strain curves for RS9.5B mixture subjected to different temperatures and loading rates

Material Group 2 consists of four mixtures from New Hampshire and five mixtures from New York. The New Hampshire mixtures are designated as NHeXX and the New York mixtures are designated as NYbXX and NYdXX, where XX represents the RAP percentage of those mixtures. Table 5.3 presents a summary of these mixtures' properties. Details regarding specimen fabrication, testing, dynamic modulus and S-VECD characteristics, and ranking of Group 2 mixtures can be found in Sabouri et al. (2015). The TSRST results are presented later in the Discussion of Results section to verify the proposed fracture prediction methodology.

Table 5.3. Mixture Properties for Material Group 2: New Hampshire and New York Mixtures

Mix Name	Binder Grade	AC (%)	NMAS (mm)	RAP (%)	Target Air Voids (%)
NHe00	PG 64-28	5.9	12.5	0	6.0
NHe20	PG 64-28	5.7	12.5	20	6.0
NHe30	PG 64-28	5.3	12.5	30	6.0
NHe40	PG 64-28	5.4	12.5	40	6.0
NYb30	PG 58-28	5.2	12.5	30	6.0
NYb40	PG 58-28	5.2	12.5	40	6.0
NYd20	PG 64-22	5.2	12.5	20	6.0
NYd30	PG 64-22	5.2	12.5	30	6.0
NYd40	PG 64-22	5.2	12.5	40	6.0

Material Group 3 consists of nine Superpave 12.5 mm laboratory-produced New Hampshire mixtures. Table 5.4 presents the volumetric properties of those mixtures. The reason we used these mixtures in this study was to investigate the effects of the binder PG, RAP content, and asphalt binder content on the predicted fracture temperature in the TSRST. Details about the mixture fabrication and testing method can be found in Sabouri et al. (2015). The objective of the work by Sabouri et al. 2015 was to evaluate the effects of changes in binder contents, RAP contents, and virgin binder grade on the fatigue cracking performance of a typical New Hampshire mixture. The optimum binder content was determined using the Superpave volumetric mixture design and then was changed by ± 0.5 percent to produce the mixtures with different fatigue performance. Also, a softer binder, PG 58-28, was used as an alternative to the PG 64-28 binder to evaluate the effect of virgin binder grade on the fatigue performance. More details regarding dynamic modulus and S-VECD characteristics of Group 3 mixtures can be found in Sabouri et al. (2015).

Material Group 4 includes mixtures that were systematically aged as part of the NCHRP Project 09-54. These mixtures were taken from asphalt concrete pavement sections constructed in Texas, South Dakota, and Washington as part of the LTPP SPS-8 program. The other mixture is an atypical surface mixture used in North Carolina that was aged for an extended amount of time. Table 5.5 presents the mixture details for Material Group 4. Details regarding the aging conditions, sample fabrication, testing, and dynamic modulus and S-VECD properties can be found elsewhere (Kim et al. 2018).

Table 5.4. Mixture Properties for Material Group 3: New Hampshire Mixtures with Changing Mixture Designs

Mix Name	Binder Grade	AC (%)	RAP (%)	Target Air Voids (%)
NHe5820-opt	PG 58-28	Optimum-0.5	20	6
NHe5840-opt	PG 58-28	Optimum-0.5	40	6
NHe6400-opt	PG 64-28	Optimum-0.5	00	6
NHe6400 opt	PG 64-28	Optimum	00	6
NHe6420-opt	PG 64-28	Optimum-0.5	20	6
NHe6420opt	PG 64-28	Optimum	20	6
NHe6440-opt	PG 64-28	Optimum-0.5	40	6
NHe6440opt	PG 64-28	Optimum	40	6
NHe6440+opt	PG 64-28	Optimum+0.5	40	6

Table 5.5. Details for Material Group 4: Texas, Washington, South Dakota, and North Carolina Mixtures

Mixture Name	RAP Content (%)	Aging Duration at 95°C (number of days)
TX-STA	0	0
TX-4D	0	4
TX-16D	0	16
WA-STA	0	0
WA-4D	0	4
WA-8D	0	8
SD-STA	0	0
SD-4D	0	4
SD-8D	0	8
RS9.5B-STA	30	0
RS9.5B-4D	30	4
RS9.5B-7D	30	7
RS9.5B-17D	30	17

5.5. Development of Dissipated Pseudo Strain Energy Failure Criterion

VECD theory is based on three main factors: (1) the viscoelastic behavior of the material, which can be modeled by utilizing the elastic-viscoelastic correspondence principle that is based on pseudo strain, ϵ_R , (2) the work potential theory that models the evolution of microcracks using parameters that can be obtained at the macroscale level, and (3) the time-temperature superposition principle that is valid for different damaged levels of the material and helps to combine the effects of time and temperature into the reduced time parameter. The basic equations that are necessary to model the behavior of asphalt concrete from its intact State up to the level of macrocrack formation are as follows.

The strain energy density function is given in Equation (5.1),

$$W^R = f(\varepsilon^R, S) \quad (5.1)$$

The stress-pseudo strain relationship is given in Equation (5.2), and the damage evolution law is given in Equation (5.3)

$$\sigma = \frac{\partial W^R}{\partial \varepsilon^R} \quad (5.2)$$

$$\frac{dS}{d\xi} = \left(-\frac{\partial W^R}{\partial S} \right)^\alpha \quad (5.3)$$

Where W^R is the pseudo strain energy, ε^R is the pseudo strain, S is the internal State variable that represents damage, α is the damage evolution rate, σ is stress, and ξ is reduced time. As mentioned before, the VECD formulation governs the region of the material in which micro damage does not coalesce or localize into a single dominant macrocrack. Equation (5.4) expresses the relationship of the pseudo strain, ε^R , to the governing induced strain.

$$\varepsilon^R(\xi) = \frac{1}{E_R} \int_0^\xi E(\xi - \tau) \frac{d\varepsilon}{d\tau} d\tau \quad (5.4)$$

Where E_R is the reference modulus (typically taken as 1) that is used for dimensional compatibility and τ is a dummy time parameter used for integration. Pseudo strain energy is defined as the area under the stress versus pseudo strain curve, shown in Figure 5-2 (a).

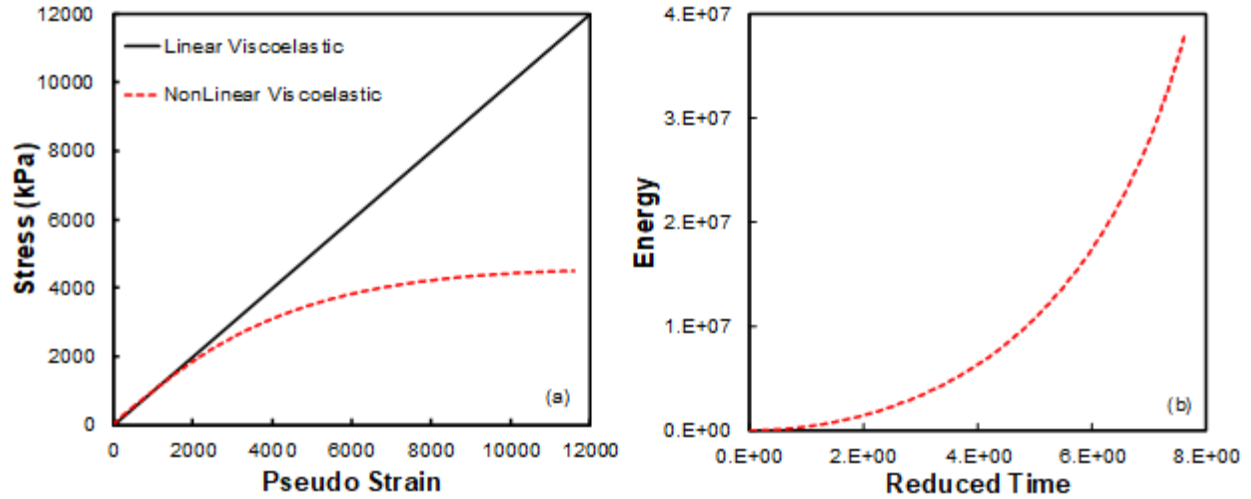


Figure 5-2. Induced stress in uniaxial direct tension monotonic test: (a) stress versus pseudo strain and (b) evolution of dissipated pseudo strain energy as a function of reduced time Equation (5.5) expresses the relationship for defining pseudo strain energy in linear

$$W^R = \frac{1}{2} \times \sigma \times \varepsilon^R \quad (5.5)$$

VECD theory is able to keep track of the material's integrity at any instance of time and predict induced stress, as shown in Equation (5.6)

$$\sigma = C \times \varepsilon^R \quad (5.6)$$

Where C is pseudo stiffness. According to Daniel and Kim (2002), pseudo stiffness is related to the internal damage State of the material, S , and can be expressed as Equation (5.7).

$$C = 1 - C_{11} S^{C_{12}} \quad (5.7)$$

Where C_{11} and C_{12} are the material parameters, and pseudo stiffness (C) varies from 1 (undamaged State) to 0 (totally damaged). It should be noted that, depending on the applied load, the C at failure changes and is always greater than 0. Equation (5.3) through Equation (5.7) can be combined to give Equation (5.8) that correlates the internal damage of the material, S , to the strain history of the material.

$$\frac{dS}{d\xi} = \left(\frac{1}{2} C_{11} C_{12} S^{C_{12}-1} \right)^\alpha \times \left(\frac{1}{E_R} \times \int_0^\xi E(\xi - \tau) \frac{d\varepsilon}{d\tau} d\tau \right)^{2\alpha} \quad (5.8)$$

Keshavarzi and Kim (2016) proved that Equation (5.8) can be employed to predict the evolution of induced stress in a direct tension monotonic test by using the results obtained from cyclic fatigue tests. They also showed that the S-VECD model can predict the strength mastercurve for asphalt concrete. Figure 5-3 presents the representative results of the study from Keshavarzi and Kim (2016).

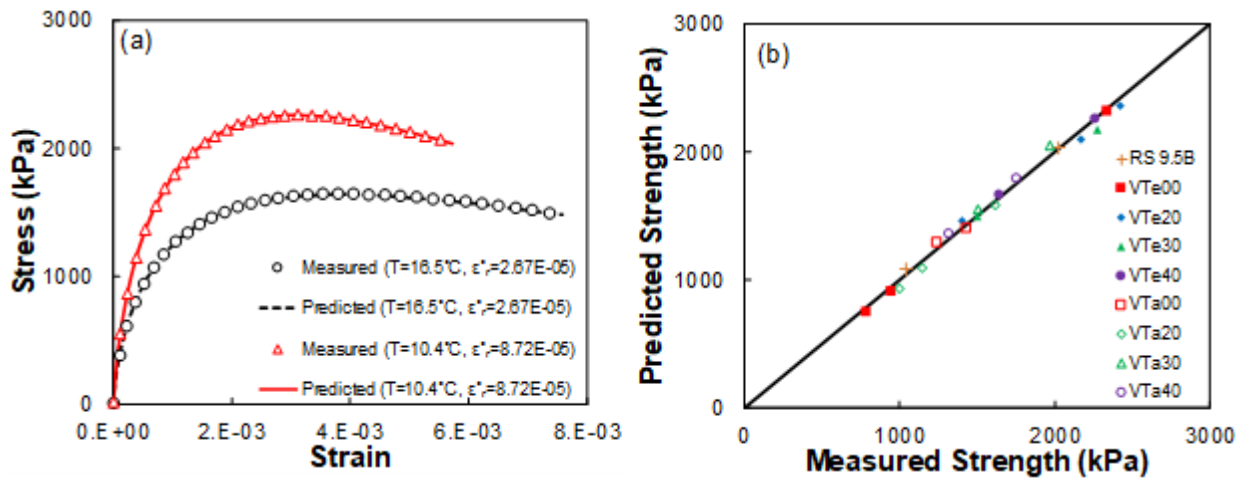


Figure 5-3. Prediction of induced stress and measured strength based on S-VECD theory: (a) measured versus predicted induced stress in the uniaxial direct tension monotonic test for VTe20 mixture, (b) predicted versus measured strength for Material Group 1.

As suggested by Chehab (2002), the fracture parameters measured from TSRSTs can be predicted using averaged results obtained using the strength and failure strain criteria. However, the strength-based failure criterion is not adequate to predict thermal cracking behavior under realistic thermal loading conditions encountered in service. Figure 5-4 shows an example that can be used to illustrate this point whereby a bilinear strain history is applied to the representative volume element (RVE). Figure 5-4 (a) and (b) present the changes in pseudo stiffness and damage parameter, respectively that are due to the bilinear strain history. In the first

loading segment, the specimen is loaded with the constant strain rate of 10^{-5} strain/second. In the second segment of loading, the strain rate changes to 10^{-6} strain/sec, as shown in Figure 5-4 (a). Figure 5-4 (b) shows the stress that is due to the bilinear strain history presented in Figure 5-4 (a); this stress is calculated using the S-VECD model. Due to the history-dependent nature of asphalt mixtures, the induced stress decreases in Segment 2 even though the strain increases during that segment. Although the stress decreases in Segment 2, the damage continues to increase, and the pseudo stiffness, i.e., the material's integrity, also decreases in Segment 2. If the strain continues to increase in Segment 2, the RVE sample will eventually fail even though the stress at failure is less than the peak stress at the end of Segment 1. The thermal loading history in the field consists of many cases similar to the strain history shown in Figure 5-4 (a), and therefore, the strength criterion is not adequate to capture failure that is due to thermal changes in the field. DPSE criterion described in Equation (5.9).

$$DPSE = \int_0^{\xi_f} \varepsilon_R^2 (1 - C) d\xi \quad (5.9)$$

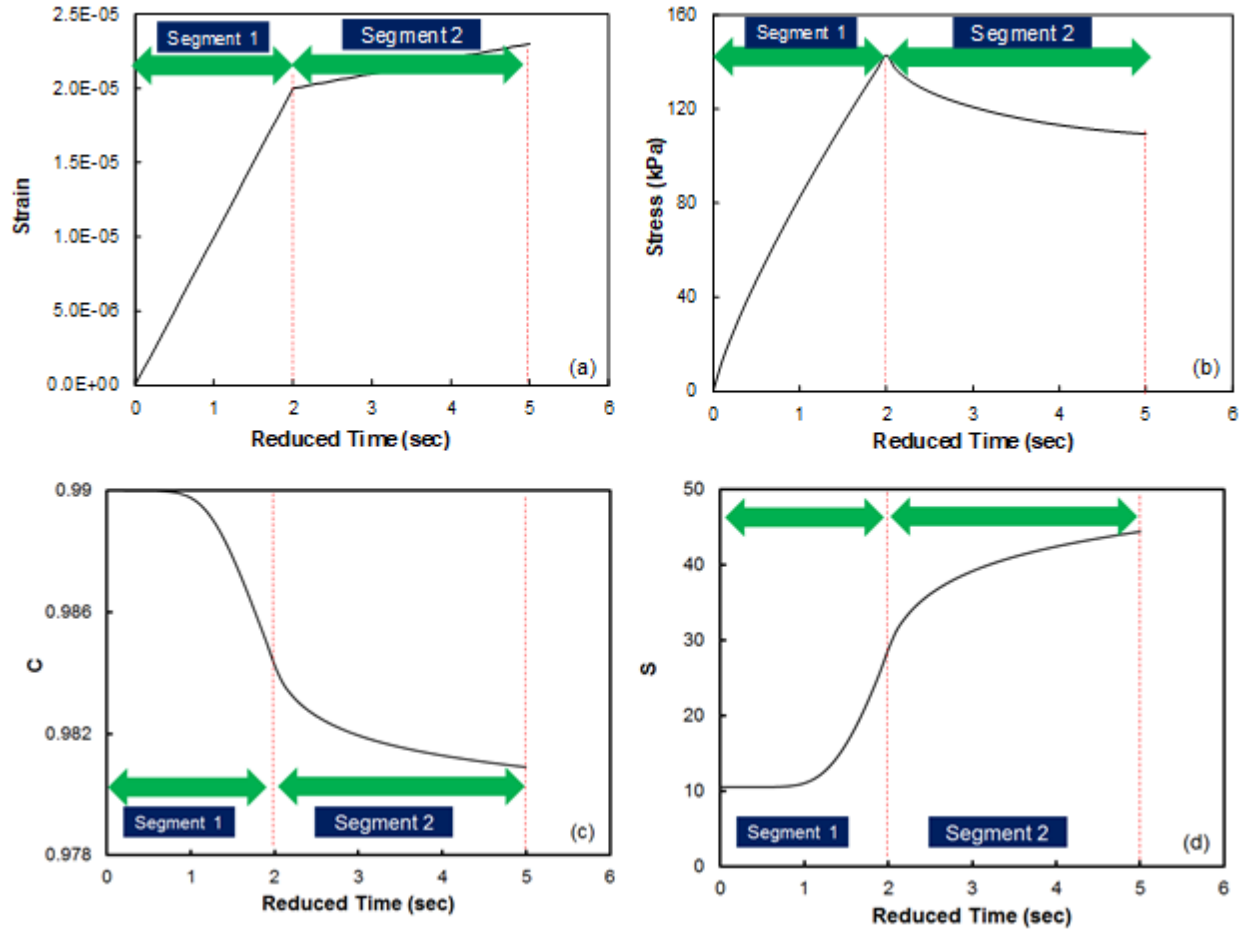


Figure 5-4. Example of bilinear strain history for RVE sample: (a) strain history, (b) induced stress within the sample, (c) decrease in pseudo stiffness calculated from the S-VECD model, and (d) increase in damage parameter calculated from the S-VECD model.

Where DPSE is the dissipated pseudo strain energy and ζ_f is the reduced time at failure. As aforementioned, the time-temperature shift factor is valid for the damaged State of the material, which means that, for any given reduced strain rate, there is a unique induced stress-strain curve. As a result, the associated DPSE is a unique function of the reduced strain rate. Keshavarzi and Kim (2016) proved that S-VECD model can capture the damage evolution induced in an asphalt mixture in direct tension monotonic tests. Keshavarzi and Kim's finding is significant because the DPSE under monotonic loading can be predicted using S-VECD model that is characterized by the AMPT dynamic modulus and cyclic fatigue tests. Figure 5-5 presents

the measured DPSE as a function of reduced strain rate for the Vermont mixtures in Material Group 1.

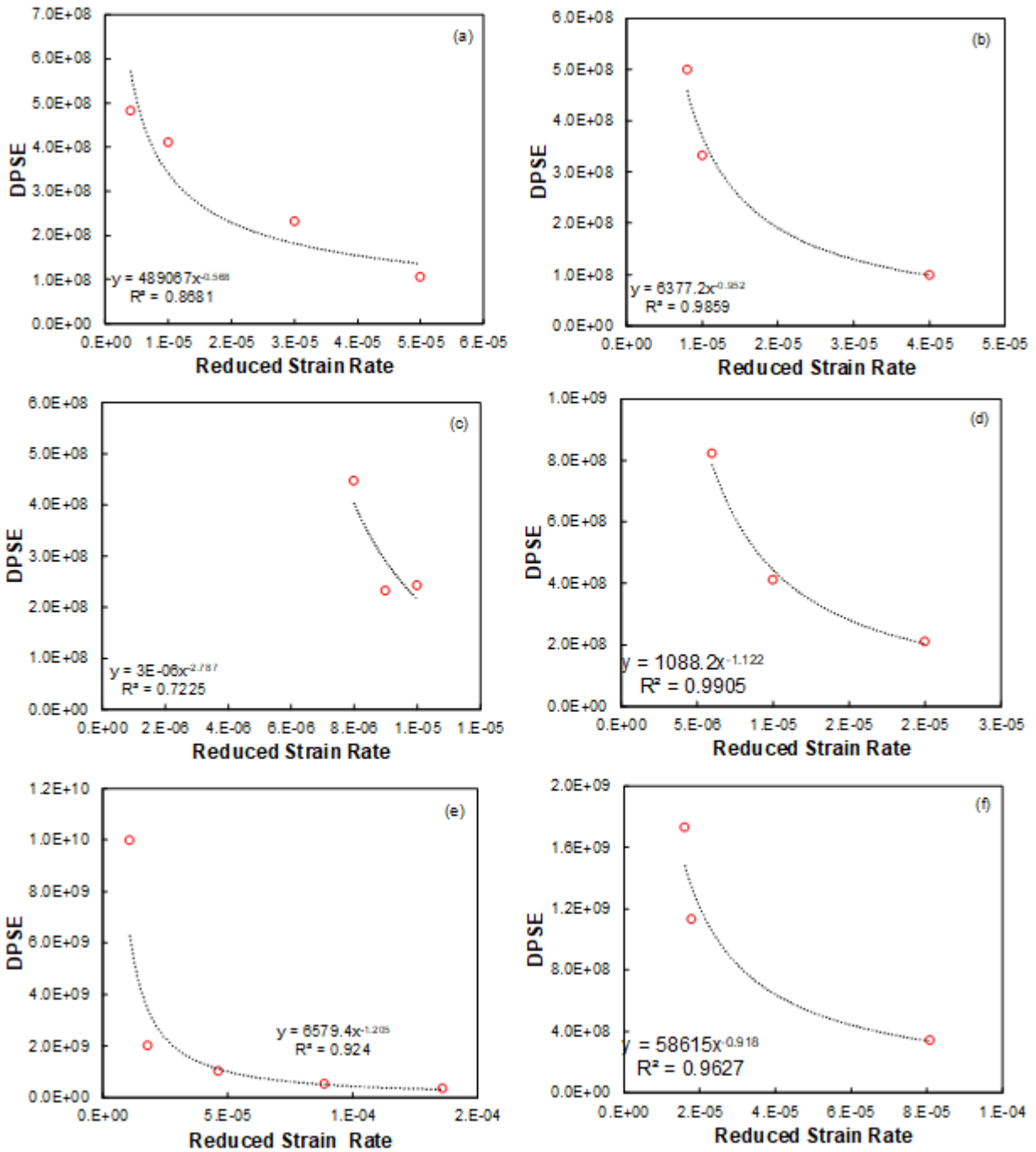


Figure 5-5. Dissipated pseudo strain energy mastercurves for Vermont mixtures: (a) VTa00, (b) VTa20, (c) VTa30, (d) VTa40, (e) VTE00, and (f) VTe20.

Figure 5-6 presents a comparison between the measured DPSE values and the corresponding values obtained using S-VECD model.

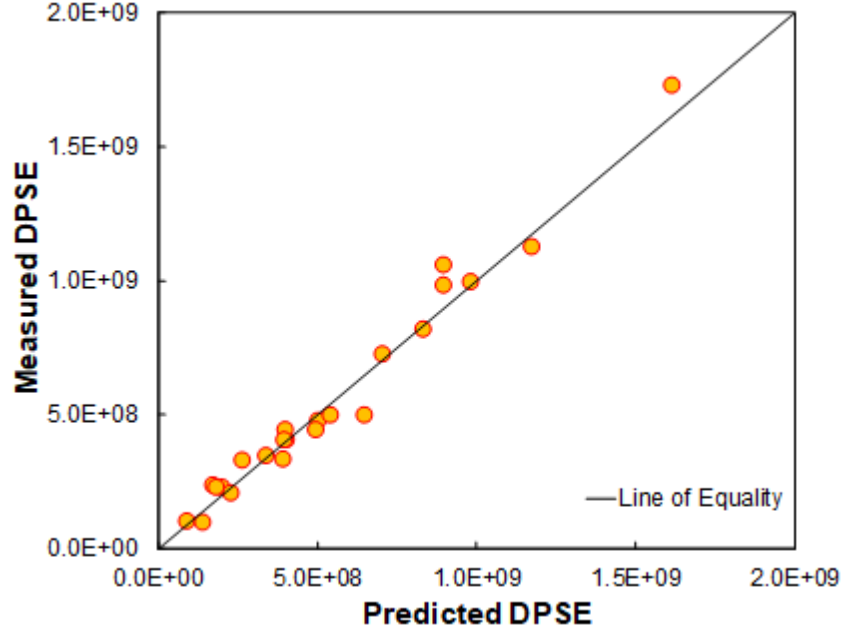


Figure 5-6. Measured versus predicted dissipated pseudo strain energy for mixtures in Material Group 1.

It should be noted that the effect of the initial damage, or the damage level at which the test Starts, should be reflected in the failure criterion. The magnitude of the damage changes the material’s integrity, which S-VECD theory recognizes through the decrease in pseudo stiffness (C). Equation (5.10) presents the DPSE failure criterion for different initial damage levels (i.e., C_0) for the VTa00 mixture. In developing Figure 5-7, Equation (5.9) should be modified to become Equation (5.10).

$$DPSE = \int_0^{\xi} \varepsilon_R^2 \times (C_0 - C) d\xi \tag{5.10}$$

Where C_0 represents the damage level when the loading Starts. Equation (5.10) suggests that the maximum tolerable DPSE is a function of the reduced strain rate and initial damage level

(Equation (5.9)). Figure 5-7 shows the effect of C_0 and reduced strain rate on the DPSE failure criterion. Figure 5-7 shows that increasing the reduced strain rate and the initial damage level (C_0) can significantly reduce the damage tolerance of the material. In predicting the fracture temperature and fracture stress in TSRSTs, the DPSE criterion can be developed for four different initial damage levels shown in Figure 5-7, i.e., $C_0 = 0.99$, $C_0 = 0.9$, $C_0 = 0.8$, and $C_0 = 0.7$.

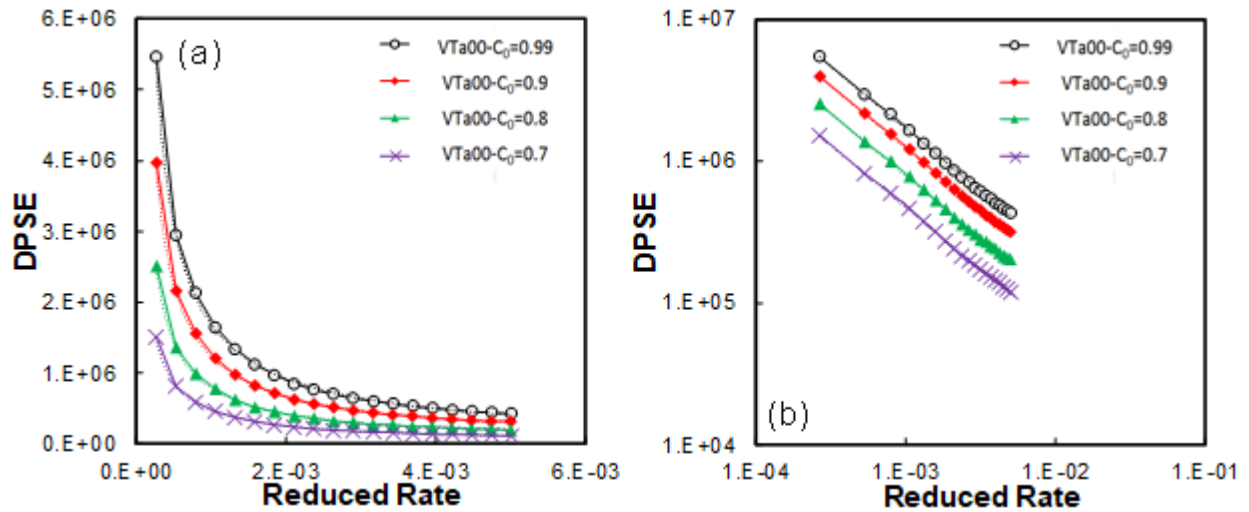


Figure 5-7. Dissipated pseudo strain energy criteria for VTa00 mixture at different initial damage levels: (a) in arithmetic scale and (b) in log-log scale.

5.6. Application of DPSE Failure Criterion to Prediction of TSRST Results

In the previous section, the DPSE failure threshold is measured and predicted based on the constant reduced strain rate test. The ability to predict the fracture temperature and fracture stress that are measured in the TSRST is the final goal of the suggested failure criterion. The total deformation and total strain of the specimen are zero in TSRSTs. Total strain can be decomposed into two components: thermal strain and mechanical strain, as expressed in Equation (5.11).

$$\varepsilon^{total} = \varepsilon^{mechanical} + \varepsilon^{thermal} = 0 \quad (5.11)$$

Where $\varepsilon_{\text{mechanical}}$ is the mechanical strain and $\varepsilon_{\text{thermal}}$ is the thermal strain. Equation (5.11) can be modified to become Equation (5.12) to express the mechanical strain based on the thermal strain.

$$\varepsilon^{\text{mechanical}} = -CTC \times (T - T_0) \quad (5.12)$$

Equations (5.8) and (5.12) can be combined to become Equation (5.13) to give the evolution of damage during a TSRST.

$$\frac{dS}{d\xi} = \left(\frac{1}{2} C_{11} C_{12} S^{C_{12}-1} \right)^\alpha \times \left(\frac{1}{E_R} \times \int_0^\xi E(\xi - \tau) \frac{d(CTC \times (T - T_0))}{d\tau} d\tau \right)^{2\alpha} \quad (5.13)$$

It should be noted that T_0 is the equilibrium temperature for the test and is considered to be the same as the Starting temperature of the test. In this paper, we consider the CTC to be a function of temperature and calculated it based on the procedure discussed in Keshavarzi et al. (2019). Table 5.6, Table 5.7, and

Table 5.8 present the values of the thermal coefficients used in this study, which are in turn used in Equation (5.14) to calculate the CTC of the mixtures as a function of temperature.

$$CTC(T) = CTC_g + (CTC_L - CTC_g) \times \frac{e^{\frac{T-T_g}{R}}}{1 + e^{\frac{T-T_g}{R}}} \quad (5.14)$$

Table 5.6. Thermal Coefficients for Material Groups 1 and 2

Mixture Name	Thermal coefficients			
	CTC _L	CTC _g	T _g	R
VTa00	8.62E-06	2.61E-05	- 35.74	6.13
VTa20	5.52E-06	0.000022	- 39.03	15.08
VTa30	1.76E-05	2.54E-05	- 29.78	2.514
VTa40	0.000019	2.55E-05	- 29.66	1.57
VTe00	1.04E-05	2.61E-05	- 32.55	5.189
VTe20	1.04E-05	2.61E-05	- 32.55	5.189
VTe30	1.15E-05	2.83E-05	- 31.28	6.751
VTe40	1.15E-05	2.83E-05	- 31.28	6.751
NHe00	6.78E-06	2.59E-05	-37.3	4.704
NHe20	6.78E-06	2.59E-05	-37.3	4.701
NHe30	6.78E-06	2.59E-05	-37.3	4.707
NHe40	6.77E-06	2.59E-05	- 37.32	4.686
NYb30	6.77E-06	2.59E-05	- 37.33	4.686
NYb40	6.77E-06	2.59E-05	- 37.33	4.686
NYd20	6.78E-06	3.95E-05	-37.3	4.705
NYd30	2.63E-06	8.00E-06	- 34.71	5.411
NYd40	2.58E-05	7.11E-06	- 36.72	4.161

Table 5.7. Thermal Coefficients for Materials Groups 3 and 4

Mixture Name	Thermal coefficients			
	CTC _L	CTC _g	T _g	R
NHe5820-opt	2.61E-05	6.69E-06	- 38.85	5.593
NHe5840-opt	2.61E-05	1.20E-05	-30.2	3.101
NHe6400-opt	2.61E-05	1.11E-05	- 31.48	4.797
NHe6400opt	2.61E-05	1.11E-05	- 31.48	4.797
NHe6420-opt	2.61E-05	1.23E-05	- 29.95	4.143
NHe6420opt	2.63E-05	1.18E-05	- 30.32	6.257
NHe6440-opt	2.60E-05	1.05E-05	- 32.36	4.262
NHe6440opt	2.63E-05	7.89E-06	- 36.44	5.929
NHe6440+opt	2.63E-05	7.89E-06	- 36.44	5.629
TX-STA	3.38E-05	4.94E-06	- 24.92	15.8
TX-4D	2.61E-05	8.50E-06	- 35.89	4.519
TX-16D	2.60E-05	1.06E-05	- 32.61	4.522
WA-STA	2.58E-05	9.21E-06	- 34.36	2.466
WA-4D	2.61E-05	1.02E-05	- 32.57	4.519
WA-16D	2.61E-05	1.23E-05	- 29.95	4.243
SD-STA	2.59E-05	6.78E-06	-37.3	4.702
SD-4D	2.66E-05	1.23E-05	- 28.84	4.111

Table 5.8. Thermal Coefficients for Material Group 4

Mixture Name	Thermal coefficients			
	CTC _L	CTC _g	T _g	R
SD-8D	2.61E-05	1.00E-05	- 32.99	4.693
RS9.5B-STA	2.59E-05	6.78E-06	- 37.31	4.701
RS9.5B-4D	2.62E-05	6.77E-06	- 36.46	5.724
RS9.5B-7D	2.63E-05	8.00E-06	-34.7	5.41
RS9.5B-17D	2.59E-05	6.78E-06	- 37.31	4.699

Figure 5-8 presents the steps that were taken to predict the fracture temperature and fracture stress in the TSRSTs using the DPSE failure criterion. The first step calculates the induced stress, pseudo stiffness, and reduced strain (Equation (5.15)) that occur during the test.

$$\varepsilon_r = CTC \times a_T \times \frac{dT}{dt} \quad (5.15)$$

To determine the stress, the S value during a TSRST is calculated as a function of time using Equation (5.13). Then the pseudo stiffness (C) can be determined from Equation (5.7) using the calculated value of S . Finally, the stress can be calculated by substituting C and the pseudo strain that has been determined from Equation (5.4) into Equation (5.6). The second step calculates the DPSE for any instance of time during the test (Equation (5.9)). The third step interpolates the maximum allowable DPSE based on the current pseudo stiffness value of the material. The interpolation is performed for the instantaneous reduced strain rate. Finally, Steps 4 and 5 are used to calculate the fracture temperature and fracture stress.

Figure 5-9 presents a sample of the calculations required for Steps 1 and 2, and Figure 5-10 presents a sample of the calculations required for Steps 3 to 5. Figure 5-9 (a) shows that the reduced strain rate that corresponds to the instance of failure is determined. Figure 5-10 (b) shows that, based on the given time-temperature shift factor coefficients and CTC of the mixture, the temperature that corresponds to the failure reduced strain rate is determined. Figure 5-10 (c) shows that the fracture stress can be determined from the calculated relationship between stress and temperature. Verification of the induced stress during the test and a comparison of the predicted fracture stress and temperature results are discussed in the next section.

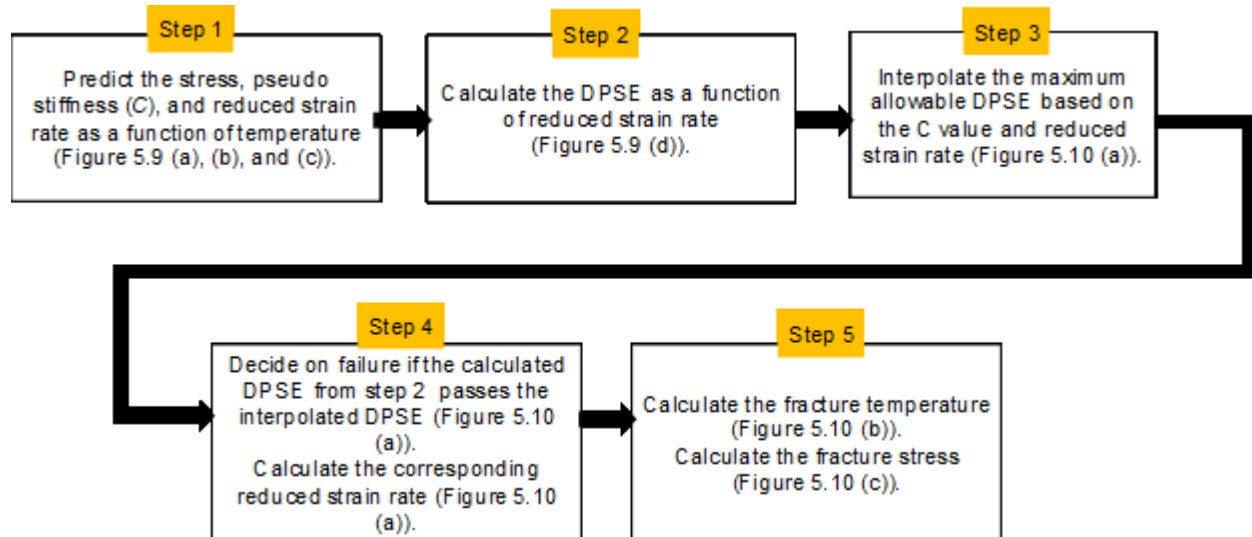


Figure 5-8. Steps for failure detection in a TSRST using the DPSE failure criterion.

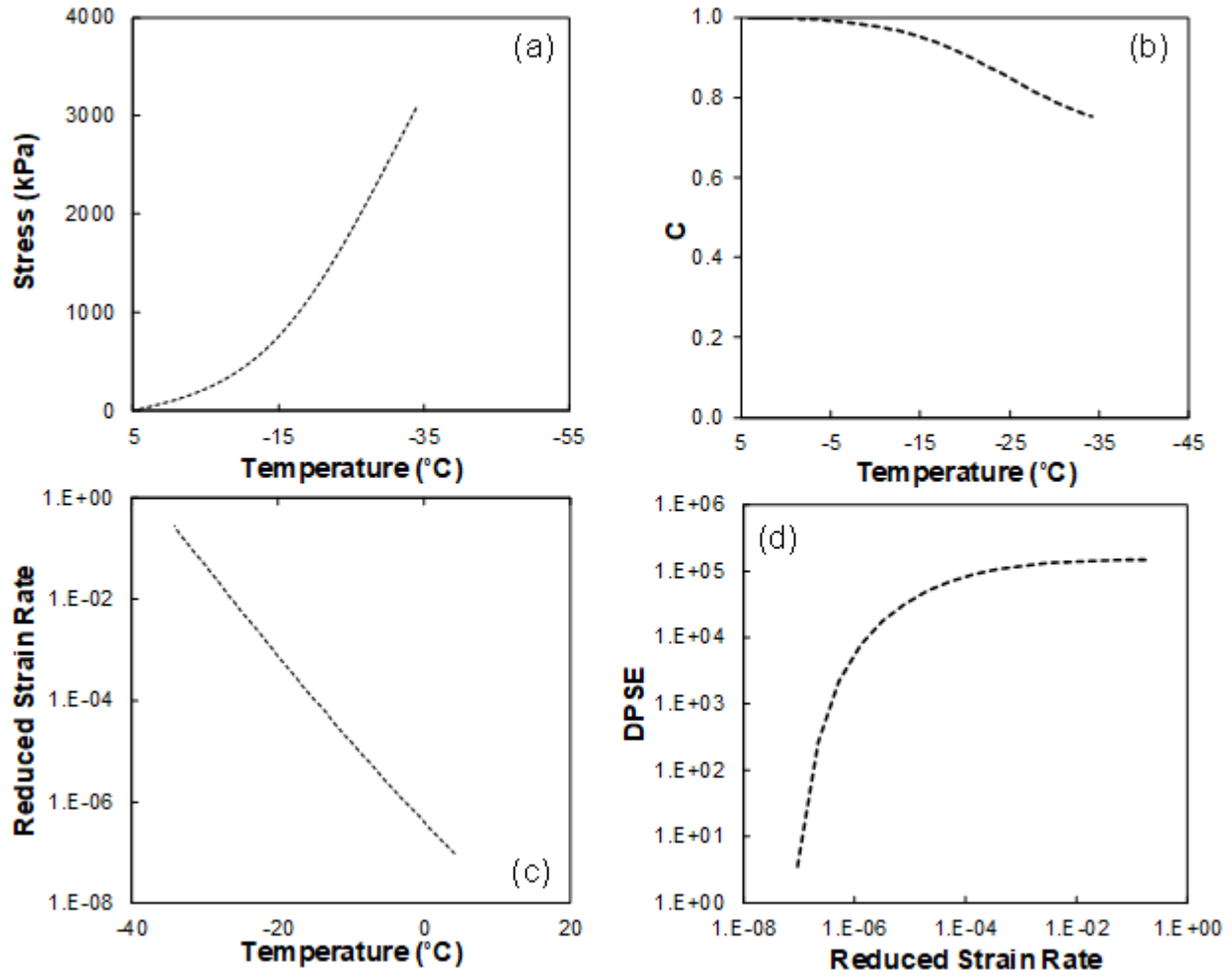


Figure 5-9. Prediction of TSRST results using S-VECD theory: (a) induced stress as a function of temperature, (b) pseudo stiffness variation as a function of temperature, (c) evolution of reduced strain rate as a function of temperature, and (d) evolution of DPSE as a function of reduced strain rate.

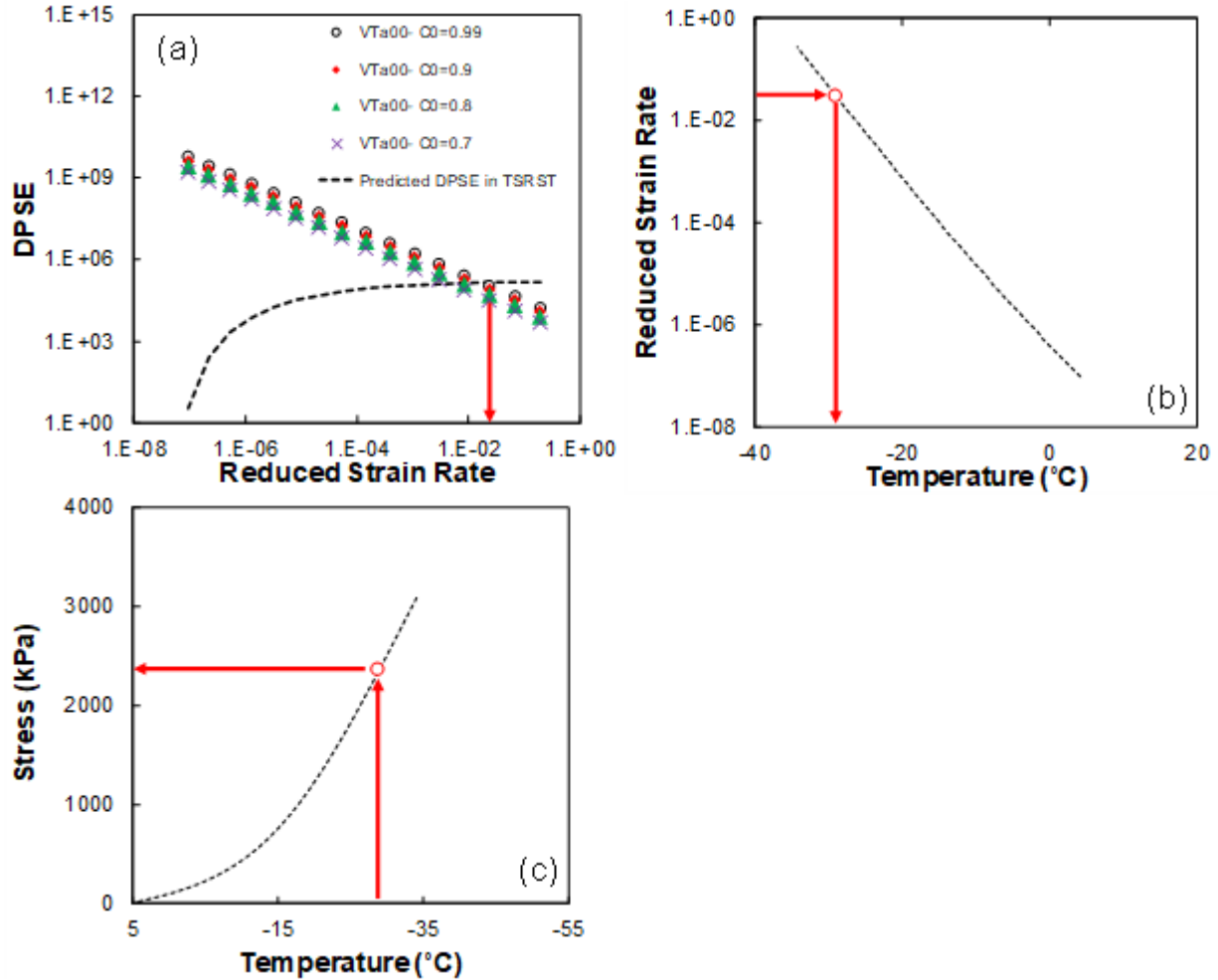


Figure 5-10. Prediction of TSRST fracture stress and fracture temperature using S-VECD theory: (a) interpolation of DPSE for any C value, (b) prediction of fracture temperature from the reduced strain rate, and (c) prediction of fracture stress from fracture temperature.

5.7. Verification of Proposed Methodology for Prediction of TSRST Results

In predicting the TSRST fracture results, the temperature at the middle radius of the sample is used as the temperature of the sample and is denoted as inside temperature. The heat transfer function (Equation (5.16)) was solved using the Crank-Nicolson method to obtain that temperature at each instance of time. The air temperature of the sample is assumed to drop at the rate of -10°C/hr .

$$\frac{\partial T}{\partial t} = k \frac{\partial^2 T}{\partial x^2} \quad (5.16)$$

Where T is temperature, k is thermal diffusivity, and x is the spatial coordinate. The thermal diffusivity is assumed to be equal to $5 \times 10^{-7} \text{ m}^2/\text{°C}$. It should be noted that the diameter of the asphalt mixture specimen used for the TSRSTs is 54 mm. Therefore, we decided to calculate the temperature distribution inside a 54-mm diameter sample, as shown in Figure 5-11.

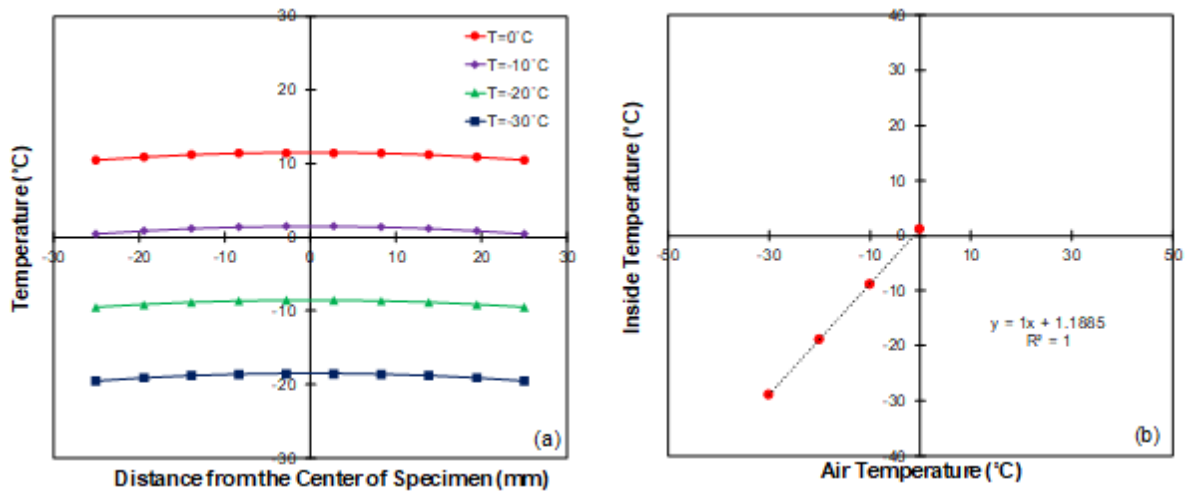


Figure 5-11. Predicted temperatures in a circular asphalt sample: (a) temperature distribution inside the sample and (b) inside temperature as a function of air temperature.

Figure 5-12 to Figure 5-15 present the measured and predicted stress values as functions of temperature for the first and second experimental groups of mixtures, respectively.

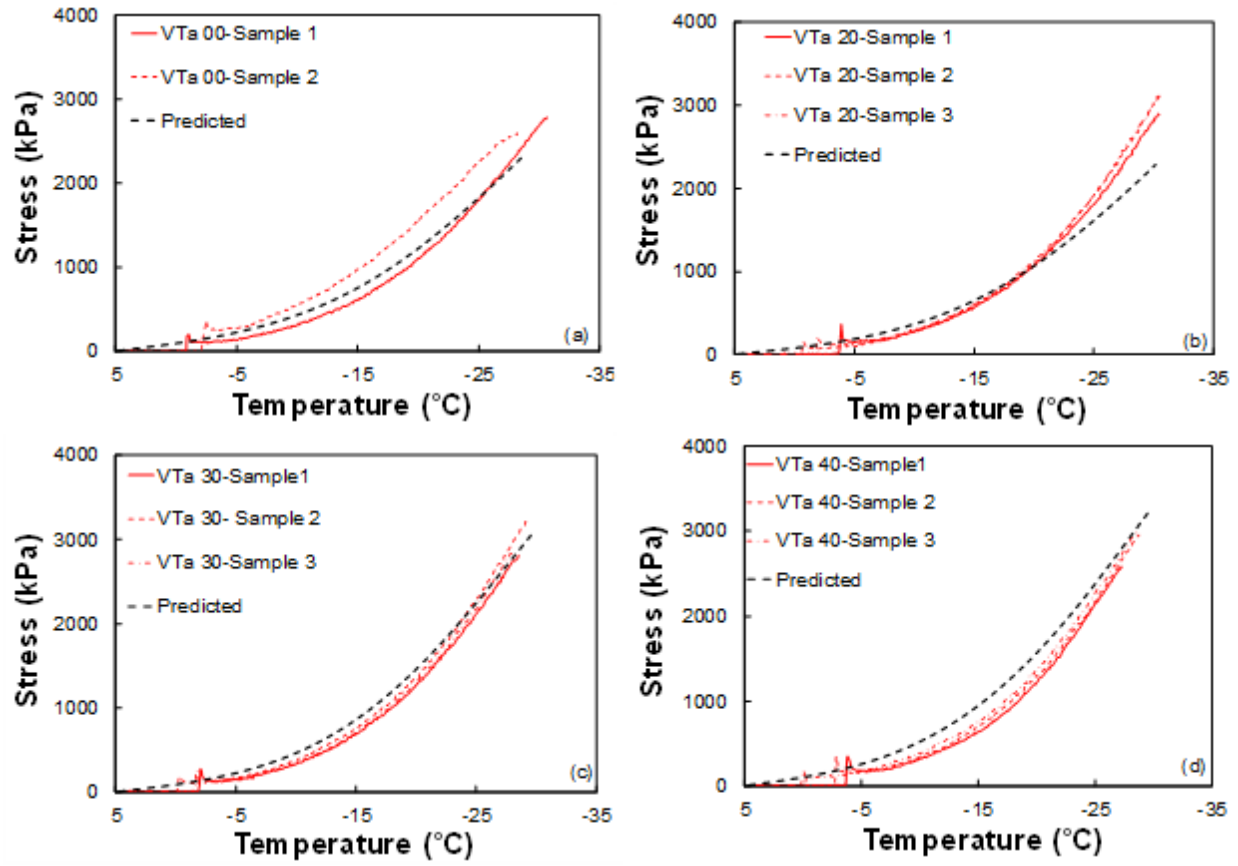


Figure 5-12. Measured and predicted stress values as a function of temperature for the Vermont mixtures: (a) VTa00, (b) VTa20, (c) VTa30, and (d) VTa40.

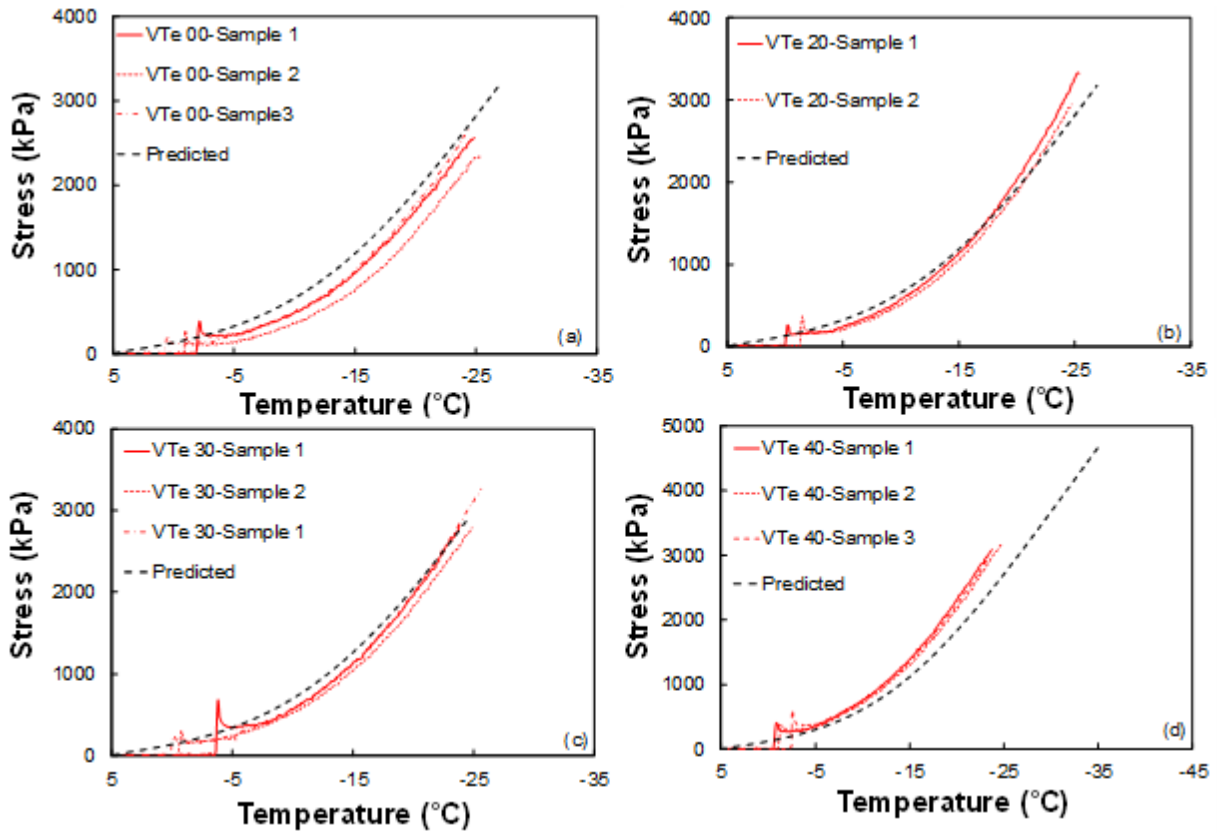


Figure 5-13. Measured and predicted stress values as a function of temperature for the Vermont mixtures: (a) VTe00, (b) VTe20, (c) VTe30, and (d) VTe40.

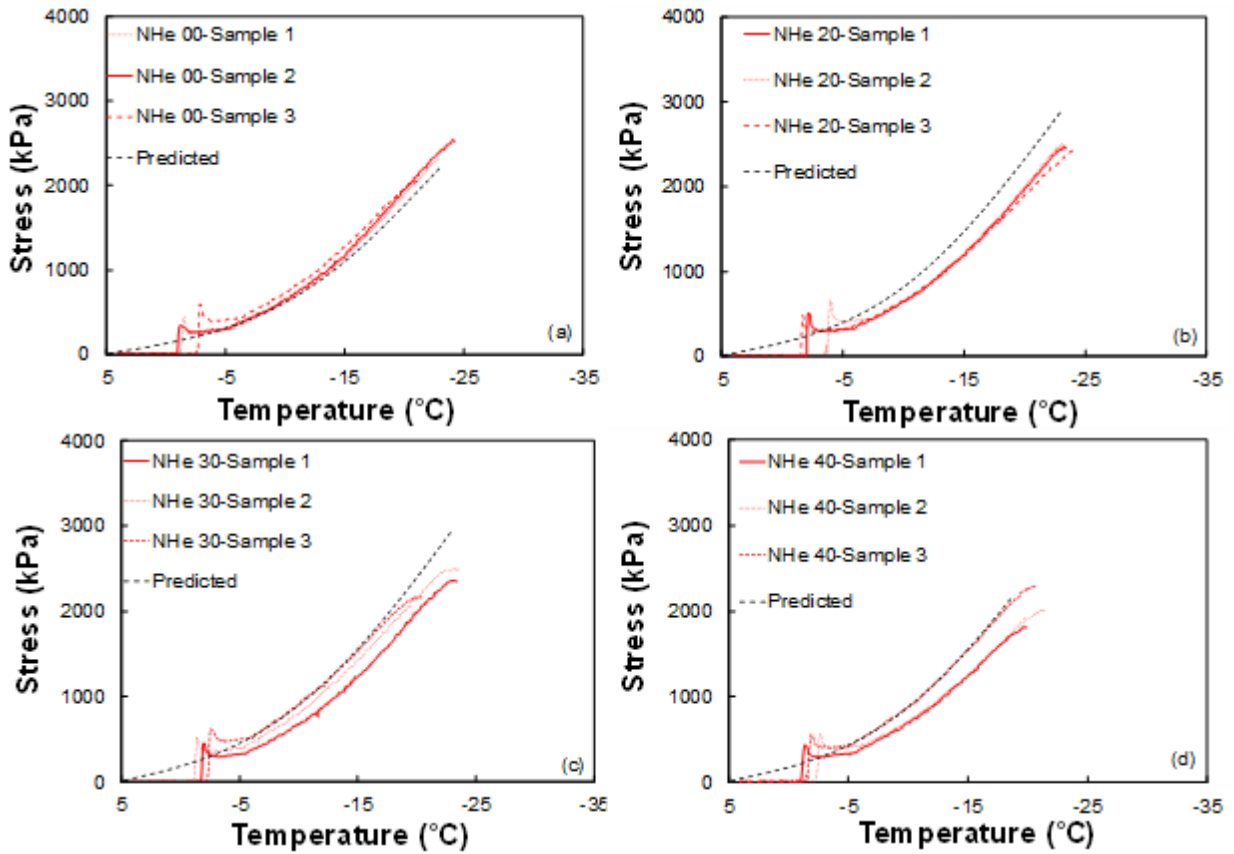


Figure 5-14. Measured and predicted stress values as a function of temperature for the New Hampshire mixtures in Material Group 2: (a) NHe00, (b) NHe20, (c) NHe30, (d) NHe40, (e) NYb30, (f) NYb40, (g) NYd20, (h) NYd30, and (i) NYd40.

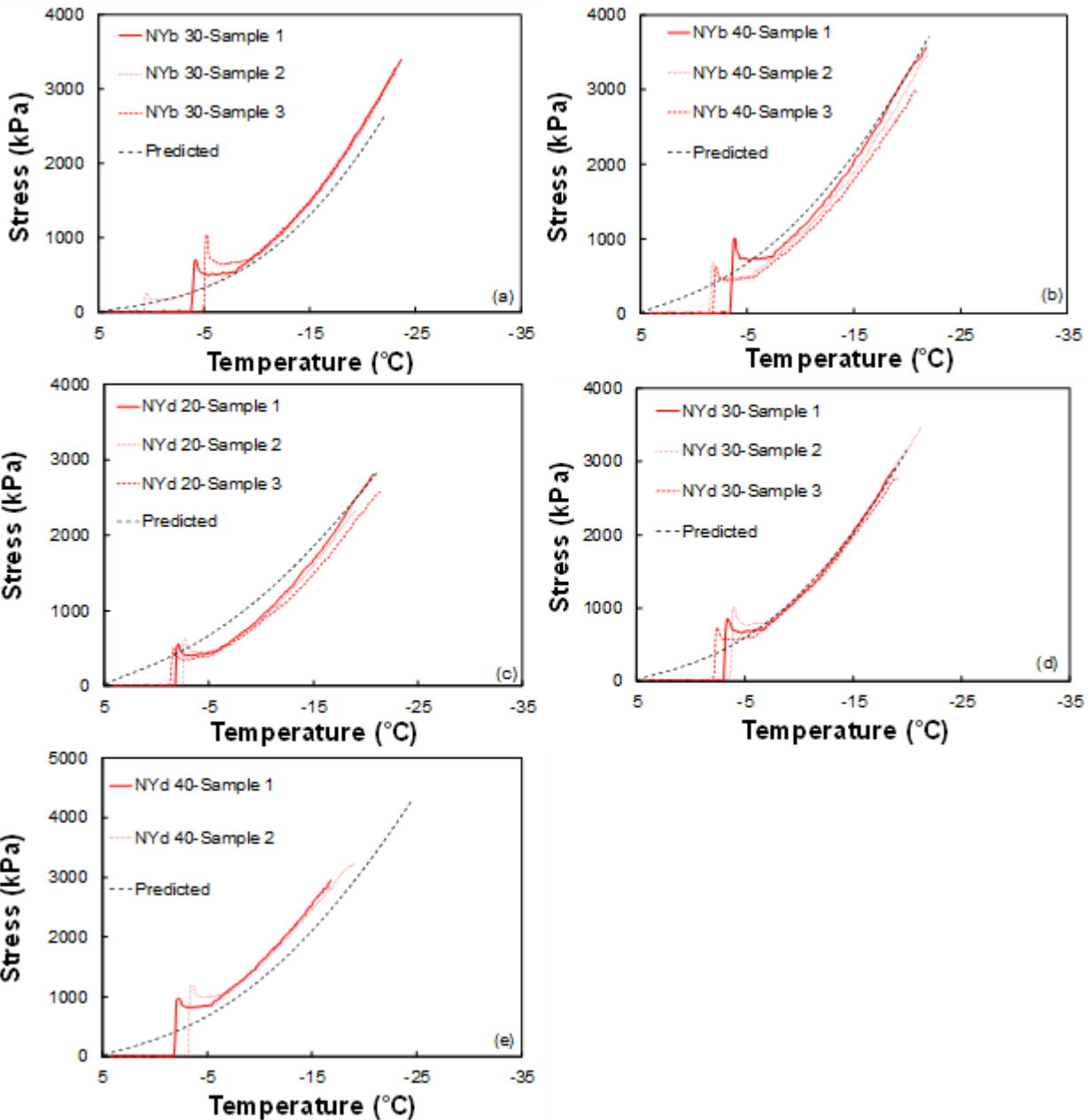


Figure 5-15. Measured and predicted stress values as a function of temperature for the New York mixtures in Material Group 2: (a) NYb30, (b) NYb40, (c) NYd20, (d) NYd30, and (e) NYd40.

Figure 5-16 presents a comparison of the results for the first and second experimental groups of mixtures between the predicted versus averaged measured fracture temperatures (Figure 5-16 (a)) and fracture stress values (Figure 5-16 (b)), respectively. Figure 5-16 (a) shows that the DPSE failure criterion is able to predict the fracture temperature that is measured by the TSRST with reasonable accuracy. However, much greater variability is observed for the fracture

stress prediction in Figure 5-16 (b). It is believed that the intrinsic flaws in the test specimens are attributed to this larger variability in the fracture stress prediction.

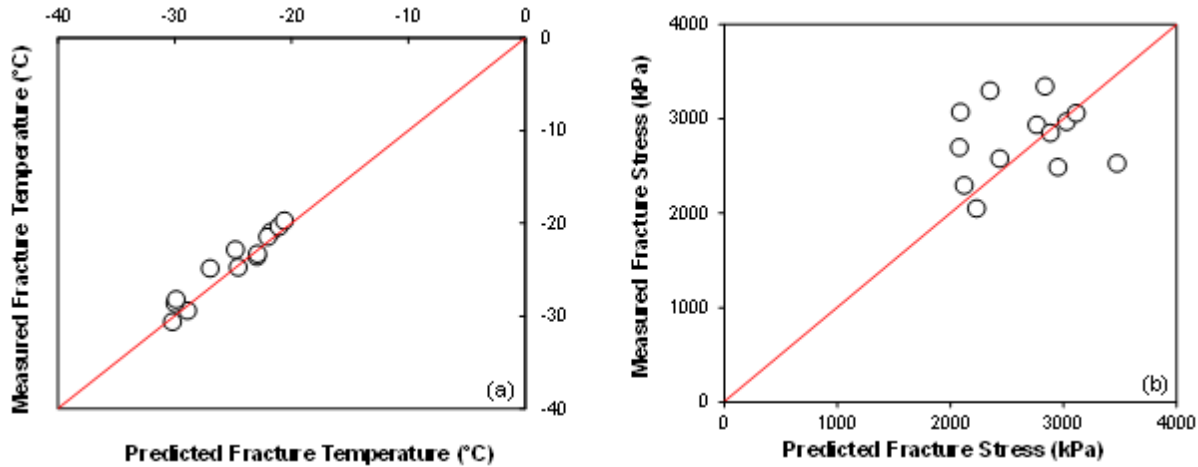


Figure 5-16. Comparisons between averaged measured and predicted values for Material Groups 1 and 2: (a) fracture temperature and (b) fracture stress.

Figure 5-17 presents the predicted fracture temperatures for the mixtures in Material Group 3. Figure 5-17 (a) and Figure 5-17 (b) prove that the DPSE failure criterion can rank the mixtures based on RAP content and binder content. Once the RAP content increases for the NHe5820-opt and NHe5840-opt mixtures and the NHe6400-opt, NHe6420-opt, and NHe6440-opt mixtures, the fracture temperature decreases. Also, Figure 5-17 (c) shows that, as the binder content increases for the NHe6440-opt, NHe6440opt, and NHe6440+opt mixtures, the predicted fracture temperature decreases. Finally, Figure 5-17 (d) shows that the use of softer virgin binder decreases the fracture temperature for the NHe5820-opt and NHe6420-opt mixtures and the NHe5840-opt and NHe6440-opt) mixtures. These observations are in line with findings in the literature (Jung and Vinson 1994, Marasteanu et al. 2007). Figure 5-18 shows that the DPSE criterion can rank the mixtures based on aging level. Once the aging increases, the fracture temperature decreases significantly.

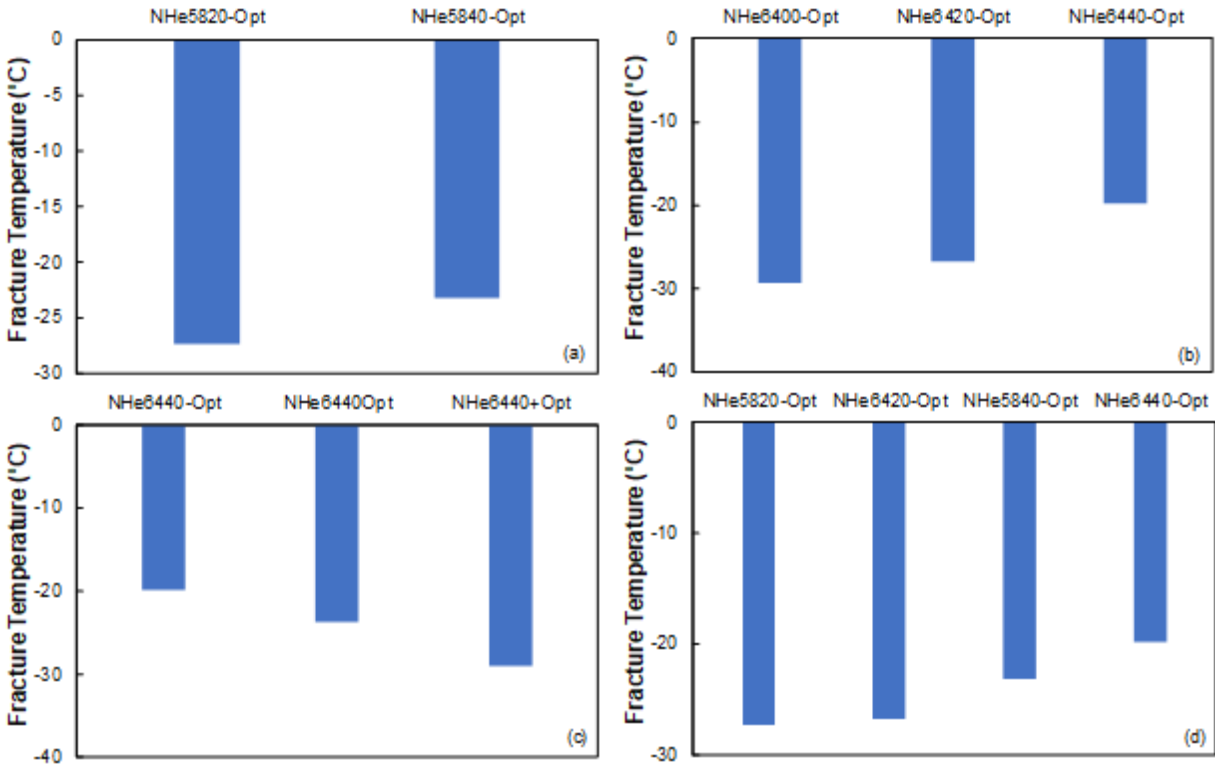


Figure 5-17. Predicted fracture temperatures for Material Group 3: (a) NHe5820-opt and NHe5840-opt, (b) NHe6400-opt, NHe6420-opt, and NHe6440-opt, (c) NHe6440-opt, NHe6440opt, and NHe6440+opt, and (d) NHe5820-opt, NHe6420-opt, NHe5840-opt, and NHe6440-opt.

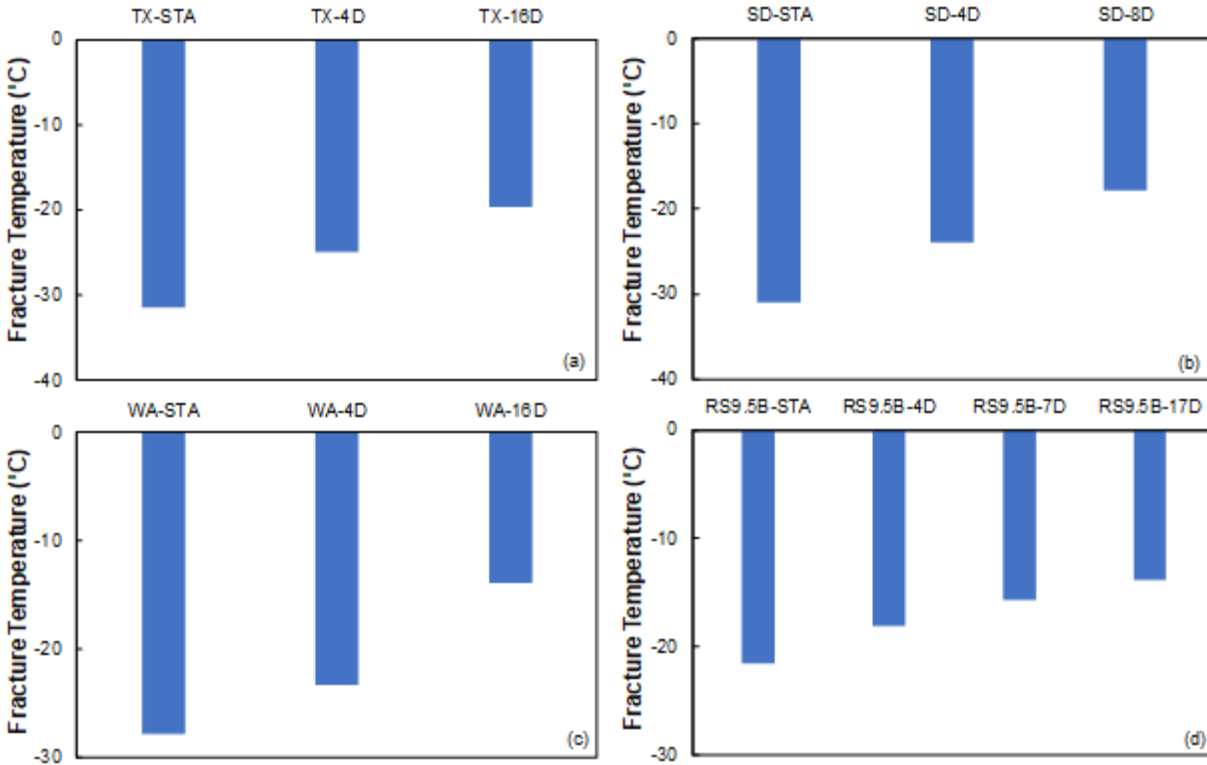


Figure 5-18. Predicted fracture temperatures for Material Group 4: (a) Texas mixture, (b) South Dakota, (c) Washington mixture, and (d) North Carolina mixture.

5.8. Conclusions

This paper presents a new failure criterion that can help predict the failure of asphalt concrete mixtures in uniaxial direct tension monotonic tests and TSRSTs. The failure criterion correlates the DPSE of asphalt mixtures with the applied reduced strain rate. The criterion was used to predict measured fracture results (i.e., fracture stress and fracture temperature) in TSRSTs. This study found that the fracture stress and fracture temperature measured in TSRSTs can be predicted with reasonable accuracy using the suggested failure criterion and S-VECD model. Mixtures that cover a range of RAP contents, binder contents, virgin binder grades, and aging levels were selected and used to verify the reasonableness and accuracy of the proposed failure criterion. The ability to predict the fracture stress and fracture temperature measured via the TSRST using the S-VECD model and the suggested DPSE failure criterion is of substantial

practical and technical importance because it allows the prediction of both fatigue cracking and thermal cracking using a single set of tests, i.e., AMPT dynamic modulus and cyclic fatigue tests.

CHAPTER 6. FLEXTC: A THERMAL CRACKING ANALYSIS FRAMEWORK FOR ASPHALT PAVEMENTS

6.1. Abstract:

Low-temperature cracking is one of the most prevalent types of distress in asphalt pavements in regions where the air temperature undergoes a significant daily drop. This paper proposes a new analysis framework, FlexTC, for predicting the performance of asphalt pavements subjected to air temperature variations. FlexTC is able to analyze a pavement's response to the imposed temperature variation and predict the associated thermal stress and thermal damage via Fourier transform methodology. FlexTC updates the material properties based on the given temperature variation over time and pavement depth, the damage level, and the aging evolution. FlexTC also utilizes the simplified viscoelastic continuum damage (S-VECD) theory to update the thermal-induced damage and to define the dissipated pseudo strain energy failure criterion to predict the material's failure.

For this study, eight pavement sections constructed at the North Carolina Department of Transportation's research facility, MnROAD, and three synthetic were used to verify the accuracy and applicability of the FlexTC framework. The DF was found to be able to differentiate the pavement sections in terms of their expected and/or observed performance. The performance rankings based on FlexTC predictions are compatible with observed cracking in the field-constructed sections.

6.2. Introduction:

Thermal cracking is the predominant failure mode for pavement sections that have been constructed in cold regions where significant air temperature drops induce stress in the pavement layers (Marasteanu et al. 2007). This type of stress, hereafter referred to as thermal stress, causes

damage, referred to as thermal damage. Once the level of damage exceeds the mixture's tolerance threshold, macrocracks begin to form in asphalt pavement sections. Moreover, significant fluctuations in the daily air temperature also lead to the accumulation of damage within pavement section sublayers and lower the pavement's capacity for resistance to cracking as the pavement ages. Both severe thermal shots and daily thermal fluctuations work together to create transverse cracks (Keshavarzi and Kim 2019). This phenomenon is not limited to cold regions. Thermal cracking often occurs in warm regions where stiff binder is used to resist permanent deformation (Alavi 2014).

Thermal cracking depends on many parameters, including the pavement's structure, the asphalt mixture properties, environmental loading, and pavement aging. Thermal cracking is considered to be top-down cracking in which the induced thermal contraction has a gradient throughout the depth of the pavement and each sublayer is restrained against movement in the longitudinal direction (Hass et al. 1987, Roque et al. 1993). The asphalt sections experience contraction and expansion when they are subjected to daily air temperature fluctuations. Cooling events cause the material to contract and, because of the long length of the pavement section (in the direction of traffic flow) and the width of the pavement section, the plane-strain condition is dominant and tension stress is induced in the pavement layers. The magnitude of the induced stress depends on the rate of the temperature drop, the current temperature, the tendency of the mixture to contract, and the mixture's stiffness.

This paper introduces a new structural framework to predict the thermal cracking performance of asphalt pavements. The proposed framework, called FlexTC, employs the simplified viscoelastic continuum damage (S-VECD) model to characterize asphalt mixture behavior at low temperatures. The use of the S-VECD model in FlexTC allows the prediction of

both fatigue cracking (top-down and bottom-up) and thermal cracking using a single set of test methods. The tests are performed using an Asphalt Mixture Performance Tester (AMPT).

The remainder of the paper is organized as follows. A review of the current literature concerning thermal cracking predictions is provided prior to introducing the proposed FlexTC. The Methodology section provides details regarding thermal loading, thermal stress, and thermal damage calculations. Eleven mixtures at different aging levels were used in this study to validate the proposed framework. The Materials and Testing section of this paper discusses the study mixtures' properties and the methodology that was used to correlate the aging duration in the field to the aging duration in the laboratory. The effects of aging on the dynamic modulus mastercurve, phase angle mastercurve, time-temperature shift factor, damage characteristic curve, and dissipated pseudo strain energy (DPSE) failure criterion are discussed in the Results section. The Results section also presents the daily thermal stress, reduced strain rate, pseudo stiffness (C), and DPSE evolution over time. The Discussion section presents the predicted fracture temperature from thermal stress restrained specimen testing (TSRST) and damage factor (DF) for studied pavement sections. The DF values are compared against the field-observed data.

6.3. Existing Thermal Cracking Prediction Models

Current frameworks for thermal cracking predictions can be categorized as either empirical or mechanistic (Marasteanu et al. 2007). Empirical models are regression equations that are based on observations of cracked field sections. These models involve the important parameters that affect the performance of asphalt sections subjected to thermal loading. For example, Fromm and Phang (1972) developed regression equations to express a thermal cracking index as a function of binder, aggregate, and base layer properties. They studied 33 pavement sections that were constructed in northern and southern Ontario, and their thermal cracking index

was later used by the Ontario Department of Transportation to help determine the severity of observed transverse cracking (Alavi 2014). Hass et al. (1987) also developed a regression equation to predict transverse crack spacing in airport asphalt pavement sections. Their model uses pavement survey data and extensive laboratory test results. Hass et al. (1987) studied 26 pavement sections throughout Canada to develop their regression equation and determined that the important parameters that affect thermal cracking are the penetration-viscosity number, thickness of the asphalt layer, minimum temperature at the site, and the mixture coefficient of thermal contraction (CTC). Hass et al. (1987) also developed empirical-based formulas based on limited loading patterns that are specific to geographical regions and material and structural properties. However, the limitations of the databases for which these empirical-based formulas were developed makes the application of empirical methodology to other geographical regions or different pavements section layouts questionable. Moreover, empirical methods are not able to capture cracking at the fundamental level (Alavi 2014).

A thermal cracking performance model, referred to as TCMModel, was developed as part of the Strategic Highway Research Program to evaluate and eventually supplement performance grade (PG) binder specifications (Hiltunen and Roque 1994). Later, TCMModel was implemented into the Mechanistic-Empirical Pavement Design Guide software (Buttlar et al. 2008). The goal of TCMModel is to predict the amount (frequency) of thermal cracking in pavement sections as a function of time. TCMModel consists of three modules: the thermal stress calculation, the crack propagation calculation, and the crack amount prediction. In the first module, the induced thermal stress is calculated as a function of time. In the second module, crack propagation is calculated based on the amplitude of the stress intensity factor for each day and the crack depth is calculated based on Paris' law. The third module uses a calibration/transfer function to

correlate crack depth to crack spacing. TCMModel predictions are based on the tensile strength of the asphalt mixture and do not account for the quasi-brittle behavior of asphalt concrete that causes a relatively large fracture process zone (FPZ) that is formed ahead of the crack tip. However, the FPZ cannot be fully addressed by Paris' law. Furthermore, TCMModel does not address the dependency of the asphalt mixture's strength, which is measured by indirect tension tests, on rate and temperature.

Another thermal cracking model was developed at the University of Illinois at Urbana-Champaign and introduced as the Illi-TC model (Dave et al. 2013). The main improvement of Illi-TC over its predecessor, TCMModel, is that it employs the cohesive zone model (CZM) for crack propagation. The CZM is able to capture the mechanisms of crack propagation more accurately than TCMModel. The IlliTC also employs three modules: (i) pre-analysis, which is designed to reduce the computational costs and selects the loading events, which are referred to as 'critical events' and impose stress that is more than 80% of the material strength, (ii) a crack propagation module that analyzes the pavement sections for ± 12 hours around the critical event, and (iii) a crack amount module that transfers the calculated crack depth to crack spacing using a probabilistic function. However, the CZM included in IlliTC cannot account for the rate and temperature dependency of asphalt concrete. In addition, IlliTC does not update the material strength, which is used in the pre-analysis to select the critical events and is measured via indirect testing, based on the updated damage magnitude. If the effect of damage on material strength is considered in the analysis, then the number of critical events may increase significantly.

Researchers at the University of Nevada, Reno developed a comprehensive model called the Thermal Cracking Analysis Package (TCAP) (Alavi 2014). TCAP includes four main

modules for the prediction of: (i) the pavement temperature profile, (ii) oxidative aging, (iii) thermal stress, and (iv) thermal cracking events. The pavement temperature module predicts the temperature distribution throughout the depth of the asphalt section and over time. The effect of oxidative aging in the second module is captured through the change in carbonyl level and is considered in the thermal stress calculation (the third module). Note that the oxidative aging model developed at Texas A&M University is implemented in the TCAP software (Alavi 2014). TCAP also is able to predict the carbonyl in asphalt binder at any depth within the asphalt layer over the analysis period (Alavi 2014). The mechanical properties of asphalt mixtures (i.e., linear viscoelasticity, the CTC, and fracture) can be estimated as a function of the carbonyl level. The third module, thermal stress predictions, involves the analysis of one-dimensional viscoelastic rods that are assumed to be restrained at both ends and subjected to given temperature variations. The fourth module, the prediction of thermal cracking, is based on passing the threshold of the mixture aging-dependent parameter. This parameter, which is called crack initiation stress, is determined from uniaxial thermal stress-strain tests and is defined as the stress level at which the tangential stiffness of the mix that is measured during the test starts to decrease. TCAP also incorporates aging evolution in its framework although it does not consider cumulative damage. In addition, the fracture properties measured in uniaxial thermal stress-strain tests vary as a function of cooling rate and initial temperature, and considerable testing is required to obtain the whole range of fracture properties. The fracture properties are tested at a very high cooling rate (i.e., -10°C/hr) in the uniaxial thermal stress-strain tests to facilitate the testing time, but the actual cooling rate in the field is much lower (Cortez et al. 2011).

6.4. FlexTC

The evaluation of different thermal cracking prediction frameworks should be based on technical and practical perspectives. On the technical side, a framework should be able to keep track of the damage induced in a pavement during its service life. In addition, it should be able to capture the rate and temperature dependency of asphalt concrete. From a practical perspective, a workable framework should not require an excessive testing effort (and thus costs) for the material characterization program that would make the framework impractical.

To this end, this paper proposes a new framework to predict the thermal cracking performance of asphalt pavements. The proposed model, called FlexTC, uses the S-VECD model to trace the damage accumulation that is due to temperature changes and to define failure using the DPSE concept. FlexTC utilizes the Enhanced Integrated Climatic Model (EICM) to predict pavement depth temperatures based on the given air temperature history. FlexTC also uses Fourier transform to calculate the daily thermal stress in pavement sections. Thermal damage is represented by the DF, which ranges from 0 to 1 to indicate intact to cracked materials, respectively.

The input material properties that are needed to run FlexTC include dynamic modulus and phase angle mastercurves that are determined by dynamic modulus tests, the damage characteristic curve and DPSE failure criterion that are determined by AMPT cyclic fatigue tests, and the CTC of the asphalt mixture. The material properties measured by the dynamic modulus and cyclic fatigue tests are used to predict fatigue cracking (both top-down and bottom-up) using FlexPAVETM, which is a three-dimensional VECD finite element program for moving load analysis (Eslaminia et al. 2012). Therefore, the only additional material property needed in FlexTC is the CTC, which can be measured or predicted using a predictive model. One of the

major strengths of FlexTC from a practical perspective is that, with the addition of the CTC, the material characterization efforts for fatigue cracking predictions can be employed also to predict thermal cracking performance. The following sections provide information about the various components of FlexTC.

6.4.1. Input Material Properties

Dynamic modulus and phase angle: The degree of the stress development is a function of CTC and material's stiffness. Researchers have studied and suggested various ways to predict mixture stiffness for a wide range of temperatures and frequencies based on different function forms (Olard and Di Benedetto 2003, Rowe and Sharrock 2011, Witczak and Fonseca 1996) or from volumetric properties (Majidifard et al. 2019). One of the challenges in using dynamic modulus in thermal cracking prediction is that the mixture dynamic modulus test commonly used by the asphalt pavement community is done at temperatures much higher than critical temperatures for thermal cracking. Therefore, extrapolation is necessary to use the dynamic modulus test results in thermal cracking prediction. Keshavarzi et al. (2019a) investigated different forms of dynamic modulus mastercurves and time-temperature shift factors and found that together the 2S2P1D function (Olard and Di Benedetto 2003) for the mixture dynamic modulus mastercurve and a second-order polynomial function for the time-temperature shift factor (Witczak and Fonseca 1996) are able to predict mixture modulus at low temperatures from dynamic modulus data determined between 4°C and 40°C. Details regarding this work are available elsewhere (Keshavarzi et al. 2019b).

Damage characteristic curve: The S-VECD model is a framework that has gained much attention due to its ability to keep track of the material's integrity (Underwood et al. 2010). The S-VECD framework is able to predict the evolution of microdamage within the material using

parameters that are measurable at the macroscale (Keshavarzi and Kim 2016). S-VECD theory, which is based on Schapery's work potential theory (Schapery 1987), which in turn was built upon thermodynamic principles, quantifies damage by defining an internal STATE variable (S). Kim and Little (1990) were the first researchers to apply Schapery's nonlinear viscoelastic theory to materials with distributed damage in order to describe the behavior of sand asphalt under controlled strain cyclic loading. Researchers later applied Kim and Little's VECD theory to describe asphalt concrete behavior under both controlled stress and controlled strain loading (Lee and Kim 1990). Also, research conducted by Daniel and Kim (2002) as part of a WesTrack project showed that the damage characteristics of asphalt concrete are independent of the mode of loading and can be determined using a simple test, i.e., the constant crosshead rate monotonic test. Findings from Lee and Kim (2008) and Daniel and Kim (2002) have extended the range of VECD theory's applications. In addition, Chehab et al. (2003) extended VECD theory further by proving that time-temperature superposition in the linear State is valid for a highly damaged State of asphalt concrete. The material property that resulted from these works is the damage characteristic curve, which describes the reduction of the material's integrity that is due to the increase in damage.

More recently, Keshavarzi and Kim (2016) were able to show that the induced stress within a representative volume element sample in a uniaxial direct tension monotonic test can be predicted by using the data measured in a uniaxial direct tension cyclic fatigue test. Keshavarzi and Kim (2019b) later measured the dissipated pseudo strain energy (DPSE) of a mixture and correlated it to the induced reduced strain rate in a uniaxial direct tension monotonic test. They were able to develop a failure criterion based on the DPSE measurements and proved that the developed methodology can predict the fracture stress and fracture temperature in TSRST.

Another significant outcome of Keshavarzi and Kim's work is that they have proven that the DPSE measured in TSRST can be predicted using the S-VECD model that is characterized by AMPT dynamic modulus and cyclic fatigue tests (Keshavarzi and Kim 2016).

CTC: The temperature variation causes asphalt mixture to contract, which in turn induces stress when the material is not free to contract. The temperature variation can be translated to induced thermal displacement through the CTC parameter. The CTC determines how much displacement is imposed on the material and, as a result, has a significant effect on the predicted thermal cracking performances of pavement sections. This research employed the methodology developed by Keshavarzi et al. (2019c) to estimate the CTC of the study mixtures.

Aging: An asphalt mixture's resistance to thermal loading, which can be determined in displacement-controlled tests, depends on the induced stress, the ability of the material to relieve the stress, and the material's resistance to tolerate the damage associated with the induced stress. Aging, which refers herein merely to the effect of the environment and includes oxidative aging, ultraviolet radiation, and steric hardening, increases the material's stiffness. As a result, aging also increases the induced stress for a given drop in temperature. Aging decreases the material's viscosity, which is expressed in change of phase angle measured by dynamic modulus tests, and the material's ductility. Thus, aging makes the asphalt mixture more prone to cracking. FlexTC benefits from findings of the National Cooperative Highway Research Program (NCHRP) Project 09-54 whereby mixtures were aged in the laboratory and the measured material properties were correlated to field data (Kim et al. 2018, Elwardany et al. 2018a).

6.5. Methodology:

6.5.1. Thermal Loading:

Hourly air temperature variations can be viewed based on hourly, daily, monthly, seasonal, and/or yearly segments. The variation of each of these segments is dependent on different rates. Fourier transform can be used to study the rate for any of these time segments and hence can help detect the relative importance of each segment. Figure 6-1 presents the magnitude of the Fourier transform of the surface temperature of a pavement constructed at the North Carolina Department of Transportation's research facility, MnROAD. Four time segments are defined for each year: (a) Segment 1 covers the daily thermal variation ranges from 0.041 Hz (= 1/24) to 1 Hz, (b) Segment 2 covers the monthly thermal variation from 0.0012 Hz (= 1/720) to 0.041 Hz, (c) Segment 3 covers the seasonal thermal variation ranges from 0.000463 Hz (= 1/2160) to 0.0012 Hz, and (d) Segment 4 covers the season-to-season variation and is expanded from 0.000114 Hz (= 1/8760) to 0.000463 Hz. Figure 6-1 also shows that the greatest magnitude belongs to the daily segment, Segment 1, which also has the greatest frequency value (0.041 Hz to 1 Hz). Based on this observation and the fact that the asphalt mixture stiffness increases based on loading frequency, then thermal stress analysis for each day is able to capture the destructive effect of the air temperature variations.

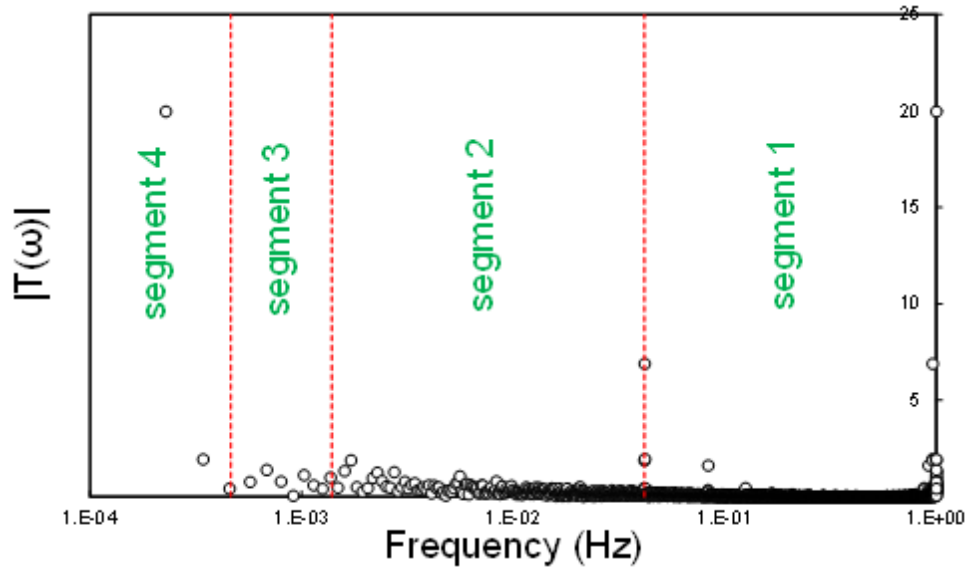


Figure 6-1. Magnitude of Fourier transform of surface temperatures for a MnROAD pavement section.

6.5.2. Structural Analysis

The response of an asphalt pavement subjected to thermal loading can be determined by assuming that the pavement in both the traffic direction (longitudinal direction) and transverse direction (width direction) is long and wide enough that the plane-strain condition is applicable. Using this assumption in FlexTC, the pavement section can be divided into sublayers that act independently, as shown in Figure 6-2.

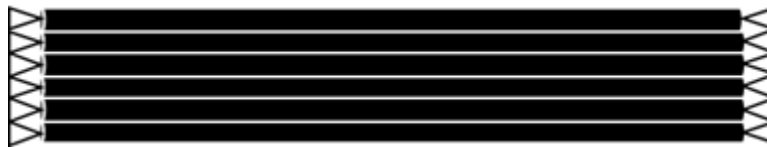


Figure 6-2. Schematic view of sublayers assumed in FlexTC

The pseudo strain-strain relationship for asphalt concrete can be expressed by Equation (6.1).

$$\varepsilon_R(\xi) = \frac{1}{E_R} \times \int_0^{\xi} E(\xi - \tau) \frac{d\varepsilon}{d\tau} d\tau$$

(6.1)

Where ε_R is the induced pseudo strain, ζ is the reduced time at which the thermal stress response is desired, τ is the integration parameter, E is the relaxation modulus in terms of the Prony series, and ε is the strain. Equation (6.2) presents the Prony series representation of the relaxation modulus.

$$E(t) = E_\infty + \sum_{j=1}^m E_j e^{-\frac{t}{\rho_j}} \quad (6.2)$$

Where E_∞ is the equilibrium modulus, and E_j and ρ_j are the elastic components and relaxation time associated with the m th Maxwell component model, respectively (Chehab and Kim 2008). The thermal strain term in Equation (6.3) comes from the induced temperature variation. Thermal strain depends on the rate of the temperature variation, the temperature at which that rate occurs, and the CTC, as expressed by Equation (6.3). FlexTC uses Equation (6.4) to consider the variation of CTC to temperature.

$$\begin{aligned} \varepsilon &= CTC \times (T - T_0) \rightarrow \\ \frac{d\varepsilon}{d\tau} &= \frac{d}{d\tau} (CTC \times (T - T_0)) \rightarrow \\ \frac{d\varepsilon}{d\tau} &= \varepsilon_r = CTC \times \frac{dT}{d\tau} = CTC \times a_T \times \frac{dT}{dt} \end{aligned} \quad (6.3)$$

Where T_0 is the equilibrium temperature, a_T is the time-temperature shift factor value, and t is the time parameter.

$$CTC = CTC_g + (CTC_l - CTC_g) \times \frac{e^{\frac{T-T_g}{R}}}{1 + e^{\frac{T-T_g}{R}}} \quad (6.4)$$

Where CTC_g and CTC_l are the coefficients of contraction below and above glassy temperature, T_g is the glassy temperature, and R is the regression constant related to the volume change. The equilibrium temperature, T_0 , is calculated based on Equation (6.5)

$$T_0 = \frac{\int_0^{\xi_{day}} T d\xi}{\xi_{day}} \quad (6.5)$$

$$a_T = \int_0^t \frac{d\zeta}{a_1 T^2(\zeta) + a_2 T(\zeta) + a_3} \quad (6.6)$$

Where a_1 , a_2 , and a_3 are the time-temperature shift factor parameters, and ζ is the time parameter. Combining Equation (6.1) and Equation (6.3) expresses the relationship of the induced pseudo strain in the sublayers to the material properties and induced temperature variation, as shown in Equation (6.7).

$$\varepsilon_R(t) = \frac{1}{E_R} \times \int_0^t E(t-\tau) \times \frac{d}{d\tau} (CTC \times (T - T_0)) d\tau \quad (6.7)$$

Each sublayer experiences some level of damage, and the magnitude of that damage must be included in the analysis framework. FlexTC uses S-VECD theory to account for the damage level in the stress calculation. Equation (6.8) presents the damage characteristic curve that is used in FlexTC to keep track of damage.

$$C = 1 - C_{11} S^{C_{12}}$$

(6.8)

Where C is pseudo stiffness and represents the material integrity, S is the internal damage parameter, and C_{11} and C_{12} are the material parameters. The pseudo stiffness varies from 1 for

the undamaged State to 0 for the failed State. The thermal stress can be expressed by Equation(6.9).

$$\sigma(t) = C \times \varepsilon_R(t) \quad (6.9)$$

The evolution of the damage parameter as a function of thermal loading can be expressed by Equation (6.10). Equation (6.10) gives a relationship that can be used to calculate the thermal stress by accounting for the current State of damage of the material.

$$\frac{dS}{dt} = \left(\frac{1}{2} \times C_{11} \times C_{12} \times S^{C_{12}-1} \right)^\alpha \left(\int_0^t E(t-\tau) \times CTC \times a_T \times \frac{dT}{d\tau} d\tau \right)^{2\alpha} \quad (6.10)$$

Equation (6.10) should be solved at the end of each day to update the damage magnitude. Solving Equation (6.7) in the time domain is a computationally expensive task. The Fourier transform technique is used to simplify the solution (Keshavarzi et al. 2019c). Fourier transform is defined here as Equation (6.11).

$$f(\omega) = \int_{-\infty}^{\infty} f(t) \times e^{-i\omega t} dt \quad (6.11)$$

Where f is the Fourier transform of a generic function, f ; and ω is the temporal frequency. Details about the application of Fourier transform can be found elsewhere (Keshavarzi et al. 2019b). Applying Fourier transform to Equation (6.7) gives Equation (6.12).

$$\varepsilon_R(\omega) = E^*(\omega) \times FT \{ CTC \times (T - T_0) \} \quad (6.12)$$

FlexTC uses the DPSE failure criterion to detect failure and calculate the DF for all the sublayers in the asphalt pavements. DPSE is defined here as Equation (6.13).

$$DPSE = \int_0^{\xi} \xi_R^2 \times (1-C) d\xi \leq a(C_0) \times \varepsilon_r^{b(C_0)} \quad (6.13)$$

Where ε_r is the reduced strain rate, shown in Equation (6.3), a and b are the material properties that depend on the current damage level (i.e., C_0). Details about the DPSE failure criterion and its dependency on damage level are available elsewhere (Keshavarzi and Kim 2019b). Finally, the thermal cracking performances of a pavement section is defined by the DF. The DF is defined as the ratio of the DPSE as a function of the current reduced strain rate to the maximum DPSE, which is defined based on the failure criterion. Figure 6-3 presents a sample calculation for defining the DF based on DPSE failure criterion methodology. In Figure 6-3, d_1 and d_2 are the cumulative DPSE, from the intact State of the material to the current State, and the available capacity of the material to tolerate damage for the same reduced strain rate, respectively.

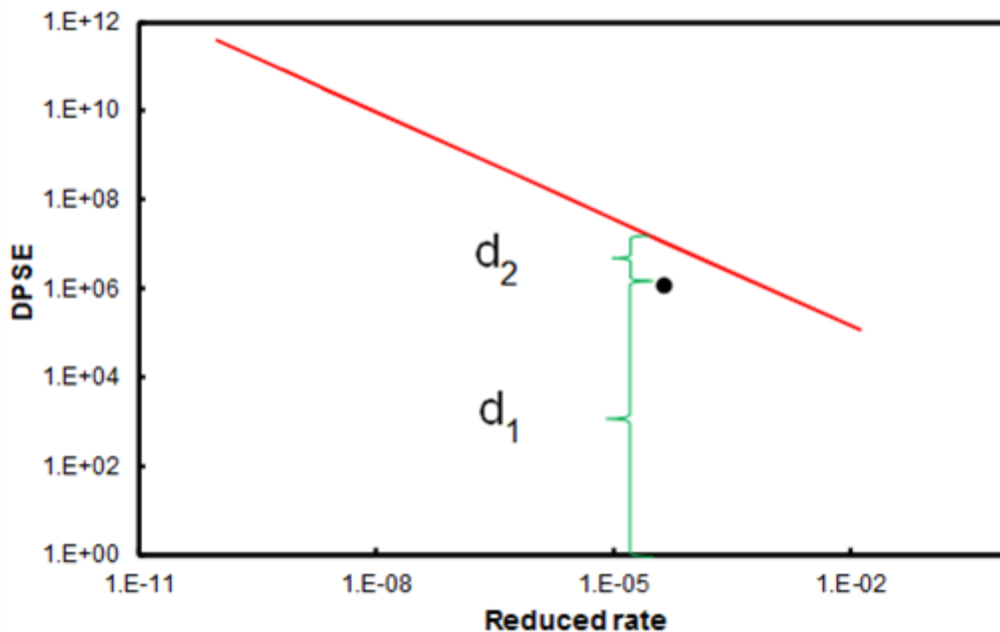


Figure 6-3. Example for defining the damage factor based on the DPSE failure criterion.

Equation (6.14) expresses the proximity of each point in the pavement section to the failure envelope in terms of the DF.

$$DF = \frac{d_1}{d_1 + d_2} \quad (6.14)$$

Thermal stress, thermal damage, reduced strain rate, and DPSE evolution are presented in the Results section of this paper. Figure 6-4 presents a schematic view of the implemented computational algorithm in FlexTC.

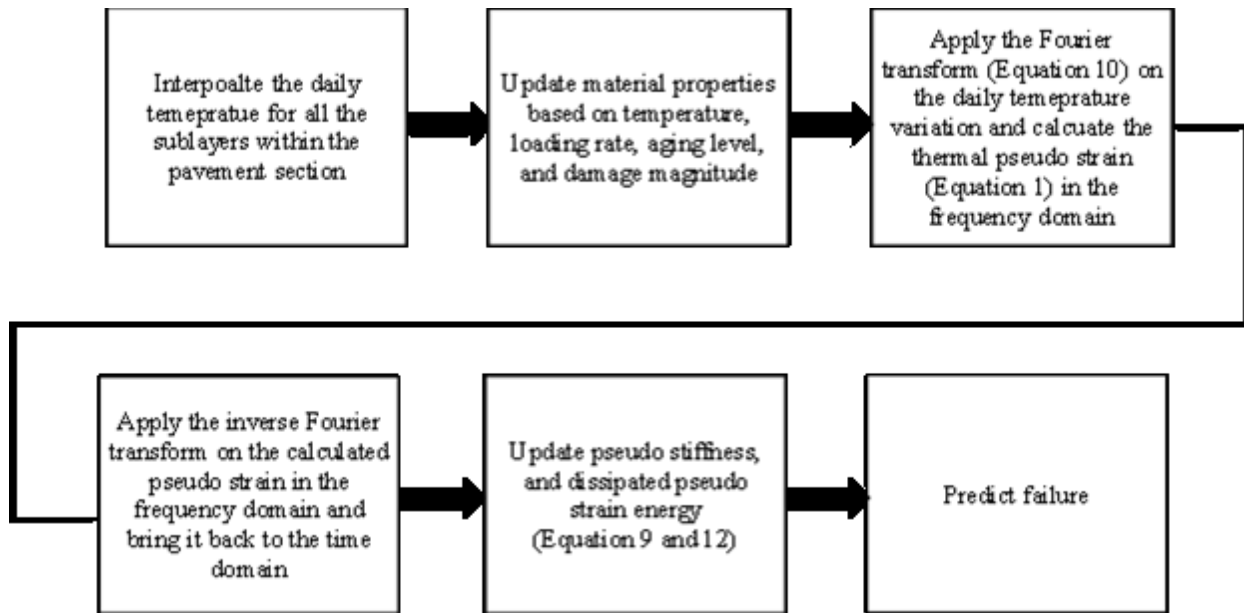


Figure 6-4. Algorithm implemented in FlexTC for calculating pseudo strain, thermal stress, pseudo stiffness, and dissipated pseudo strain energy, and detecting failure.

6.5.3. Study Pavement Sections

Figure 6-5 and Table 6.1 present a schematic view of the structures and details of the pavement sections used in this study, respectively.

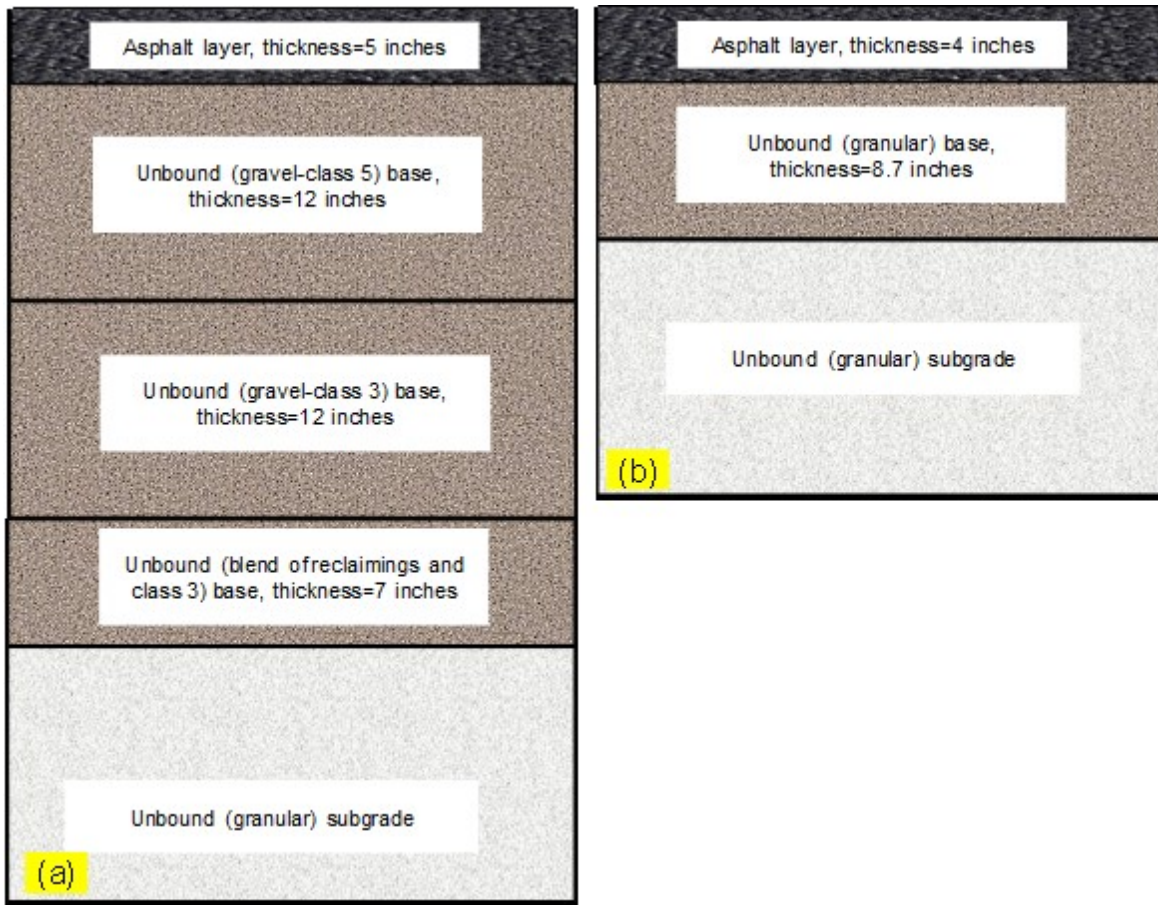


Figure 6-5. Layouts of study sections: (a) MnROAD sections and (b) North Carolina sections

Table 6.1. Details Regarding Pavement Sections Used in This Research

Section	Construction Date	First Rehabilitation/End of Life	Section Latitude (degree)	Section Longitude (degree)	Climatic Zone
MnROAD	1-Aug-08	1-Aug-10	45.261334	-93.700017	Wet, freeze
North Carolina	1-Aug-08	1-Aug-17	NA	NA	Wet, non-freeze

6.6. Materials and Test Methods

This research employed eight mixtures that were used to construct pavement sections at MnROAD. The cracking data reported for the MnROAD sections were used in this research to

verify the accuracy of the proposed procedure. In addition, three synthetic pavement sections that were made from typical surface mixtures (RS 9.5B mixtures) used in North Carolina were used in this study to further verify the accuracy of the FlexTC framework. Table 6.2 presents the study mixtures and their sources and properties.

Table 6.2. Properties of Study Mixtures

Mixture ID	Location/Source	RAP %	RAS %	NMAS (mm)	AC %	Binder Grade	Design Air Voids %
Cell 16	North Carolina	20	5	9.5	5.0	PG 64S-22	4
Cell 17	North Carolina	10	5	9.5	5.3	PG 64S-22	4
Cell 18	North Carolina	20	0	9.5	5.1	PG 64S-22	4
Cell 19	North Carolina	20	0	9.5	5.7	PG 64S-22	3
Cell 20	North Carolina	30	0	12.5	5.0	PG 52S-34	4
Cell 21	North Carolina	20	0	9.5	5.2	PG 58H-34	4
Cell 22	North Carolina	20	0	12.5	5.4	PG 58H-34	4
Cell 23	North Carolina	15	0	12.5	5.2	PG 64E-34	4
RS 9.5B 0	North Carolina	0	0	9.5	6.6	PG 64-22	4
RS 9.5B 30	North Carolina	30	0	9.5	5.8	PG 58-28	4
RS 9.5B 50	North Carolina	50	0	9.5	5.2	PG 58-28	4

Note: RAP is reclaimed asphalt pavement; RAS is recycled asphalt shingles; NMAS is nominal maximum aggregate size; AC is asphalt cement; PG is performances grade.

The ultimate goal of this research was to verify the ability of FlexTC to determine each section's performances and compare it to the expected performances. Expected performances can be estimated based on a mixture's volumetric properties. To this end, eight pairs of mixtures were selected from the MnROAD sections. Table 6.3 provides a list of these pairs and the reasons for their comparative pairings.

Table 6.3. Selected Mixture Pairs in MnROAD Sections

		Reason
Pair 1	Cell 16	Difference in RAP contents
	Cell 17	
Pair 2	Cell 17	Difference in RAP and RAS contents
	Cell 18	
Pair 3	Cell 16	Difference in RAS contents
	Cell 18	
Pair 4	Cell 18	Difference in air void contents
	Cell 19	
Pair 5	Cell 20	Difference in RAP contents
	Cell 21	
Pair 6	Cell 21	Limestone presence and difference in NMAS
	Cell 22	
Pair 7	Cell 18	Difference in binder PG
	Cell 21	
Pair 8	Cell 22	Difference in binder PG
	Cell 23	

The Standard method used for the long-term aging of asphalt mixtures for performances testing proposed by NCHRP 9-54 was followed in this study to simulate a minimum of two levels of aging: long-term aging (LTA) and short-term aging (STA) (NCHRP 09-54). This aging procedure was developed, calibrated, and validated using component materials of pavement sections that were subjected to up to 21 years of field aging (Elwardany et al. 2018b). The North Carolina mixtures were aged for different durations to create different aging levels: mild, intermediate, and high. Table 0 4 summarizes the durations for which each mixture was aged.

Table 6.4. Aging Durations for Eleven Mixtures

Mixture ID	Aging Durations in Addition to Short-Term Aging (Days)
RS9.5B 0	4, 7, 17
RS9.5B 30	2, 4, 7, 17
RS9.5B 50	4, 7, 17
Cells 16-23	3

The study mixtures were tested at each aging level to obtain their linear viscoelastic and fatigue properties. Because this aging procedure is resource-expensive, the properties were measured at only a few aging levels, and the mixture properties at the remaining aging levels of interest were interpolated from the measured properties. Each aging level (duration in days) at 95°C can be translated into field aging for a certain climate and depth of pavement. This work was accomplished using the climatic aging index (CAI), another product of NCHRP 9-54 (Elwardany et al. 2018a). The CAI is used to determine the laboratory aging duration that matches a given level of field aging at any location and pavement depth of interest using the pavement temperature hourly data obtained from the EICM, as shown in Equation (6.15). The measured material properties for the North Carolina mixtures are shown only for STA and four days of LTA in this paper. A broad set of materials from road sections across the United States and Canada was used to calibrate the CAI by determining the laboratory aging durations that matched field aging conditions at various pavement depths (Elwardany et al. 2018a).

$$t_{oven} = CAI = \sum_{i=1}^N C_1 d^{C_2} e^{\frac{C_3}{T_i}} \quad (6.15)$$

where t_{oven} is the laboratory loose mixture oven aging duration (days) at 95°C, d is the depth below the pavement surface (cm), T_i is the hourly pavement temperature (Kelvin), and C_1 ,

C_2 , and C_3 are the fitting parameters. The C_1 , C_2 , and C_3 values are 0.0437, -0.426, and -1, 60, 1.167, respectively.

6.6.1. Test Methods

Small performance test specimens, 38 mm in diameter and 110 mm in height, were fabricated using a Superpave Gyrotory Compactor according to AASHTO PP 99.

6.6.1.1. Dynamic Modulus Testing

Dynamic modulus testing at multiple temperatures and frequencies was carried out according to AASHTO TP 132. The eight study mixtures were tested at three temperatures (4°C, 20°C, and 40°C) and at six test frequencies ranging from 0.1 to 25 Hz.

6.6.1.2. AMPT Cyclic Fatigue Testing

Cyclic fatigue testing was conducted using an AMPT in accordance with AASHTO TP 133. The testing frequency was 10 Hz. Multiple tests were conducted for each mixture using different strain levels.

6.6.1.3. Correlating Measured Data to Field Conditions

The CAI can be used to correlate the duration of aging in the laboratory to realistic field conditions. The CAI varies as a function of time and depth. Table 6.5 and Table 6.6 present the CAI values for the North Carolina and North Carolina sections, respectively.

Table 6.5. Climatic Aging Index Values as Functions of Time and Depth for MnROAD Sections

North Carolina		Years				
		0	2	4	8	15
Depth (mm)	6	0	1.4	2.7	5.4	10.2
	18	0	0.8	1.7	3.3	6.2
	30	0	0.6	1.3	2.6	4.8
	42	0	0.5	1.1	2.2	4.1

Table 6.6. Climatic Aging Index Values as Functions of Time and Depth for North Carolina Sections

North Carolina		Years				
		0	2	4	8	15
Depth (mm)	6	0	2	3.9	7.9	14.8
	18	0	1.2	2.3	4.7	8.8
	30	0	0.9	1.8	3.6	6.7
	42	0	0.7	1.4	2.9	5.4

The CAI data reported in Table 6 5 and Table 6 6 were used to interpolate the mixture property measurements at different aging levels and calculate the properties at each time and pavement depth. The depth values given in Table 6 5 and Table 6 6 are the coordinates at the center of each sublayer. FlexTC uses interpolation to calculate the corresponding field data based on the laboratory measured data. Details regarding the interpolation procedure for the dynamic modulus mastercurve, damage characteristic curve, and DPSE failure criterion are as follows.

Dynamic modulus mastercurve: FlexTC selects two sets of measured data that correspond to CAI values that are lower and higher, respectively, than each specific CAI condition in the field. For example, if the CAI value for a North Carolina section after eight years at the pavement depth of 18 mm is 4.7 days, then FlexTC uses the dynamic modulus data

sets that were measured after 4 and 8 days of oven-draft aging. FlexTC interpolates the data for each frequency and temperature based on the storage modulus. The interpolated values are fitted to the 2S2P1D function to obtain fitting parameters, i.e., the 2S2P1D dynamic modulus mastercurve function parameters and time-temperature shift factor coefficients, which then are used in the thermal stress calculation.

Damage characteristic curve: The same procedure as used for dynamic modulus fitting is used to interpolate the C and S values. The power function, Equation (6.13), is used to fit the data and calculate the C_{11} and C_{12} parameters.

DPSE failure criterion: FlexTC uses the interpolated dynamic modulus mastercurve and damage characteristic curve to calculate the failure envelope. The procedure for calculating the DPSE corresponds to different initial damage levels (0.99, 0.9, 0.8, 0.7, and 0.5), and an exponential function is fitted to obtain the a and b parameters in Equation (6.13). Details about the failure detection algorithm can be found elsewhere (Keshavarzi and Kim 2019c).

6.7. Results:

6.7.1. Measured Mixture Properties:

Figure 6-6 to Figure 6-10 present the test data, which include the dynamic modulus mastercurves, phase angle mastercurves, time-temperature shift factors, and damage characteristic curves for all the tested materials at different aging levels.

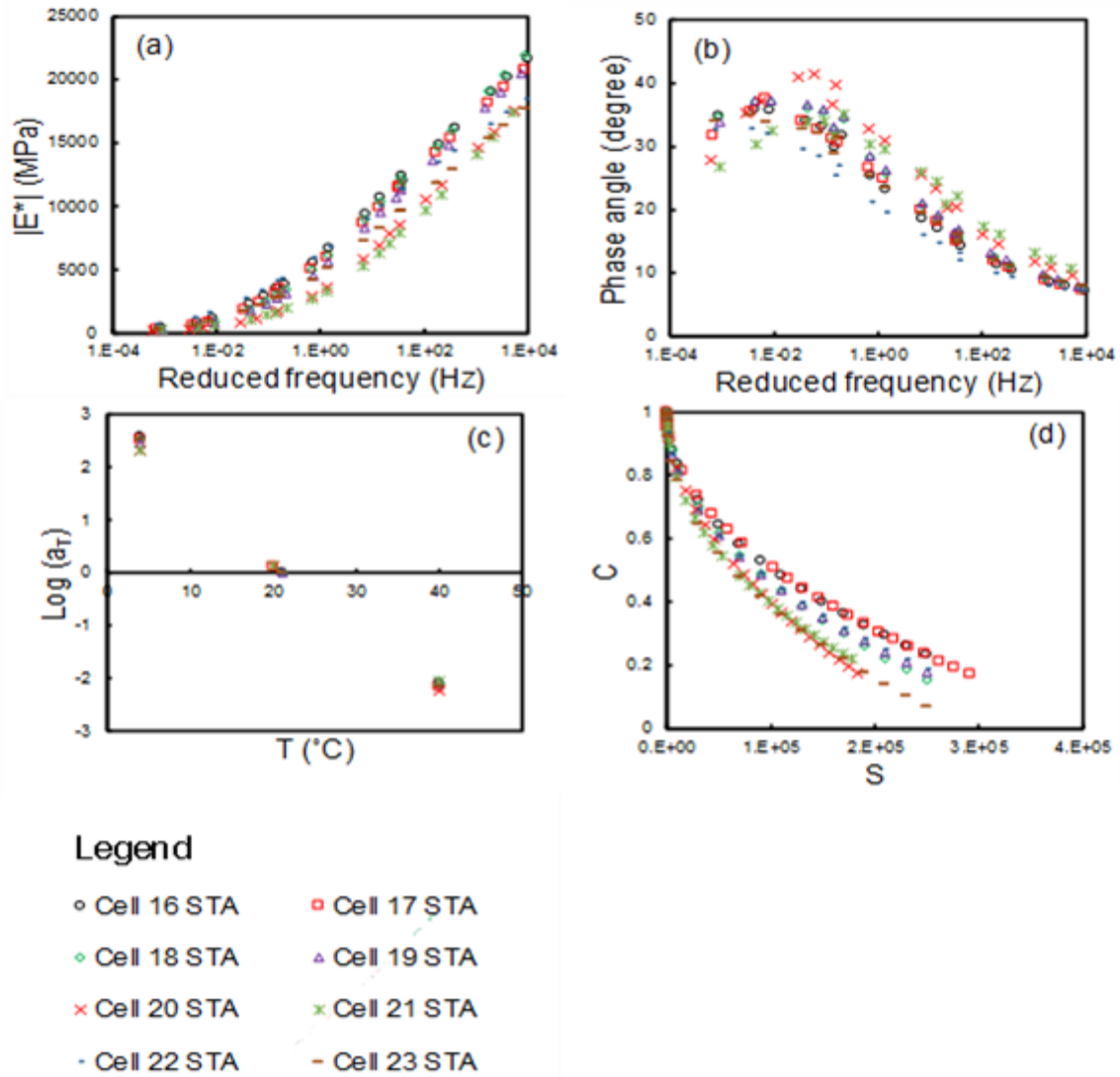


Figure 6-6. Measured material properties at short term aging (STA): (a) dynamic modulus mastercurves, (b) phase angle mastercurves, (c) time-temperature shift factors, and (d) damage characteristics for MnROAD sections.

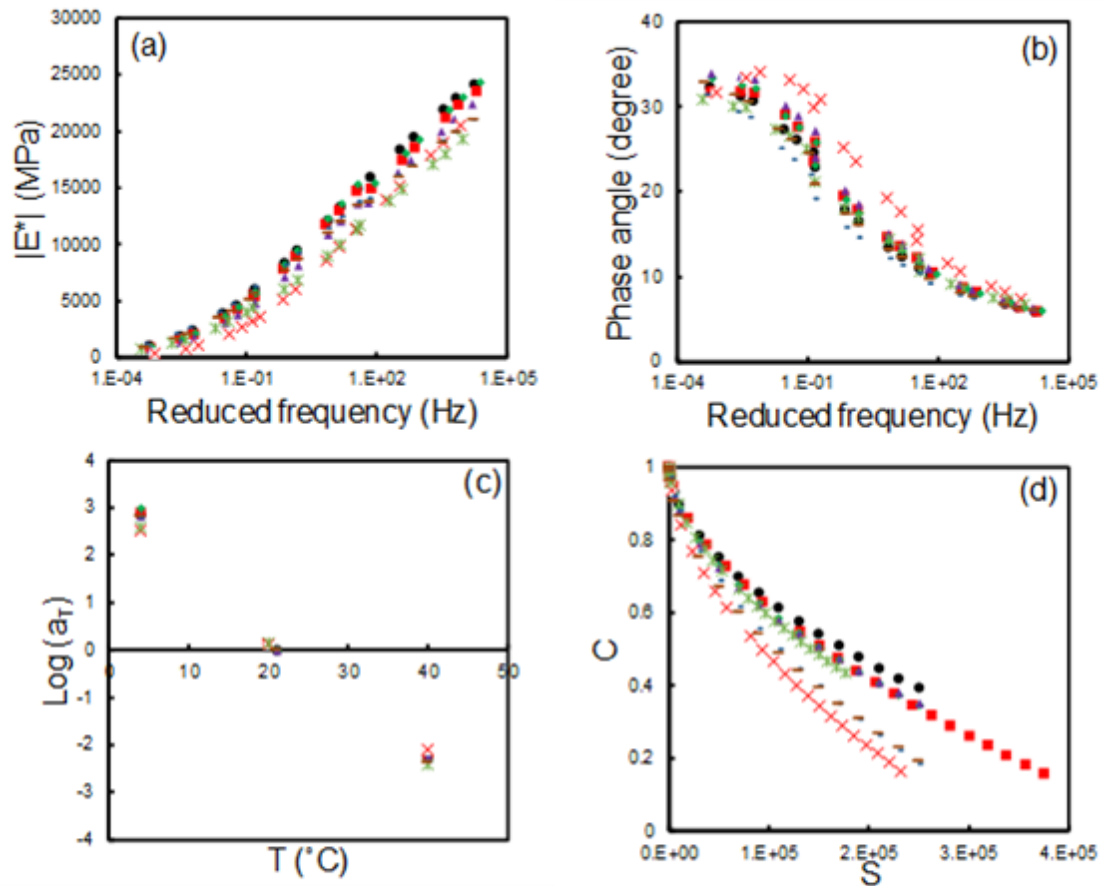
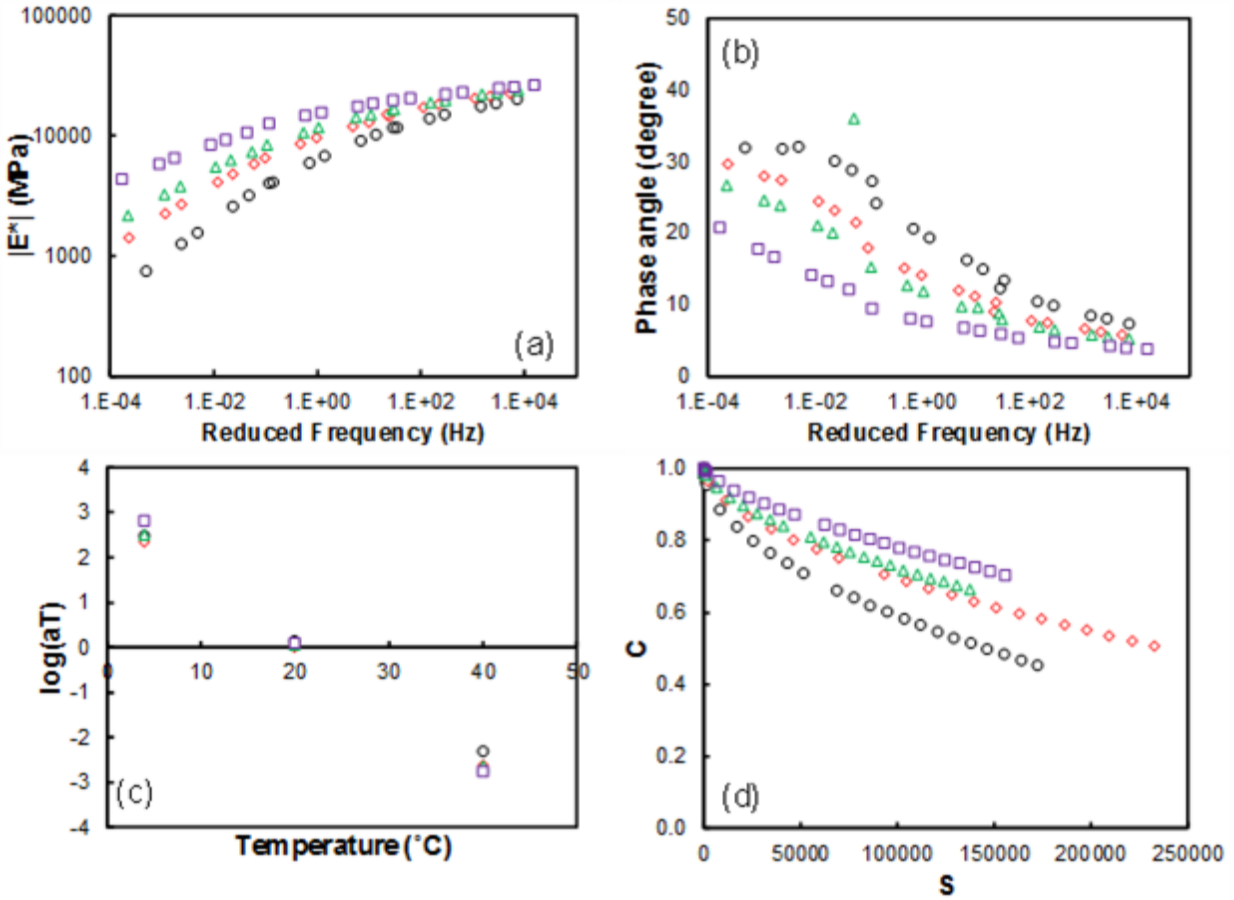


Figure 6-7. Measured material properties at long-term aging (LTA): (a) dynamic modulus mastercurves, (b) phase angle mastercurves, (c) time-temperature, and (d) damage characteristics for MnROAD sections.



Legend

- ORS 9.5B 50-STA
- ◇ RS 9.5B 50-4D
- △ RS 9.5B 50-7D
- RS 9.5B 50-17D

Figure 6-8. Measured material properties at short term aging (STA): (a) dynamic modulus mastercurves, (b) phase angle mastercurves, (c) time-temperature shift factors, and (d) damage characteristics for North Carolina sections.

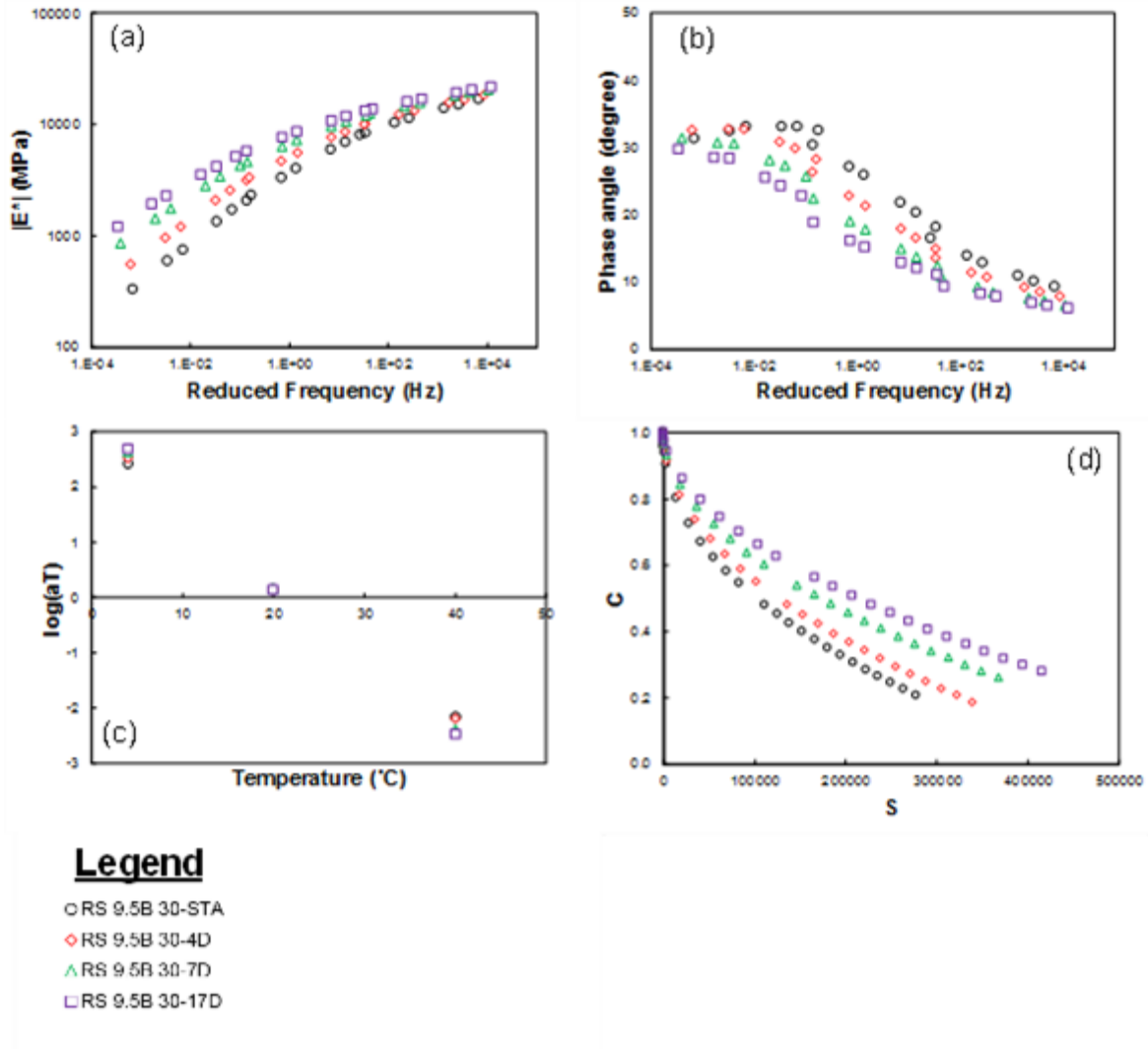
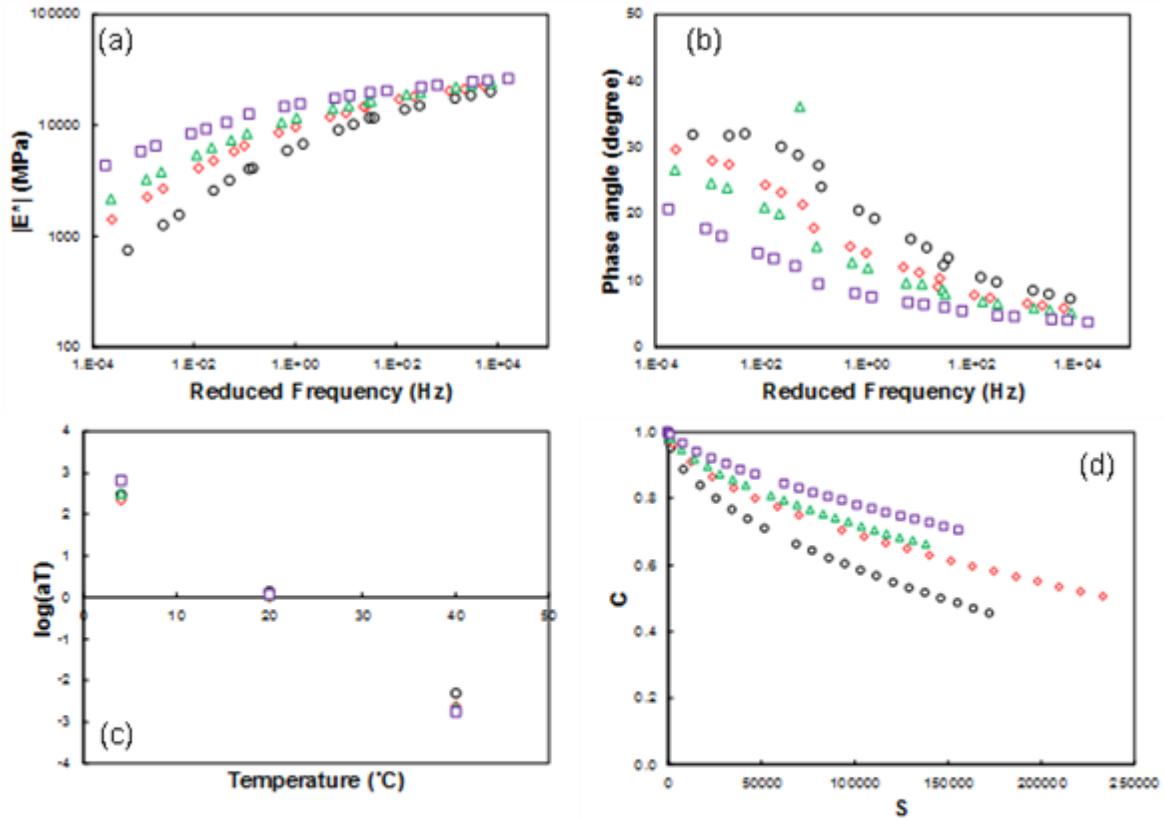


Figure 6-9. Measured material properties at long term aging (LTA): (a) dynamic modulus mastercurves, (b) phase angle mastercurves, (c) time-temperature shift factors, and (d) damage characteristics for North Carolina sections.



Legend

- ORS 9.5B 50-STA
- ◊ RS 9.5B 50-4D
- △ RS 9.5B 50-7D
- ◻ RS 9.5B 50-17D

Figure 6-10. Material properties at different aging levels for RS 9.5B 50: (a) dynamic modulus mastercurves, (b) phase angle mastercurves, (c) time-temperature shift factors, and (d) damage characteristic curves.

Figure 6-11 presents the predicted DPSE results for the tested materials under STA and LTA conditions. The DPSE failure criterion was used to determine the failure envelope for the asphalt mixtures. DPSE is a function of the initial damage level (i.e., C_0) and the aging level. Figure 6-11 shows that aging lessens the material's ductility and lowers the DPSE failure envelope.

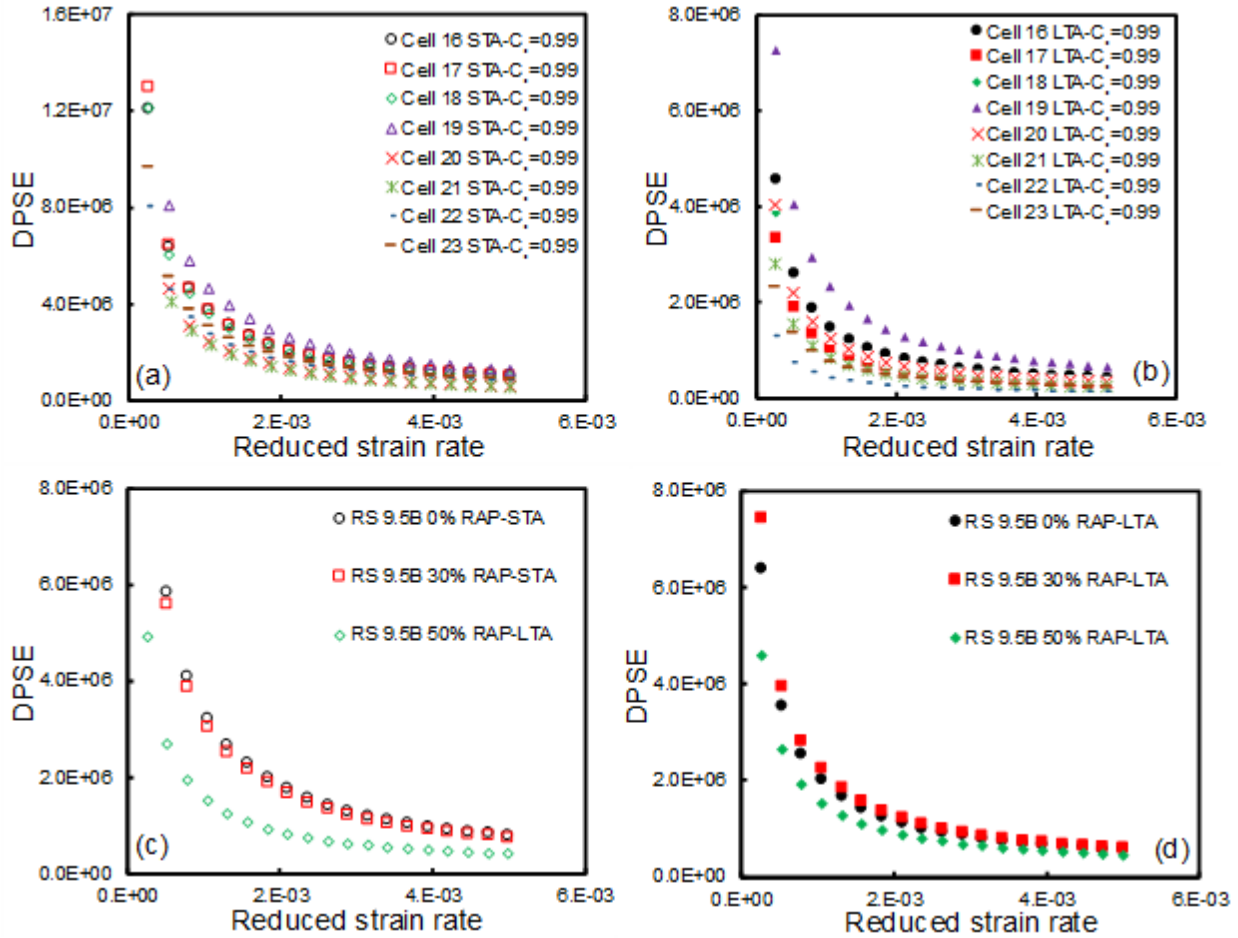


Figure 6-11. Predicted DPSE of MnROAD and North Carolina mixtures: (a) DPSE at STA for MnROAD mixtures, (b) DPSE at LTA for MnROAD mixtures, (c) DPSE at STA for North Carolina mixtures, and (d) DPSE at LTA for North Carolina mixtures.

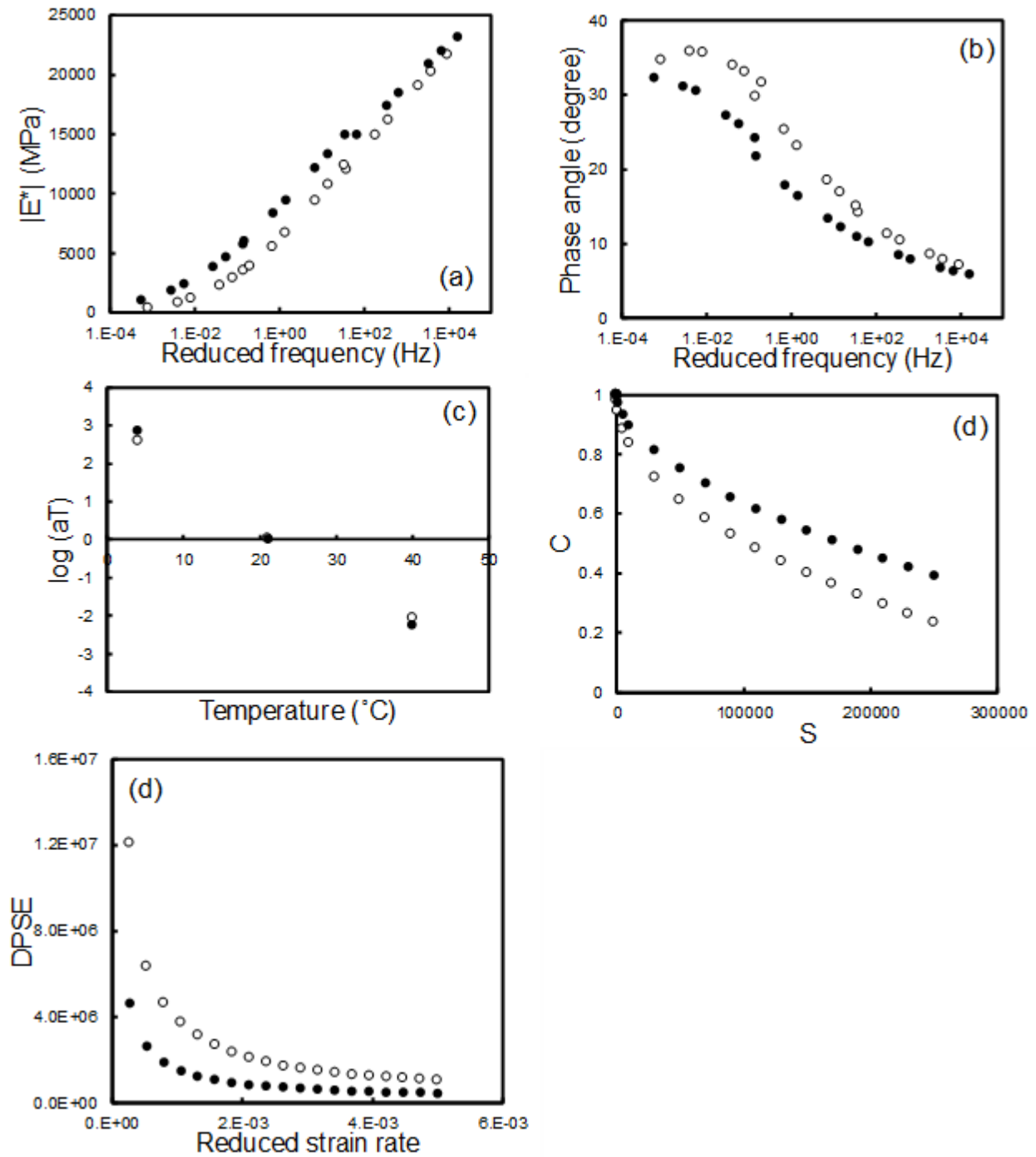


Figure 6-12. Comparisons between measured and predicted material properties under STA (open circles) and LTA (filled circles) for Cell 16: (a) measured dynamic modulus mastercurves, (b) measured phase angle mastercurves, (c) measured time-temperature shift factors, (d) measured damage characteristic curves, and (e) predicted DPSE values.

Figure 6-12 presents comparisons of the measured material properties between STA and LTA conditions for the Cell 16 mixture. A significant increase is evident in the dynamic modulus values when the aging duration is increased, as shown in Figure 6-12 (a). The phase angle, on the other hand, drops when the age level increases, as shown in Figure 6-12 (b). The time-temperature shift factor determines the reduced strain rate that is applied to the material. As is evident from Figure 6-12 (c), aging causes an increase in the time-temperature shift factor at lower temperatures. This phenomenon makes the applied reduced rate (Equation(6.3)) higher for aged materials and makes them more susceptible to cracking. The damage characteristic curves, which indicate the level of accumulated damage under fatigue loading, show an upward shift with aging, as shown in Figure 6-12 (d). For the same value of C, the STA curve shows less accumulated damage than the LTA curves. These trends are expected because the damage characteristic curves of stiffer materials tend to be located higher in the graph than the curves of softer materials. Figure 6-12 (e) present the comparison of predicted DPSE failure criterion as aging level increases from STA to LTA condition. As it is apparent from Figure 6-12 (e), aging decreases the tolerable dissipated pseudo strain energy of asphalt mixtures for a wide range of frequency.

6.8. Structural Simulation Results

The procedure described in the Methodology section was used to calculate the thermal stress and thermal damage, update the DPSE, detect failure, and calculate the DF. Figure 6-13 presents the induced thermal stress results at different pavement depths for one of the pavement sections (RS9.5B 0%) that was constructed in North Carolina. Figure 6-13 shows that the thermal stress decreases as the pavement depth increases. This trend derives from the fact that lower layers of asphalt experience lower levels of temperature variation. Figure 6-14 presents the

thermal damage in the same pavement section. As shown, the top surface experiences more damage (lower C value) than the lower layers. Figure 6-14 (a) shows that, at lower pavement depths, the C value increases and the material experiences less damage than nearer the surface. Figure 6-14 (b) presents the DPSE evolution and shows that less damage is experienced in the asphalt layers located at the bottom of the section compared to layers nearer the surface. This outcome is due to the fact that the top layers of an asphalt pavement section are exposed to air temperature variations and thus experience more damage than deeper layers.

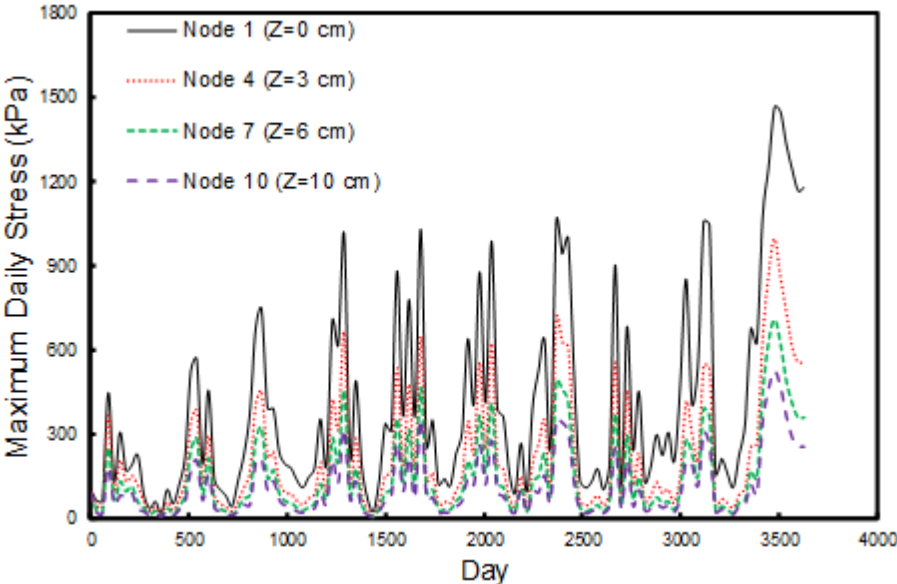


Figure 6-13. Maximum induced daily thermal stress as a function of pavement depth and day for a synthetic section located in North Carolina (RS 9.5B 0%RAP).

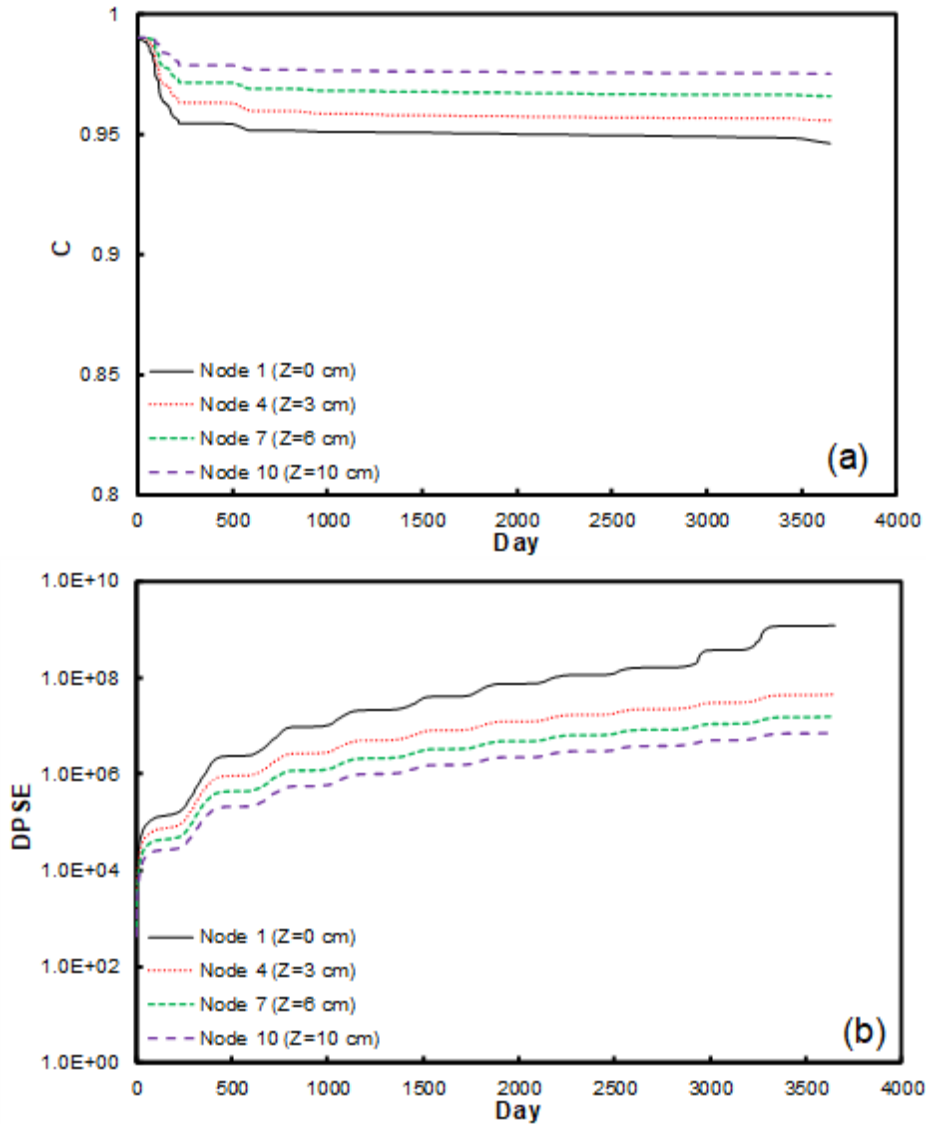


Figure 6-14. Evolution of thermal damage-related parameters as function of time and pavement depth for a pavement section constructed in North Carolina (RS 9.5B 0%RAP): (a) pseudo stiffness (C) evolution vs. time (day) for different nodes and (b) DPSE evolution vs. time (day) for different nodes in terms of pavement depth.

Figure 6-15 presents the daily thermal stress and temperature variations. Three regions can be defined in the Figure: Region 1 corresponds to the beginning of the day when the air temperature and, correspondingly, the surface temperature drops gradually. As a result, the thermal stress increases and reaches its highest magnitude at 7:00 AM. Region 2 corresponds to the time of day when the air temperature and surface temperature increase. As result, the thermal

stress starts to decrease. Region 3 corresponds to the end of the day when the pavement Starts to cool down and the thermal stress begins to increase.

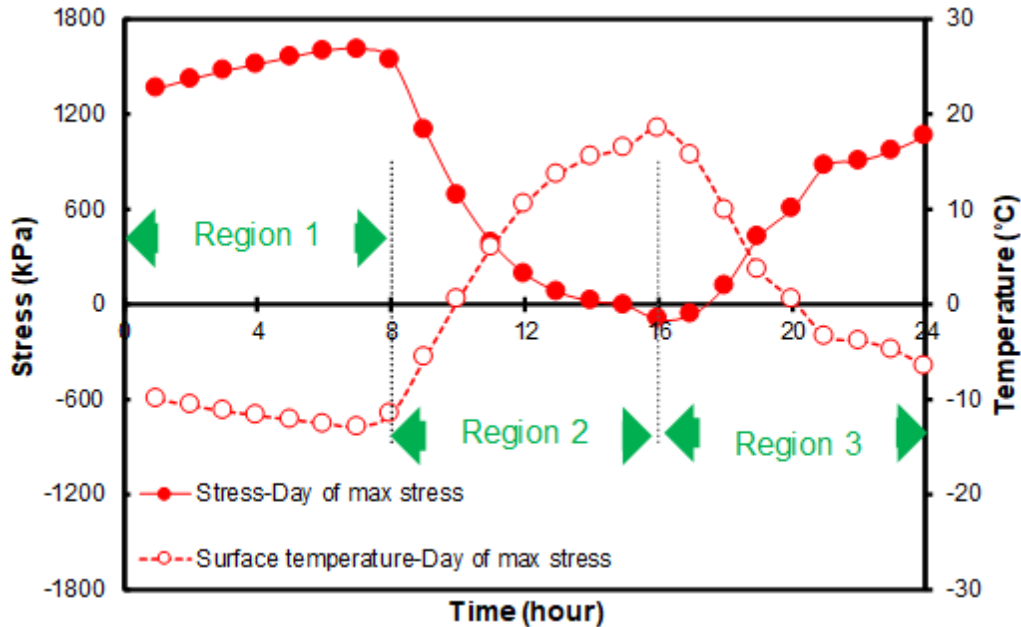


Figure 6-15. Thermal stress and temperature variations for the day at which maximum stress occurs at the pavement surface.

Figure 6-16 presents the daily thermal stress and temperature variations. Three regions can be defined in this figure:

1. Region 1 corresponds to the beginning of the day when the air temperature and, correspondingly, the surface temperature drops gradually. As a result, the thermal stress increases and reaches its highest magnitude at 7:00 AM.
2. Region 2 corresponds to the time of day when the air temperature and surface temperature increase. As a result, the thermal stress Starts to decrease.
3. Region 3 corresponds to the end of the day when the pavement Starts to cool down and the thermal stress begins to increase.

The induced thermal stress, defined as Equation (6.9), depends on the reduced strain rate, defined in Equation (6.3). For the sake of clarification, the day at which the maximum stress occurs and the history of the temperature and corresponding reduced strain rate for that day in addition to ± 24 hours of that day can provide clues for this phenomenon. Figure 6-16 presents the temperature and reduced strain rate for the day of maximum thermal stress and ± 24 hours of that day. As shown, three regions also are defined here. According to Figure 6-16, the day during which the maximum thermal stress occurs also shows the maximum reduced strain rate and minimum temperature.

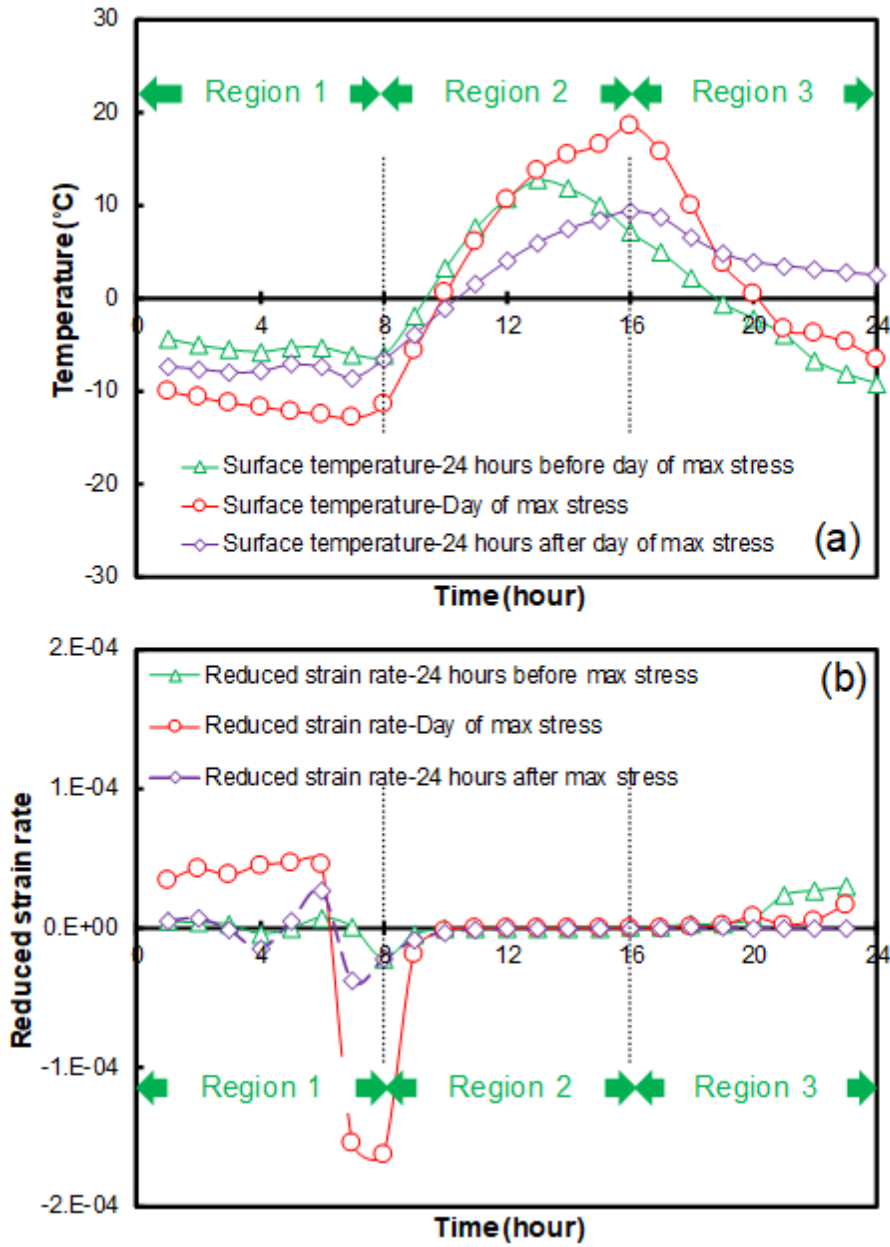


Figure 6-16. Temperature and reduced strain rate evolution as a function of time for surface of the section and for day of maximum thermal stress and ± 24 hours of that day: (a) temperature distribution and (b) reduced strain rate.

Once the daily thermal stress variation and reduced strain rate are known, the DPSE can be calculated versus time. Once the DPSE, expressed as a function of reduced strain rate, passes the failure criterion, failure can be detected.

Equation (6.16) expresses the proximity of each point in the pavement section to the failure envelope in terms of the DF.

$$DF = \frac{d_1}{d_1 + d_2} \quad (6.16)$$

With the definition of DF based on Equation (6.16) in hand, the maximum experienced damage can be used to evaluate the effect of thermal loading on the pavement sections.

6.9. Predicted Fracture Temperature in TSRST:

Figure 6-17 presents the predicted fracture temperature for the mixtures used in this study. As it can be seen from Figure 6-17, aging has a significant effect on the predicted fracture temperature of asphalt mixtures studied in this study.

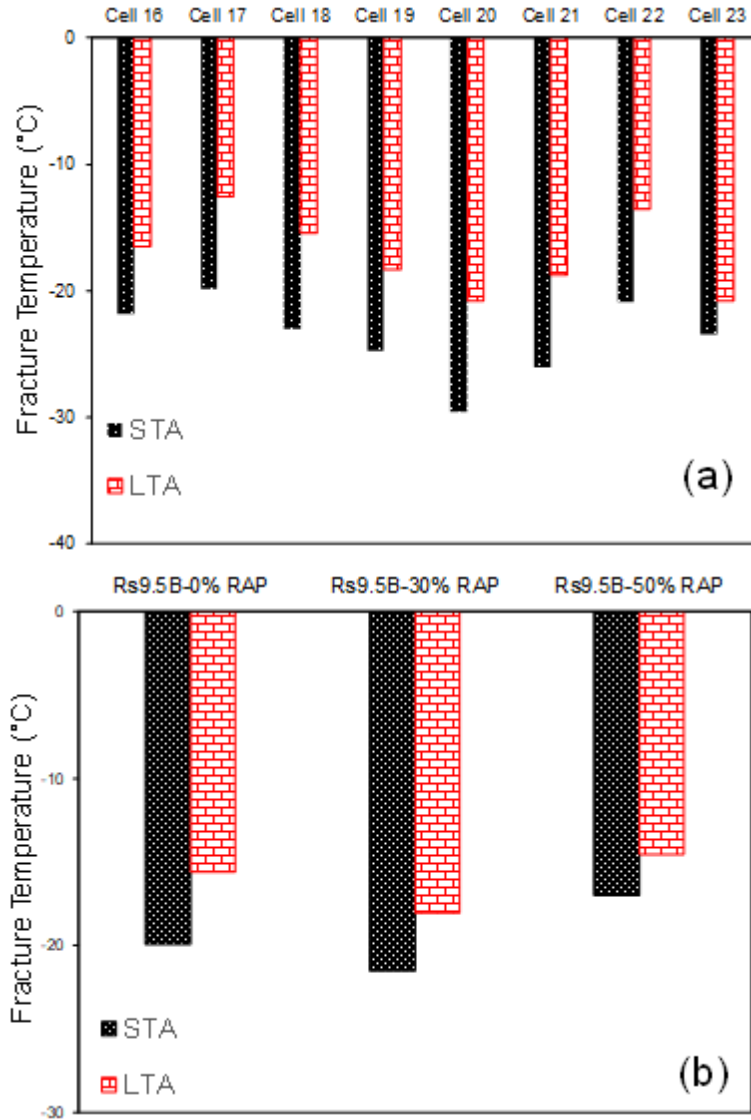


Figure 6-17. Predicted fracture temperature for mixtures studied in this study: (a) MnROAD section's materials and (b) North Carolina mixtures

6.10. Predicted Maximum Experienced DF

Figure 6-18 presents the maximum *DF* for each point in the MnROAD pavement sections as a function of depth. The cells in the legend are arranged based on field performance, where Cell 20 shows the best performance and Cell 17 shows the worst.

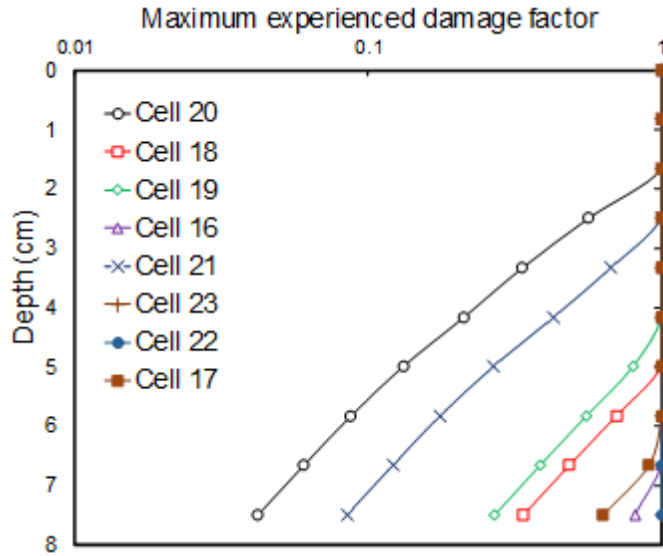


Figure 6-18. Maximum experienced damage as a function of depth for eight cells constructed in Phase III of MnROAD test facility.

Figure 6-19 presents a comparison of the *DFs* of the three North Carolina synthetic pavement sections. As shown, the ranking based on the *DF* is compatible with the ranking for the predicted fracture temperatures for the TSRST.

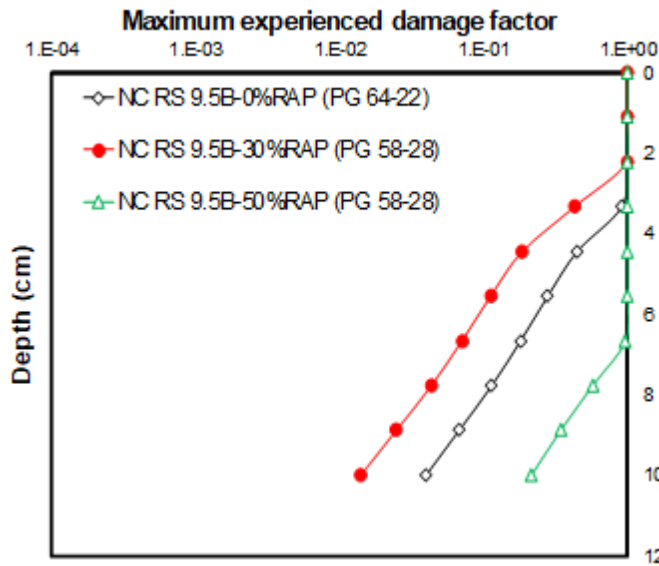


Figure 6-19. Maximum experienced damage as a function of depth for three synthetic sections constructed in North Carolina.

6.11. Discussion of Results

A DF value of 1.0 represents failed or cracked material. As shown in Figure 6-19, the NC RS 9.5B 0%RAP and NC RS 9.5B 30% RAP sections have the same predicted crack depth (around 2 cm deep) but the magnitudes of the DF are different for the points located below the crack. In addition, Cells 20 and 21 in Figure 6-18 have approximately the same depth of cracks but different DF distributions below the cracks. These two observations indicate that the DF is a more sensitive criterion for predicting the performance of asphalt sections subjected to thermal loading than crack depth.

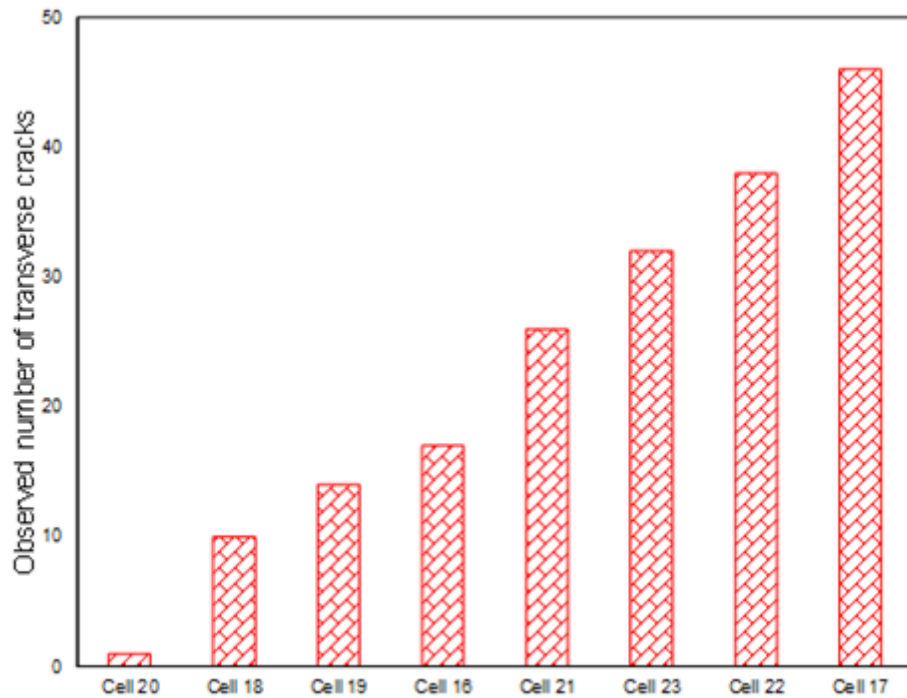


Figure 6-20. Number of transverse cracks based on field survey data for MnROAD sections.

Figure 6-20 presents the observed field data for the MnROAD sections. Figure 6-20 shows that Cell 20 exhibited the best performance (fewest number of cracks) and Cell 17 exhibited the worst performance (most cracks). The DF distribution shown in Figure 6-18 suggests that Cell 17 has a considerably higher DF at each sublayer compared to Cell 20. Further

verification can be made by pairing the MnROAD mixtures and comparing the rankings based on expectations derived from the volumetric properties (Table 6.2), field data (Figure 6-20), predicted TSRST results (Figure 6-17), and DFs (Figure 6-18).

Table 6.7 presents the comparative study results for the MnROAD sections in which a tick mark indicates the better performance of the pair for these parameters. Table 6.7 also shows that the rankings predicted by FlexTC match expectations for all the pairs. Pair 1 consists of two mixtures that have different RAP contents. Cell 17 has the higher RAP content and, as expected, its performance suffered due to that higher RAP content. This expectation is not in line with the field ranking, but FlexTC was able to capture that discrepancy. The field cores indicated that Cell 17 suffered from delamination at the interface of two construction lifts, even in the areas outside the wheel path. The presence of delamination may have slowed the propagation of transverse cracks and, as a result, Cell 17 shows fewer transverse cracks. The TSRST ranking follows the FlexTC ranking. As shown in Table 6.7, FlexTC is able to follow the field ranking, expected ranking, and TSRST ranking for Pairs 2, 4, 5, and 6. Pair 3 was intended to be used to investigate the effects of air void content. Pair 3 is expected to exhibit better performance when the air void content is reduced, whereas the field data do not follow this expectation. In this case, the rankings obtained from TSRST and FlexTC match expectations. The field core data show that Cell 18 experienced some delamination at the interface of two construction lifts for areas outside the wheel path. The presence of delamination reduced the relative stiffness of the untracked asphalt layer and hindered transverse cracking propagation.

Pair 8 was intended to be used to investigate the effects of the binder PG on the performance of the constructed section. Pair 8 is expected to exhibit better performance when the low PG is decreased from -22 (PG 64S-22 in Cell 18) to -34 (PG 58H-34 in Cell 21). In this case,

whereas the FlexTC and TSRST rankings follow the expected trend, the field data do not. As mentioned, Cell 18 experienced delamination at the interface of construction lifts. The presence of delamination makes the comparison of the cells' performance difficult.

The reason (or reasons) that the field observations does not follow the expected trends for Pairs 3 and 8 is unclear. Note that both pairs include Cell 18. The better-than-expected performance of Cell 18 seems to have affected the rankings of Pairs 3 and 7. MnDOT will continue monitoring the performance of the MnROAD sections. As more condition survey data become available, they will be used to evaluate the Fleck's ability to predict the thermal cracking performance of asphalt pavements.

Table 6.7. Comparisons of Expected Data, Field Survey Data, Predicted Fracture Temperatures, and FlexTC Rankings for MnROAD Pavement Sections

Pair Number	Target Cells	Expected	Field	Predicted TSRST	FlexTC
1	16		✓	✓	
	17	✓			✓
2	17				
	18	✓	✓	✓	✓
3	18		✓		
	19	✓		✓	✓
4	16				
	18	✓	✓	✓	✓
5	21	✓	✓	✓	✓
	22				
6	22				
	23	✓	✓	✓	✓
7	18		✓		
	21	✓		✓	✓

6.12. Conclusion

This paper presents a new structural framework, FlexTC, for predicting the performance of asphalt pavements subjected to thermal loading. FlexTC considers daily thermal variations

and the aging evolution over time and depth. FlexTC also updates the material properties after each daily thermal loading. FlexTC uses the DF parameter to express the damage level for each sublayer in the pavement sections. Eight sections from two different areas of the United States were used to verify the accuracy of FlexTC. The FlexTC rankings agree with the predicted fracture temperatures obtained from TSRST. Also, the results show that the rankings that are based on predicted DFs from FlexTC match the expected trends based on engineering intuition in all cases and match the field observations for most cases.

REFERENCES

- Akentuna, M. Laboratory Investigation of Low-Temperature Performance of Asphalt Mixtures, PhD dissertation, *Ohio University*, 2017.
- Alavi, M.Z. Comprehensive Methodologies for Analysis of Thermal Cracking in Asphalt Concrete Pavements, PhD dissertation, *University of Nevada*, Reno, 2014.
- Bahia, H., Tabatabaee, H., and Velasquez, R., 2012. Asphalt Thermal Cracking Analyser (ATCA), *7th RILEM International Conference on Cracking in Pavements*, 4, pp. 147–156.
- Bahia, H.U. and Anderson, D.A., 1993. Glass Transition Behavior And Physical Hardening Of Asphalt Binders (With Discussion), " *Proceedings of the Association of Asphalt Paving Technologists*, 62, 93–129.
- Barker, J.B., Authority, T., Biehler, A.D., Dot, P., Brown, L.L., Dot, M., Clark, W.A. V, Angeles, L., Ekern, D.S., and Dot, V., 2008. Calibration And Validation Of The Enhanced Integrated Climatic Model For Pavement Design, *National Cooperative Highway Research Program (NCHRP)*, Report 602.
- Bodin, D. G., Pijaudier, C., Roche, C., Piau, J. M., Chabot, A., 2004. Continuum Damage Approach To Asphalt Concrete Fatigue Modeling, *Journal of Engineering Mechanics*, 130, pp. 700-708.
- Cao, W., Norouzi, A., Kim Y.R., 2016. Application Of Viscoelastic Continuum Damage Approach To Predict Fatigue Performance Of Binzhou Perpetual Pavements, *Journal of Traffic and Transportation Engineering (English Edition)*, 3, pp. 104-115.
- Castorena, C., Kim, Y.R., Pape, S., Lee, K, L., 2017. Development Of Small Specimen Geometry For Asphalt Mixture Performance Testing, *National Cooperative Highway Research Program (NCHRP)*, Project 181.
- Chehab, G.R., 2002. Characterization Of Asphalt Concrete In Tension Using A Viscoelastoplastic Model, North Carolina State University, PhD dissertation.
- Christensen, D.W., and Bonaquist, R., 2015. Improved Hirsch Model for Estimating the Modulus of Hot Mix Asphalt, *Road Materials and Pavement Design*, 16 (sup 2), pp. 254–274.
- Daniel, J.S., Bennert, T., Kim, Y. R., Mogawer, W., Congalton, A., Menshing, D., Sabouri, M., ElwardaNY, M., 2014. Evaluation of Plant Produced RAP Mixtures in the Northeast: Phase I interim report, TPF 5 (230).
- Dave, E. V, Buttlar, W.G., Leon, S.E., Behnia, B., Paulino, G.H., 2013. Illitic – Low-Temperature Cracking Model For Asphalt Pavements, *Road Materials and Pavement Design*, 14 (sup 2), pp. 57–78, 2013.

Donal W. Christense, R.B., 2003. Ternary Property Maps For Asphalt CoNcrete", *Journal of the Association of Asphalt Paving Technologists*, 72, pp. 38–73.

Eslaminia, M., Guddati, M.N., 2016. Fourier-Finite Element Analysis Of Pavements Under Moving Vehicular Loading, *International Journal of Pavement Engineering*, 17 (7), pp. 602–614.

Eslaminia, M., Thirunavukkarasu, S., Guddati, M.N., Kim, Y.R., 2012. Accelerated Pavement PerformaNce Modeling Using Layered Viscoelastic Analysis, *7th RILEM International ConfereNce on Cracking in Pavements*, 4, pp. 497–506.

Ghanbari, A., Underwood, B, S., and Kim, Y. R., 2019. Development Of Rutting Index Parameter Based On Stress Sweep Rutting And Permannet Deformation Shift Model, *International Journal of Pavement Engineering*, under review.

Gilan, Siamak., Mashadi Ali, A., and Ramezaniapour, A., 2011. Evolutionary fuzzy function with support vector regression for the prediction of coNcrete compressive strength, *Computer Modeling and Simulation (EMS), Fifth UKSim European Symposium on IEEE*.

Huang, Y. H., 2003. Pavement Analysis and Design, 2nd edition, Prentice Hall, *Englewood Cliffs*.

MyeRS, L.A., 2000. Development And Propagation Of Surface - Initiated Longitudinal Wheel Path Cracks In Flexible Highway Pavements, *UniveRSity of Florida, PhD dissertation*, 2000.

Roque, R., Zou, J., Kim, Y.R., Baek, C., Thirunavukkarasu, S., Underwood, B.S., Guddati, M., 2010, Top-Down Cracking Of Hot-Mix Asphalt LayerS: Models For Initiation And Propagation, *National Coopearative Highway Research Program (NCHRP)*, Report 1-42A.

Sakhaeifar, M., Underwood, B. S., Ranjithan, S. R., Kim, Y.R., Jackson, N., 2009, Application Of Artificial Neural Networks For Estimating Dynamic Modulus Of Asphalt CoNcrete, *Transportation Research Record: Journal of the Transportation Research Board*, (2127), pp. 173–186.

Finn, F., Saraf, C.L., Kulkarni, R., Nair, K., SMITH, W., Abdullah, A., 1977. User's Manual For The Computer Program Cold.

Fromm, H. J, Phang, W.A., 1972, A Study Of TransveRSe Cracking Of Bituminous Pavements, *Proceedings of the Association of Asphalt Paving Technologists*, 41, pp. 383–423.

Jones, G. M., Darter, M. I., 1968, Thermal Expansion-Contraction Of Asphaltic CoNcrete, *Journal of the Association of Asphalt Paving Technologists*, 37, pp. 56–97.

Han, T, S., Ural, A., Chen, C, S., Zehnder, A., Ingraffea, A., Billington, S., 2002, Delamination Buckling And Propagation Analysis Of Honeycomb Panels Using A Cohesive Element Approach, *International Journal of Fracture*, 115 (2), pp. 101–123.

- Hass, R., Meyer, F., Assaf, G., Lee, H., 1987, A Comprehensive Study Of Cold Climate Airport Pavement Cracking, *Association of Asphalt Paving Technologists* (AAPT), 56, pp. 198–245.
- Hills, J.F., Brien, D., 1966. The Fracture Of Bitumens And Asphalt Mixes By Temperature Induced Stresses, *Proceedings, the Association of Asphalt Paving Technologists*, 35, pp. 292–309.
- Hiltunen, D.R., Roque, R., 1994. A Mechanics-Based Prediction Model For Thermal Cracking Of Asphaltic CoNcReTe Pavements, *Journal of the Association of Asphalt Paving Technologists*, 63, pp. 81–117.
- Huet, C., 1963. Etude par une méthode d'impédance du comportement viscoélastique des matériaux hydrocarbonés.
- Islam, M.R., and Tarefder, R, A., 2014. Determining Thermal Properties Of Asphalt CoNcReTe Using Field Data And Laboratory Testing, *Construction and Building Materials*, 67, pp. 297–306.
- Jahangiri, B., Majidifard, H., Meister, J., Buttlar, W., 2019. Performance Evaluation Of Asphalt Mixtures With Reclaimed Asphalt Pavement And Recycled Asphalt Shingles In Missouri, *Transportation Research Record*, 2673 (2), pp. 392–403.
- Jung, D, H., Vinson, T,S., 1994. Low-Temperature Cracking: Test Selection, *Strategic Highway Research Program* (SHRP) A-400, 1994.
- Kandiyoti, R., Herod, A, A., 2006. Arrhenius Equation. A-to-Z Guide to Thermodynamics, *Heat and Mass Transfer, and Fluids Engineering*. Available from: http://iehmtu.edata-center.com/toc/chapt_a/ch01s148.html.
- Kennedy, T, W., Cominsky, R.J., Harrigan, E. T., Leahy, R, B., 1990. The SHRP Asphalt Research Program : 1990 Strategic Planning Document, Report No. UWP-90-007.
- Keshavarzi, B., Bakhshi, A., 2013. A New Approach For Consideration Of Earthquake Low Cycle Fatigue Phenomena On Reinforced Concrete Frames, 15th World Conference on Earthquake Engineering, Lisbon, Portugal.
- Keshavarzi, B., Ghanbari, A., Kim, Y.R., 2019a. Extrapolation of dynamic modulus data for asphalt concrete at low temperatures, *Road Materials and Pavement Design*, under review.
- Keshavarzi, B. and Kim, Y., 2019b. Investigation Into Fatigue Damage Growth Direction In Asphalt Concrete Pavement Sections Based On Simplified Viscoelastic Continuum Damage (S-VECD) Theory". *International Journal of Pavement Engineering*, under review.
- Keshavarzi, B., Kim, Y.R., 2016. A Viscoelastic-Based Model For Predicting The Strength Of Asphalt Concrete In Direct Tension, *Construction and Building Materials*, 122, pp. 721–727.

- Keshavarzi, B., Mocelin, D., Kim, Y.R., 2019c. A Composite Model For Predicting The Coefficient Of Thermal Contraction (CTC) Of Asphalt CoNcReTe Mixtures, *Mechanics Of Time Dependent Materials*, under review, 2019c.
- Keshavarzi, B., Mocelin, D., Saleh, N., Kim, Y.R., 2019d. FlexTC-Thermal Cracking Analysis Framework For Asphalt CoNcReTe Pavement Sections, *International Journal of Pavement Engineering*, under review.
- Kim, S., Wargo, A., PowerS, D., 2010. Asphalt CoNcReTe Cracking Device To Evaluate Low Temperature PerformaNcE Of HMA.", *Association of Asphalt Paving Technologists (AAPT)*, 79, pp. 157–188.
- Kim, Y.R., 2008. Modeling of Asphalt Cocnrete, *American Society of Civil EngineeRS*.
- Kim, Y.R., Castorena, C., ElwardaNY, M., Underwood, B.S., Gundla, A., Gudipudi, P., Farrar, M.J., Glaser, R.R., 2018. Long-Term Aging of Asphalt Mixtures for PerformaNcE Testing and Prediction, National Cooperative Highway Research Program (NCHRP), Project 09-54.
- Kreyszig, E., 2010. AdvaNCed Engineering Mathematics, *JOHN WILEY & SONS, INC*.
- Lytton, R. L., Pugahl, D. E., Michalak, C. H., Liang, H. S., Dempsey, B. J., 1993. An Integrated Model of the Climatic Effects on Pavements, *Federal Highway Administration*, Report No. FHWA-RD-90-033.
- Majidifard, H., Tabatabaee, N., Buttlar, W., 2019a. Investigation Short-Term Binder PerformaNcE Of High-RAP Mixtures Containing Waste Cooking Oil, *Journal of Traffic and Transportation Engineering (English Edition)*, Vol. 6(4), pp. 396-406.
- Majidifard, H., Jahangiri, B., Buttlar, W, G., Alavi, A, H., 2019b. New Machine Learning-Based Prediction Models For Fracture Energy Of Asphalt Mixtures, *Measurment*, 135, pp. 438–451, 2019b.
- Marasteanu, M., Li, X., Clyne, T., Voller, V., Timm, D., Newcomb, D., 2004. Low Temperature Cracking Of Asphalt CoNcReTe Pavements, *North Carolina Department of Transportation*, Report No. MN/ RC-2004-23.
- Marasteanu, M., Zofka, A., Turos, M., Li, X., Velasquez, R., Li, X., Buttlar, W., Paulino, G., Braham, A., Dave, E., Ojo, J., Bahia, H., Williams, C., Bausano, J., Gallistel, A., McGraw, J., 2012. Investigation Of Low Temperature Cracking In Asphalt Pavements Phase II, North Carolina Department of Transportation, Research Project, Report No. 2012-23.
- Mashadi Ali, A. An Integrated Framework for Assessing the Dynamics of Population Growth and Climate Change for Urban Water Resources Managment. MSc dissertation. *North Carolina STAte UniveRSity*, 2014.
- Mehta, Y.A., Chrislensen, D.W., Stoffels, S.M., 1999. Determination Of Coefficient Of Thermal Contraction Of Asphalt CoNcReTe Using Indirect Tensile Test, *Journal of Association of Asphalt Paving Technologists*, 68 (814), pp. 349–368.

- Mensingh, D.J., Rahbar-Rastegar, R., Underwood, B.S., Daniel, J.S., 2016. Identifying Indicators For Fatigue Cracking In Hot-Mix Asphalt Pavements Using Viscoelastic Continuum Damage Principles, *Transportation Research Record: Journal of the Transportation Research Board*, vol. 2576, pp. 28–39.
- Norouzi, A., Sabouri, M., Kim, Y. R., 2015. Evaluation Of The Fatigue Performance Of High RAP Asphalt Mixtures, *International Journal of Pavement Engineering*, 17, pp. 1-17.
- Norouzi, A, Sabouri, M, Kim Y.R., 2017. Fatigue Life And Endurance Limit Prediction Of Asphalt Mixtures Using Energy-Based Failure Criterion, *International Journal of Pavement Engineering*, 18(11), pp. 1-14.
- Sefidmazgi, N. R., Tashman, L. Bahia, H., 2012. Internal Structure Characterization Of Asphalt Mixtures For Rutting Performance Using Imaging Analysis, *Road Materials and Pavement Design*, 13 (sup 1), pp. 21-37.
- Rahbar-rastegar, R., Dave, E. V., Daniel, J.S., Fatigue And Thermal Cracking Analysis Of Asphalt Mixtures Using Continuum-Damage And Cohesive-Zone Models, *Journal of Transportation Engineering, Part B: Pavements*, 144(4), pp. 1–11.
- Rahbar-rastegar, R., Daniel, J. S., Reinke, G., 2017. Comparison Of Asphalt Binder And Mixture Cracking Parameters, *Road Materials and Pavement Design*, 18 (sup 4), pp. 211-233.
- Rashidi, M., Mazari, M., and Saghafi, M., 2019. Multivariate Global Sensitivity Analysis Of Rocking Responses Of Shallow Foundations Under Controlled Rocking, *International Conference on Case Histories in Geotechnical Engineering*, Geo-congress.
- Rashidi, M., Saghafi, M., and Takhtfirrozeh, H., 2018. Genetic Programming Model For Estimation Of Settlement In Earth Dams, *International Journal of Geotechnical Engineering*, 1-10.
- Saghafi, M., Asgharzadeh, S. M. M., Fathi, A., and Hosseini, A., 2019a. Image Processing Method To Estimate The Wearing Condition Of Slurry Seal Mixtures, *Transportation and Development Institute (T&DI), International Airfield and Highway Pavements Conference, Chicago, USA*.
- Saghafi, M., Tabatabaee, N., and Nazarian, S., 2019b. Performance Evaluation Of Slurry Seals Containing Reclaimed Asphalt Pavement, *Transportation Research Record: Journal of the Transportation Research Board*.
- Roy, Y.A. Dodds, Jr., R.H., 2001. Simulation Of Ductile Crack Growth In Thin Aluminum Panels Using 3-D Surface Cohesive Elements, *International Journal of Fracture*, 110, pp. 21–45.
- Sabouri, M., 2014. Development Of A Unified Fatigue Failure Criterion For Asphalt Mixtures And Its Applications To Reclaimed Asphalt Pavement (RAP) Mixtures, North Carolina State University, PhD dissertation.

Sabouri, M., Daniel, J.S., Kim, Y.R., 2015. A Comprehensive Evaluation Of The Fatigue Behavior Of Plant-Produced RAP Mixtures, *Road Materials and Pavement Design*, vol. 16 (sup 2), 29-54.

Schapery, R., 1987. Deformation And Fracture Characterization Of Inelastic Composite Materials Using Potentials, *Polymer Engineering and Science*, 27, pp. 63–75.

Schapery, R.A., 1984. Correspondence Principles And A Generalized J-Integral For Large Deformation And Fracture Analysis Of Viscoelastic Media, *International Journal of Fracture*, 25, pp. 195–223

Song, S, H., Paulino, G. H., Buttlar, W, G., 2006. A Bilinear Cohesive Zone Model Tailored For Fracture Of Asphalt Concrete Considering Viscoelastic Bulk Material, *Engineering Fracture Mechanics*, 73 (18), pp. 2829-2848.

Tabatabaee, H.A., Velasquez, R., Bahia, H.U., 2012. Modeling Thermal Stress In Asphalt Mixtures Undergoing Glass Transition And Physical Hardening, *Transportation Research Record: Journal of the Transportation Research Board*, 2296 (1), pp. 106-114.

Teymourpour, P. Bahia, H.U., 2014. Effects Of Binder Modification On Aggregate Structure And Thermovolumetric Properties Of Asphalt Mixtures, *Transportation Research Record: Journal of Transportation Research Board*, 2445 (1), pp. 21-28.

Timm, D.H., Guzina, B.B., 2003. Prediction Of Thermal Crack Spacing, *International Journal of Solids and Structures*, 40, pp. 125–142.

Underwood, B.S., Kim, Y.R., 2011. Experimental Investigation Into The Multiscale Behaviour Of Asphalt Concrete, *International Journal of Pavement Engineering*, 12, pp. 357–370.

Underwood, B.S., Kim, Y.R., 2012. Comprehensive Evaluation Of Small Strain Viscoelastic Behavior Of Asphalt Concrete, *Journal of Testing and Evaluation*, 40 (4), pp. 622–632.

Underwood, B.S., Kim, Y.R., Guddati, M. N., 2010. Improved Calculation Method Of Damage Parameter In Viscoelastic Continuum Damage Model, *International Journal of Pavement Engineering*, 11 (6), pp. 459–476.

Valikhani, A., Jahromi, A., and Azizinamini, A., 2018. Experimental Investigation Of High-Performing Protective Shell Used For Retrofitting Bridge Elements, No. 18-05142.

Valikhani, A., Jahromi, A., Azizinamini, A., 2017. Retrofitting Damaged Bridge Elements Using Thin Ultra High Performance Shell Elements, No. 17-02047.

Velasquez, R., Bahia, H., 2013. Critical Factors Affecting Thermal Cracking Of Asphalt Pavements: Towards A Comprehensive Specification, *Road Materials and Pavement Design*, vol. 14, pp. 187–200.

Wang, Y. D., Ghanbari, A., Underwood, B. S., and Kim, Y. R., 2018. Development of a Performance-Volumetric Relationship for Asphalt Mixtures", *Transportation Research Record*, 2673 (6), pp. 416-430.

Williams, M.L., Landel, R.F., Ferry, J.D., 1955. The Temperature Dependence of Relaxation Mechanisms in Amorphous Polymers and other Glass-forming Liquids". *Journal of the American Chemical Society*, 77 (14), pp. 3701–3707.

Witczak, M., Fonseca, O., 1996. Revised Predictive Model for Dynamic (Complex) Modulus of Asphalt Mixtures, *Transportation Research Record*, 1540 (1), pp. 15–23.

Yin, H.M., Buttlar, W.G., Paulino, G.H., 2007. Simplified Solution for Periodic Thermal Discontinuities in Asphalt Overlays Bonded to Rigid Pavements, *Journal of Transportation Engineering*, 133 (1), pp. 39–46.

Yoo, P., Al-Qadi, I., Elseifi, M., Janajreh, I., 2006. Flexible Pavement Responses to Different Loading Amplitudes Considering Layer Interface Condition and Lateral Shear Forces, *International Journal of Pavement Engineering*, 7 (1), pp. 73–86.

Young, J.F., Mindess, S., Bentur, A., Gray, R.J., 1998. The Science and Technology of Civil Engineering Materials, *Prentice Hall*.

Zhang, J., Sabouri, M., Guddati, M. N., Kim, Y. R., 2014. Development of a Failure Criterion for Asphalt Mixtures under Fatigue Loading, *Road Materials and Pavement Design*, 14, pp. 1-15.

Zhu, Y., Dave, E. V., Rahbar-Rastegar, R., Daniel, J.S., and Zofka, A., 2017. Comprehensive Evaluation of Low-Temperature Fracture Indices for Asphalt Mixtures, *Road Materials and Pavement Design*, 18, pp. 467–490.

APPENDICES

APPENDIX A. APPLYING NON-UNIFORM FOURIER FINITE METHOD IN ANALYZING ASPHALT CONCRETE PAVEMENTS

A.1. Abstract:

This paper proposes an efficient algorithm for applying non-uniform Fourier transform to analyze asphalt pavements. The methodology decreases the required number of frequencies in a Fourier transform framework, leading to significant savings in computational effort. In the first step of the proposed method, several frequencies are selected based on geometric gradation to interpolate the linear viscoelastic properties of asphalt concrete. In the second step, the frequency response function (FRF) is interpolated to other intermediate frequencies that are necessary to accurately capture the Fourier transform of the load with large rest periods. The sparse frequency grid used for the computationally expensive FRF computation leads to large savings in computational effort, leading to efficient analysis of pavement systems. The accuracy of the proposed methodology is verified at the material level (analysis of representative volume elements) and at the structural level (analysis of pavements).

A.2. Introduction

Stress-strain analysis is an important component of mechanistic-empirical pavement design and pavement life predictions. Predicting asphalt pavement performance requires two tools: a material-level framework and a structural analysis framework. Using these tools, a computational framework can predict asphalt concrete behavior and help pavement engineers gain a better understanding of design scenarios throughout the life of the pavement (Eslaminia and Guddati 2015).

The candidate analysis algorithm that is selected to predict pavement performance should be able to consider the effects of realistic loading conditions, such as moving loads (Keshavarzi

and Kim 2019f), loading time-to-rest period ratio on pavement performance. For example, moving load analysis is important to simulate the bending behavior of asphalt layers under loading that is critical for bottom-up and top-down cracking predictions. Bottom-up fatigue cracking is associated mainly with induced bending at the bottom of asphalt layers under moving loads (Roque et al. 2010, Myers 2000). Top-down cracking, however, is associated with the bending-induced tension at the surface of the pavement away from the tire, which constitutes a negative bending mechanism (You et al. 2006). Thus, analysis of asphalt pavements under moving loads is necessary in order to investigate this negative bending mechanism. The other aforementioned loading conditions (loading time-to-rest period ratio and mixed traffic spectra) have similarly complex effects that also must be addressed by the candidate analysis algorithm.

The incorporation of realistic loading conditions in pavement response and performance analyses is possible, but imposes a huge computational cost, especially when the time-dependent viscoelastic nature of asphalt concrete is addressed in a rigorous manner. In order to remedy this shortcoming, North Carolina State University (NCSU) researchers developed layered viscoelastic pavement analysis for critical distress software (formerly known as LVECD software and now trademarked as FlexPAVETM 1.1). The FlexPAVETM 1.1 software uses numerical algorithms to capture both the viscoelastic nature of asphalt concrete as well as applied moving loads in three-dimensional analysis. FlexPAVETM 1.1 uses simplified viscoelastic continuum damage (S-VECD) theory to predict pavement cracking performance. An overview of S-VECD literature can be found elsewhere (Keshavarzi and Kim 2016). FlexPAVETM 1.1 reduces the pavement structure analysis from three-dimensional analysis to one-dimensional analysis using the Fourier finite element concept, which clearly has the effect of reducing the final computational cost (Eslaminia et al. 2012).

In this study, a geometrical progression approach that requires fewer frequencies was adopted to reduce the computational time of FlexPAVETM 1.1 even further. The main motivation behind this approach is that the dynamic modulus of asphalt concrete, which is a function of loading frequency and temperature and can be expressed in mastercurve format by using the time-temperature superposition principle, reaches its asymptotic value at very high and very low reduced frequencies (Keshavarzi et al. 2019c, Majidifard et al. 2019). This behavior facilitates the use of non-uniform frequency increments to perform Fourier transform. This study used one section at the National Center for Asphalt Technology (NCAT) test track, which is representative of a region with intermediate to high-level temperature, and one section from the New York Infrastructure Technology (MIT) testing facility, which is representative of a cold-temperature region, to verify the validity and accuracy of the proposed methodology. The details of dynamic modulus testing and results are reported elsewhere (Norouzi et al. 2017, Rahbar-Rastegar et al. 2017). FlexPAVETM 1.1 assumes linear elastic modulus for base and subgrade. More details on the nonlinear behavior of unbounded materials can be found elsewhere (Rashidi et al., 2019, Rashidi et al., 2018, Saghafi et al., 2019a, Saghafi et al., 2019b).

A.3. Preliminaries: Fourier finite Element and the Associated Computational Cost

Layered viscoelastic analysis is able to capture the viscoelastic behavior of asphalt concrete; however, long computing time in time domain makes this approach impractical for the long-term performance prediction of asphalt pavement by State highway agencies and contractors. The Fourier transform technique reduces the computing time significantly and makes layered viscoelastic moving load analysis more feasible for routine pavement analysis. The Fourier transform in time and space transforms layered viscoelastic analysis to a one-dimensional problem for each of the selected frequencies. It is applicable to one as well as three-

dimensional problems (Eslaminia et al. 2012). The details of the material response in one-dimensional loading as well as structural analysis procedure for three-dimensional loading condition are discussed below.

A.3.1. Uniaxial Analysis

The stress-strain relation in the uniaxial direction can be expressed by Equation (A.1).

$$\sigma(t) = \int_0^t E(t-\tau) \frac{d\varepsilon}{d\tau} d\tau \quad (\text{A.1})$$

Where $\sigma(t)$ is developed stress, $E(t)$ is relaxation modulus in term of Prony series, and ε is the strain. Equation (A.2) presents the Prony series representation of the relaxation modulus.

$$E(t) = E_\infty + \sum_{j=1}^m E_j e^{-\frac{t}{\rho_j}} \quad (\text{A.2})$$

Where E_∞ is the equilibrium modulus, E_j and ρ_j are the elastic components and relaxation time associated with the m-th Maxwell component model (Kim 2009). Performing the integration in the time-domain requires large computational cost. One way to reduce the computational cost is to employ Fourier transform. The following definition of Fourier transform is employed in this paper (Equation (A.3)) (Kreyszig 2010).

$$f(\omega) = \int_{-\infty}^{\infty} f(t) e^{-i\omega t} dt$$

(A.3)

Where f the Fourier is transform of a generic function f ; and is the temporal frequency.

Applying the Fourier transform on Equation (A.1) will give Equation (A.4)

$$\sigma = E\varepsilon \quad (\text{A.4})$$

Where σ , E , and ε denotes the stress, modulus, and strain values in the frequency domain respectively. The maximum frequency for which the response should be calculated can be obtained from Equation(A.5).

$$\omega_{\max} = \frac{2\pi}{dt} \quad (\text{A.5})$$

Where dt denotes the increment size in the time domain. The increment in the frequency domain can be calculated from Equation

$$d\omega = \frac{2\pi}{t_{\max}} \quad (\text{A.6})$$

Where t_{\max} is the duration of traffic loading including both time and resting time. The material response can be calculated in the frequency domain by having: (a) the loading for different frequencies, (b) (complex) dynamic modulus in the frequency domain, and (c) the maximum and the increment values of frequency. It should be noted that the relaxation modulus can be decomposed into two real parts: (a) real (or storage modulus) which is shown by E' , and (b) imaginary (or loss modulus) which is shown by E'' (Equation).

$$\begin{aligned} E^*(\omega) &= E'(\omega) + iE''(\omega) \\ E'(\omega) &= E_{\infty} + \sum_{j=1}^m \frac{\omega^2 E_j \rho_j^2}{1 + \omega^2 \rho_j^2} \\ E''(\omega) &= \sum_{j=1}^m \frac{\omega E_j \rho_j}{1 + \omega^2 \rho_j^2} \end{aligned} \quad (\text{A.7})$$

A.3.2. Three-dimensional Analysis

Pavement structural analysis involves all the three spatial dimensions. For viscoelastic material, the constitutive relation should reflect the time dependency of material. The spatial coordinates are represented as x , y , and z , where x represents the direction perpendicular to traffic, the y represents the traffic direction, and the z denotes the depth direction. The strain-displacement relation can be expressed by Equation (A.8) in the time domain.

$$\boldsymbol{\varepsilon} = \left[\varepsilon_{xx} \quad \varepsilon_{yy} \quad \varepsilon_{zz} \quad \gamma_{yz} \quad \gamma_{zx} \quad \gamma_{xy} \right]^T = \begin{bmatrix} \frac{\partial}{\partial x} & 0 & 0 \\ 0 & \frac{\partial}{\partial y} & 0 \\ 0 & 0 & \frac{\partial}{\partial z} \\ 0 & \frac{\partial}{\partial z} & \frac{\partial}{\partial y} \\ \frac{\partial}{\partial z} & 0 & \frac{\partial}{\partial y} \\ \frac{\partial}{\partial y} & \frac{\partial}{\partial x} & 0 \end{bmatrix} \begin{Bmatrix} u_x \\ u_y \\ u_z \end{Bmatrix} = B\mathbf{u} \quad (\text{A.8})$$

Where $\boldsymbol{\varepsilon}$ vector is the strain vector, \mathbf{u} is the displacement vector, and B is the strain-displacement matrix. The stress-strain relation can be expressed by Equation (A.9).

$$\boldsymbol{\sigma} = \left[\sigma_{xx} \quad \sigma_{yy} \quad \sigma_{zz} \quad \sigma_{yz} \quad \sigma_{zx} \quad \sigma_{xy} \right]^T = \int_0^t \mathbf{C}(t-\tau) \frac{d\boldsymbol{\varepsilon}}{d\tau} d\tau \quad (\text{A.9})$$

Where C contains the material constitutive relations and explained elsewhere (Keshavarzi and Kim 2019f). Equilibrium equation can be expressed through Equation(A.10).

$$\mathbf{B}^T \boldsymbol{\sigma} = \mathbf{f} \quad (\text{A.10})$$

In three-dimensional analysis, the Fourier transform can be defined as follow (Equation(A.11)).

$$f(\omega, k_x, k_y) = \int_{-\infty}^{\infty} \int_{-\infty}^{\infty} \int_{-\infty}^{\infty} f(t, x, y) e^{-ik_y y} e^{-ik_x x} e^{-i\omega t} dy dx dt \quad (\text{A.11})$$

Where k_x and k_y are spatial frequencies. Applying Fourier transform on Equation (A.1) will lead to Equation (A1.28).

$$\sigma = i\omega C(\omega) \varepsilon \quad (\text{A.12})$$

Although the application of Fourier transform in pavement analysis is able to reduce the computational cost associated with the three-dimensional analysis of moving load, it still requires a considerable computational resource when it comes to large rest to pulse ratio and analyzing the pavement sections response to traffic spectra. This problem may get worse when stress distribution associated with damage is considered. Motivated by this observation, a novel computation algorithm to reduce the computational cost is developed and presented below.

A.4. The Algorithm of Fourier-based Structural Analysis

As evident from Figure A-1, the computational effort is directly proportional to the number of frequencies for which the analysis is performed, which depends on the spectrum of the load as well as the time dependent material properties of the constituent materials and the pavement geometry. In the context of pavement analysis, it turns out that the analysis needs to be performed at 100 frequencies. The duration of loading, which include both tire passing and resting times, is calculated based on tire pressure magnitude, axle loading value, and rest to pulse ratio. For realistic loading, it appears that the ratio of 10 for resting time to loading time is enough for engineering accuracy. In the next section, we propose a modified algorithm where the analysis can be performed at less than 100 frequencies for typical pavement analysis.

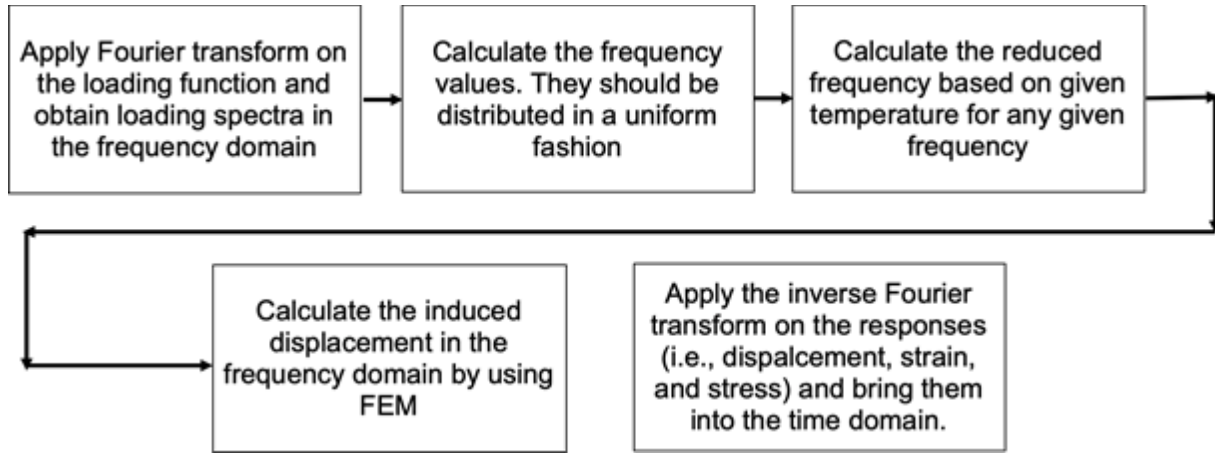


Figure A-1. The algorithm for calculating pavement response by using Fourier transform in time and space.

A.5. Overview of the Proposed Algorithm

Consider an asphalt concrete pavement section which is subjected to a moving traffic. The Fourier-finite element algorithm gets the passing traffic loading function and apply Fourier transform on it. The pavement structure should be analyzed for any single frequency and waveform available in the loading spectra. The frequency response function (FRF) can be utilized to calculate the pavement displacement induced by passing traffic (Equation (A.13)).

$$\hat{u} = RF(\omega) f(\omega) \quad (\text{A.13})$$

Where u is the induced displacement and f is the loading function. As it can be observed from Equation (A.13), the induced displacement is a function of FRF and loading. FRF depends on material properties and pavement section geometry. Because the pavement section dimensions are much bigger than the loading dimensions, the effect of pavement geometry can be ignored.

Due to the fact that the mixture moduli of the asphalt concrete mixtures reach to asymptotic values at both high and low reduced frequencies, the FRF function can be interpolated with non-uniform graded frequencies distributed in the frequency domain. One way

to pick those non-uniformly distributed frequencies is to use the geometrical progression approach. Figure A-2 presents the position of frequencies that were picked to interpolate the mixture moduli from.

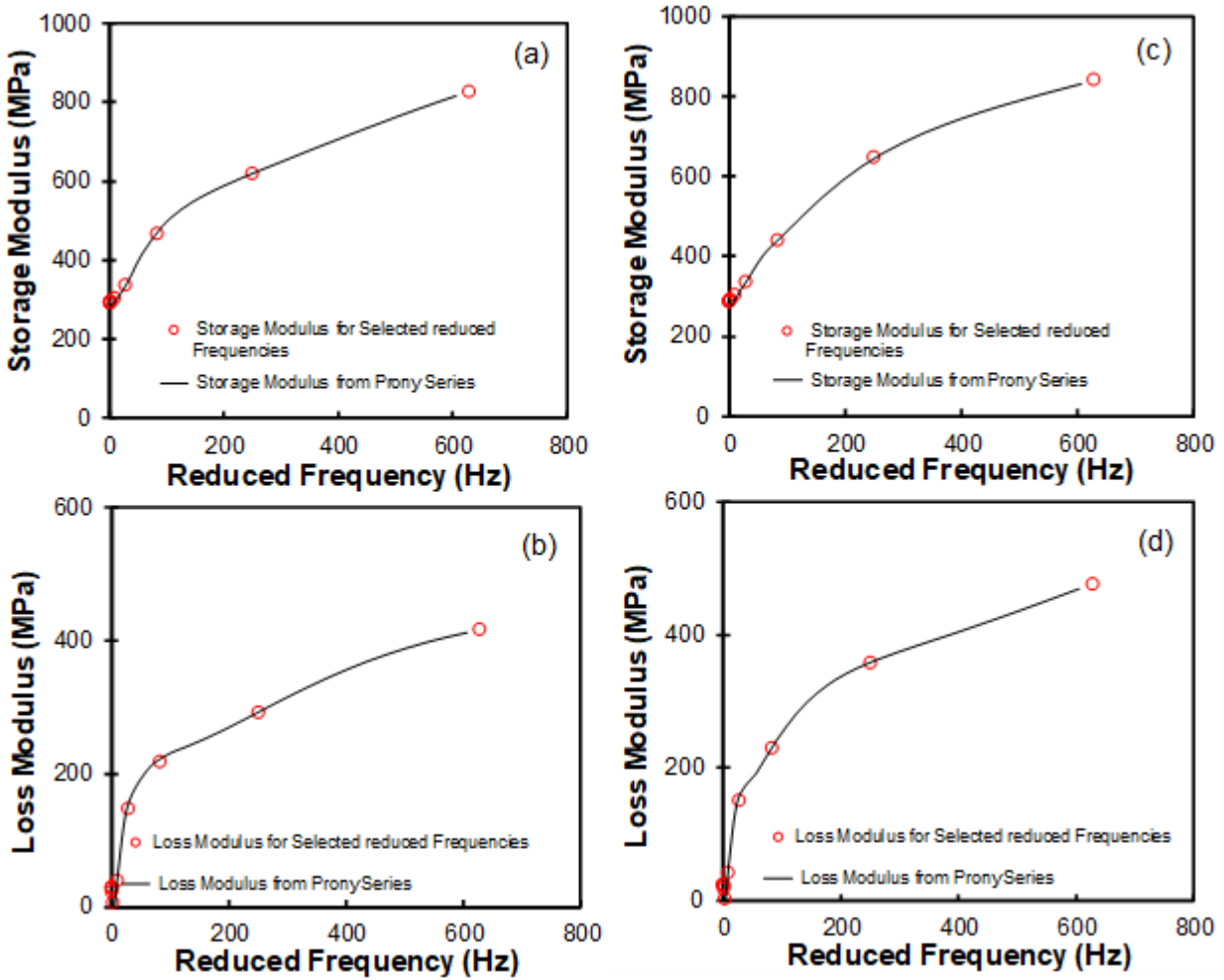


Figure A-2. Selected frequencies picked by using geometrical progression approach: (a) storage modulus for NCAT-OGFC, (b) loss modulus for NCAT-OGFC, (c) storage modulus for MIT-control, and (d) loss modulus for MIT-Control

The geometrical progression rate of 3.0 is used in this paper. It should be noted that the interpolation is done by using the piecewise second order polynomial. The values presented for those frequencies are shown in Figure A-2. As it can be seen from Table A.1, all the selected frequencies are increased by a factor of 3. The only exception to this rule is the first and last

frequencies. The reason behind that dissimilarity is to avoid extrapolation for choosing dynamic modulus values.

Table A.1. Selected frequency values (Hz)

Frequency number	ω_1	ω_2	ω_3	ω_4	ω_5	ω_6	ω_7	ω_8	ω_9	ω_{10}
Value	0.00	0.11	0.34	1.03	3.08	9.25	27.76	83.28	249.84	628.32

Figure A-3 presents the results of the interpolation. As it can be observed from Figure A-3, the suggested interpolation algorithm is able to interpolate the mixture moduli with an acceptable accuracy.

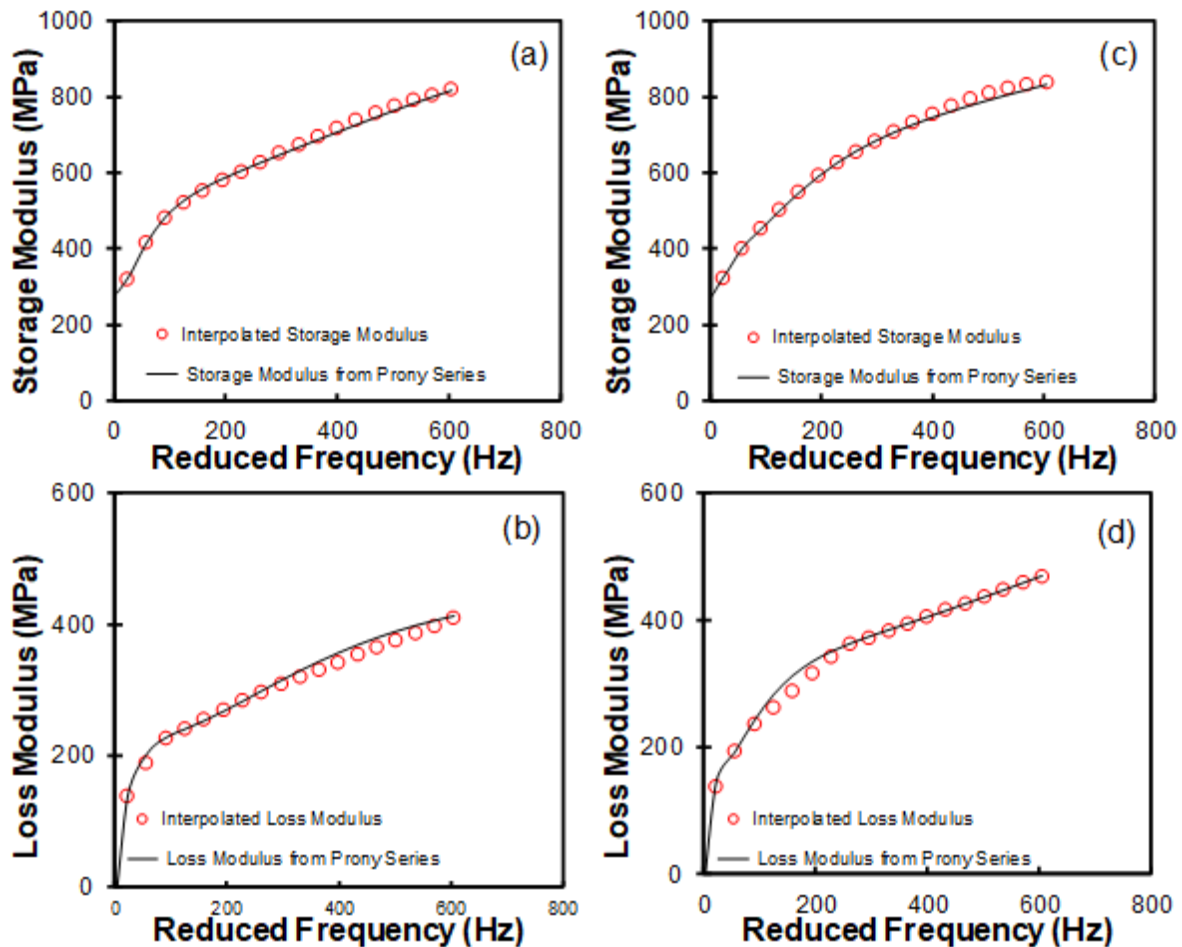


Figure A-3. The results of interpolation method for predicting the storage and loss modulus of mixtures: (a) storage modulus for NCAT-OGFC, (b) loss modulus for NCAT-OGFC, (c) storage modulus for MIT-control, and (d) loss modulus for MIT-control

On the outset, the loading function needs to be interpolated based on the same frequency grading that was picked for FRF function. Figure A-4 presents the result of that interpolation. As it can be observed from Figure A-4, the interpolation methodology is not accurate for the loading function. This means that the mesh size should be reduced in order to increase the accuracy.

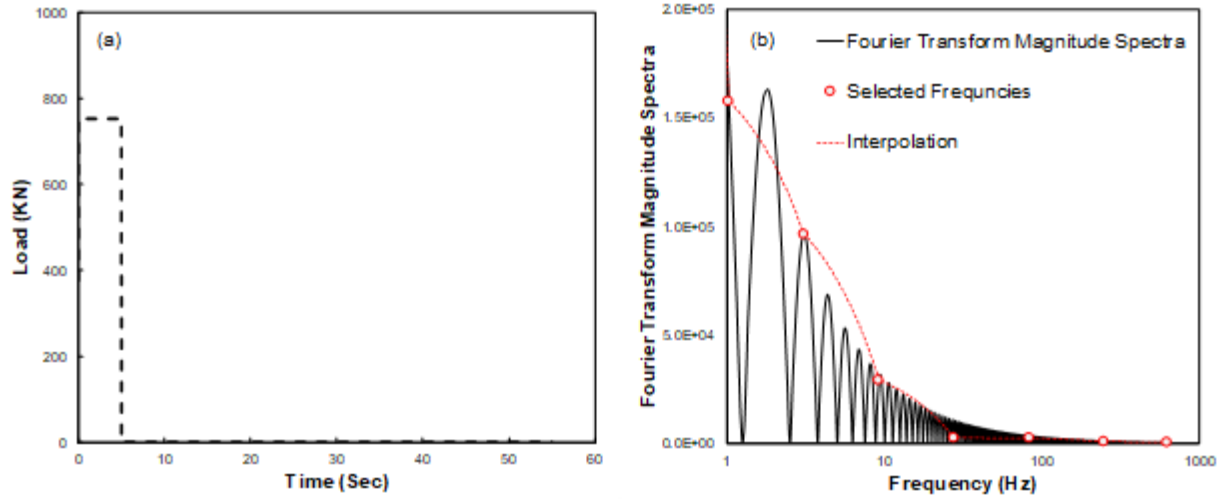


Figure A-4. Typical tire loading magnitude and corresponding Fourier transform spectra: (a) tire loading in the time domain and (b) Fourier spectra magnitude, position of selected frequencies, and interpolation based on selected frequencies

Recognizing the fact that the FRF calculation is the costly part of the analysis, we propose to use coarse-graded frequency to interpolate the FRF values by assuming unit-value loading function for each of the frequencies. Having the FRF values for each of frequency, the FRF can be interpolated for all the frequencies that are required for load interpolation. The final displacement function in the frequency domain can be obtained from multiplying the interpolated-FRF function to the loading function (Equation (A.14))

$$u(\omega) = FRF(\omega) \times f(\omega) \quad (A.14)$$

The proposed procedure should be verified for both material-level and structural-level. The results of verification study are reported in the next section. Figure A-5 presents the summary of

the proposed non-uniform approach. Calculation of strain and stress components is in the same way as mentioned in Figure A-1.

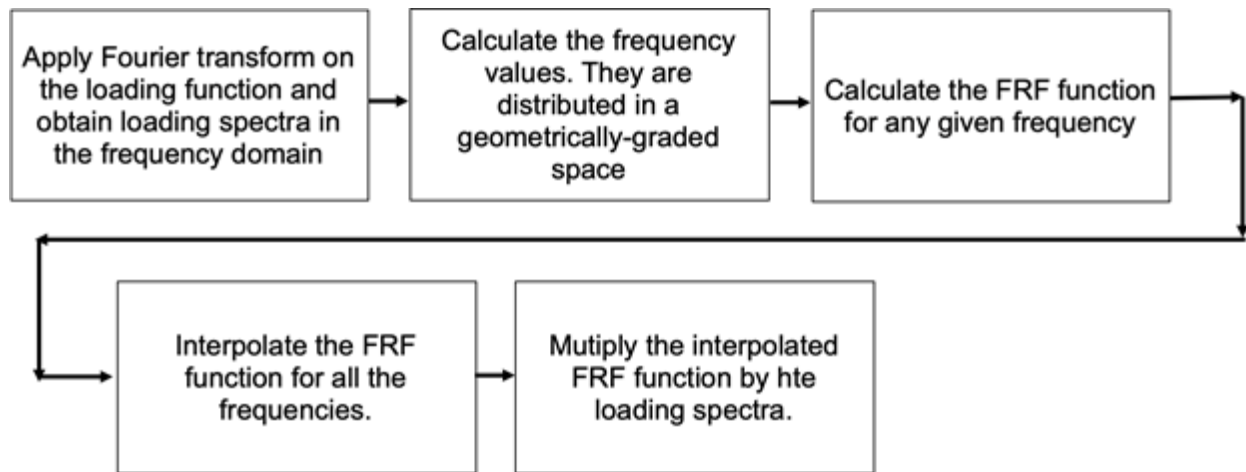


Figure A-5. Overview of the proposed methodology for the non-uniform method

A.6. Verification

The material-level verification considers a representative volume element (RVE) subjected to three types of loading: (a) sine wave, (b) block loading, and (c) random loading. The RVE sample temperature can also be changed to study the accuracy of the proposed algorithm under wide range of reduced frequencies. On the structural-level, the algorithm can also be used to interpolate the pavement displacement under the traffic loading. Due to the fact that the bending stress is used to predict cracking, this paper compares the bending stress calculated from the suggested methodology and the corresponding values obtained through using the reference calculation.

A.6.1. Material level verification

Three different types of loading (sin wave, square-block loading, and multiple axle loading) are selected to evaluate the validity and accuracy of the proposed method. Figure A-6 shows three types of loadings which are considered to be applied to the RVE sample of the

asphalt mixtures. The sine and block loading shapes are typical loading types that are applied from tire loading. The random loading, which is generated by Matlab® program, is used as an example for generalized loading and ultimate testing of the proposed procedure.

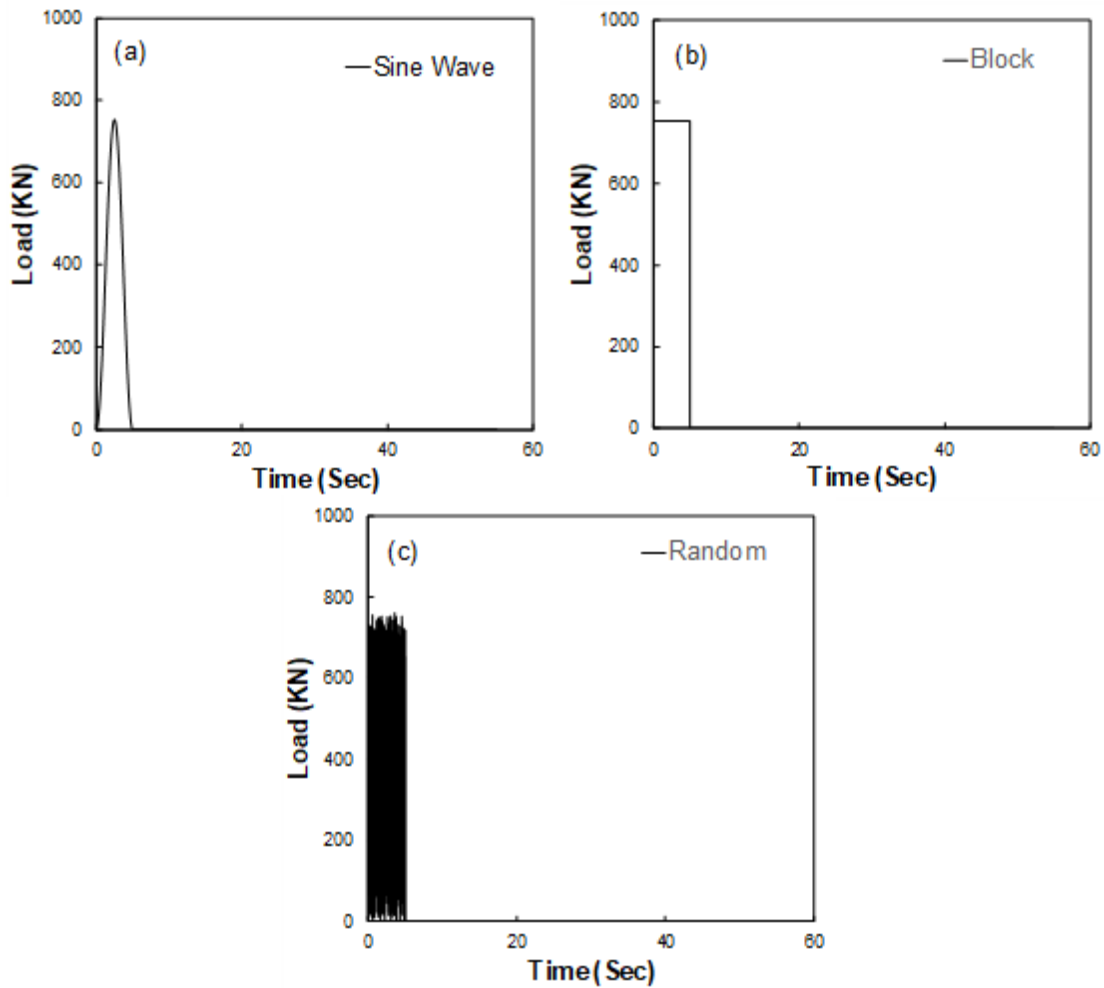


Figure A-6. Three types of loading applied on RVE sample: (a) sine wave loading, (b) block loading, and (c) random loading

Figure A-7 shows the real, imaginary and absolute values of the loading patterns in the frequency domain. The superposition principle can be applied to both layered viscoelastic and nonlinear viscoelastic analysis frameworks. For doing that, as mentioned before, a unit load is applied to the mixture for selected frequencies. Interpolation is performed to find the material

response for all other frequencies available in the frequency domain. The response can be obtained by multiplying the force value at each frequency of the material response obtained from the unit load spectra. Inverse Fourier transform is applied to the obtained response to bring response back into the time domain.

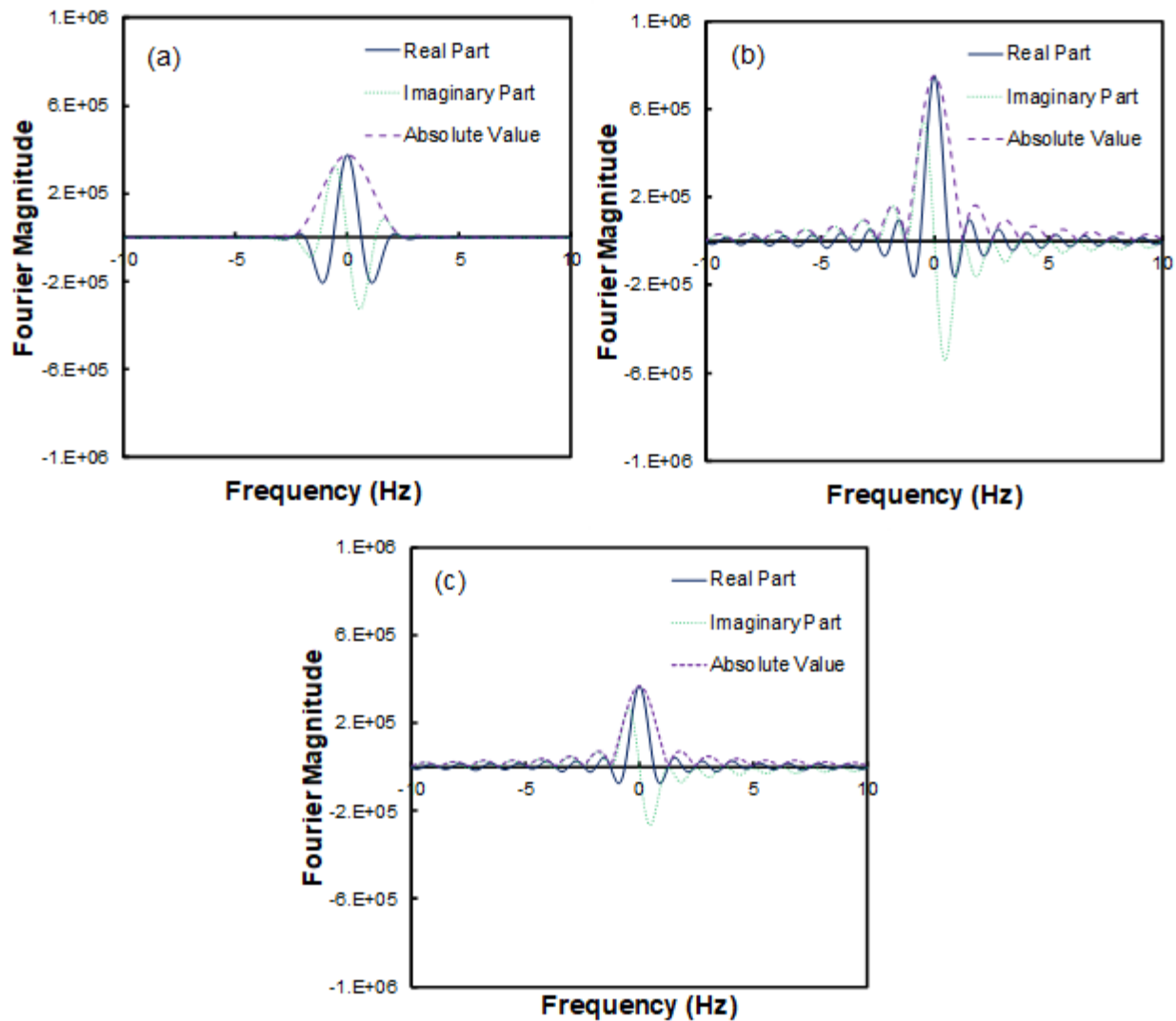


Figure A-7. Different types of loading applied on asphalt mixture: (a) sine wave, (b) block wave, and (c) loading corresponds to the multiaxial truck

Figure A-8 and Figure A-9 show the result of the proposed approach; the reference response and the approximate response obtained from the suggested methodology. As observed

from Figure A-8 and Figure A-9, the approximate response matches with the reference response with a very high accuracy.

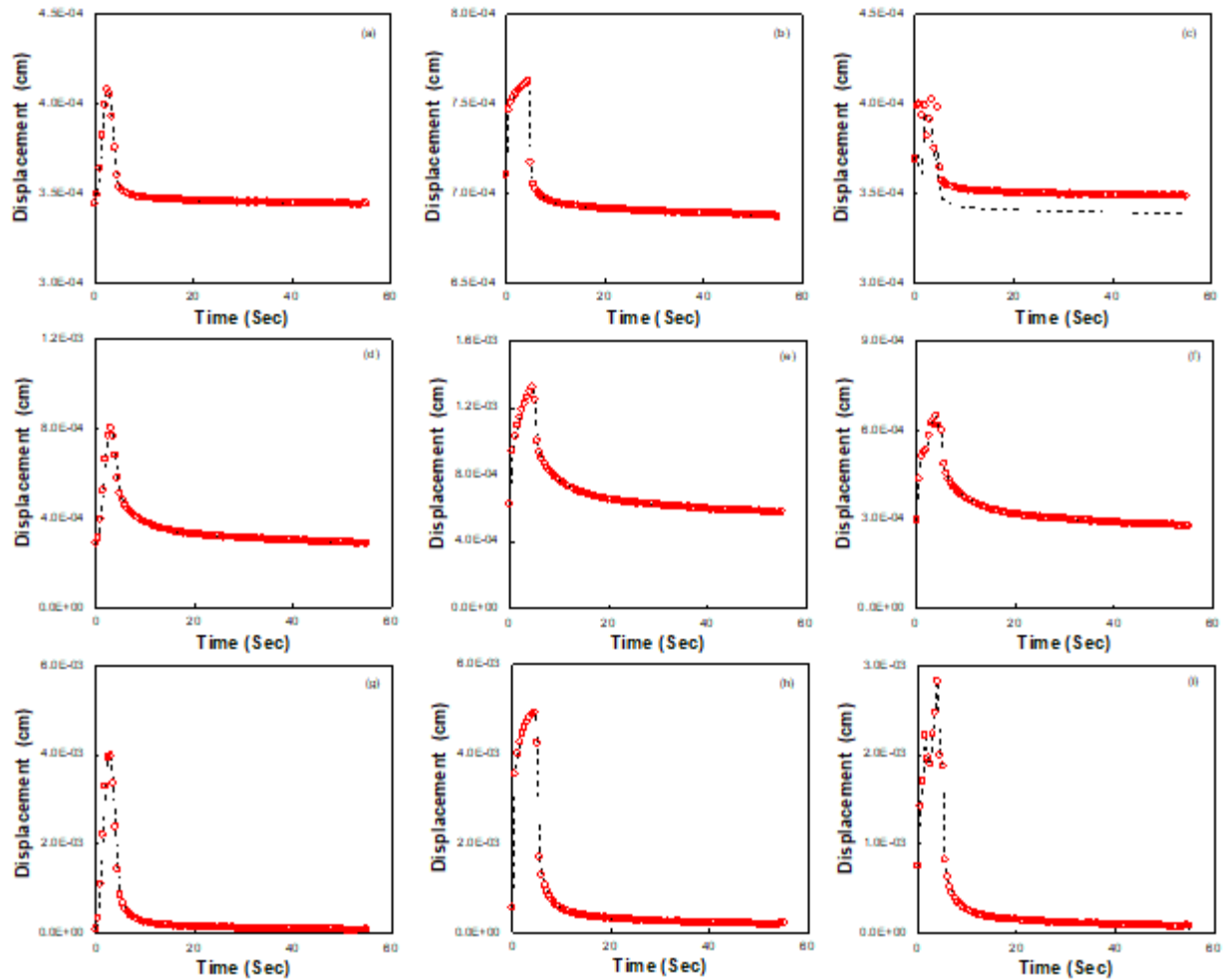


Figure A-8. Reference versus approximate response for NCAT-OGFC mixture, material-level verification: (a) Sinusoidal loading at 10°C, (b) Block loading at -10°C, (c) multiple axle loading at -10°C, (d) Sinusoidal loading at 20°C, (e) Block loading at 20°C (f) multiple axle loading at 20°C, (g) Sinusoidal loading at 54°C, (h) Block loading at 54°C, and (I) multiple axle loading at 54°C (Note: Dashed line represents the results from Fourier transform approach whereas circles represent the results from non-uniform Fourier transform approach)

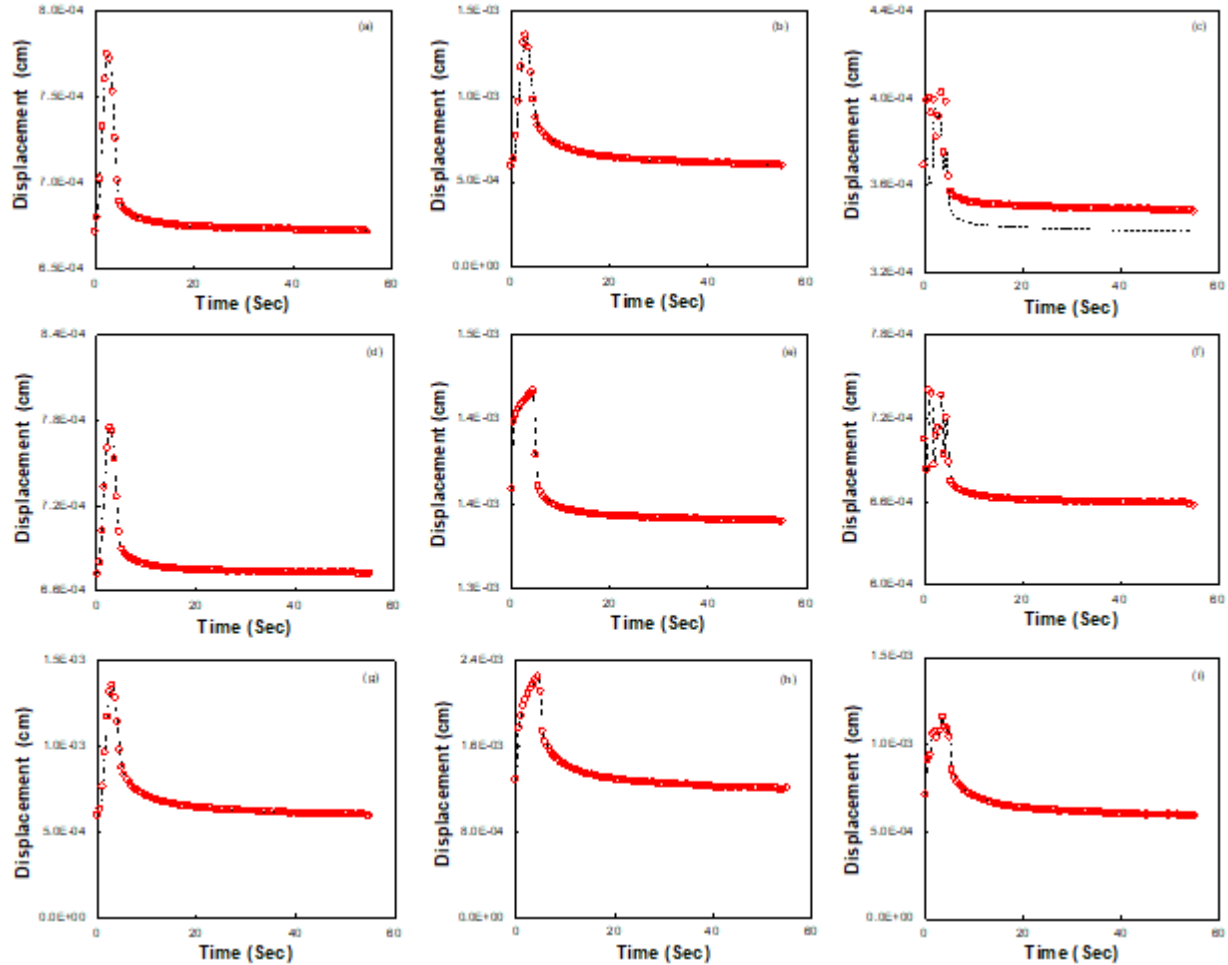


Figure A-9. Reference versus approximate response for MIT-Control mixture, material-level verification : (a) Sinusoidal loading at -10°C , (b) Block loading at -10°C , (c) multiple axle loading at -10°C , (d) Sinusoidal loading at 20°C , (e) Block loading at 20°C (f) multiple axle loading at 20°C , (g) Sinusoidal loading at 54°C , (h) Block loading at 54°C , and (I) multiple axle loading at 54°C (Note: Dashed line represents the results from Fourier transform approach whereas circles represent the results from non-uniform Fourier transform approach)

A.7. Structural Level Verification

As mentioned before, one section from the NCAT testing facility and one section from MIT sections are used to evaluate the accuracy of the proposed method. The temperature distribution is a governing factor on the pavement response. Figure A-10 shows temperature distribution in depth of pavement sections used in NCAT and MIT sections.

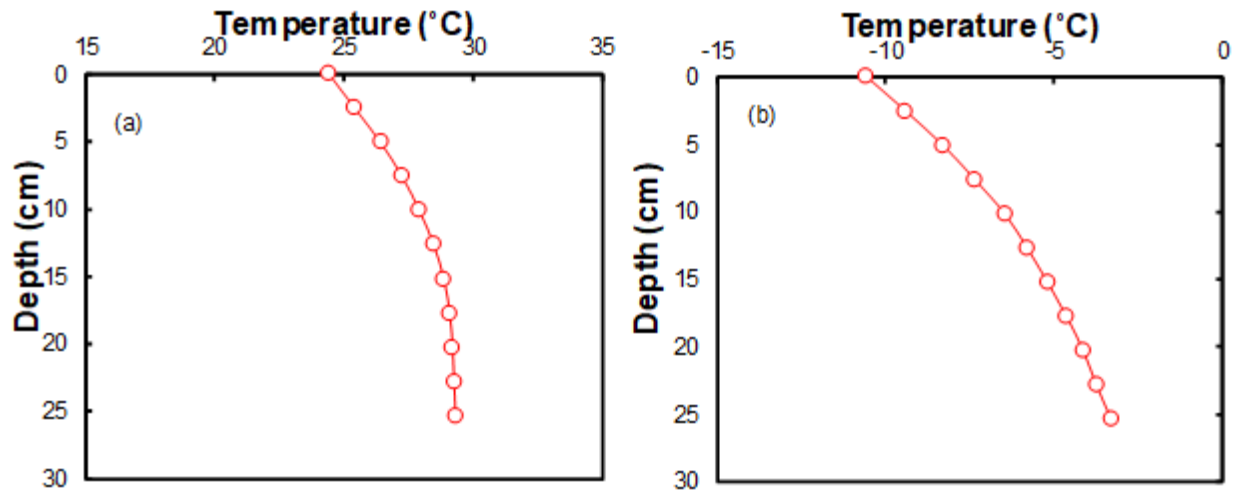


Figure A-10. Temperature distribution through the pavement section depth: (a) NCAT section and (b) MIT section

In order to examine the accuracy of the proposed solution, different points should be examined within the asphalt pavement section to consider both bending and shear dominated regions. Figure A-11 shows the schematic view of the selected points in the NCAT and MIT pavement sections. Table A.2 and Table A.3 present the coordinates of the selected point in the NCAT and MIT sections respectively.

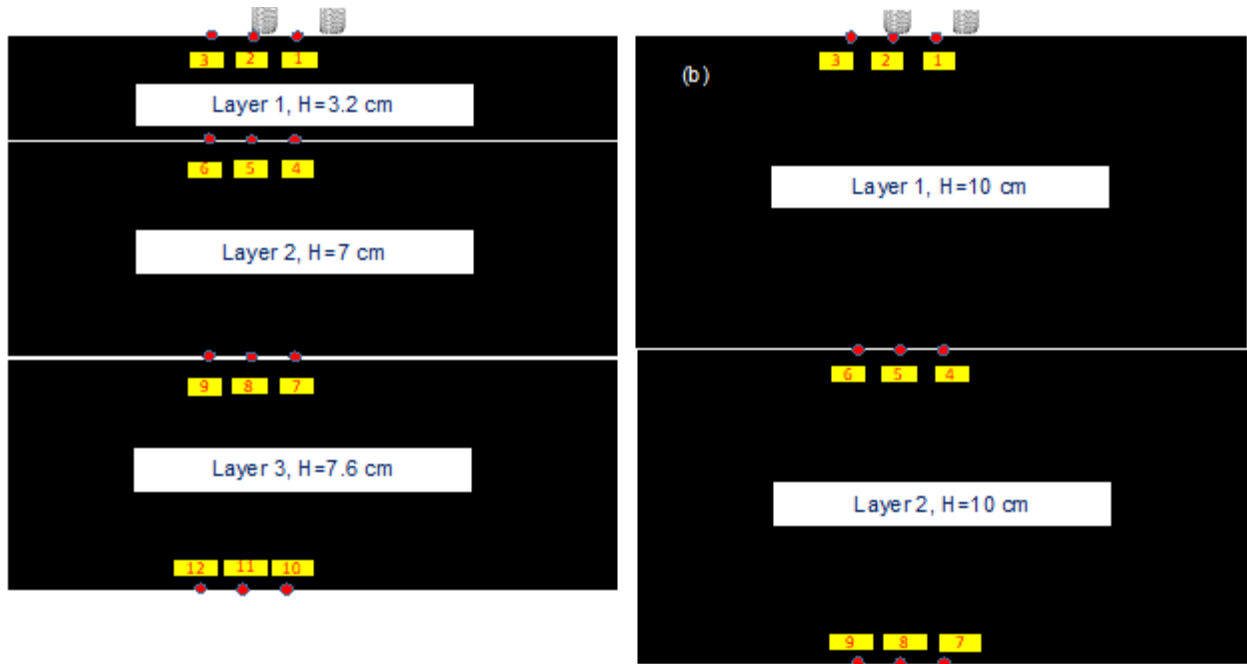


Figure A-11. The schematic view of the selected point's location within the pavement sections: (a) NCAT and (b) MIT

Table A.2. Coordinates of the selected points in the NCAT sections

		X (cm)		
		0	15	40
Z (cm)	0	Point 1	Point 2	Point 3
	3.2	Point 4	Point 5	Point 6
	10.2	Point 7	Point 8	Point 9
	17.8	Point 10	Point 11	Point 12

Table A.3. Coordinates of the selected points in the MIT sections

		X (cm)		
		0	15	40
Z (cm)	0	Point 1	Point 2	Point 3
	10	Point 4	Point 5	Point 6
	20	Point 7	Point 8	Point 9

Figure A-12 presents the result obtained from the proposed method along with the result calculated from reference method for the NCAT-OGFC sections. As it can be understood from Figure A-12 the proposed methodology is quite compatible with the reference response. Figure A-13 shows the result for the MIT test section.

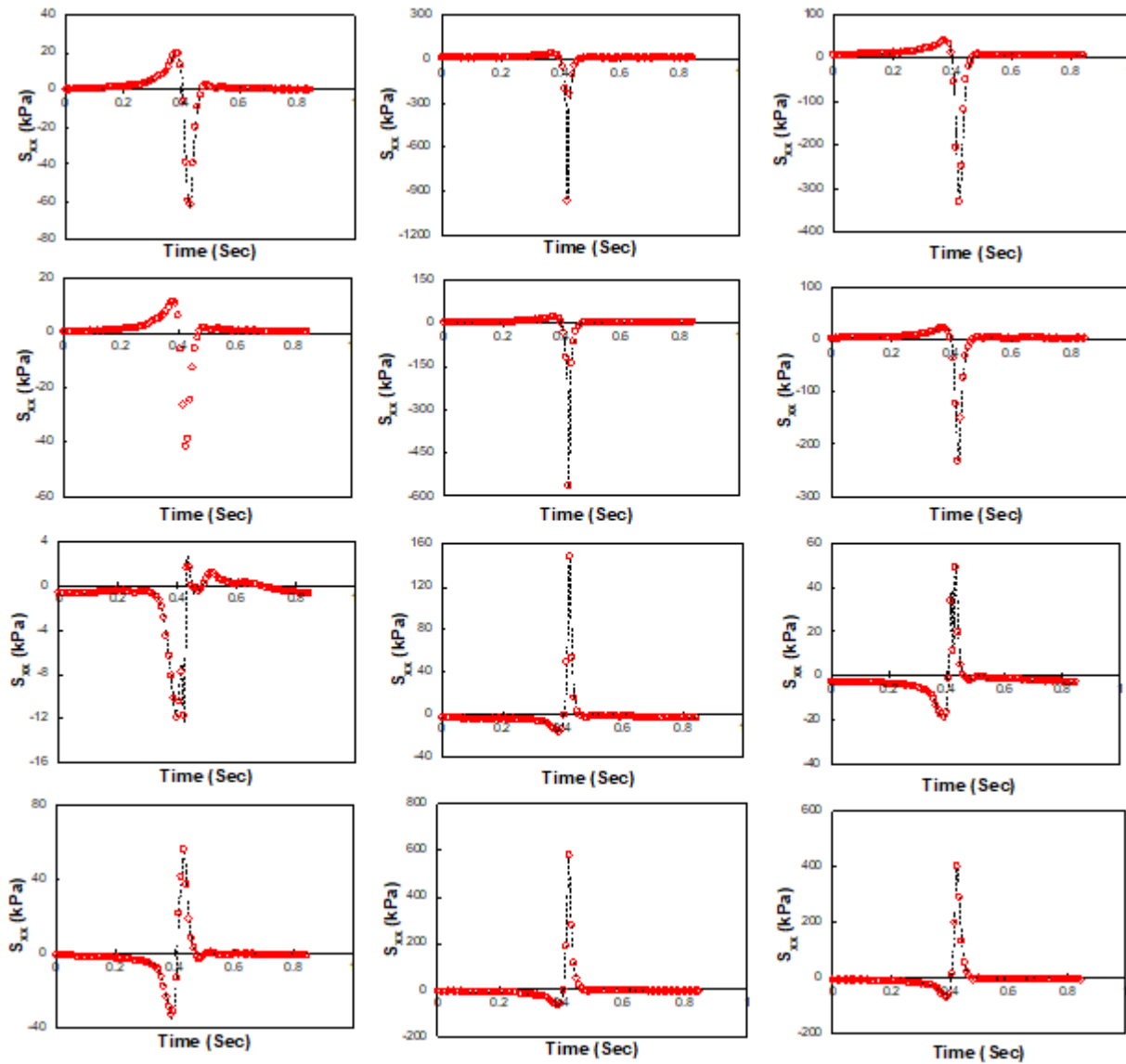


Figure A-12. Reference response and predation results obtained from the proposed methodology for NCAT-OGFC section

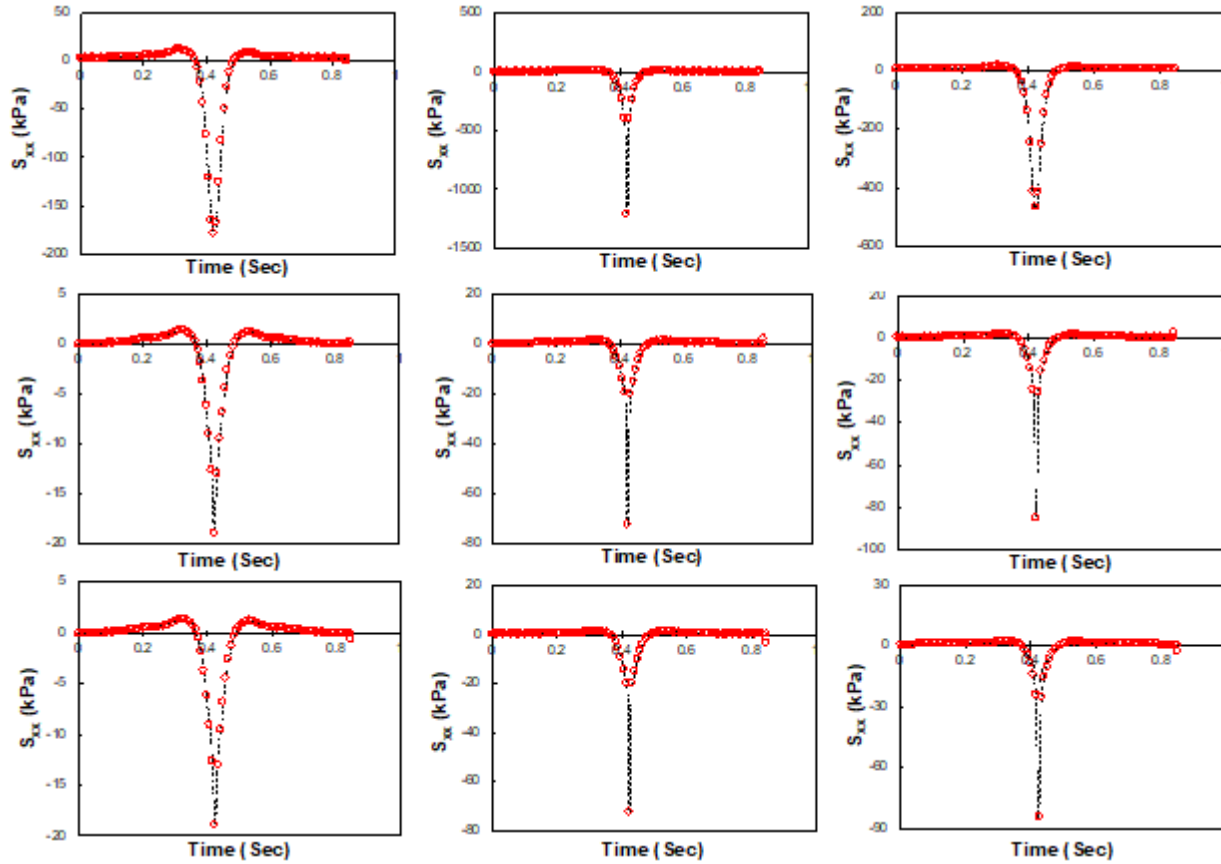


Figure A-13. Reference response and predation results obtained from the proposed methodology for MIT-Control section

A.8. Conclusion:

A new method is proposed to apply the non-uniform Fourier transform in Fourier-finite element methodology. The new methodology proposes to use a geometrically-graded frequency distribution in the frequency domain. It is shown that the interpolation algorithm is able to capture the storage and loss modulus of asphalt mixtures. The proposed algorithm is able to capture the induced displacement for the RVE samples under a wide range of loading shapes and temperature range. It is illustrated that the predicted bending stresses from the proposed algorithm are in-match with the corresponding values from uniformly-graded frequency approach. The compatibility of the proposed approach to the uniformly-spaced frequency is verified for two pavement sections that are located in cold and warm regions. The application of

the proposed algorithm is able to reduce the computational cost associated with the pavement response analysis.

**APPENDIX B. INVESTIGATION INTO FATIGUE DAMAGE GROWTH
DIRECTION IN ASPHALT CONCRETE PAVEMENT SECTIONS BASED ON
SIMPLIFIED VISCOELASTIC CONTINUUM DAMAGE (S-VECD) THEORY**

B.1. Summary:

Modeling the fatigue cracking performance of asphalt concrete using continuum damage theories is an approach that has gained international attention in recent years. One such model, the viscoelastic continuum damage (VECD) model, is used in this research to study the fatigue performance of asphalt pavements. VECD theory requires the adoption of direction as the axis of anisotropy that occurs due to crack growth. The two options that are available for finding the damage growth direction utilize either the maximum experienced stress or the maximum experienced strain (or maximum experienced pseudo strain). The FlexPAVETM 1.1, formally known as LVECD, software was used in this paper to capture both the top-down and bottom-up cracking that occurs in pavements due to moving loads and to investigate the ability of the two damage growth direction options to predict damage growth. Three pavement sections that have different thicknesses (i.e., thin, intermediate, and thick) are studied to fully understand the effects of the fatigue damage direction on the mechanisms and magnitude of the fatigue cracking within the asphalt pavements. The results show that the strain-based method leads to more damage at the top and less damage at the bottom of the pavement than the stress-based method. Also, it was found that the damage determined at the top of the pavement using the strain-based method is governed by the so-called Poisson's effect, whereas the stress-based method calculates damage based on the negative bending effect on top of the pavement and the bending stress at the bottom of the pavement.

B.2. Introduction

Fatigue cracking due to repeated traffic loadings is one of the major types of distress found in asphalt concrete pavements. Fatigue cracks allow water to enter a pavement section, thus leading to deterioration of the pavement structure that in turn reduces the pavement's serviceability. Therefore, the prediction of fatigue cracking in hot mix asphalt plays a crucial role in flexible pavement design and preservation. Fatigue cracking depends on many parameters, including the pavement's structure, asphalt mixture properties, and environmental conditions. Therefore, mechanistic models that enable pavement engineers to understand and model fatigue cracking for a wide range of actual experienced situations without excessive testing would be a valuable prediction tool for pavement engineers.

Modeling fatigue cracking of asphalt concrete using continuum damage theories has gained much attention recently (Underwood, B.S., et al., 2010, Valikhani et al., 2018, Valikhani et al., 2017). Continuum damage theories assume that the viscoelastic and viscoplastic responses of the material depend on the internal State variables of the material. These types of models are successful because they can predict macroscale behavior by measuring observable parameters (e.g., stresses and strains). Schapery's work potential theory (Schapery 1987), which was built upon thermodynamic principles, is one of these continuum damage theories whereby damage is quantified as an internal State variable. Nonlocal elastic-based continuum damage also has been proposed to quantify damage (Bazant and Pijaudier 1989, Bodin et al., 2004, Keshavarzi and Bakhshi 2012).

Kim and Little (1990) were the first researchers to apply Schapery's nonlinear viscoelastic theory to materials with distributed damage in order to describe the behavior of sand asphalt under controlled strain cyclic loading. They later applied their viscoelastic continuum

damage (VECD) theory to describe asphalt concrete behavior under both controlled stress and controlled strain loading (Lee and Kim 1998). Also, research conducted by Daniel and Kim as part of the WesTrack project showed that the damage characteristics of asphalt concrete are independent of the mode of loading and can be determined using a simple test, such as the constant crosshead rate monotonic test (Daniel and Kim 2002). Findings from (Chehab 2002) and (Underwood et al. 2006) have extended the range of VECD theory's applications. For example, Chehab extended VECD theory by proving that time-temperature superposition (t-TS) is valid in asphalt concrete not only in the linear viscoelastic range but also for a highly damaged State of asphalt concrete (Chehab 2002). Underwood et al. (2006) applied time-temperature superposition principle to both modified and unmodified asphalt concrete mixtures used in the Federal Highway Administration Accelerated Load Facility (FHWA-ALF) in McLean, Virginia. The Underwood et al.'s study proved that time-temperature superposition and VECD theory can successfully predict mixture behavior under complex loading histories (Underwood et al. 2010).

Sabouri and Kim (2014) found a characteristic relationship between the rate of released pseudo strain energy and the pavement's fatigue life that is independent of strain amplitude and temperature. That is, the fatigue life of an asphalt mixture can be assessed using this relationship. The application of this characteristic relationship has been verified for reclaimed asphalt pavement (RAP) and non-RAP mixtures, modified and unmodified mixtures, and warm mix asphalt mixtures (Sabouri et al., 2015, Norouzi et al. 2015, Mensching et al., 2016, Rahbar-Rastegar et al., 2017). In addition, Keshavarzi and Kim (2016) developed a methodology for predicting asphalt concrete's rate-dependent strength by applying VECD theory to cyclic test results.

Prediction of fatigue cracking performance of asphalt pavement requires material models as well as structural model. Layered elastic analysis is one of the basic approaches for pavement structural analysis. It assumes that a pavement section consists of some horizontal layers located on top of each other. The Fourier-Bessel transform is utilized to calculate the pavement's responses. The effect of viscoelasticity and the evolving nature of distress growth are some important issues that make layered elastic analysis questionable, however.

Layered viscoelastic analysis is able to capture the viscoelastic behavior of asphalt concrete; however, long computing time in time domain makes this approach impractical for the long-term performance prediction of asphalt pavement by State highway agencies and contractors. The Fourier transform technique reduces the computing time significantly and makes layered viscoelastic moving load analysis more feasible for routine pavement analysis. With the goal of capturing the three-dimensional stress and damage evolution under moving loads, FlexPAVETM, formally known as LVECD, was developed at North Carolina State University on the foundation of the Fourier transform layered viscoelastic analysis.

Predicting damage evolution using a pavement performance prediction program such as FlexPAVETM 1.1 requires the understanding of micro cracking direction a priori, which is clear by recognizing that damage evolution under traffic loading causes anisotropy. Constitutive theory depends on the direction of the axis of anisotropy, and any change in that direction may lead to a significant difference with regard to the final amount of damage (Kim et al., 2008). This paper investigates the effect of two different ways of determining damage growth direction (i.e., stress-based and strain-based) on both damage growth mechanism and the final amount of damage.

B.3. Theoretical Background

B.3.1. Viscoelastic Damage Theory

VECD theory is based on three main principles: (1) the pseudo strain-based elastic-viscoelastic correspondence principle to account for the viscoelastic nature of asphalt concrete; (2) the work potential continuum damage theory to model the effect of micro cracking on the macroscale-level behavior of the material; and (3) the t-TS principle with growing damage to unite the effects of time/rate and temperature. Pseudo strain in uniaxial mode is defined in Equation(B.1):

$$\varepsilon^R = \frac{1}{E_R} \int_0^t E(t-\tau) \frac{d\varepsilon}{d\tau} d\tau \quad (\text{B.1})$$

Where ε^R is the pseudo strain, E_R is the reference modulus, $E(t)$ is the relaxation modulus, t is time, ε is strain, and τ is the integration variable. The pseudo strain energy density function is expressed in Equation(B.2):

$$W^R = f(\varepsilon^R, S) \quad (\text{B.2})$$

Where W^R is the pseudo strain energy density, and S is the internal State variable representing damage. The stress-pseudo strain relationship is expressed in Equation(B.3):

$$\sigma = \frac{\partial W^R}{\partial \varepsilon^R} \quad (\text{B.3})$$

Where σ is stress, The damage evolution law is expressed in Equation (B.4) :

$$\frac{dS}{dt} = \left(-\frac{\partial W^R}{\partial S} \right)^\alpha \quad (\text{B.4})$$

Where α is the damage evolution rate, and t is reduced time. All the formulations that are presented in this paper pertain only to the region of the material behavior prior to localization, i.e., before the damage coalesces and localizes into a single dominant macrocrack. The VECD model assumes that a material is isotropic when it is undamaged and that the growth of damage under loading leads to local transverse isotropy. The pseudo strain energy density function, W^R , can be written as Equation (B.5) by using viscoelastic fracture mechanics and the correspondence principle for viscoelastic materials.

$$\begin{aligned}
 W^R &= \frac{1}{2} \left[A_{11} (e_v^R)^2 + A_{22} (e_d^R)^2 + 2A_{12} e_d^R e_v^R + A_{44} \left((\gamma_{12}^R)^2 + (e_s^R)^2 \right) \right] \\
 e_v^R &= \epsilon_{11}^R + \epsilon_{22}^R + \epsilon_{33}^R \\
 e_d^R &= \epsilon_{33}^R - \frac{e_v^R}{3} \\
 e_s^R &= \epsilon_{11}^R - \epsilon_{22}^R
 \end{aligned} \tag{B.5}$$

where $\epsilon_{11}^R, \epsilon_{22}^R, \epsilon_{33}^R, \gamma_{12}^R, \gamma_{13}^R, \gamma_{23}^R$ are pseudo strains along the local axis, and $A_{11}, A_{22}, A_{12},$ and

A_{44} , parameters are defined in Equation (B.6):

$$\begin{aligned}
 A_{11} &= \frac{1}{9} \left[C(S) + 2 \frac{1+\nu}{1-2\nu} \right] \\
 A_{22} &= C(S) + \frac{1}{2} \frac{1-2\nu}{1+\nu} \\
 A_{12} &= \frac{1}{3} [C(S) - 1] \\
 A_{44} &= \frac{1}{2} \frac{1}{1+\nu}
 \end{aligned} \tag{B.6}$$

Pseudo strain can be defined as shown in Equation (B.7):

$$\epsilon_{kl}^R(t) = \frac{1}{E_R} \int_0^t E(t-\tau) \frac{d\epsilon_{kl}}{d\tau} d\tau \tag{B.7}$$

According to Equation (B.7), each component in the pseudo strain vector is proportional to its corresponding element in the strain vector. This observation indicates that the maximum principal pseudo strain direction is directed toward the direction of the maximum principal strain. When the local axis is also the principal axis, the shear strain is zero and Equation (B.5) changes to Equation(B.8):

$$W^R = \frac{1}{2} \left[A_{11} (e_v^R)^2 + A_{22} (e_d^R)^2 + 2A_{12} e_d^R e_v^R + A_{66} (e_s^R)^2 \right] \quad (\text{B.8})$$

Applying Equation (B.8) to Equation (B.5) yields Equation (B.9):

$$\frac{dS}{dt} = \left(-\frac{1}{2} \frac{\partial C}{\partial S} \right)^\alpha \left(\frac{1}{9} (e_v^R)^2 + \frac{2}{3} e_v^R e_d^R + (e_d^R)^2 \right) = \left(-\frac{1}{2} \frac{\partial C}{\partial S} \right)^\alpha \left(\frac{1}{3} e_v^R + e_d^R \right)^{2\alpha} \quad (\text{B.9})$$

According to Equation (B.5), Equation (B.8) can be simplified further, as shown in Equation (B.10)

$$\frac{dS}{dt} = \left(-\frac{1}{2} \frac{\partial C}{\partial S} \right)^\alpha (\varepsilon_3^R)^{2\alpha} \quad (\text{B.10})$$

Where ε_3^R is the maximum principal pseudo strain and C is the pseudo stiffness. ε_3^R can be defined according to two different methods based on (a) the convolution integral of maximum principal strain Equation (B.11), hereinafter referred as *strain-based* method) and (b) the maximum principal stress and stress-pseudo strain relationship (Equation (B.12), hereinafter referred as *stress-based* method).

$$\varepsilon_3^R(t) = \int_0^t E(t-\tau) \frac{d\varepsilon_{\max}(\tau)}{d\tau} d\tau \quad (\text{B.11})$$

$$\varepsilon_3^R = \frac{\sigma_{\max}}{C} \quad (\text{B.12})$$

where ε_{max} and σ_{max} are the maximum principal strain and maximum principal stress, respectively. This paper investigates the damage growth direction and damage magnitude based on these two methods.

B.3.2. Damage Calculations in the FlexPAVETM 1.1 Program

One of the failure criteria that are implemented in the FlexPAVETM 1.1 program is the G^R failure criterion. This failure criterion can be used to predict the remaining number of cycles for each point within pavement section layout. G^R failure criterion is based on the rate of release of pseudo strain energy. Equation (B.13) defines the G^R failure criterion. Details of the G^R -based failure criterion can be found elsewhere (Sabouri and Kim 2014).

$$G_R = \frac{1}{N_f^2} \int \varepsilon_R^2 (1-C) \quad (B.13)$$

The rate of pseudo strain energy release should be calculated for all the loading cycles. The FlexPAVETM 1.1 needs to know the pseudo stiffness, C , for all the remaining cycles of loading. This prediction can be done by using Equation(B.14).

$$\frac{\partial C}{\partial N} = \Delta C \left(\frac{C}{C_0} \right)^{1+\alpha} \left(\frac{\log(C)}{\log(C_0)} \right)^{(1+\alpha)\left(1-\frac{1}{b}\right)} \quad (B.14)$$

where ΔC is decrease in pseudo stiffness for one cycle of loading, and C_0 is the current value of pseudo stiffness. Equation(B.9) shows that S evolution is proportional to the $\varepsilon_R^{2\alpha}$. This shows that value of pseudo strain has a considerable effect on the rate of damage evolution.

B.3.3. Study Pavements and Material Properties

In order to investigate the effects of the damage evolution direction on the damage growth mechanisms and damage magnitude, three different pavement structures were considered in this study. Figure B-1 shows details of those sections. Traffic volumes used for performance assessment of these pavements were 0.2 million, 0.6 million, and 3 million equivalent single-axle loads (ESALs) for 20 years life. These values were taken from (Huang 2003) and justified to provide the reasonable damage magnitude within each section.

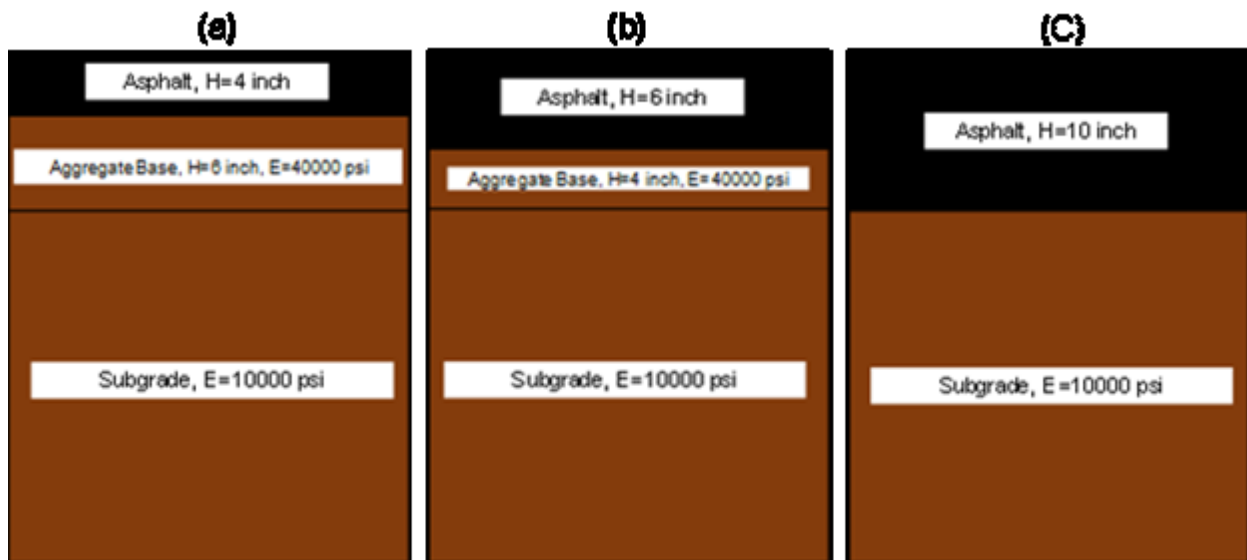


Figure B-1. Section layouts: (a) thin pavement (4-inch), (b) intermediate pavement (6-inch), and (c) thick pavement (10-inch)

The FlexPAVE™ 1.1 program requires the dynamic modulus values and fatigue properties for all the asphalt concrete layers. In this study, dynamic modulus and cyclic fatigue test results of the field cores from the Wisconsin section as part of the Long-Term Pavement Performance (LTPP) program were used. The dynamic modulus test and the cyclic fatigue test were performed using the Asphalt Mixture Performance Tester (AMPT) in accordance with the AASHTO TP 132 and TP 133, respectively. The details of dynamic modulus and S-VECD testing are reported elsewhere (Keshavarzi and Kim 2016). Figure B-2 (a) and (b) present the

dynamic modulus mastercurves in log-log scale and semi-log scale, respectively. Figure B-2 (c) and (d) show the damage characteristic curve and G^R -based failure criterion of the selected mixture, respectively.

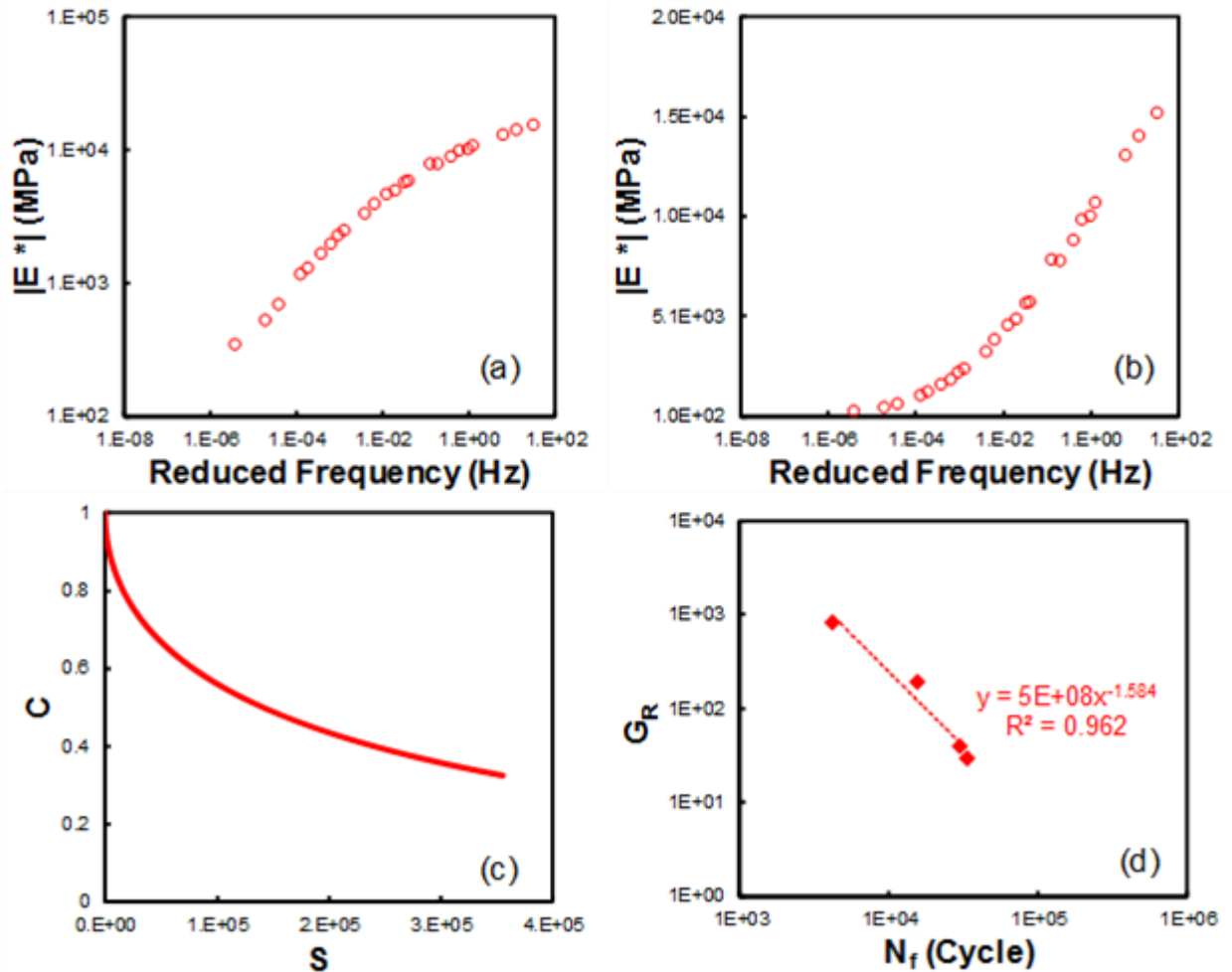


Figure B-2. Material properties: (a) dynamic modulus mastercurve in log-log scale (b) dynamic modulus mastercurve in semi-log scale, (c) damage characteristic curve, and (d) GR failure criterion

B.4. Discussion of Results

B.4.1. Damage at Different Locations and for Different Thicknesses

As was discussed in previous section, value of pseudo strain has a considerable effect on the rate of damage evolution. Increase in the pavement thickness reduces the strain and pseudo

strain and therefore yields large decrease in the experienced damage of the section. Figure B-3 proves this observation. According to Figure B-3, the pseudo stiffness evolution depends heavily on section thicknesses. This observation comes from the fact that induced bending stress in the pavement section is inversely proportional to section's modulus of inertia. The modulus of inertia is proportional to third power of section thickness. In this way, section thickness plays a significant role on the induced pseudo stiffness. Figure B- also shows that the effect of pavement thickness on pseudo stiffness reduction varies as a function of the evaluation location. It can be seen that top points in the pavement have less decrease in their pseudo stiffness value in comparison with bottom points. The reason for this outcome is the lower value of the induced bending stress in the top points compared with the bottom points when the material properties are the same. Note that the bending mechanisms for the top points and bottom points are different.

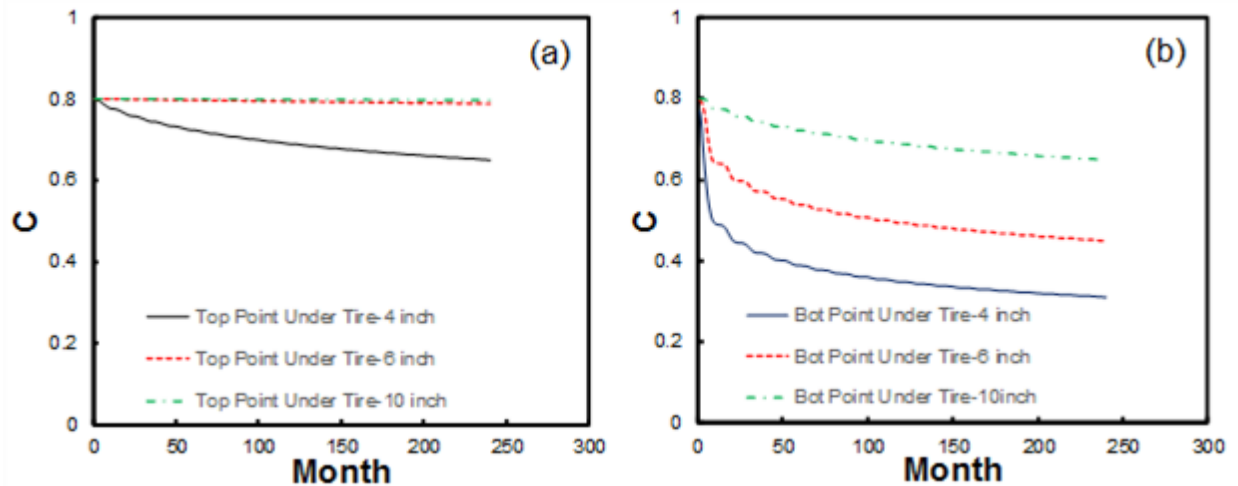


Figure B-3. Reduction in pseudo stiffness for different points and different section layouts: (a) top points and (b) bottom points

The FlexPAVE™ 1.1 program is able to calculate the rate of release of pseudo strain energy after finding the pseudo stiffness evolution in time. This value can be plotted against the number of cycles and compared against the given G^R failure line. Failure is defined when the rate

of release of pseudo strain energy versus number of cycles line intersects with the G^R failure line, and the number of cycles to failure (i.e., N_f) is the number of cycles at the intersection. This calculation is done for all the points in pavement section throughout the fatigue life prediction. Figure B-4 shows the intersection (denoted by circle) of developed released pseudo strain energy versus number of cycles for different points in all the studied sections. As it can be observed from Figure B-4, all bottom points fail while top points do not intersect G^R line. This is mainly due to the fact that developed bending stresses are much higher in the bottom of pavements in comparison with corresponding values for top of pavements. It should be noted that the 2α power form in Equation (B.9) increases the difference in induced stresses for damage increment.

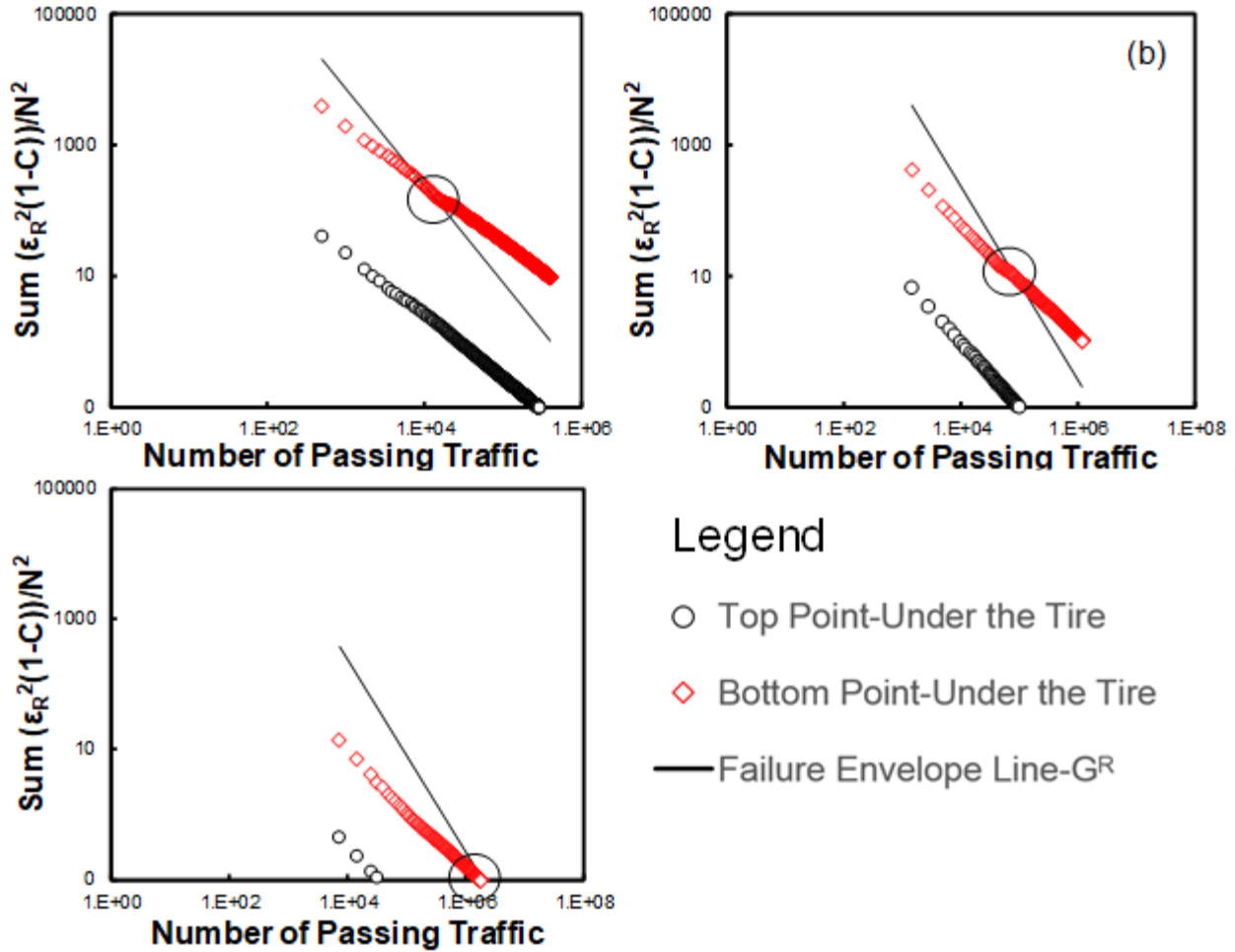


Figure B-4. Predictions of number of cycles to failure for different points and for different thicknesses: (a) 4 inches, (b) 6 inches, and (c) 10 inches (Circle indicates the point of failure)

B.5. Damage Mechanism

The FlexPAVE™ 1.1 program calculates the damage increment for one cycle of loading. After finding this incremental damage (i.e., ΔC) for that specific cycle, it then tries to extrapolate the ΔC for the remaining cycles of loading according to the C versus S relationship (i.e., along the damage characteristic curve). Therefore, the damage growth mechanism will remain the same for all the cycles of loading throughout the pavement life. Figure B-5 shows the contours for the direction of the axis of anisotropy within a global coordinate system for both stress-based and strain-based methods. When the strain-based method is used, the direction of the axis of

anisotropy is represented by the angle between the maximum principal strain direction and the vertical direction. When the stress-based method is used, the direction of the axis of anisotropy is represented by the angle between the maximum principal stress direction and the vertical direction.

Figure B-5 (a), (c), and (e) show the axis of anisotropy for 4-iNCh, 6-iNCh, and 10-iNCh thick pavements using the strain-based method, respectively. It can be seen from these figures that the axis of anisotropy under the wheel is mostly vertical, although the pattern of the angles under the wheel in the 4-iNCh pavement is different from that in the thicker pavements. The axis of anisotropy plots for the three pavements using the stress-based method is shown in Figure B- (b), (d), and (f). The pattern of the axis of anisotropy in the three figures is similar. Reasons for this difference between the strain-based method and stress-based method are explored by investigating the stress values calculated for the three pavements using both strain- and stress-based methods.

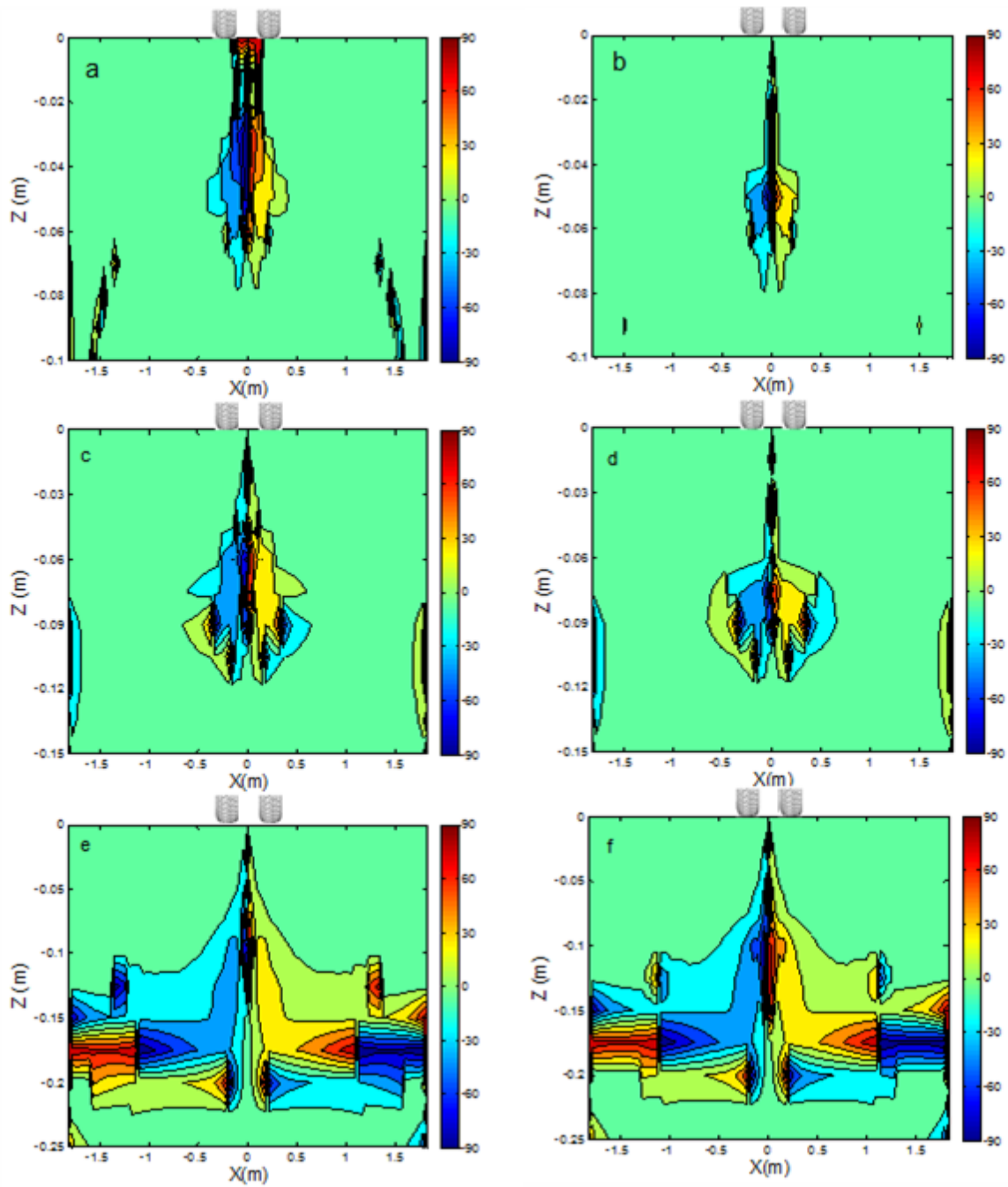


Figure B-5. Angles from the vertical direction (i.e., direction of the axis of anisotropy): (a) 4-iNCh pavement using strain-based method, (b) 4-iNCh pavement using stress-based method, (c) 6- inch pavement using strain-based method, (d) 6-iNCh pavement using stress-based method, (e) 10-iNCh pavement using strain-based method, and (f) 10-iNCh pavement using stress-based method

Figure B-6 and Figure B-7 present the normal stress values for the top and bottom points of the different pavement structures based on the strain-based method and the stress-based

method, respectively. In these figures, x, y, and z coordinates represent the direction perpendicular to the traffic direction, the traffic direction, and the depth direction, respectively. The thick solid lines represent the developed maximum pseudo strain for one cycle of loading. As can be observed from Figure B-6 (a), the strain-based method gives the maximum developed pseudo strain for a thin pavement when the tire is right on top of the pavement. This can be understood by noticing the fact that the maximum induced vertical stress (i.e., σ_{zz}) coincide with the maximum developed pseudo strain.

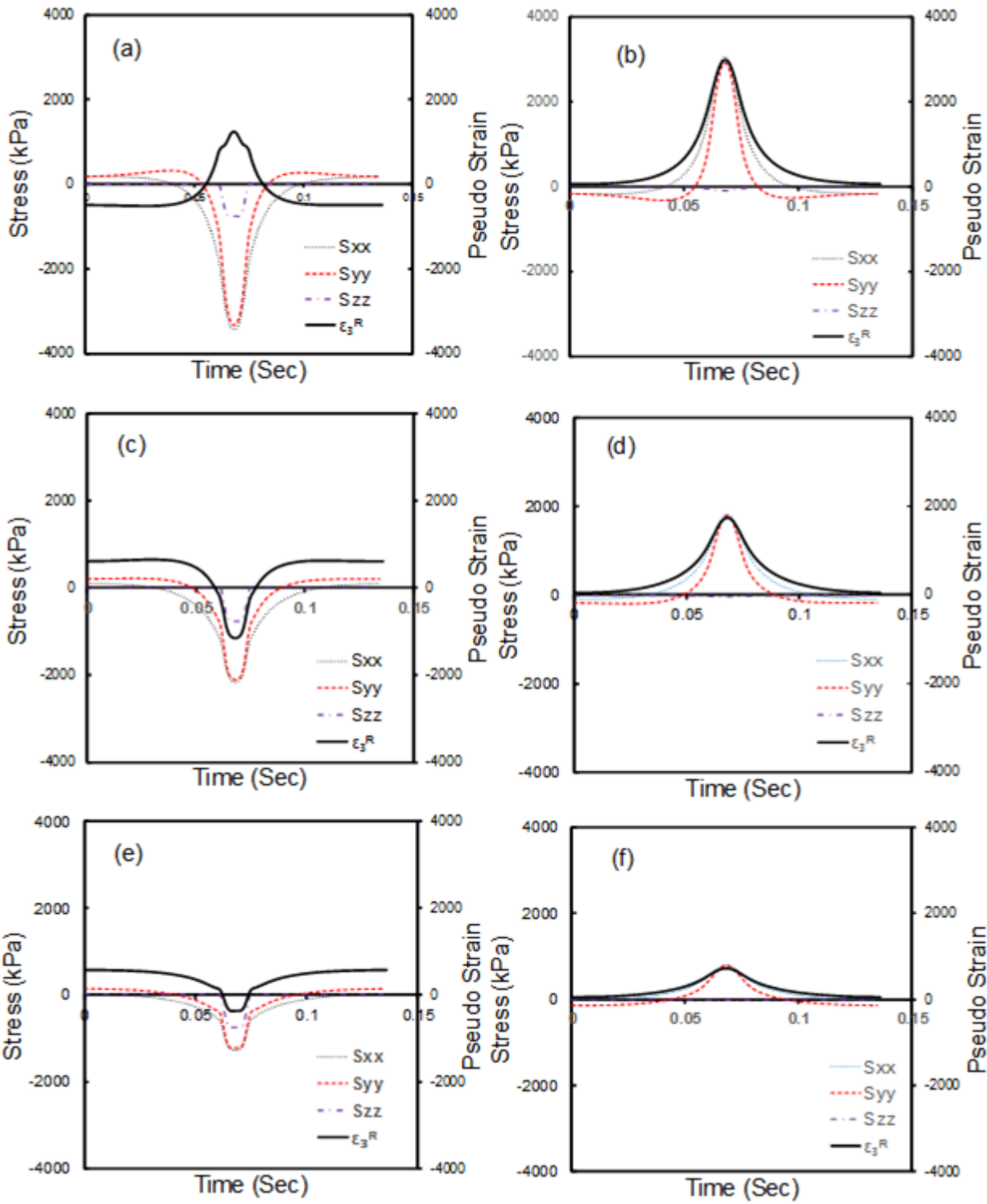


Figure B-6. Bending stress and pseudo strain variation for one cycle of loading using the strain-based method: (a) top point of 4-iNCh pavement, (b) bottom point of 4-iNCh pavement, (c) top point of 6-iNCh pavement, (d) bottom point of 6-iNCh pavement, (e) top point of 10-iNCh pavement, and (f) bottom point of 10-iNCh pavement

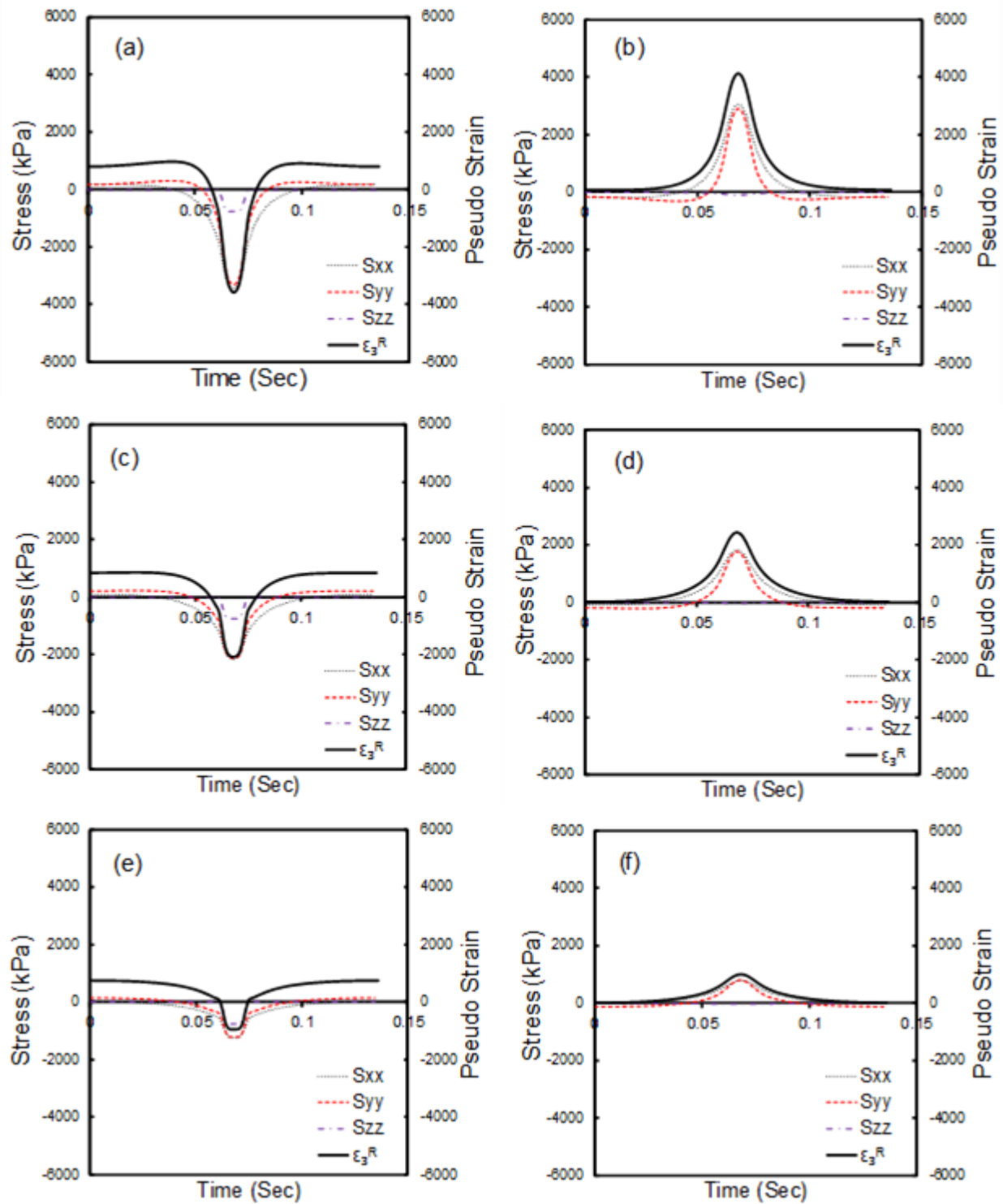


Figure B-7. Bending stress and pseudo strain variation for one cycle of loading using the stress-based method: (a) top point of 4-iNCh pavement, (b) bottom point of 4-iNCh pavement, (c) top point of 6-iNCh pavement, (d) bottom point of 6-iNCh pavement, (e) top point of 10-iNCh pavement, and (f) bottom point of 10-iNCh pavement

It can be observed from Figure B-6 (a), (c), and (e) that the maximum pseudo strain in z direction for the 4-iNCh pavement (shown in Figure B-6 (a)) is positive, indicating tensile State, whereas that for the 6-iNCh and 10-iNCh pavements (shown in Figure B-7 (c) and (e)) is negative, indicating compressive State. This observation is due mainly to the Poisson's effect. The generalized Hooke's law can explain this behavior, as shown in Equation(B.15).

$$\varepsilon_{zz} = \frac{1}{E} (\sigma_{zz} - \nu\sigma_{xx} - \nu\sigma_{yy}) \quad (\text{B.15})$$

where ε_{zz} is the strain in the z direction, σ_{xx} , σ_{yy} , and σ_{zz} are the normal stresses in x, y, and z directions, respectively, and ν is Poisson's ratio. As observed from Equation (B.15), large negative bending stress levels (σ_{xx} and σ_{yy}) in the 4-iNCh pavement can cause significant positive strain. This positive strain in z direction is causing damage in the 4-iNCh pavement. However, in the 6-iNCh and 10-iNCh pavements, bending stresses are not large enough to cause positive ε_{zz} under the wheel. Therefore, ε_{zz} under the wheel is in compression.

The strain-based method leads to large damage growth in the z direction when the tire is right on top of the pavement for the thin pavement. For the intermediate and thick pavement sections, the damage growth mechanism changes to negative bending for the top point. This outcome is due mainly to the fact that the thickness increment reduces the bending stress (i.e., σ_{xx} and σ_{yy}) while keeping the compressive stress constant. As a result, the direction of the axis of anisotropy lies along the global horizontal axis, which means that the angle should be zero (Figure B-6 (c) and (e)).

Figure B-6 indicates that the stress-based method switches the top-down damage growth mechanism for top-down cracking from the Poisson's effect-dominated criterion to the negative bending-governed criterion. The stress-based method increases the maximum induced pseudo

strain at the bottom of all the section layouts. Equation (B.16) is able to explain this observation more clearly. Figure B-5 (b), (d), and (f) show that the direction of the axis of anisotropy is oriented along the horizontal axis for the top and bottom points of different sections.

$$\varepsilon_{xx} = \frac{1}{E} (\sigma_{xx} - \nu\sigma_{yy} - \nu\sigma_{zz}) \quad (\text{B.16})$$

According to Equation (B.16), some part of σ_{yy} is subtracted from maximum induced stress σ_{xx} . In this way, the value of pseudo-strain calculated from the strain-based method is lower than the stress-based method. Equation (B.17) shows the value of pseudo strain from the stress-based method.

$$\varepsilon_{xx}^R = \frac{\sigma_{xx}}{C} \quad (\text{B.17})$$

Although the stress-based method leads to higher levels of bottom-up damage than the strain-based methodology due to the elimination of the Poisson's effect, it reduces the top-down cracking for all the sections. That reduction comes mainly from the fact that the Poisson's effect helps a pavement experience more top-down cracking by adding bending stress in different directions.

B.5.1. Damage Magnitude

Figure B-8 shows the maximum induced pseudo strain values that are obtained from the stress-based and strain-based methods and demonstrates the damage direction effect on the pseudo strain distribution that is obtained from different pavement structures.

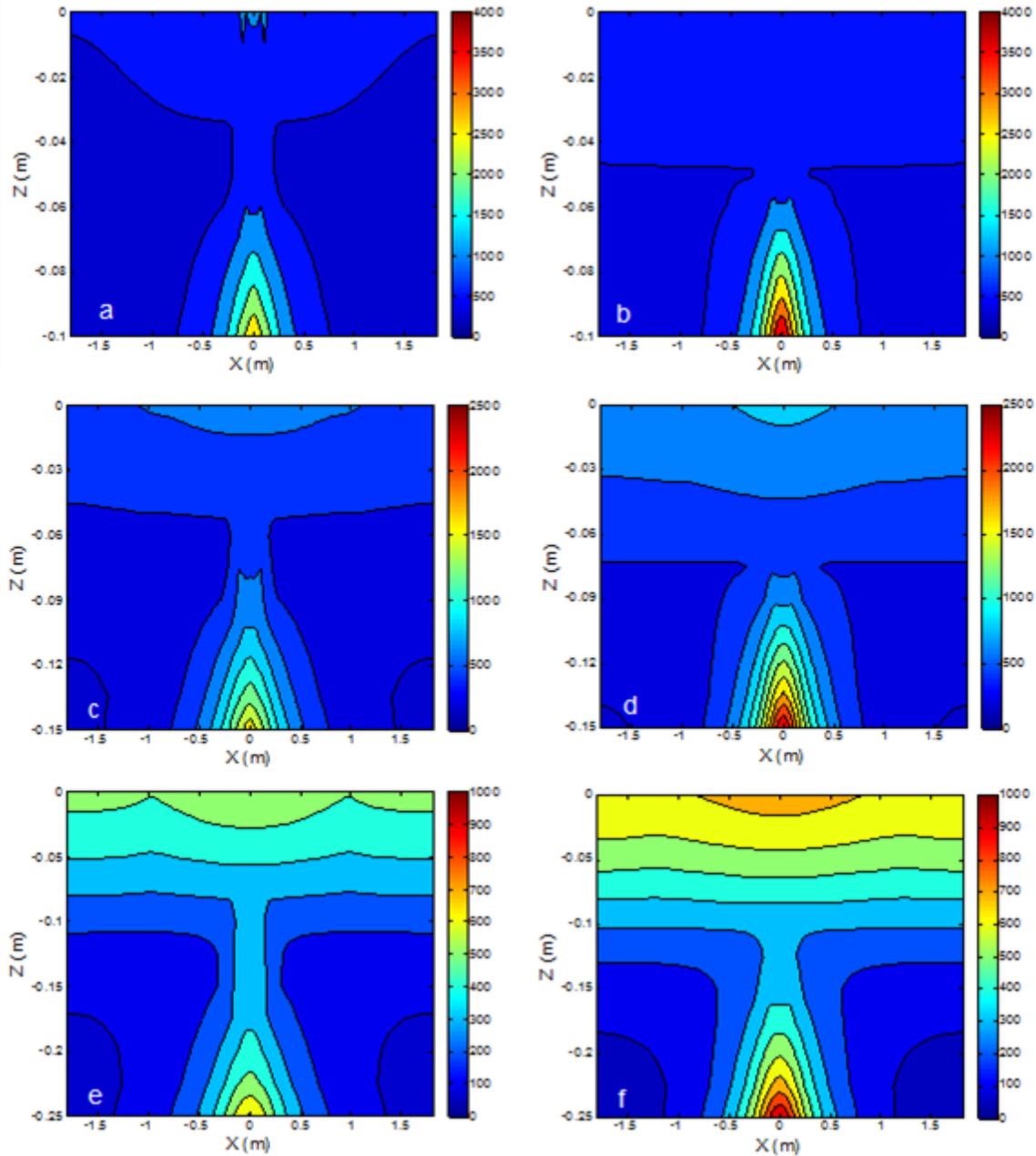


Figure B-8. Maximum developed pseudo strain obtained from different direction scenarios for all section layouts: (a) 4-iNCh pavement, strain-based, (b) 4-iNCh pavement, stress-based, (c) 6-iNCh pavement, strain-based, (d) 6-iNCh, stress-based, (e) 10-iNCh pavement, strain-based, and (f) 10-iNCh, stress-based

Figure B-9 shows the amount of cracking for all pavement sections as obtained from the stress-based and strain-based methodologies. As discussed in the previous chapter, damage calculation mechanism which is based on stress-based method, reduces the top-down cracking while increases the bottom-up cracking.

As mentioned before, the value of pseudo strain is given the power of 2α . In this way, small increase in calculated pseudo stiffness can give a huge increase in the value of calculated damage. The effects of this changes are shown in Figure B-8. Figure B-8 shows the stress-based method gives much more bottom-up cracking in comparison with strain-based. Figure B-9 (a) shows much more top-down cracking in comparison with Figure B-8 (d). This damage shown in Figure B-9 (a) comes from the Poisson's effect. Comparing the value of induced pseudo strain from either method would lead to conclusion that the bottom-up cracking should be more severe in stress-based method.

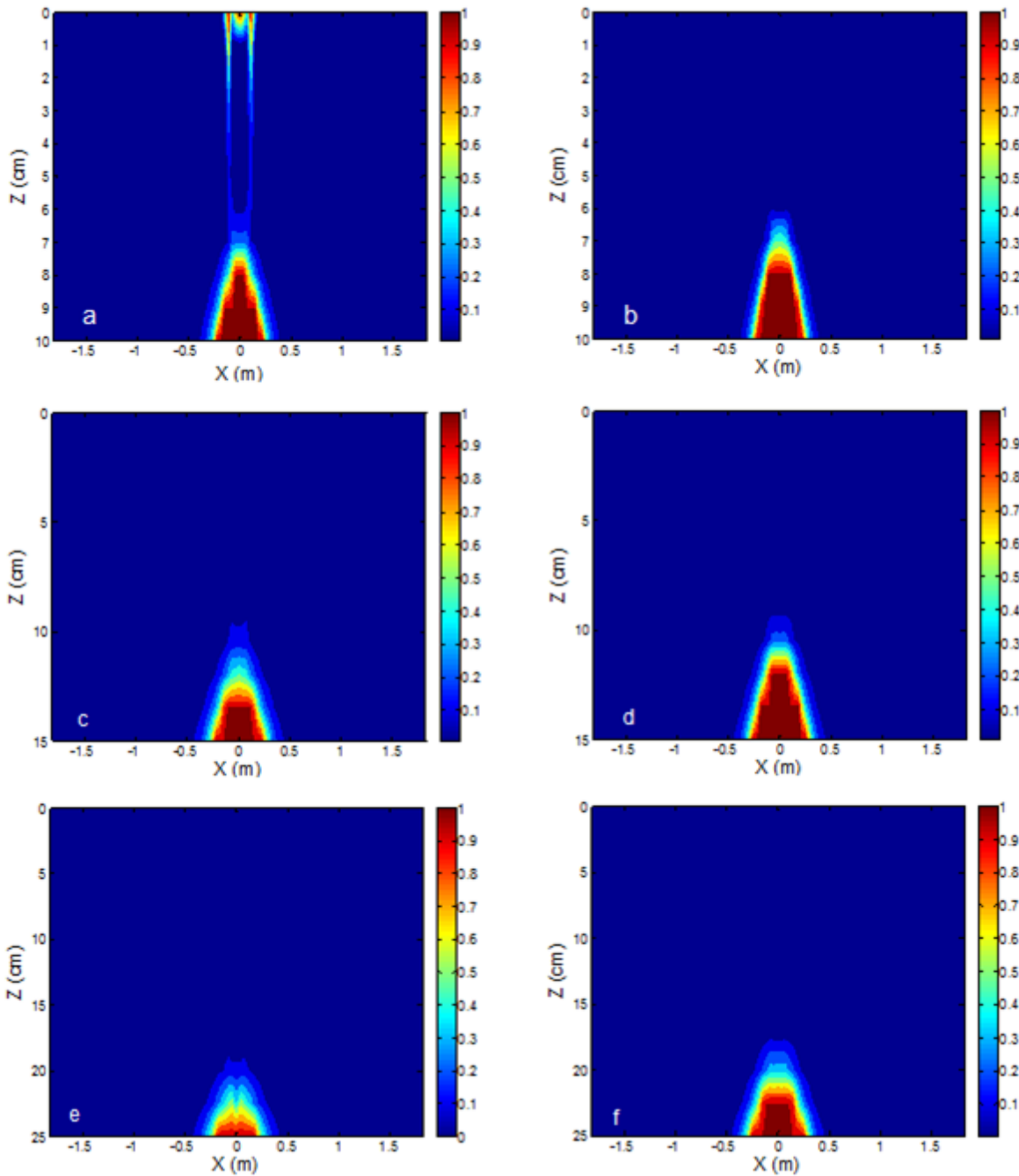


Figure B-9. Damage contours after 20 years of traffic loading obtained from different direction scenarios for all section layouts: (a) 4-iNCh, strain-based, (b) 4-iNCh, stress-based, (c) 6-iNCh, strain-based, (d) 6-iNCh pavement, stress-based, (e) 10-iNCh pavement, strain-based, and (f) 10-iNCh, stress-based